

A NEAR-INFRARED SELECTED GALAXY REDSHIFT SURVEY



GEORG FEULNER

A NEAR-INFRARED SELECTED GALAXY REDSHIFT SURVEY

Dissertation

an der
Fakultät für Physik
der
Ludwig-Maximilians-Universität München

vorgelegt von

Georg Feulner
aus Wasserburg am Inn

München, den 22. Oktober 2004

1. Gutachter: Prof. Dr. Ralf Bender
2. Gutachter: Prof. Dr. Harald Lesch

Tag der mündlichen Prüfung: 22. Dezember 2004

Für

Theodor Feulner

1931 — 1984

Zusammenfassung (Summary)

Galaxien, gravitativ gebundene Systeme bestehend aus Sternen, Gas, Staub und Dunkler Materie, haben sich aus kleinen Dichtefluktuationen im frühen Universum gebildet. Diese kollabieren aufgrund ihrer Eigengravitation, im Gas bilden sich Sterne, die wiederum im Laufe ihres Daseins das umgebende Medium mit schweren Elementen anreichern. Galaxien sind also laufend Veränderungen unterworfen. Diese Entwicklung der Galaxien im Universum zu verstehen gehört zu den wichtigen Zielen der modernen Astrophysik.

Die Entwicklung läßt sich verfolgen, indem man Galaxien bei verschiedenen Entfernungen untersucht. Dank der endlichen Ausbreitungsgeschwindigkeit des Lichtes kann man so Galaxien zu verschiedenen kosmischen Zeiten beobachten. Dazu muß die Entfernung, bestimmt über die kosmologische Rotverschiebung z , für sehr viele Galaxien gemessen werden. Dies kann beispielsweise durch die spektroskopische Vermessung von Spektrallinien geschehen.

In dieser Arbeit präsentiere ich eine von mir konzipierte, durchgeführte und ausgewertete spektroskopische Durchmusterung von Galaxien, die aus einem Katalog von Nahinfrarotgalaxien ausgewählt wurden. Diese spektroskopische Untersuchung wird ergänzt durch eine umfangreichere im sichtbaren Licht ausgewählte Durchmusterung, für die die Rotverschiebung aus der Helligkeit bei verschiedenen Wellenlängen zwischen 4500\AA und 22000\AA ermittelt wurde. Neben der Diskussion der Beobachtungen und Datenanalyse steht vor allem die Untersuchung von Galaxien bei verschiedenen Rotverschiebungen bis $z = 1$ im Vordergrund. Dies entspricht etwa einer Zeit, zu der das Universum nicht einmal halb so alt war wie heute.

Dabei konnte gezeigt werden, daß sich die Leuchtkraftfunktion, das heißt die differentielle Verteilung der Galaxienleuchtkräfte, in den letzten 8 Mrd. Jahren deutlich entwickelt hat: Mit wachsender Rotverschiebung ist eine Zunahme der Helligkeit bei gleichzeitiger Abnahme der Anzahldichte feststellbar. Dieser Effekt ist bei kürzeren Wellenlängen ausgeprägter als bei längeren.

Weiterhin wurde die Sternentstehungsrate der Galaxien gemessen, die im gleichen Zeitraum mit der Rotverschiebung ansteigt. Dieser Anstieg wurde mit einem analytischen Modell verglichen, das aus numerischen Simulationen der Galaxienentwicklung abgeleitet wurde. Es zeigt sich, daß dieser Anstieg flacher verläuft als bisher gemessen, aber gut mit der Vorhersage des angesprochenen Modells übereinstimmt.

Schließlich wurde der Zusammenhang zwischen Sternentstehungsrate und stellarer Masse untersucht. Es zeigt sich, daß sich das Anwachsen der Sternentstehungsrate mit zunehmender Rotverschiebung über alle stellaren Massen verteilt, im Gegensatz zu früheren Untersuchungen, die vor allem die massereichen Systeme für diesen Anstieg verantwortlich machten. Außerdem zeigt sich, daß die massereichsten Galaxien bei allen Rotverschiebungen die ältesten Sterne enthalten.

Contents

German Summary (Zusammenfassung)	vii
List of Figures	xii
List of Tables	xiii
List of Abbreviations & Acronyms	xv
1 Studying Galaxy Evolution with Redshift Surveys	1
1.1 The Formation of Galaxies in the Universe	1
1.2 Observing Galaxies at Low and High Redshift	13
1.3 Statistical Properties of Galaxies	21
1.4 Thesis Outline	28
2 The Munich Near-Infrared Cluster Survey	29
2.1 Introduction	29
2.2 The MUNICS Project	30
2.3 MUNICS <i>B</i> -Band Imaging	32
2.4 MUNICS-Deep	34
3 A Near-Infrared–Selected Redshift Survey	35
3.1 Selection of the Spectroscopic Sample	35
3.2 Spectroscopic Observations	37
4 Analysing Multi-Object Spectroscopy Data	41
4.1 Motivation	41
4.2 Basic Data Reduction	42
4.3 MOS Reduction	43
4.4 Catalogue Construction	48
5 The Spectroscopic Catalogue and its Properties	53
5.1 Number of Spectra and Object Classes	53
5.2 Confidence Classes	53
5.3 Redshift Distribution	54
5.4 Accuracy of Redshift Determination	55
5.5 Colours, Magnitudes, and Redshifts	57

5.6	Redshift Sampling Rate and Sky Coverage	58
5.7	Redshift Success Rate	61
5.8	Extremely Red Objects	62
5.9	Test of Object Classification	63
5.10	Stars in the Spectroscopic Catalogue	63
6	Near-Infrared Galaxy Luminosity Function	67
6.1	Introduction	67
6.2	Computing the Luminosity Function	68
6.3	Converting to Absolute Magnitudes	70
6.4	The <i>K</i> -band Luminosity Function	71
6.5	The <i>J</i> -band Luminosity Function	72
6.6	KS Tests of Luminosity Function Evolution	75
6.7	Likelihood Analysis of Luminosity Function Evolution	79
6.8	Improved Local Luminosity Functions from the 6dFGS	81
6.9	Luminosity Functions: The Connection to Theory	85
6.10	Comparison to Galaxy Formation Models	88
7	Construction of Optically Selected Catalogus	91
7.1	Catalogue Construction	91
7.2	Photometric Redshifts	95
7.3	Star–Galaxy Separation	103
8	Evolution of Optically Selected Galaxies	105
8.1	Comparison of <i>I</i> - and <i>K</i> -Band Selected Galaxies	105
8.2	Luminosity Functions	108
8.3	The Galaxy Luminosity Density	115
8.4	The Star-Formation Rate Density	118
8.5	Downsizing: Connecting Star Formation and Mass	122
9	Summary and Conclusions	131
9.1	Summary of Results	131
9.2	Interpretation	134
A	Spectroscopic Completeness	159
B	Comparison of Photometry	161
C	Selection of PSF Stars	165
	Acknowledgements	177
	Curriculum Vitae (Lebenslauf)	179

List of Figures

1.1	Primordial nucleosynthesis	6
1.2	Temperature fluctuations in the CMB	9
1.3	Angular power spectrum of CMB from WMAP	11
1.4	Look-back time versus redshift	12
1.5	Photometric selection of galaxies in the ‘redshift desert’	19
1.6	Photometric selection of Lyman-break galaxies	20
1.7	The evolution of the stellar mass function	24
1.8	The cosmic star formation density	26
1.9	Downsizing: Cowie <i>et al.</i> (1996)	27
2.1	MUNICS field geometry	30
2.2	<i>B</i> -band galaxy number counts	33
3.1	Object classification in $J - K$ vs. K diagram and based on χ^2	37
4.1	Illumination function of MOSCA with Grism Green 500	44
4.2	Definition of extraction and sky apertures	45
4.3	Wavelength calibration lamp spectrum	47
4.4	Test of quality of flux calibration	48
4.5	Spectrum analysis and quality control plot	49
4.6	Confidence class examples	52
5.1	Redshift distribution	56
5.2	Large-scale structure in S2F1 and S6F5	57
5.3	Histogram of redshift differences; comparison to SDSS EDR	58
5.4	Colour and magnitude distributions, part 1	59
5.5	Colour and magnitude distributions, part 2	60
5.6	Redshift sampling rate	61
5.7	Redshift success rate	61
5.8	Sky coverage	62
5.9	Comparison of photometric and spectroscopic object classification	64
5.10	$V - J$ colour histogram of stars	64
5.11	Composite stellar spectra	65
6.1	$k(z)$ corrections	71
6.2	K -band luminosity function from spectroscopic observations	73

6.3	<i>J</i> -band luminosity function from spectroscopic observations	74
6.4	Kolmogorov–Smirnov test for M_K : MUNICS <i>versus</i> local samples . .	76
6.5	Kolmogorov–Smirnov test for M_J : MUNICS <i>versus</i> local samples . .	76
6.6	Kolmogorov–Smirnov test for M_K and M_J for different redshifts . . .	77
6.7	Likelihood estimate for luminosity function evolution	81
6.8	6dFGS-DR1: Redshift histogram and luminosity functions	84
6.9	LF evolution based on 6dFGS	85
6.10	Halo mass function and galaxy luminosity function	87
6.11	Comparison of <i>K</i> -band luminosity function to semi-analytic models .	89
7.1	Completeness fractions for MUNICS_I and MUNICS_B	94
7.2	Template galaxy SEDs, distribution of SED types	96
7.3	Photometric redshift examples	97
7.4	Photometric redshift histograms	99
7.5	Comparison of photometric and spectroscopic redshifts	100
7.6	Comparison of <i>K</i> , <i>I</i> and <i>B</i> -selected photometric redshifts	101
7.7	M_I and M_B versus photometric redshift	102
7.8	Comparison of photometric and spectroscopic object classification . .	104
8.1	Colour distribution of <i>K</i> , <i>I</i> and <i>B</i> -band selected galaxies	107
8.2	Photometric redshift probability distributions	108
8.3	Selection effects and the LF	110
8.4	MUNICS_I: <i>B</i> -band LF	111
8.5	MUNICS_I: <i>B</i> -band LF evolution	112
8.6	MUNICS_I: <i>I</i> -band LF	113
8.7	MUNICS_I: <i>I</i> -band LF evolution	114
8.8	MUNICS_I: <i>K</i> -band LF	115
8.9	MUNICS_I: <i>K</i> -band LF evolution	116
8.10	MUNICS_I: Evolution of LF in <i>B</i> , <i>I</i> and <i>K</i>	117
8.11	MUNICS_I: Galaxy luminosity density	119
8.12	Star formation rate density from MUNICS & FDF	121
8.13	Downsizing: SFR <i>versus</i> M_K	123
8.14	Downsizing: [OII] equivalent width <i>versus</i> M_K	124
8.15	Downsizing: Specific SFR <i>versus</i> stellar mass (MUNICS_I)	125
8.16	Downsizing: Specific SFR <i>versus</i> stellar mass (MUNICS_B)	126
8.17	Downsizing: Specific SFR <i>versus</i> stellar mass (MUNICS_K)	127
8.18	Downsizing: Specific SFR <i>versus</i> stellar mass for different ages . . .	128
8.19	Evolution of SSFR with redshift	129
A.1	Completeness of spectroscopy in MUNICS	160
B.1	MUNICS_K & MUNICS_I: Comparison of photometry	161
B.2	MUNICS_I & MUNICS_B: Comparison of photometry	163
C.1	Selection of PSF stars in the MUNICS fields	166

List of Tables

1.1	Cosmological parameters from WMAP	3
1.2	Important cosmic epochs	8
1.3	Galaxies at $z > 5$	22
2.1	Completeness limits for MUNICS	31
2.2	MUNICS fields	31
2.3	MUNICS B -band observations and calibration	32
3.1	Results of test of image-based object classification	36
3.2	Observing runs	38
3.3	Technical characteristics of spectrographs	39
3.4	Typical exposure times of spectroscopic observations	39
4.1	Description of confidence classes	50
4.2	Small part of spectroscopic catalogue	51
5.1	Spectroscopy of MUNICS fields	54
5.2	Distribution of confidence classes	55
6.1	K -band luminosity function data	77
6.2	J -band luminosity function data	78
6.3	Kolmogorov–Smirnov test for M_K : MUNICS <i>versus</i> local samples	78
6.4	Kolmogorov–Smirnov test for M_J : MUNICS <i>versus</i> local samples	79
6.5	Summary: Measurements of the K -band luminosity function	82
6.6	Summary: Measurements of the J -band luminosity function	83
6.7	Summary: Measurements of the H -band luminosity function	83
7.1	Number of detected objects	93
7.2	Parameters of analytic approximation to redshift histograms	101
8.1	MUNICS_I: Schechter parameters	117
8.2	MUNICS_I: LF evolution	118
8.3	Slope of SFRD at low redshift: Previous results	120
8.4	Slope of SFRD at low redshift: Best-fitting parameters	122

List of Abbreviations & Acronyms

To help readers from a non-astronomical background to find their way in the jungle of astronomical abbreviations and acronyms, the meaning of (hopefully) all of those which can be found in this work is given below. Common abbreviations for astronomical journals which are used in the bibliography of this thesis are set in italics.

2dFGRS	2-degree Field Galaxy Redshift Survey
2MASS	2-Micron All-Sky Survey
<i>A&A</i>	<i>Astronomy and Astrophysics</i>
ACS	Advanced Camera for Surveys
AGN	Active Galactic Nucleus, Nuclei
<i>AJ</i>	<i>The Astronomical Journal</i>
<i>ApJ</i>	<i>The Astrophysical Journal</i>
<i>ApJS</i>	<i>The Astrophysical Journal Supplement Series</i>
<i>ARA&A</i>	<i>Annual Reviews of Astronomy and Astrophysics</i>
Boojums	Blue Objects Observed Just Undergoing Moderate Starburst
CAFOS	Calar Alto Faint Object Spectrograph
CCD	Charge-Coupled Device
CDFS	Chandra Deep Field South
CfA	Harvard-Smithsonian Center for Astrophysics
CFRS	Canada–France Redshift Survey
CMB	Cosmic Microwave Background
COBE	Cosmic Background Explorer
DRG, DRGs	Distant Red Galaxy, Galaxies
EFOSC	ESO Faint Object Spectrograph
ERO, EROs	Extremely Red Object, Objects
ESO	European Southern Observatory
FDF	FORS Deep Field
FP	Fundamental Plane (of elliptical galaxies)
FORS	FOcal Reducer and Spectrograph
FWHM	Full Width at Half Maximum

GOODS	Great Observatories Origins Deep Survey
HDF	Hubble Deep Field
HET	Hobby-Eberly Telescope
HST	Hubble Space Telescope
IMF	Initial Mass Function
IRAF	Image Reduction and Analysis Facility
IRAM	Institut de Radio Astronomie Millimétrique
IRAS	InfraRed Astronomical Satellite
JCMT	James Clerk Maxwell Telescope
LAE, LAEs	Lyman-Alpha Emitter, Emitters
LBG, LBGs	Lyman-Break Galaxy, Galaxies
LF, LFs	Luminosity Function, Functions
LRS	Low-Resolution Spectrograph
<i>MNRAS</i>	<i>Monthly Notices of the Royal Astronomical Society</i>
MOS	Multi-Object Spectroscopy
MOSCA	Multi-Object Spectrograph for Calar Alto
MUNICS	MUnich Near-Infrared Cluster Survey
NICMOS	Near-Infrared Camera and Multi-Object Spectrometer
<i>PASJ</i>	<i>Publications of the Astronomical Society of Japan</i>
<i>PASP</i>	<i>Publications of the Astronomical Society of the Pacific</i>
<i>Phys. Rev.</i>	<i>Physical Review</i>
PSF	Point-Spread Function
RMS	Root Mean Square
SAM, SAMs	Semi-Analytic Model, Models
SCUBA	Sub-mm Common-User Bolometer Array
SDSS	Sloan Digital Sky Survey
SED	Spectral Energy Distribution
SFH	Star Formation History
SFR	Star Formation Rate
SFRD	Star Formation Rate Density
SPIE	Society of Photo-optical Instrumentation Engineers
SSFR	Specific Star-Formation Rate
UDF	(Hubble) Ultra Deep Field
ULIRG, ULIRGs	Ultra-Luminous InfraRed Galaxy, Galaxies
UV	Ultra-Violet
VLT	Very Large Telescope
WFPC 1, 2	Wide-Field Planetary Camera 1, 2
WMAP	Wilkinson Microwave Anisotropy Probe

Chapter 1

Introduction: Studying Galaxy Evolution with Redshift Surveys

In this thesis results for the evolution of galaxies derived from a near-infrared selected galaxy redshift survey are presented. This chapter will provide an introduction to cosmology and galaxy formation (Section 1.1; see, e.g., Peebles 1980, Carroll *et al.* 1992, Peebles 1993, Peacock 1999, Coles & Lucchin 1995, Longair 1998), followed by a brief outline of results concerning the selection of galaxies at different cosmic epochs and their characteristics (Section 1.2), and a summary of statistical properties of galaxy populations used to trace their evolution (Section 1.3). Readers who are only interested in a summary of techniques and results in the field of galaxy evolution are kindly asked to skip Section 1.1. However, I do believe it to be important to place research results in a broader context.

1.1 Setting the Stage: The Formation of Galaxies within the Framework of Cosmology

1.1.1 The Cosmological Standard Model

The evolution of the universe on large scales is governed by gravity which, on the other hand, is described by the *field equations* of Einstein's General Theory of Relativity (Einstein 1916, Weinberg 1972)

$$\mathcal{R}_{ij} - \frac{1}{2}\mathcal{G}_{ij}\mathcal{R} - \Lambda\mathcal{G}_{ij} = \frac{8\pi G}{c^4}\mathcal{T}_{ij}. \quad (1.1)$$

Here \mathcal{R}_{ij} and \mathcal{R} are the Ricci tensor and scalar, respectively (describing space curvature), \mathcal{G}_{ij} is the metric tensor (connected to space-time distances), G is the gravitational constant, c the speed of light, \mathcal{T}_{ij} is the energy-momentum tensor (describing the energy and mass density), and Λ is the cosmological constant (Weinberg 1972). In brief, the field equations characterise the interaction between mass (or energy) and the curvature of space: Mass curves space-time, and a curved space-time in turn affects the motion of particles in a way which was classically described as gravitational force.

The cosmological principle states that the universe is homogeneous and isotropic on large scales. This assumption was not invented to make physicists' lives easier, of course, but can to some extent be verified for large cosmic scales. In this case the metric of the universe fortunately takes a simple form known as the *Robertson-Walker metric* (Robertson 1935, 1936a, b, Walker 1935):

$$ds^2 = c^2 dt^2 - R^2(t) \left[\frac{dr^2}{1-kr^2} + r^2 (d\theta^2 + \sin^2 \theta d\phi^2) \right] \quad (1.2)$$

Here (r, θ, ϕ, t) are the space-time coordinates, $R(t)$ is an unknown function describing the dynamic evolution of the universe, and k can – by choice of units for r – be fixed to $+1$, 0 or -1 for positively curved, flat and negatively curved space, respectively (Weinberg 1972).

Using this form of space-time metric, relatively simple formulae can be derived for the dynamic behaviour of the universe (Friedmann 1922). These *Friedmann equations* read

$$\begin{aligned} \dot{R}^2 &= \frac{8\pi G}{3} \rho R^2 + \frac{1}{3} c^2 \Lambda R^2 - k c^2 \\ \ddot{R} &= -\frac{4\pi G}{3} R \left(\rho + 3 \frac{p}{c^2} \right) + \frac{1}{3} c^2 \Lambda R \end{aligned} \quad (1.3)$$

In these equations, ρ denotes the total energy density of the universe, p is the pressure, Λ is the cosmological constant, and k is the curvature of space, i.e. $k = +1$ for a closed, $k = -1$ for an open, and $k = 0$ for a flat universe (Weinberg 1972). This geometrical curvature of space is governed by the density of the universe. Together with a knowledge of the equation of state $p(\rho)$ the Friedmann equations can be solved for $R(t)$. Furthermore we define the critical density ρ_c as

$$\rho_c \equiv \frac{3H^2}{8\pi G} \quad (1.4)$$

where the famous *Hubble parameter* H , the current value of which, usually just called the *Hubble constant*

$$H_0 \equiv H(t_0) \equiv h 100 \text{ km s}^{-1} \text{ Mpc}^{-1}, \quad (1.5)$$

impertinently tried to escape from precise determination for decades, is given by the rate of expansion of the universe,

$$H = \frac{\dot{R}}{R}. \quad (1.6)$$

The we can re-write the first of the two Friedmann equations in the following form:

$$\frac{kc^2}{H^2 R^2} = \Omega_m + \Omega_r + \Omega_\Lambda - 1 \quad (1.7)$$

Table 1.1: Cosmological parameters from WMAP and combination of WMAP with other data (Spergel *et al.* 2003), except for $\Omega_{r,0}$.

Quantity	Value	Comment
$\Omega_{r,0}$	$\sim 10^{-4}$	radiation, relativistic particles (Peacock 1999)
$\Omega_{b,0}$	0.047 ± 0.006	baryonic matter
$\Omega_{m,0}$	0.29 ± 0.07	baryonic and dark matter
$\Omega_{\Lambda,0}$	0.73 ± 0.07	dark energy, computed from $\Omega_{\text{tot},0} - \Omega_{m,0}$
$\Omega_{\text{tot},0}$	1.02 ± 0.02	total density budget
h	0.72 ± 0.05	Hubble constant

where we have defined the *density parameters* Ω for the matter component (Ω_r), for the radiation and relativistic particles (Ω_r) and for the cosmological constant Λ (Ω_Λ), respectively, by setting

$$\Omega \equiv \frac{\rho}{\rho_c}. \quad (1.8)$$

Quite obviously, the curvature of the universe (as represented by the constant k) is directly connected to the density parameter(s) of the universe: If they add up to one, then space is flat ($k = 0$). It also shows that the knowledge of the density parameters of the universe's constituents and the knowledge of the Hubble constant suffice to describe the evolution of the scale factor.

Note that the density parameters are time-dependent quantities and scale differently with redshift: $\Omega_\Lambda(z) = \Omega_{\Lambda,0}$, $\Omega_m(z) = \Omega_{m,0}(1+z)^3$ and $\Omega_r(z) = \Omega_{r,0}(1+z)^4$. According to measurements of the cosmic microwave background (combined with other cosmological experiments), the contributions of the main constituents of the universe can be found in Table 1.1.

One family of world models described by the Friedmann equations are models for an expanding universe. After Hubble's discovery of the redshift-distance relation (Hubble 1929), which was soon interpreted as evidence for a cosmological expansion, the Big Bang model for the history of the universe emerged. In this scenario, the universe expands from a hot initial state. The precise history of this expansion is governed by the energy content of the cosmos.

1.1.2 The Cosmological Redshift

In the first half of the 20th century, it was discovered that the spectral lines of galaxies are, in general, shifted towards longer wavelength.¹ To quantify this shift, we define the redshift z of a galaxy as

¹Local gravitational attraction results in peculiar velocities superimposed on the general fbw. Hence some very near-by galaxies like the Andromeda galaxy show blue-shifted spectra.

$$z \equiv \frac{\lambda_{\text{obs}} - \lambda_{\text{emit}}}{\lambda_{\text{emit}}}, \quad (1.9)$$

where λ_{obs} is the observed wavelength of a spectral line, while λ_{emit} is the wavelength as emitted by the galaxy.

This redshift of galaxies is interpreted as a result of the universe's expansion. As shown above, assuming that the universe is homogeneous and isotropic, the expansion is described by the variation of the scale factor $R(t)$, and it can be easily shown that

$$1 + z = \frac{R(t_{\text{obs}})}{R(t_{\text{emit}})}, \quad (1.10)$$

where the evolution of the scale factor $R(t)$ is governed by the Friedmann equations (1.3).

1.1.3 The Early Phases in the Life of the Universe

The Planck Epoch

We will briefly summarise the early stages in the universe's life. The cosmos starts out in an era where it was governed by the weird (and unknown) laws of quantum gravity. This period, known as the *Planck epoch*, is characterised by the Planck time $t_{\text{p}} \simeq 10^{-43}$ s.² Classical gravity is invalid during this epoch, and since we lack a theory of quantum gravity any physical phenomena at these times belong to the realm of speculation.

Inflation

Cosmic inflation, a phase of exponential expansion of the universe at $t \sim 10^{-35}$ s (Guth 1981, see Narlikar & Padmanabhan 1991 for a review), has been proposed to solve

²The Planck time t_{p} (as well as the Planck length ℓ_{p} and the Planck mass m_{p}) is given by a 'natural' combination of the fundamental constants G (the gravitational constant), c (the speed of light in vacuum) and h (Planck's constant):

$$\begin{aligned} t_{\text{p}} &= \left(\frac{Gh}{c^5} \right)^{1/2} \simeq 10^{-43} \text{ s} \\ \ell_{\text{p}} &= \left(\frac{Gh}{c^3} \right)^{1/2} \simeq 10^{-35} \text{ m} \\ m_{\text{p}} &= \left(\frac{hc}{G} \right)^{1/2} \simeq 10^{-7} \text{ kg} \end{aligned} \quad (1.11)$$

(1.12)

Planck introduced these quantities as part of a truly universal system of units which Planck advertised as "Einheiten [...], welche [...] ihre Bedeutung für alle Zeiten und für alle, auch ausserirdische und aussermenschliche Culturen nothwendig behalten und welche daher als «natürliche Maasseinheiten» bezeichnet werden können." (Planck 1899) The Planck mass can also be derived equalling the Schwarzschild radius $r_{\text{S}} = 2Gm/c^2$ and the Compton wavelength $\lambda_{\text{C}} = h/(mc)$, thus illustrating its meaning as the transition to quantum gravity.

several intriguing difficulties of the standard model, but may also serve as a source of the initial fluctuations needed for forming structures in an otherwise rather boring homogeneous universe (see Section 1.1.4).

One of the problems of the standard model is the ‘flatness problem’, or the question: Why is the curvature of the cosmos so close to zero? Inflation solves this naturally: A small region of space, exponentially expanded to very many times its original size, will finally have a flat geometry – (almost) irrespective of its initial curvature.

In much the same way inflation also solves the ‘horizon problem’: Why does the cosmos look so similar everywhere, although its individual parts cannot all have been causally connected given the finite speed of light? Again, a phase of exponential expansion, where the universe observed today originates from a small, causally connected region of space could solve this problem.

The Thermal History of the Universe

The early history of our cosmos is largely governed by its temperature. To understand this *thermal history* it is essential to know the way temperature evolves with cosmic time. A hot initial state with steadily decreasing temperature is one of the key ingredients of the hot big bang model which so successfully explains things like cosmic nucleosynthesis and the cosmic microwave background radiation discussed below. The temperature of the radiation filling the universe is related to the expansion. Assuming that we measure a temperature T_0 for the background radiation field today, the temperature T_r of the radiative component scales with the redshift z in the following way:

$$T_r = T_0(1 + z) \quad (1.13)$$

This can be derived from the energy density ϵ_r of black body radiation which is $\epsilon_r \propto T^4$. On the other hand, this energy density is proportional to the number density n of photons times their energy $h\nu$. From the fact that $n \propto (1 + z)^3$ and $\nu \propto (1 + z)$ (the cosmic redshift), equation (1.13) follows immediately.

Big Bang Nucleosynthesis

During the first few minutes after the Big Bang, the light elements deuterium (D or ${}^2_1\text{H}$), helium (${}^3_2\text{He}$ and ${}^4_2\text{He}$) and lithium (${}^7_3\text{Li}$) were formed in a process named primordial nucleosynthesis (Boesgaard & Steigman 1985, Tytler *et al.* 2000). Heavier elements cannot be produced because of the lack of stable elements with atomic masses of 5 and 8, and because of the increasing importance of the Coulomb barrier, particularly in a cooling universe. Within the standard model, primordial nucleosynthesis is one of the key tests of the hot big bang scenario because it makes relatively precise predictions for the relative abundances of those light elements depending on *only one* cosmological parameter, the baryon-to-photon ratio $\eta \equiv n_b/n_\gamma$ (see Figure 1.1).³ The other two

³*Baryons* are all strongly interacting elementary particles with half-integral spin and relatively high mass. They consist of three quarks. Prominent examples are the nucleons, protons and neutrons. The two other particle families are the *leptons* (no strong interaction, relatively low mass, half-integral spin, e.g.

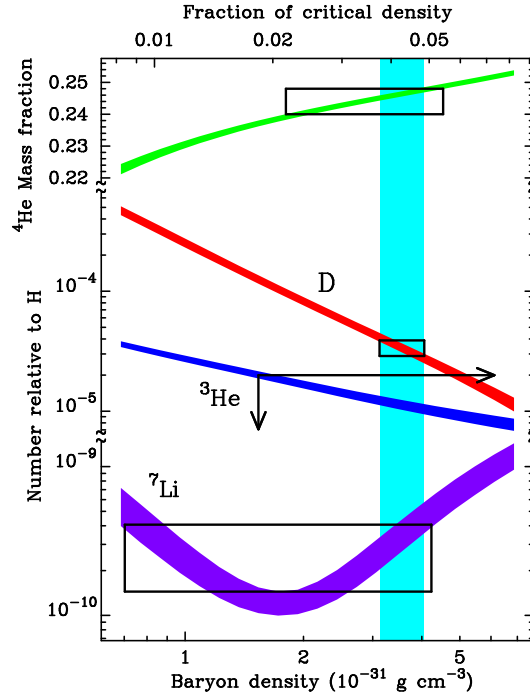


Figure 1.1: Abundances of light elements as a function of the baryon-to-photon ratio η (here expressed by the baryon density) as predicted by models of big bang nucleosynthesis (for $h = 0.65$; taken from Tytler *et al.* 2000). The rectangles represent the 95% confidence regions for measured abundances.

important parameters for primordial nucleosynthesis are the number of neutrinos and the decay time of the neutron.

The general trend with η in Figure 1.1 can be easily understood: The higher the baryon density, the earlier nucleosynthesis starts, and hence the more nucleons end up in heavier elements. The dip in the abundance of lithium is due to the fact that ${}^7_3\text{Li}$ is produced via two channels, either ${}^4_2\text{He}({}^3_1\text{H}, \gamma){}^7_3\text{Li}$ or ${}^4_2\text{He}({}^3_2\text{He}, \gamma){}^7_4\text{Be}$ and subsequent decay (Yang *et al.* 1984).

The successful prediction of the observed abundance ratios of the light elements is a strong piece of evidence in favour of the hot big bang model.

Matter-Radiation Equality

In the beginning the universe was dominated by radiation, i.e. the energy density of radiation ε_r greatly exceeded the one contained in matter ε_m : $\varepsilon_r \gg \varepsilon_m$. However, since with cosmic time the radiative energy density drops off as $\varepsilon_r \propto T^4 \propto (1+z)^4$ (see equation (1.13)) while the matter energy density decreases with $\varepsilon_m \propto \rho \propto (1+z)^3$, there is a time when $\varepsilon_r = \varepsilon_m$: Matter and radiation contribute equal amounts to the cosmic energy budget. At this epoch (at $z_{\text{eq}} \simeq 3300$) of matter-radiation equivalence the universe

the electron and the neutrinos) and the *mesons* (integral spin, higher mass, e.g. the pions).

evolves from a radiation-dominated world to the matter-dominated universe we know today. Moreover, this is the time when density fluctuations in the matter component can begin to grow to form the structures observed today.

Recombination, Decoupling the the Surface of Last Scattering

At early times matter and radiation were tightly coupled by the process of Thomson scattering. However, as the universe expands, there is a dramatic shift in the rate between the typical collision time-scale and the time-scale for the cosmic expansion: While the collision time-scale τ_c grows as $\tau_c \propto \rho_m^{-1} \propto (1+z)^3$, the cosmic expansion evolves more slowly as $\tau_H \propto (1+z)^{-3/2}$ (for a matter-dominated universe). Hence there exists a transition period in cosmic history when scattering takes place on time-scales growing larger than the rate of cosmic expansion. This marked change in the history of the universe is known as the *decoupling* of radiation and matter.

At some point the coupling of matter and radiation certainly had to end: When the temperature fell to $T \lesssim 10^4$ K, the electrons and the ions combined for the first time in cosmic history, an event which is somewhat unfortunately known as the *epoch of recombination*. At that time, the intimate liaison between matter and radiation, mediated by the process of Thomson scattering of photons with free electrons, finally comes to a doleful end. However, this is not an instantaneous process: Ionisation degrees X of $X = 0.9$ is reached at $z \sim 1500$, $X = 0.5$ at $z \sim 1400$, and at $z \sim 1300$ the ionisation is still 10% ($X = 0.1$).

All this is closely related to the background radiation field which we will discuss below. The background photons were free to travel after decoupling, and the time when their optical depth τ was equal to one ($\tau = 1$) is known as the time of *last scattering*. These three time-scales are closely related but follow from different definitions. To clarify matters, I have summarised these epochs in Table 1.2.

The Cosmic Microwave Background

The cosmic microwave background is the relic radiation from the hot big bang. It was discovered by chance (Penzias & Wilson 1965, Dicke *et al.* 1965), although there had been theoretical considerations predicting this kind of radiation before.

The cosmic background radiation we observe today has a almost perfect blackbody spectrum⁴ corresponding to a temperature of $T = 2.726 \pm 0.002$ K (Fixsen *et al.* 1996). However, small temperature fluctuations of the order $\Delta T/T \sim 10^{-5}$ are observed in the CMB. These can be interpreted as signatures of density perturbations in the epoch of recombination and will be discussed in more detail in Section 1.1.4.

⁴According to Planck's law, the radiation intensity $B_\nu(T)$ emitted by a black body at temperature T and frequency ν is given by

$$B_\nu(T) = \frac{2h}{c^2} \frac{\nu^3}{\exp\left(\frac{h\nu}{kT}\right) - 1}, \quad (1.14)$$

where c is the speed of light, k is Boltzmann's constant, and h is Planck's constant.

Table 1.2: Summary of important epochs in the history of our universe showing their redshift, time, (radiation) temperature and definition. z_{eq} , z_{rec} and z_{dec} are calculated using the formulae given in Kolb & Turner (1990) with the cosmological parameters presented in Spergel *et al.* (2003).

Redshift	Time	Temperature	Event
	10^{-43} s	10^{32} K	Planck epoch: realm of quantum gravity
	10^{-35} s	10^{27} K	epoch of inflation (?): exponential expansion, first seeds of structure
	10^{-7} s	10^{14} K	formation of nucleons (protons and neutrons)
	15 min	10^8 K	end of primordial nucleosynthesis
$z_{\text{eq}} \simeq 3300$	0.06 Myr	9000 K	matter-radiation equality (energy densities equal: $\epsilon_r = \epsilon_m$)
$z_{\text{rec}} \simeq 1260$	0.43 Myr	3400 K	recombination (ionisation rate $X = 0.5$)
$z_{\text{dec}} \simeq 1160$	0.49 Myr	3200 K	decoupling (mean free path equal to Hubble radius: $\lambda = r_{\text{H}}$)
$z_{\text{ls}} \simeq 1100$	0.53 Myr	3000 K	“last scattering”: origin of CMB (optical depth $\tau = 1$) “dark ages”
$z \simeq 30$	0.1 Gyr	85 K	first stars (population III)
$z \simeq 17 \pm 5$	0.2 Gyr	49 K	re-ionisation complete (WMAP; Spergel <i>et al.</i> 2003)
$z = 6.6$	0.8 Gyr	21 K	highest redshift galaxy known today (Kodaira <i>et al.</i> 2003)
$z = 6.4$	0.9 Gyr	20 K	highest redshift quasar known today (Fan <i>et al.</i> 2003)
$z \sim 3$	2.2 Gyr	11 K	Lyman-break galaxies
$z \sim 2$	3.2 Gyr	8 K	cosmic star-formation rate of galaxies begins to decrease
$z \sim 1$	5.8 Gyr	6 K	redshift limit as probed by MUNICS
$z = 0$	13.7 Gyr	3 K	today

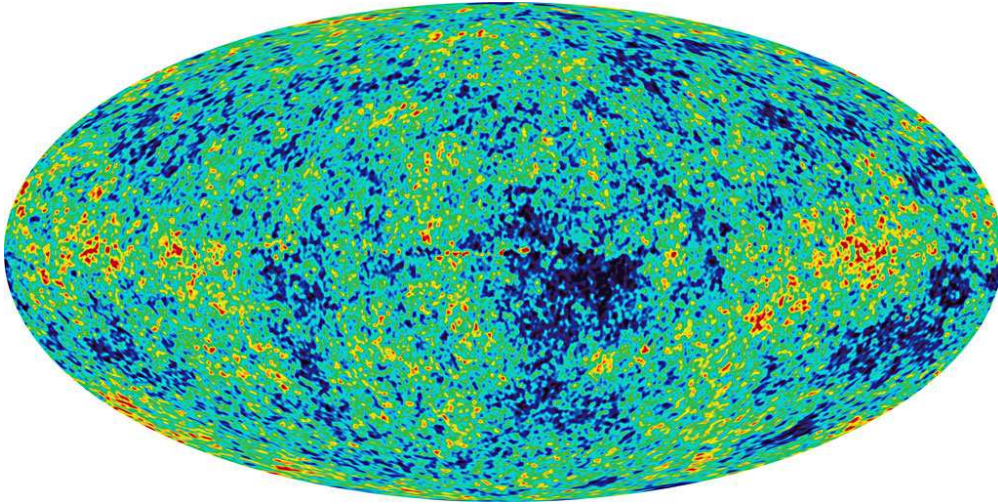


Figure 1.2: Temperature fluctuations in the cosmic microwave background as measured by WMAP (Spergel *et al.* 2003).

1.1.4 Formation of Structure in the Universe

The General Picture

The homogeneity of the universe on large scales is well established. It is also evident from the cosmic microwave background (CMB) the temperature of which is highly homogeneous with fluctuations $\Delta T/T \sim 10^{-5}$. Today, however, we observe prominent structure in the form of galaxies, clusters and super clusters. For example, the density in a galaxy is about 10^5 times the average density of the universe, and clusters of galaxies reach over-densities of $10^2 \dots 10^3$. So how did this structure form?

It is thought to have developed from small initial fluctuations in the universe’s density. The foot prints of these fluctuations can still be observed in the temperature variations in the CMB (see Figure 1.2). The microwave background mirrors the fluctuations at $z \sim 1100$, when, at the end of the epoch of recombination of electrons and ions, the universe became transparent to electromagnetic radiation (“surface of last scattering”).

These fluctuations then grew under the influence of the gravitational interaction mainly caused by the dark matter present in the universe. At a later time the baryonic gas streamed into these dark matter haloes, formed stars and thus created the luminous matter observed in galaxies.

The first stars, the so-called “population III stars”⁵, formed at redshifts $z \sim 20 \dots 30$ in mini dark-matter haloes of $\mathcal{M} \sim 10^6 M_{\odot}$. Due to the lack of heavy elements present in today’s stellar objects they had vastly different properties: Their typical masses were close to $\sim 100 M_{\odot}$, and they ended their brief life enriching the universe with the first

⁵The name ‘population III’ tries to extend the concept of stellar populations introduced by Baade (1944), defining ‘population I’ as containing luminous blue stars, dust and gas (like the Milky Way disk or open clusters), and ‘population II’ as composed of red stars with essentially no gas and dust (elliptical galaxies, bulges and globular clusters are examples).

heavy elements (Bromm & Larson 2004).

In a universe dominated by cold dark matter – which is the favoured model these days – galaxies grow hierarchically: The first structures to form are low-mass objects which then grow by subsequent merging to the massive galaxies observed today.

However, while the gravitational dynamics of cold dark matter can be easily modelled and very successfully explains the large-scale properties of the cosmic matter distribution, the situation on galaxy-size scales is less clear. The reason is the “dirty physics” of gas cooling, star formation, and stellar feedback on the surrounding gas which escapes detailed calculations by means of its complexity.

Linear Theory of Density Perturbations

Imagine small perturbations in the matter density ρ and the velocity field u which can be parameterised as $\rho(x, t) = \bar{\rho}(t)(1 + \delta(x, t))$ and $u = \dot{R}x + v$, where x are comoving coordinates, and the density contrast δ and the peculiar velocity v represent small perturbations. Inserting this into the basic equations of fluid dynamics, the equation of continuity, Euler’s equation and Poisson’s equation, neglecting higher order perturbations, and introducing Fourier transformed quantities $\delta(x, t) = \sum_k \delta_k(t) \exp(ik \cdot x)$, we obtain the linear perturbation equation for a matter-dominated universe

$$\frac{d^2 \delta_k}{dt^2} + 2 \frac{\dot{R}}{R} \frac{d\delta_k}{dt} - \left(4\pi G \bar{\rho} - \left(\frac{c_s k}{R} \right)^2 \right) \delta_k = 0, \quad (1.15)$$

where c_s is the sound speed. Equation (1.15) is a wave equation with decaying and non-decaying solutions. So how much do perturbations grow in our universe? We have already shown that at $z \sim 1100$ we observe temperature fluctuations in the CMB corresponding to density fluctuations in the baryonic component of $\delta_b \simeq 5 \cdot 10^{-5}$. How much would these fluctuations grow until today? For a universe with the density parameters $\Omega_{m,0} \simeq 0.3$ and $\Omega_\Lambda \simeq 0.7$ (similar to the ones given in Table 1.1), the growth of structure is about 80% of the growth observed in a Einstein-de Sitter universe with $\Omega_{m,0} = 1$, $\Omega_\Lambda = 0$ universe (Carroll *et al.* 1992). For the Einstein-de Sitter universe, the scale factor R grows as $R \propto t^{2/3}$, and the non-decaying solution of the linear perturbation equation as $\delta_k \propto t^{2/3} \propto R \propto (1+z)$. Thus, baryonic fluctuations of the amplitude observed in the CMB could grow to $\delta_b < 0.05$ today, much less than the density contrast observed in galaxies and clusters today. Hence “dark matter” is needed to explain the structures in our universe today!

Density Fluctuations and the Cosmic Microwave Background

One very important finding about the CMB is the existence of temperature fluctuations of the order $\Delta T/T \simeq 10^{-5}$ (see Figure 1.2). These are interpreted as imprints of still small density fluctuations in the early universe which are the seeds of the structure observed in the local universe: For adiabatic perturbations, fluctuations in temperature T are connected to variations in the baryonic density ρ_b by

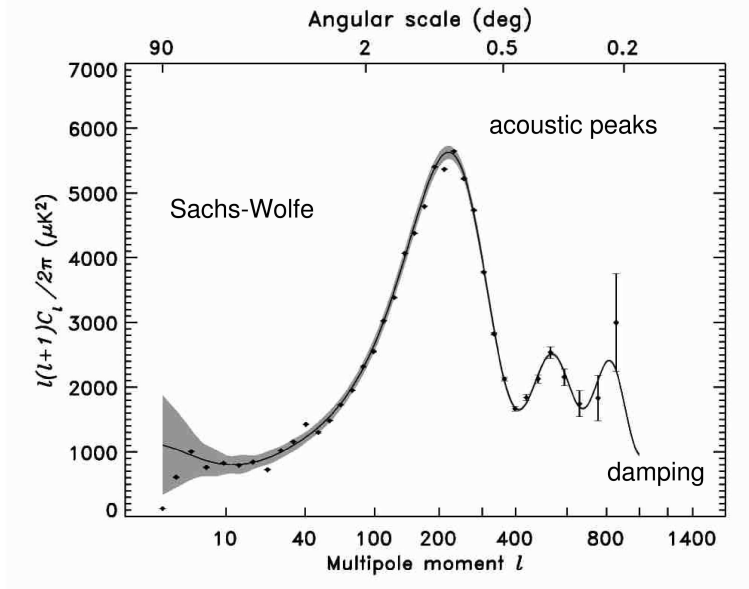


Figure 1.3: The angular power spectrum (more precisely $l(l+1)C_l/2\pi$ with C_l defined in equation (1.18)) of temperature fluctuations in the cosmic microwave background as measured by the WMAP satellite (points, Hinshaw *et al.* 2003) as well as the best-fitting model (line, Spergel *et al.* 2003).

$$\frac{\Delta\rho_b}{\rho_b} = 3 \frac{\Delta T}{T}. \quad (1.16)$$

Note that the power spectrum of these temperature fluctuations in the CMB are an efficient way to derive cosmological parameters (see e.g. Hu & Dodelson 2002, Scott & Smoot 2004).

To get the angular power spectrum, the temperature variations on the sky are expressed through a sum over spherical harmonics:

$$\frac{\Delta T(\theta, \phi)}{T} = \sum_{l=0}^{\infty} \sum_{m=-l}^{+l} a_{lm} Y_{lm}(\theta, \phi) \quad (1.17)$$

The angular power spectrum C_l is then computed from the coefficients a_{lm} by

$$C_l \equiv \langle |a_{lm}|^2 \rangle = \frac{1}{2l+1} \sum_{m=-l}^{+l} a_{lm} a_{lm}^* \quad (1.18)$$

The most accurate measurement of this angular power spectrum so far was done with the WMAP satellite and is shown in Figure 1.3 (Hinshaw *et al.* 2003).

The general shape of this curve can be understood in terms of three distinct effects. On large angular scales ($l \lesssim 100$) the dominant contribution is from the *Sachs-Wolfe effect* (Sachs & Wolfe 1967): Density fluctuations $\Delta\rho$ correspond to fluctuations in the

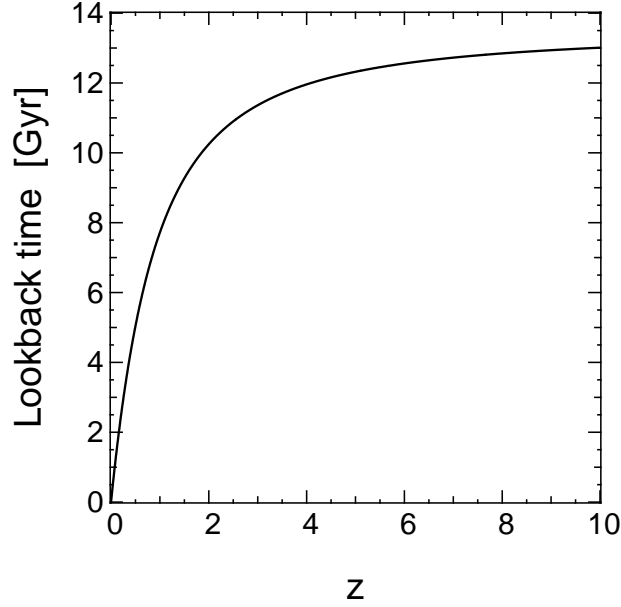


Figure 1.4: The cosmological look-back time versus redshift. A cosmology with $\Omega_m = 0.3$, $\Omega_\Lambda = 0.7$ and $H_0 = 70 \text{ km s}^{-1} \text{ Mpc}^{-1}$ was assumed.

gravitational potential $\Delta\Phi$ leading to (I) gravitational redshift and (II) time dilation for photons climbing out of the potential well:

$$\frac{\Delta T}{T} = \underbrace{\left(\frac{\Delta\Phi}{c^2}\right)}_{\text{I}} + \underbrace{\left(-\frac{2}{3} \frac{\Delta\Phi}{c^2}\right)}_{\text{II}} = \frac{1}{3} \frac{\Delta\Phi}{c^2} \quad (1.19)$$

The Sachs-Wolfe effect is responsible for the low- l plateau in the angular power spectrum shown in Figure 1.3.

At intermediate scales ($100 \sim l \lesssim 1000$) we can see prominent peaks in the angular power spectrum (see Figure 1.3). These are caused by gravity-driven acoustic oscillations before recombination and are thus called the *acoustic peaks*. The position of the peaks is connected to the sound horizon at the time of last scattering and therefore probes the curvature of the universe (i.e. Ω), while its height is governed by the baryon content Ω_b of the universe.

On the smallest scales ($1000 \lesssim l$) the oscillations are damped by two effects. The first is *Silk damping* (Silk 1968): Radiation diffuses out of the perturbation and the fluctuations are damped. The second effect is due to the finite thickness of the last-scattering ‘surface’: We expect a number of independent fluctuations smaller than this thickness along each line of sight, and we expect these random superpositions to statistically reduce the amplitudes of the oscillations.

1.1.5 Looking Back: Redshift and Galaxy Evolution

We live in an evolving universe. But how can we study the evolution of galaxies with cosmic time? Since the life times of human beings are much shorter than the age of the universe, we obviously cannot do this for individual galaxies. But due to the finite speed of light we can study galaxies at different epochs in the cosmological history: The higher the redshift at which we observe galaxies, the longer it took their light to travel to our telescopes, and thus the younger are the galaxies we see at this redshift. This is expressed by the cosmic look-back time, which is shown in Figure 1.4 for a “standard” cosmological model with $\Omega_m = 0.3$, $\Omega_\Lambda = 0.7$ and $H_0 = 70 \text{ km s}^{-1} \text{ Mpc}^{-1}$, close to the values determined by the Wilkinson Microwave Anisotropy Probe (WMAP; Spergel *et al.* 2003, see Table 1.1). With the MUNICS redshift survey described in this thesis, we can investigate the evolution of galaxy populations since $z \sim 1$, when the universe had only half of its present age.

1.2 The Evolution of Galaxies with Cosmic Time: Observing Galaxies From Low to High Redshift

In the last decades we have learned a lot about the evolution of galaxies in the universe. Much of this progress is due to improved observational techniques allowing us to study both larger samples of local galaxies and deeper samples probing galaxies out to redshifts $z \sim 5$ or beyond.

In principle we can distinguish several different methods to obtain samples of galaxies. Firstly, there are *wide-field surveys* which, being usually not very deep, provide large numbers of galaxies at lower redshifts. Secondly, one can invest observing time on deep exposures of smaller fields, so-called ‘pencil-beam surveys’, which trace galaxies out to high redshift. Thirdly, one can use broad-band photometric information to select galaxies at different redshifts. Extremely Red Objects (EROs) and Lyman-Break Galaxies (LBGs), amongst others, fall into this category.

It is important to note that with different selection techniques one builds up samples of galaxies from different populations and at different redshifts. The challenge remains to construct a unifying picture of galaxy formation and evolution from these different samples.

In the following, I will summarise important observational results on galaxy samples drawn from different selection schemes.

1.2.1 Surveys of the Local Universe

In recent years, shallow surveys have started to map the local universe in large areas of the sky. They greatly increase our knowledge of our cosmic neighbourhood and provide important comparison data for studies at higher redshifts. The Sloan Digital Sky Survey (SDSS, York *et al.* 2000) will eventually have mapped one quarter of the sky down to $r'_{AB} \simeq 23$ mag in five optical bands, and will have taken spectra of extragalactic objects down to $r'_{AB} \simeq 18$ mag. In the near-infrared, the Two-Micron All Sky Survey (2MASS, Jarrett *et al.* 2000) will map the entire sky in the near-infrared filters

J , H and K_s with a limiting K -band magnitude of $K_s \simeq 13.5$. In parallel, large spectroscopic surveys like the 2-degree Field Galaxy Redshift Survey (2dFGRS, Folkes *et al.* 1999) provide catalogues of thousands of redshifts for galaxies, mapping a considerable portion of the local universe. The 2dFGRS contains more than 220 000 galaxies with $b_J \leq 19.45$ in 1500 square degrees selected from photographic plates of the APM survey (Maddox *et al.* 1990a).

1.2.2 The Universe at Midlife

By the 1980s, the increased number of 4-m class telescopes and advances in electronic detector technology enabled deeper surveys of the universe out to redshifts $z \sim 1$, when the universe had about half of its present age (see Colless 1997, Ellis 1997 for reviews).

Many traditional surveys were conducted in the B band using photographic plates at Schmidt telescopes (Schmidt 1931, Wilson 2004). When multi-object spectrographs became available at 4-m class telescopes, many groups started follow-up observations of these surveys. One noteworthy redshift survey of that kind is the Autofib Redshift Survey probing the evolution of the luminosity function out to redshifts $z \sim 0.8$ with roughly 1700 galaxy redshifts (Ellis *et al.* 1996, Heyl *et al.* 1997).

In the middle of the 1990s, the I -band selected Canada–France Redshift Survey (CFRS) marked an important point in the study of galaxy evolution with redshift surveys. The selection in the I band made it possible to study the evolution of the evolved, massive galaxies rather than star forming galaxies picked up in the more traditional B -band selected samples. The CFRS comprises spectra of more than 1000 objects with $17.5 \leq I_{AB} \leq 22.5$, 591 of which are galaxies with secure redshifts in the range $0 \leq z \leq 1.3$. A series of papers presented not only the technical details of the survey (Lilly *et al.* 1995a, b, Le Fèvre *et al.* 1995, Hammer *et al.* 1995), but more importantly studies of the evolution of the luminosity function (Lilly *et al.* 1995c) and of the luminosity density and star formation rate density of the universe (Lilly *et al.* 1996), finding very little evolution in the luminosity and number density of red galaxies in the redshift range $0 < z < 1$.

Selection in near-infrared filters like the K -band come even closer to a selection in stellar mass. When suitable near-infrared detectors became available at large telescopes, a number of K -band selected surveys were undertaken which can probe the evolution of massive galaxies out to redshift $z \sim 1$. Examples for such surveys are the Hawaii Deep Fields (Cowie *et al.* 1994), the K20 Survey (Cimatti *et al.* 2002b) and the Munich Near-Infrared Cluster Survey (MUNICS; Drory *et al.* 2001b) on which this work is based.

1.2.3 Pencil-Beam Surveys

One way to probe the evolution of galaxies to large redshifts is to take deep exposures of small fields. These ‘pencil-beam surveys’ have the advantage that one can study galaxies out to very high redshift. Their main disadvantage, however, is the small size of the fields: Locally they probe only small volumes making statistical tests difficult.

Moreover, they are affected by the variation of the galaxy distributions over the sky, an effect which is called ‘cosmic variance’.

Ground-based deep fields include the NTT Deep Field (NDF, Arnouts *et al.* 1999), the William Herschel Deep Field (WHDF, Metcalfe *et al.* 2001) and the FORS Deep Field (FDF, Heidt *et al.* 2003).

The most notable examples for these are, of course, the Hubble Deep Fields (HDFs, Ferguson *et al.* 2000), the HDF North (Williams *et al.* 1996) and the HDF South (Williams *et al.* 2000, Casertano *et al.* 2000), taken with the fantastic spatial resolution of the Hubble Space Telescope (HST). More recently, the Hubble Ultra Deep Field (UDF), a larger deep field taken with the new Advanced Camera for Surveys (ACS) on board HST was released. Because of the high resolution, studies of galaxy morphologies and sizes as well as their evolution with redshift are of special interest.

Many studies of galaxy morphologies have been carried out in the HDFs (e.g. Abraham *et al.* 1996, Odewahn *et al.* 1996, van den Bergh *et al.* 1996, Marleau & Simard 1998, van den Bergh *et al.* 2000, Kajisawa & Yamada 2001, Conselice *et al.* 2004). One general trend is the increasing number of galaxies with irregular appearance with redshift. Part of this trend may be attributed to the fact that the observed optical regime samples the galaxies ultraviolet light. In the ultraviolet, the light is dominated by the very young hot stars located in star forming regions displaying a patchy character also in the local universe. But this cannot explain all of the evolution, especially it does not account for the increasing number of interacting systems observed in the HDFs (e.g. van den Bergh *et al.* 1996). Furthermore, Dickinson *et al.* (2003) find from an near-infrared selected sample of HDF-N galaxies that 50–75% of the present-day stellar mass density was in place by $z \simeq 1$, but only 3–14% at $z \simeq 2.7$. All this might suggest that the classical Hubble sequence of galaxy types (Hubble 1926) appeared at $1 \lesssim z \lesssim 2$.

Another important aspect which can be investigated with HDFs is the evolution of galaxy sizes. From the beginning it was obvious that the high redshift galaxies seen in the HDFs are very small, compact objects (Lowenthal *et al.* 1997, Bouwens *et al.* 2003). Analysis of recent observations taken with HST’s Advanced Camera for Surveys (ACS) in the course of the GOODS project (Great Observatories Origins Deep Survey, Giavalisco *et al.* 2004) confirm this evolutionary trend (Ferguson *et al.* 2004).

1.2.4 Extremely Red Objects

In the late 1980s and early 90s, with the advent of near-infrared imagers at large telescopes, a class of objects with very red near-infrared to optical colours was discovered, the so-called Extremely Red Objects (EROs, Elston *et al.* 1988, 1989, Hu & Ridgway 1994, Soifer *et al.* 1994, see also McCarthy 2004 for a complete review)⁶. The defining criterion is usually expressed in terms of $R - K$ colour, and typical definitions for EROs are in the range $R - K > 5 \dots 6$. From the beginning they were thought to be either luminous star-forming galaxies at very high redshifts or evolved early-type galaxies at

⁶Sometimes these objects are also called ‘Extremely Red Galaxies (ERGs)’ However, in this work we will adopt the term ERO.

redshifts $z \gtrsim 1$. EROs have a surface density at the sky of $\sim 0.4 \text{ arcmin}^{-2}$ (Thompson *et al.* 1999, Yan *et al.* 2000).

Since by the end of that decade there was more and more interest in near-infrared surveys of field galaxies, a wealth of papers on the photometric, morphological and clustering properties of EROs appeared in the literature.

The first detailed studies of one ERO called HR10 found by Hu & Ridgway (1994) revealed it to be a dusty starburst galaxy at redshift $z = 1.44$ (Graham & Dey 1996, Cimatti *et al.* 1998, Dey *et al.* 1999).

Later studies of the spectral energy distributions (SEDs) or spectroscopic observations of EROs confirmed that they are not a homogeneous class. While some authors found them to be early-type galaxies at $z \gtrsim 1$ (e.g., Elston 1989, Hu & Ridgway 1994), others found indication for star-formation or AGN activity (e.g., Graham & Dey 1996).

Most authors studying larger samples of EROs find a mix of both types. Cimatti *et al.* (1999) find that 2 out of 9 EROs they studied seem to be dusty star-bursts, while the rest are consistent with dustless evolved spheroidals at $z \gtrsim 0.8$. Similar results for bright EROs are found by Saracco *et al.* (2003) who identify massive evolved galaxies at redshifts $z > 1$. On larger samples most authors find both classes (Martini 2001, Cimatti *et al.* 2002a, Smail *et al.* 2002b, Väisänen & Johansson 2004, Yan *et al.* 2004c).

Different contributions from evolved early-type galaxies and dusty star-bursts to the ERO population found in these studies can likely be attributed to different magnitude limits, different colour selection criteria, and to field-to-field variations of the galaxy distribution (cosmic variance). Colour-colour diagrams may offer an easy way to distinguish these different populations (Pozzetti & Mannucci 2000).

Morphologically this dichotomy is confirmed. Some EROs show asymmetric morphologies (Graham & Dey 1996), others are well described by $R^{1/4}$ profiles (de Vaucouleurs 1948) typical for elliptical galaxies (Treu *et al.* 1998, Elston *et al.* 1989). Yan & Thompson (2003) investigated the morphology of more than 100 EROs from HST imaging. They find that roughly one third of the sample consists of bulge-dominated galaxies, while the rest is comprised by disks. Furthermore, they find indications of merging activity for about 20 per cent of all EROs. As with the spectral properties, morphological studies of larger samples contain a mix of E/S0-like, spiral-like and irregular morphologies (Moriondo *et al.* 2000, Cimatti *et al.* 2003, Moustakas *et al.* 2004, Yan *et al.* 2004c), with different fractions caused by different selection techniques.

It is interesting to note that there is no strong correlation between spectral type and morphological classification (Moustakas *et al.* 2004, Yan *et al.* 2004c)

Studies of the angular ERO distribution indicate that they are strongly clustered with comoving correlation lengths of the order $r_0 \simeq (10 \pm 3) h^{-1} \text{ Mpc}$, in the range of present-day elliptical galaxies (Yan *et al.* 2000, McCarthy *et al.* 2001, Roche *et al.* 2002) which have correlation lengths of $r_0 \sim 7 h^{-1} \text{ Mpc}$, with the giant ellipticals having $r_0 \sim 11 h^{-1} \text{ Mpc}$ (see McCarthy 2004 and references therein).⁷ The clustering

⁷Clustering of galaxies in space can be described by the *spatial two-point correlation function* $\xi(r)$ which can be defined in terms of the number $n(r)dV$ of galaxies which can be found in a volume element dV at a comoving distance r from any galaxy in a density field of average density n_0 :

properties of the two contributing populations differ considerably in the sense that the old ellipticals show much more correlation. Daddi *et al.* (2002) measure a much smaller correlation length of $r_0 = 2.5 h^{-1}$ Mpc for the star-forming EROs.

Radio and X-ray observations as well as optical spectroscopy reveal that only a small fraction of the ERO population is comprised of obscured AGN (Smail *et al.* 2002b, Cimatti *et al.* 2003, Yan *et al.* 2004c, Severgnini *et al.* 2004).

It has been suggested that EROs (or at least the evolved early-type galaxies contributing to the ERO population) might be an efficient tool to test current models of galaxy formation. Indeed, most present-day semi-analytic models seem to have difficulties to match the observed number density of EROs at $z \gtrsim 1$ (Cimatti *et al.* 1999, Martini 2001, Daddi *et al.* 2002, Roche *et al.* 2002, Smith *et al.* 2002).

Recently, first observations with the Spitzer Space Telescope (formerly called SIRTf, the Space InfraRed Telescope Facility, Fanson *et al.* 1998) allowed the study of infrared properties of EROs and detected EROs at redshifts $z \sim 2$ and beyond (Yan *et al.* 2004b, Wilson *et al.* 2004, Yan *et al.* 2004a).

1.2.5 Distant Red Galaxies

Recently, relatively red galaxies at redshifts $z \gtrsim 2$ were discovered. Defined by their red near-infrared colours, $J - K > 2.3$, they are referred to as Distant Red Galaxies (DRGs, Franx *et al.* 2003, van Dokkum *et al.* 2003). DRGs apparently have stellar masses comparable to those of today's early-type galaxies. Comparing DRGs and Lyman-Break Galaxies at redshifts $z \sim 3$ (see next Section) at the same rest-frame optical luminosity, the DRGs seem to be dustier, more metal rich, more massive and older (van Dokkum *et al.* 2004).

1.2.6 Submillimeter Sources

Submillimeter (sub-mm) radiation of galaxies is mainly due to the emission from warm interstellar dust. The dust component absorbs the light of young, high-mass stars in star-forming galaxies and re-emits it at rest-frame wavelengths around $\lambda \sim 100 \mu\text{m}$ (for typical dust temperatures of $T \simeq 40$ K). Quite naturally, the submillimeter emission is a measure of the galaxy's current star-formation activity. The rest-frame peak of the dust emission implies that the $k(z)$ corrections, which describe the change of flux in a given wavelength range due to the redshifting of the rest-frame spectrum, are negative, i.e. submillimeter sources are less affected by the effects of cosmological dimming (Blain & Longair 1993).

$$n(r) dV = n_0 \left[1 + \xi(r) \right] dV \quad (1.20)$$

Thus $\xi(r)$ describes the excess number of galaxies at distance r from any given galaxy. On scales smaller than $10 h^{-1}$ Mpc, the two-point correlation function can be well described by a power-law

$$\xi(r) = \left(\frac{r_0}{r} \right)^\gamma \quad (1.21)$$

with the comoving correlation length r_0 . In the local universe measurements of galaxy clustering yield $r_0 \simeq 5.7 h^{-1}$ Mpc and $\gamma \simeq 1.77$ (Peebles 1980, 1993, Longair 1998, Peacock 1999).

When the Sub-mm Common-User Bolometer Array (SCUBA, Holland *et al.* 1999) became available at the 15-m James Clerk Maxwell Telescope (JCMT), astronomers were able to make sensitive images of the sky at sub-mm wavelengths, usually at $\lambda = 850 \mu\text{m}$. They soon discovered a population of faint sub-mm sources in the distant universe (Smail *et al.* 1997). Many of these could be identified with Extremely Red Objects (EROs) in the near-infrared and optical regime (Smail *et al.* 1999), and are most likely massive, heavily star-forming and heavily obscured galaxies at redshifts $z \gtrsim 2$ (Smail *et al.* 2002a). In that respect, they are strikingly similar to the population of Ultra-Luminous InfraRed Galaxies (ULIRGs) at low redshifts which were discovered in the 1980s by the InfraRed Astronomical Satellite (IRAS).

Difficulties with the interpretation of submillimeter galaxies remain. For one, SCUBA's low angular resolution of only 15 arcsec makes optical identifications difficult. (At millimetre wavelengths the 30-m IRAM telescope offers higher resolution.) Moreover, successful follow-up spectroscopy in the optical is hard to achieve since typical SCUBA sources are very red, dusty objects.

1.2.7 Exploring the 'Redshift Desert'

We have already described the study of galaxies at redshifts $z \lesssim 1.5$ with traditional redshift surveys and of Lyman-break galaxies (LBGs) at redshifts $z \gtrsim 2.5$. The redshift range in between, i.e. $1.5 \lesssim z \lesssim 2.5$ has traditionally been difficult to bridge due to the lack of prominent spectral features at $4300 \text{\AA} \lesssim \lambda_{\text{obs}} \lesssim 9000 \text{\AA}$ characteristic for most spectrographs on this planet. Hence this regime had become known as the 'redshift desert'.

This is somewhat unfortunate, because there are many pieces of evidence – e.g. the dramatically different appearance and properties of LBGs as compared to the local galaxy population – which might suggest that at these redshifts a significant change in galaxy properties might occur.

However, Adelberger *et al.* (2004) and Steidel *et al.* (2004) show how spectra of a large number of star-forming galaxies in this redshift range can be obtained by combining photometric colour pre-selection techniques with multi-object spectroscopy using a blue-optimised spectrograph at a 10-m class telescope. The principle of the photometric selection can be seen in Figure 1.5.

So far it is unclear how the population of this galaxies relates to the LBGs at $z \sim 3$ and to galaxy samples at lower redshift, but the study of these objects will likely shed some more light on the process of galaxy evolution, especially in combination with galaxy samples at $1 \lesssim z \lesssim 2$ drawn from near-infrared selected surveys like the on-going MUNICS-Deep project briefly described in Section 2.4.

1.2.8 Lyman-Break Galaxies

The best studied sample of high redshift galaxies are the Lyman-Break Galaxies (LBGs) at $z \sim 3$ (see Giavalisco 2002 for a review). LBGs can be easily identified by optical photometry through filters designed to isolate the spectral discontinuity at $\lambda \simeq 912 \text{\AA}$ (Steidel & Hamilton 1992, 1993, Steidel *et al.* 1995). This 'Lyman break'

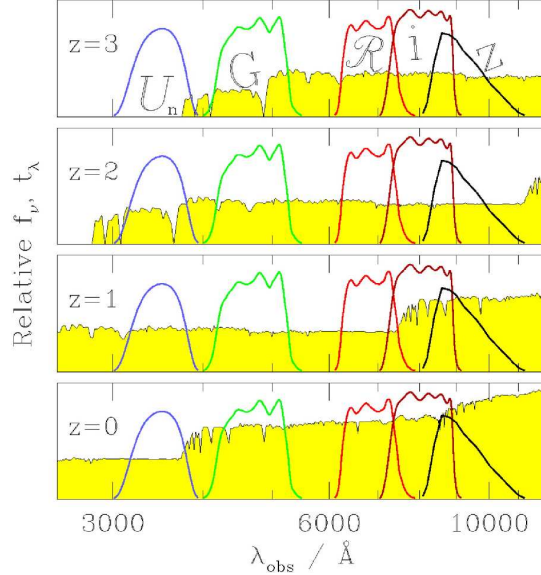


Figure 1.5: Illustration of the photometric selection technique for galaxies in the ‘redshift desert’ (taken from Adelberger *et al.* 2004). Star-forming galaxies in a given redshift interval can be selected by choosing suitable combinations of galaxy colours.

is caused by a combination of the stellar spectral energy distributions, the intrinsic opacity of galaxies to Lyman continuum photons, and the influence of absorbers along the line of sight between the galaxy and the observer. The principle of this selection technique is illustrated in Figure 1.6.

Morphological investigations of LBGs making use of the high spatial resolution of HST show that they have very compact, bright cores (sometimes multiple) and are often surrounded by a diffuse and asymmetric halo (Giavalisco *et al.* 1996, Steidel *et al.* 1996a). Star formation in these high-redshift galaxies thus occurs in very compact regions of high surface brightness. These findings might be interpreted to be evidence for a formation of the traditional Hubble sequence at lower redshifts than the LBG regime.

The spectra of LBGs resemble those of star-forming galaxies locally (Steidel *et al.* 1996b) and are remarkably uniform (Pettini *et al.* 2001). Detailed spectral analysis yields abundances of at least one tenth solar, making them rather metal rich for their epoch (Pettini *et al.* 2001). Moreover, the virial masses deduced from the measured velocity dispersions are of the order of $10^{10} M_{\odot}$ within a half-light radius of 2.5 kpc, with mass-to-light ratios of $M/L \simeq 0.15 M_{\odot}/L_{\odot}$ corresponding to stellar populations between 10^8 and 10^9 years old. Another very important finding is the existence of superwinds on galactic scales which certainly have a major effect on the star-formation histories of LBGs (Pettini *et al.* 2001).

The results on the stellar populations are confirmed from studies of the spectral energy distribution (SED) of the LBGs (Papovich *et al.* 2001, Shapley *et al.* 2001). Shapley *et al.* (2001) also find interesting correlations: more luminous galaxies are

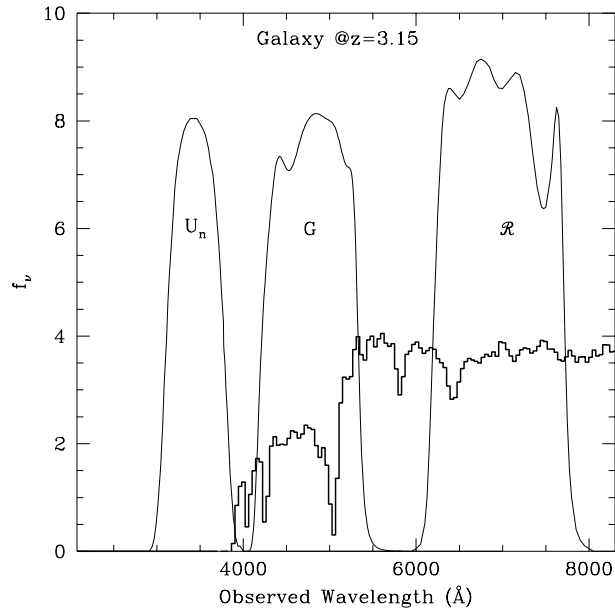


Figure 1.6: Illustration of the photometric selection technique for LBGs (taken from Steidel *et al.* 1999a). The spectrum shown is a model spectrum of galaxy at redshift $z = 3.15$. Superimposed are the transmission curves of the three filters used in the pioneering studies by Steidel & Hamilton (1992). Clearly, one can efficiently pre-select samples of high-redshift galaxies using the Lyman continuum break in their spectra.

dustier, and younger galaxies are dustier and have higher star-formation rates. They try to explain these trends with a unified model in which a short burst of very rapid star formation of the order of hundreds solar masses per year is followed by a period of reduced star formation and dust extinction. The reduction of the extinction is probably governed by the huge outflows observed in LBGs, thereby causing the metal enrichment of the IGM (Adelberger *et al.* 2003).

Many studies of the clustering properties of LBGs have been performed (e.g., Adelberger *et al.* 1998, Giavalisco *et al.* 1998, Steidel *et al.* 1998, Giavalisco & Dickinson 2001, Porciani & Giavalisco 2002). They find that LBGs are clustered with comoving correlation lengths of $r_0 \simeq 4h^{-1}$ Mpc, with amplitudes comparable to the ones observed for present-day luminous spiral galaxies (the local galaxies cluster with correlation lengths of $r_0 \simeq 5.7h^{-1}$ Mpc). This suggests that LBGs are associated with massive dark-matter haloes, and might be the progenitors of massive galaxies today.

1.2.9 Galaxies Beyond the LBG Regime

We conclude our overview of galaxies at different cosmic epochs by a summary of results on the highest redshift objects. To study galaxies beyond the realm of the Lyman-Break Galaxies (LBGs), i.e. galaxies at redshifts $z \gtrsim 4$, one has several options. One way is to rely on very deep observations like the Hubble Deep Fields (HDFs),

Ferguson *et al.* 2000, Williams *et al.* 2000, Casertano *et al.* 2000), the FORS Deep Field (FDF, Heidt *et al.* 2003) or the Ultra Deep Field (UDF) which probe the galaxy population out to $z \sim 5 \dots 6$.

Other techniques are searches for the prominent Lyman- α emission line in narrow-band images in the optical, selection of radio-emitting objects, or photometric pre-selection (see Stern & Spinrad 1999, Taniguchi *et al.* 2003b for reviews). Since radio detection methods will yield samples of galaxies whose light is mostly dominated by the emission of their active nucleus, we will not discuss this technique in detail. Also, more modern photometric methods to find high-redshift AGN (e.g. Fan *et al.* 2001) will not be described here.

One popular technique is to search for the emission of the Lyman- α line of high-redshift galaxies. This was first suggested in a pioneering paper by Partridge & Peebles (1967) and led to the discovery of a number of galaxies at redshifts larger than five (see Table 1.3). Another method uses the spectral break around $\lambda \simeq 912\text{\AA}$ and is thus similar to the pre-selection of LBGs at $z \sim 3$. The only difference is that one uses *R*-band or *I*-band drop-outs instead of *U* drop-outs as for the LBGs. This technique is also very successful (see Table 1.3).

Note that although these two methods complement each other, they are in reality not completely independent. While the Lyman-break technique relies on the continuum shape only the appearance of an emission line at the location of the break helps in identifying the break. On the other hand, apart from the intrinsic asymmetry of the Lyman- α line, one popular criterion for the identification of a single Lyman- α line is the existence of continuum flux red-wards the line, and the total lack of it blue-wards.

A variation of the drop-out approach is to use the objects' photometry in several filters together with template spectral energy distributions (SEDs) to estimate their redshift. This 'photometric redshift method' has been pioneered by Baum (1962) and Koo (1985) and is widely used for obtaining redshifts today.

Kurk *et al.* (2004) used a different approach. They performed slitless spectroscopy in the wavelength region around $\lambda \sim 9100\text{\AA}$ to search for Lyman- α emitters at $z \sim 6.5$ and found one object at $z = 6.518$.

The observed properties of these high-redshift galaxies are, of course, of particular interest. Although the number of confirmed objects at $z \gtrsim 5$ is still very small, they allow a glimpse at the very early stages of galaxy evolution. After all, at these redshifts, we see galaxies at an epoch when the universe was only 1 Gyr old.

Star-formation rates for these galaxies, as referred from their Lyman- α luminosity, are usually in the range $5 \dots 20 M_{\odot} \text{ yr}^{-1}$, considerably lower than LBGs at $z \sim 3$. Similar to other high-redshift objects, they show small physical sizes.

1.3 The Evolution of Galaxies with Cosmic Time: Statistical Properties of Galaxies

1.3.1 The Galaxy Luminosity Function

The luminosity function of galaxies is the number density of galaxies as a function of the galaxies' luminosity L , or, in astronomical language, their absolute magnitude M .

Table 1.3: List of spectroscopically confirmed galaxies at redshifts beyond 5 (following Stern & Spinrad 1999, Taniguchi *et al.* 2003b, Spinrad 2004, updated by the author).

z	Technique	Reference
6.58	narrow-band imaging	Kodaira <i>et al.</i> (2003)
6.56	narrow-band imaging, lensed	Hu <i>et al.</i> (2002)
6.55	serendipitous	Stern <i>et al.</i> (2004)
6.54	narrow-band imaging	Kodaira <i>et al.</i> (2003)
6.52	slitless spectroscopy	Kurk <i>et al.</i> (2004)
6.33	Lyman-break	Nagao <i>et al.</i> (2004)
6.17	narrow-band imaging	Cuby <i>et al.</i> (2003)
5.87	Lyman-break	Lehnert & Bremer (2003)
5.83	Lyman-break	Dickinson <i>et al.</i> (2004)
5.78	Lyman-break	Bunker <i>et al.</i> (2003)
5.77	serendipitous	Dawson <i>et al.</i> (2001)
5.75	narrow-band imaging	Rhoads <i>et al.</i> (2003)
5.74	Lyman-break	Lehnert & Bremer (2003)
5.74	narrow-band imaging, lensed	Hu <i>et al.</i> (1999)
5.70	narrow-band imaging	Rhoads <i>et al.</i> (2003)
5.69	narrow-band imaging	Ajiki <i>et al.</i> (2002)
5.67	narrow-band imaging	Rhoads <i>et al.</i> (2003)
5.66	narrow-band imaging	Taniguchi <i>et al.</i> (2003a)
5.65	Lyman-break	Lehnert & Bremer (2003)
5.64	narrow-band imaging	Hu <i>et al.</i> (1998)
5.63	serendipitous	Dawson <i>et al.</i> (2001)
5.60	Lyman-break	Weymann <i>et al.</i> (1998)
5.58	serendipitous, lensed	Ellis <i>et al.</i> (2001)
5.34	Lyman-break	Spinrad <i>et al.</i> (1998)
5.34	Lyman-break	Dey <i>et al.</i> (1998)
5.19	serendipitous	Dawson <i>et al.</i> (2001)
5.12	Lyman-break, lensed	Frye <i>et al.</i> (2002)
5.06	Lyman-break	Lehnert & Bremer (2003)
5.02	Lyman-break	Lehnert & Bremer (2003)

Plotted in logarithmic units, it shows a characteristic shape with a linear behaviour at the faint end, and a sharp cut-off at high luminosity. This characteristic shape of the luminosity function is generally described by a Schechter function,

$$\Psi(L) = \frac{\Phi^*}{L^*} \left(\frac{L}{L^*} \right)^\alpha \exp\left(-\frac{L}{L^*}\right), \quad (1.22)$$

where L^* is the characteristic luminosity, α the faint-end slope, and Φ^* the number density normalisation of the luminosity function (Schechter 1976). The corresponding

equation in absolute magnitudes reads

$$\Psi(M) = \frac{2}{5} \Phi^* \ln 10 10^{0.4(M^* - M)(1 + \alpha)} \exp\left(-10^{0.4(M^* - M)}\right). \quad (1.23)$$

Investigating the evolution of the B -band luminosity function from the Autofib Redshift Survey, Ellis *et al.* (1996) and Heyl *et al.* (1997) find that the total luminosity function evolves in the sense that the faint-end slope changes from $\alpha \simeq -1.1$ to $\alpha \simeq -1.5$ from the local universe to $z \simeq 0.5$. They also show that the LF of more quiescent galaxies does not evolve much, whereas the luminosity density of star forming galaxies declined by roughly 50% since redshift $z \simeq 0.5$. Lilly *et al.* (1995c) used the I -band selected Canada-France Redshift Survey (CFRS; Lilly *et al.* 1995b) to study the evolution of the B -band LF out to $z \sim 1$, again finding little evolution for red galaxies, but marked changes in the population of star forming objects.

Recently Gabasch *et al.* (2004a) used the FORS Deep Field (FDF; Heidt *et al.* 2003) to probe the LF evolution from ultraviolet to optical bands out to much higher redshifts. They find clear evolution in all bands with a brightening and decrease in number density with increasing redshift, where the effect is strongest in the bluest band-passes.

Studies of the rest-frame near-infrared luminosity function of field galaxies out to $z \sim 1$ find little or no evolution with redshift, as is described in more detail in Section 6.1.

1.3.2 The Stellar Mass Function of Galaxies

In the current models of galaxy formation, the stars in galaxies form from gas falling into dark matter haloes. The halo mass function is considered as one of the key predictions of the theoretical scenarios. Assuming a method to assign *stellar* masses to dark matter haloes of a given mass, it is interesting to compare stellar mass functions from models to observations.

Unfortunately, the masses of galaxies are not easily derived. The total mass can be inferred from dynamical observations, whereas the stellar mass can only be estimated from the light of the galaxy's stars. However, not all wavelength regimes are well suited for this conversion from light to mass. The ultraviolet light of galaxies, for example, is dominated by young, hot stars and thus is rather a measure of the current star formation rate in the galaxy than of the mass already accumulated in stars. The near-infrared radiation, and in particular the K -band light at $\lambda \simeq 2.2\mu\text{m}$, is mainly produced by the old, evolved stellar population in galaxies and only little affected by ongoing star formation (Rix & Rieke 1993). The (rest-frame) K -band luminosity of galaxies can therefore be considered as a good tracer of the stellar mass of galaxies.

During the last years, a number of research groups have used deep galaxy samples with near-infrared imaging to study the stellar mass function of galaxies and its evolution with redshift. At low redshifts, Bell *et al.* (2003a, b) used a combination of 2MASS (Jarrett *et al.* 2000) and SDSS to derive local representations of the baryonic and stellar mass functions, respectively.

Drory *et al.* (2001a, 2004a) used the MUNICS sample (see Section 2), a K -band selected galaxy catalogue with photometric redshifts, to study the evolution of the inte-

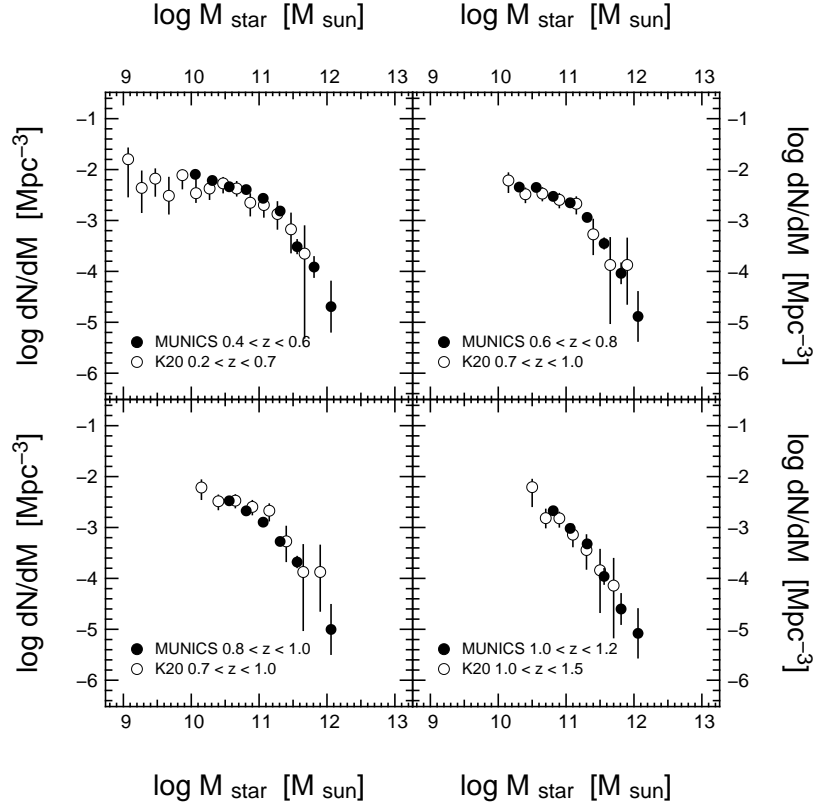


Figure 1.7: The stellar mass function of galaxies in four different redshift bins as measured from the MUNICS project (Drory *et al.* 2004a, filled symbols) and the K20 survey (Fontana *et al.* 2004, open symbols). Electronic data for the K20 mass function were kindly provided by A. Fontana.

grated stellar mass function as well as the stellar mass function itself. They find a clear evolutionary trend in the sense that with increasing redshift the number density of the most massive galaxies declines significantly. The non-integrated stellar mass function shows this trend very clearly: The number density decreases with redshift, and the high-mass cut-off of the mass function moves towards lower masses. This trend was confirmed by the results from the K20 survey (Fontana *et al.* 2004). Figure 1.7 shows the combined mass function data from MUNICS and K20 showing the evolutionary trends described above.

The decline of the stellar mass *density* with redshift was measured by Rudnick *et al.* (2003), Conselice *et al.* (2004), Drory *et al.* (2004a), Fontana *et al.* (2004), Glazebrook *et al.* (2004). Comparison with semi-analytic models shows disagreement between the model predictions and the build-up of mass in the universe as observed with deep surveys in the sense that the models seem to predict too low a number of massive systems at redshifts $1 \lesssim z \lesssim 2$.

1.3.3 The Star Formation Rate Density of the Universe

To some extent the build-up of stellar mass in the universe can be traced by measuring the star formation rate density (SFRD) as a function of redshift. The SFRD is the birthrate of stars, usually expressed in solar masses M_{\odot} per year and comoving volume.

How can we measure the current SFR of a galaxy? Ongoing star formation reveals itself mainly in three effects (see Rosa-González *et al.* 2002 for a summary). First, the short-lived, high-mass stars have very high atmospheric temperatures and hence radiate in the ultraviolet. The ultraviolet continuum radiation of galaxies is therefore a measure of the galaxies' SFR. Secondly, star formation occurs in molecular clouds which are usually associated with dust. The dust absorbs the ultraviolet photons amply emitted by the hot stars and re-emits them in the far-infrared. Thus there is a strong correlation between thermal dust emission of galaxies and the SFR. Thirdly, gaseous nebulae in the galaxies are ionised by the ultraviolet emission and emit line radiation upon recombination, resulting in a close connection between emission line strengths and SFR. The most popular emission lines used to determine the SFR are $H\alpha$ at $\lambda = 6563\text{\AA}$ and [OII] at $\lambda = 3727\text{\AA}$.

One problem with the above mentioned star-formation estimators is the role of the initial mass function (IMF)⁸ of the stars in the galaxies for calibrating the estimator, the fact that different techniques do not always yield the same result, and the influence of dust extinction which is often impossible to quantify.

Nevertheless there is reasonable agreement about the general behaviour of the SFRD as a function of redshift (see Figure 1.8). From $z = 0$ to $z \sim 2$ there is a clear rise the slope of which, however, is under debate. At higher redshifts, the situation is also far from clear. Apparently the SFRD remains on a high value for a wide redshift range before it falls off. However, because of small samples, incompleteness at high redshifts, and the problem of dust extinction the exact history of star formation at higher redshifts remains unclear.

Hernquist & Springel (2003) use physical arguments and analytic approximations to numerical simulations to derive a simple formula for the cosmic SFRD:

$$\dot{\rho}_{\star}(z) = \dot{\rho}_0 \frac{\chi^2}{1 + \alpha(\chi - 1)^3 \exp(\beta\chi^{7/4})}. \quad (1.25)$$

In this equation, $\beta \simeq 0.044$ is derived from the normalisation of the power spectrum, α is a free parameter, and χ is defined as

$$\chi(z) \equiv \left(\frac{H(z)}{H_0} \right)^{2/3} \quad (1.26)$$

⁸The *initial mass function* (IMF) describes the mass distribution of forming stars. Over a wide range of stellar masses \mathcal{M} , the IMF can be approximated by a power-law function

$$\frac{dN}{d\mathcal{M}} \propto \mathcal{M}^{-\alpha}. \quad (1.24)$$

In his seminal paper Salpeter (1955) showed that $\alpha \simeq 2.35$. This ‘‘Salpeter IMF’’ is still widely used today.

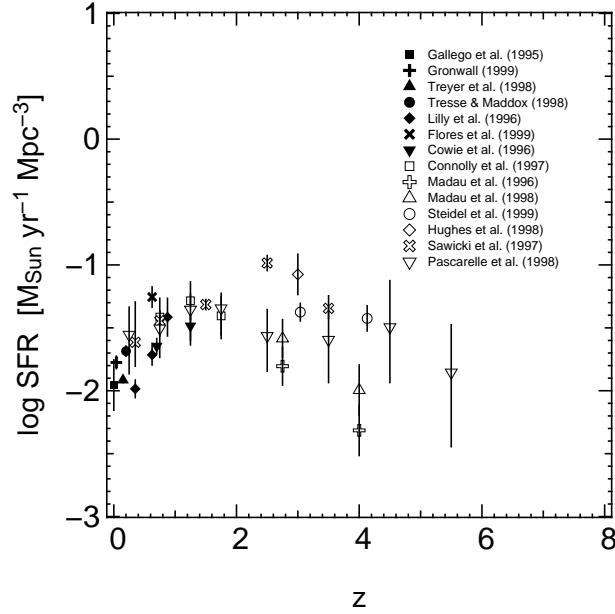


Figure 1.8: The evolution of the star formation rate density as derived from various surveys (not corrected for dust extinction). The compilation of values was taken from Somerville *et al.* (2001).

where $H = \dot{R}/R$ is the Hubble parameter, characterised by the cosmic evolution of the cosmic scaling factor R (e.g. Carroll *et al.* 1992; see Section 1.1.1):

$$H(z) = H_0 \left[\Omega_M(1+z)^3 + (1 - \Omega_{\text{tot}})(1+z)^2 + \Omega_\Lambda + \Omega_r(1+z)^4 \right]^{1/2} \quad (1.27)$$

Their analysis also offers an explanation for the general behaviour of the star-formation rate in the universe, especially for the peak in the star-formation history. At high redshifts, densities are high and cooling is therefore highly efficient and sufficient amounts of gas are available for star formation. Hence the star formation is dominated by the highest-mass haloes, and thus follows the evolution of the exponential part of the mass function. At lower redshift, on the other hand, cooling is less efficient due to the low densities and therefore governs the star-formation rate. They find a typical behaviour of $\dot{\rho}_*(z)$ at low redshifts which may be described by

$$\dot{\rho}_*(z) \propto H(z)^q \quad (z < z_{\text{peak}}), \quad (1.28)$$

where $q \simeq 4/3$. We will test this prediction with our MUNICS dataset in Chapter 8 of this thesis.

1.3.4 Downsizing: The Connection of Star Formation and Mass

Lilly *et al.* (1995c) noted that in the Canada–France Redshift Survey (CFRS) there was strong evolution in the population of blue galaxies with redshift: With increasing

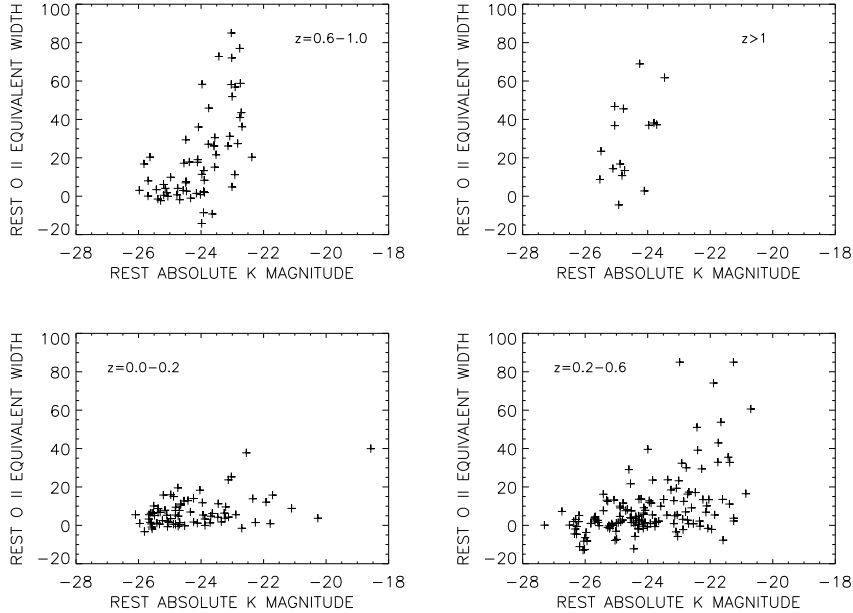


Figure 1.9: The distribution of rest-frame [OII] equivalent width *versus* rest-frame absolute K -band magnitude in four redshift bins illustrating the effect of “downsizing” (Figure 10 from Cowie *et al.* (1996), see text for details.)

redshift, they saw a population of bright blue galaxies emerging which was not present locally.

Around the same time Cowie *et al.* (1996) investigated a small spectroscopic sample of roughly 300 galaxies with $K \leq 19.5$ in two 13 arcmin^2 fields with K , I , and B -band imaging. They found a variation of the same phenomenon and termed this process “downsizing”: With increasing redshift, the locus of star-forming galaxies moves to brighter (absolute) K magnitudes, i.e. the most massive galaxies were forming at higher redshifts. This can be clearly seen from Cowie *et al.*’s original plot reproduced in Figure 1.9.

Downsizing is a very important effect because it allows direct conclusions about when the stellar mass was assembled in systems with different masses. In particular, the most massive systems had their epoch of major star formation very early in the history of the universe.

The general trend of downsizing is confirmed by many investigations which suggest that both mass assembly and star formation happen very rapidly and are completed early in massive galaxies (e.g. Kashikawa *et al.* 2003, Pozzetti *et al.* 2003, Saracco *et al.* 2003, Kodama *et al.* 2004). A similar behaviour has been observed in clusters: Tran *et al.* (2003) and Poggianti *et al.* (2004) find an increase of mass for E+A galaxies with redshift.⁹

⁹E+A galaxies were first identified in spectroscopic surveys of galaxy clusters Dressler & Gunn (1983). They exhibit the spectrum of an old, evolved galaxy, like that of an elliptical (type ‘E’) with no (or very faint) [OII] emission, but they show very strong Balmer absorption lines indicative of the presence of A-type stars. They are interpreted as post-starburst galaxies (Couch & Sharples 1987).

This seems to agree well with other pieces of evidence for early assembly in early-type galaxies (see Peebles 2002 for a review). Among these are the tight correlations observed in elliptical galaxies like the colour-magnitude relation of early-type galaxies in clusters (Bower *et al.* 1992, Aragón-Salamanca *et al.* 1993, Stanford *et al.* 1995, Ellis *et al.* 1997, Stanford *et al.* 1998, Terlevich *et al.* 2001, Holden *et al.* 2004), the ‘fundamental plane’¹⁰ of elliptical galaxies both in clusters (Bender *et al.* 1998, van Dokkum *et al.* 1998, Jørgensen *et al.* 1999, Kelson *et al.* 2000, van Dokkum & Stanford 2003, Wuyts *et al.* 2004) and in the field (van Dokkum *et al.* 2001, Treu *et al.* 2002, Gebhardt *et al.* 2003, van Dokkum & Ellis 2003, van der Wel *et al.* 2004). From the colour-magnitude relation old ages can be inferred for elliptical galaxies, and the mere existence of tight relations argues against major merging activity at lower redshifts (say $z \lesssim 1$) as would be predicted by hierarchical formation scenarios.

Other lines of evidence that massive elliptical galaxies might have been well in place at redshifts $z \gtrsim 1$ arise from studies of the chemical enrichment of galaxies and super-massive black holes in their centre. Modelling the chemical history of galaxies, Thomas *et al.* (1999) show that merging of two spirals cannot reproduce the enhancement of α elements¹¹ observed in elliptical galaxies. The correlation between black-hole mass and stellar velocity dispersion observed in bulges (Kormendy & Richstone 1995, Ferrarese & Merritt 2000, Gebhardt *et al.* 2000) on the other hand, might have been destroyed by late merging events.

1.4 Thesis Outline

This thesis is organised as follows. Chapter 2 introduces the Munich Near-Infrared Cluster Survey (MUNICS), a photometric survey in near-infrared and optical filters on which this work is based. Then, in Chapter 3, I describe a spectroscopic redshift survey based on the MUNICS catalogue, concentrating mainly on its design and the observations. Chapter 4 discusses the details of the reduction of the multi-object spectroscopic data, and Chapter 5 presents an analysis of the objects in the spectroscopic sample. One of the central chapters of this thesis, Chapter 6, discusses near-infrared field-galaxy luminosity functions derived from the spectroscopic sample and gives results on their evolution with cosmic time. Chapter 7 introduces optically selected galaxy catalogues based on photometric redshifts. The results of Chapter 6 are then compared to those from these optically selected catalogues in Chapter 8. Furthermore, in Chapter 8 we use the optically selected galaxies to study the evolution of luminosity functions, densities and the star-formation rate, as well as the connection between stellar mass and star formation. Finally I conclude this work with a summary and an interpretation of the results in the framework of galaxy evolution in Chapter 9.

¹⁰The fundamental plane (FP) of elliptical galaxies is a tight correlation between the effective radius r_e , the central velocity dispersion σ_0 and the mean surface brightness I_e within r_e (Djorgovski & Davis 1987, Dressler *et al.* 1987).

¹¹The so-called α elements Oxygen (O), Magnesium (Mg), Silicon (Si), Calcium (Ca) and Titanium (Ti) are built up by synthesising α particles, i.e. Helium-4 cores.

Chapter 2

Observing Massive Galaxies to Redshift One: The Munich Near-Infrared Cluster Survey

This chapter presents the Munich Near-Infrared Cluster Survey (MUNICS), a photometric survey in near-infrared and optical filters, on which the spectroscopic survey described in this thesis is based.

2.1 Introduction

In observational cosmology, galaxy surveys are used to study statistical properties of the galaxy population and their change with redshift. Going to higher redshift is equivalent to looking back into the past of our universe, thus it allows to study the evolution of the galaxy population with time.

Many studies have focused on the evolution of galaxies in clusters, but studying the average galaxy population in the ‘field’ instead of the very special situation of the very high-density cluster environment has gained considerable importance.

During the last few decades, most field galaxy surveys have been optically selected, mostly in the I or B band at $\lambda \simeq 8000\text{\AA}$ and $\lambda \simeq 4400\text{\AA}$, respectively (see e.g. Ellis 1997 for a review)¹. In recent years, however, there has been growing interest in the study of near-infrared-selected samples of galaxies. In particular, the K band at wavelengths of roughly $\lambda \simeq 2\mu\text{m}$ offers the unique opportunity to detect evolved galaxies, since the K -band light of galaxies is largely dominated by the radiation of the evolved stellar population (Rix & Rieke 1993, Kauffmann & Charlot 1998, Brinchmann & Ellis 2000). Also, the K -band is much less affected by the effects of dust extinction than the optical light. Moreover, in the case of the K band, the transformation which has to be applied to convert the observed flux of the redshifted spectral energy distribution of an object through a given filter to the corresponding *rest-frame*

¹Referring to the I filter as an optical band is somewhat sloppy since it is actually partly in the near-infrared. Nevertheless it has become quite common because the I band is usually observed with the same detectors as the other ‘optical’ bands.

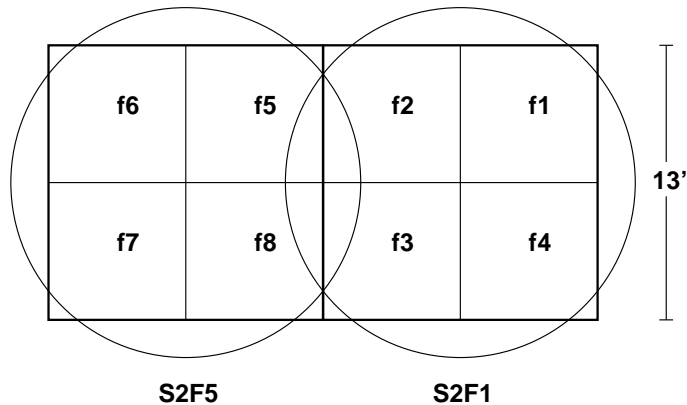


Figure 2.1: Illustration of MUNICS field geometry and field names. Each mosaic field (e.g. S2F1) consists of four pointings with the near-infrared OmegaPrime camera which are covered with one circular-aperture pointing of the CAFOS optical imager. Some of the mosaic fields actually are 2-by-4 mosaics consisting of two adjacent fields, in this case S2F1 and S2F5.

flux, the so called $k(z)$ correction, is much smaller – and indeed negative – than in the optical wavebands, and the variation of $k(z)$ corrections between different galaxy types is small. These effects reduce systematic errors introduced by applying $k(z)$ corrections during the construction of the luminosity function considerably. As another advantage of near-infrared selected surveys, the rest-frame K -band luminosity can be used to derive *stellar masses* for the galaxies, as has been done by Drory *et al.* (2001a, hereafter MUNICS III) and Drory *et al.* (2004a, hereafter MUNICS VI), for example. Obviously, this allows the direct study of the history of the assembly of stellar mass in the galaxies and thus helps to understand the mechanism of their formation.

2.2 The MUNICS Project

The Munich Near-Infrared Cluster Survey is a wide-field medium-deep imaging survey in the near-infrared and optical, and is a powerful tool to study the evolution of field galaxies out to redshifts $z \lesssim 1$, although it was initially designed to search for high-redshift galaxy clusters. This aspect of the survey is described in Botzler (2004).

Some of the MUNICS fields are targeted towards $1 < z < 2$ quasars to search for clusters in their environment (Snigula 2001), but these fields lack optical data and will not be discussed here. The main part of the survey consists of ten ‘mosaic fields’, which are 2-by-2 mosaics of near-infrared images taken with OmegaPrime at the 3.5-m telescope at Calar Alto observatory (Spain). Each 2-by-2 mosaic is covered with optical images with circular aperture from the CAFOS camera at the 2.2-m telescope at Calar Alto, as is illustrated in Figure 2.1. The field names and coordinates are listed in Table 2.2.

Near-infrared images were taken in the K' and J filters, and their reduction is described in Drory (2002) and Drory *et al.* (2001b, hereafter MUNICS I). Additional

Table 2.1: Completeness limits for the MUNICS photometric survey. All magnitudes are the 50 per cent completeness limit for point sources and refer to the Vega system.

Filter	K'	J	I	R	V	B
m_{lim} [mag]	19.1	20.9	22.3	23.6	24.0	24.0

Table 2.2: The ten MUNICS mosaic fields. The table gives the field name (see Figure 2.1), the field coordinates (right ascension α and declination δ as well as galactic coordinates l and b) for the equinox 2000.0 and the effective area of the field in square arc-minutes. For all these fields photometry in K' , J , I , R , V and B is available, and the effective area is the area of the sky covered by observations in all six filters.

Field	α (2000.0)	δ (2000.0)	l (2000.0)	b (2000.0)	Area [arcmin ²]
S2F1	03:06:41	+00:01:12	178.66	-47.67	119.1
S2F5	03:06:41	-00:13:30	178.93	-47.84	123.7
S3F1	09:04:38	+30:02:56	195.37	+40.64	116.6
S3F5	09:03:44	+30:02:56	195.32	+40.45	107.6
S4F1	03:15:00	+00:07:41	180.58	-46.05	105.6
S5F1	10:24:01	+39:46:37	180.85	+57.04	115.7
S5F5	10:25:14	+39:46:37	180.76	+57.27	105.3
S6F1	11:55:58	+65:35:55	131.90	+50.55	117.1
S6F5	11:57:56	+65:35:55	131.60	+50.62	116.5
S7F5	13:34:44	+16:51:44	349.45	+75.66	119.1
All					1146.3

optical imaging for the mosaic fields was obtained in the I , R and V filters (Feulner 2000), and, more recently, also in the B band (see Section 2.3). Object detection and photometry were carried out with YODA (Drory 2003). We produce a strictly K -band selected catalogue by running the detection algorithm on the K -band images, and then doing the photometry in all filters at the positions determined in the K -band image and appropriately transformed to the coordinate systems in the other filters. Photometry is done in elliptical apertures the shape and size of which is fixed from the K -band image of each object.

The completeness function of this K -band selected catalogue was determined by running extensive Monte-Carlo simulations with artificial objects (Snigula *et al.* 2002). The limiting magnitudes of the survey are summarised in Table 2.1. The final K' -selected photometric catalogue contains about 8000 objects (Feulner 2000, Drory 2002).

Table 2.3: Observing runs and calibration for the MUNICS B -band observations.

Date	Fields	N_B	k_B
9.1.2002	S5F1	24.03 ± 0.05	-0.25 ± 0.03
10.1.2002	S2F1, S3F1, S3F5, S5F5	23.90 ± 0.05	-0.25 ± 0.03
11.1.2002	S2F5, S4F1, S6F1, S6F5	24.03 ± 0.04	-0.27 ± 0.03
9.6.2002	S6F1, S7F5	24.40 ± 0.01	-0.35
10.6.2002	S6F1, S7F5	24.40 ± 0.07	-0.34 ± 0.04

2.3 MUNICS B -Band Imaging

While the original MUNICS catalogue contained photometry in the K' , J , I , R and V bands, we decided to do complementary observations in the B filter for all MUNICS mosaic fields. Adding more information about the blue part of the spectrum has two advantages: Firstly, the photometric redshifts (Baum 1962, Koo 1985, Bender *et al.* 2001) which are used for the bulk of the objects in the survey catalogue reach higher accuracy with more available filters. This is especially true for objects at low redshifts, where the V filter is insufficient in tracing prominent breaks in the spectral continuum. The use of photometric redshifts in MUNICS is described in detail in Drory (2002) and Drory *et al.* (2003, hereafter MUNICS II). Secondly, at redshifts $z \gtrsim 0.5$ or so the flux in the B band traces the ultraviolet part of the objects' spectral energy distribution and thus can be used to estimate the star formation rate of MUNICS galaxies.

B -band observations of the MUNICS mosaic fields were carried out 9 and 11 January 2002 and 8-10 June 2002 with the Calar Alto Faint Object Spectrograph (CAFOS) focal reducer at the 2.2-m telescope at Calar Alto Observatory (Spain).

The data were reduced in a fairly standard manner using IRAF² (Tody 1986, 1993), except for cosmic ray cleaning. The B -band data reduction is very similar to the analysis of the other optical data in MUNICS, described in Feulner (2000) and Drory *et al.* (2001b). The frames were bias/over-scan corrected and then flat-fielded using a combination of dome flats and sky flats.

Cosmic ray events were identified by searching for narrow local maxima in the image and fitting a bivariate rotated Gaussian to each maximum. A locally deviant pixel is then replaced by the mean value of the surrounding pixels if the Gaussian obeys appropriate flux ratio and sharpness criteria Gössl & Riffeser (2002). Such a procedure is much more expensive in terms of computing time (roughly 10 CPU minutes per frame) compared to standard median filtering techniques, but is much more reliable in finding cosmic ray events in the wings of objects and in cleaning long cosmic ray trails.

The re-imaging system of CAFOS causes substantial radial distortion of the image which had to be dealt with before co-adding the offset images. Therefore the frames

²IRAF, the Image Reduction and Analysis Facility, is distributed by the National Optical Astronomy Observatories, which are operated by the Association of Universities for Research in Astronomy, Inc, under cooperative agreement with the National Science Foundation.

were rectified using the known distortion equation, a polynomial of fourth order in the distance from the optical axis (K. Meisenheimer, private communication).

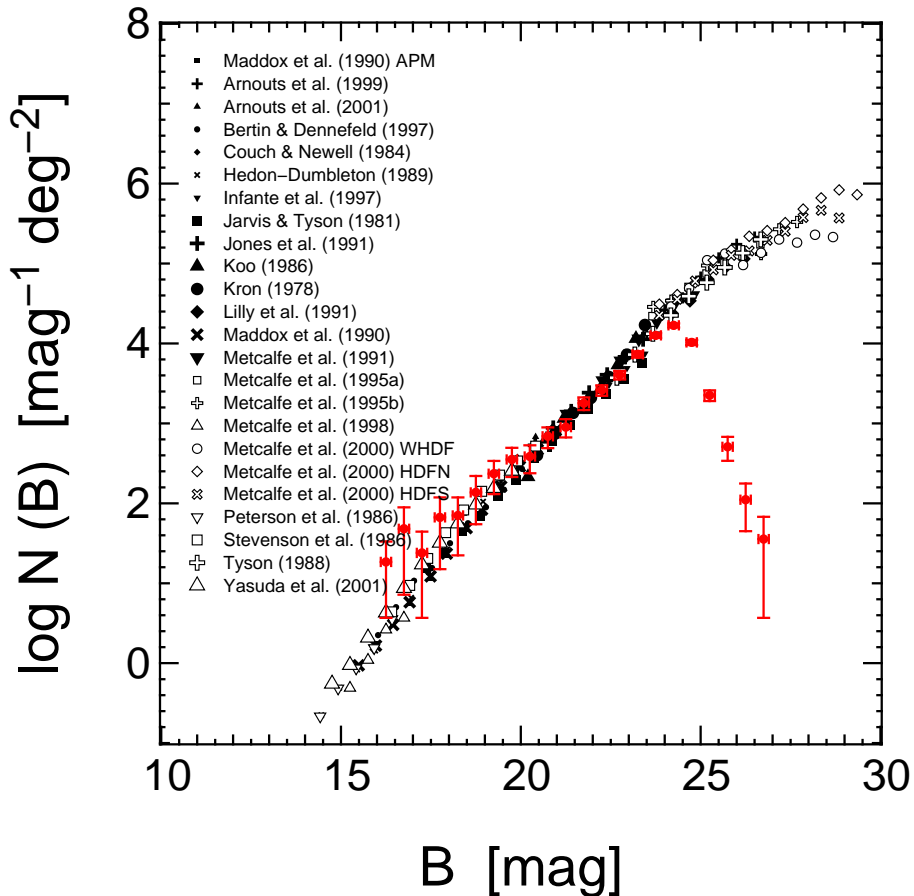


Figure 2.2: Galaxy number counts in the MUNICS *B*-band images compared to literature data. No correction for incompleteness has been applied. The published data were taken from a compilation of N. Metcalfe (private communication).

If necessary, variations in the background intensity across the frames caused by scattered light were fitted and subtracted in each individual frame. The images were then corrected for atmospheric extinction and scaled to a common photometric zero-point before finally being added using the positions of ~ 15 bright objects for determination of the offsets between the individual frames.

During photometric nights, photometric standard stars were observed (Landolt 1992). For each field, a photometric zero point and the atmospheric extinction were determined. The extinction coefficients were usually consistent with a Rayleigh atmosphere, with a few nights showing higher extinction, albeit within the variations typical for Calar Alto.

The *B* images of each field were registered against the *K'*-band image by matching the positions of ~ 200 bright homogeneously distributed objects in the frames and determining the coordinate transform from the *K'*-band system to each image in the other

four pass-bands using the tasks `XYXYMATCH` and `GEOMAP` within `IRAF`. The scatter in the determined solutions is less than 0.2 pixels RMS. Note that the frames themselves are not transformed. We only determine accurate transformations and apply these later to the apertures in the photometry process.

To show the quality of the B -band data for the MUNICS project we compare the galaxy number counts, i.e. the surface density of galaxies per magnitude bin, to published number counts (see Figure 2.2). Stars have been excluded based on their spectral energy distributions (see 7.3 for details). Note that the number counts shown in the Figure are not corrected for incompleteness at fainter magnitudes.

Clearly, the MUNICS B -band observations are reasonably complete to $B \sim 24$. It also nicely illustrates the scope of the survey: While there are surveys with much larger field which are able to find large numbers of bright (low redshift) galaxies, and the classic deep fields which probe the very faint (and very high redshift) galaxy population, MUNICS constitutes an important probe of the intermediate-redshift universe.

Furthermore, in Figure 7.1 we show the completeness functions for the B -band images of the ten MUNICS mosaic fields, based on Monte-Carlo simulations of artificial point-sources placed at random in the images. After running the object detection algorithm on the images, the fraction of re-detected artificial objects as a function of magnitude is computed. This is the quantity shown in the Figure. It is obvious that the data quality is very good and homogeneous over all ten MUNICS fields.

2.4 MUNICS-Deep

We have recently started to extend MUNICS to higher redshift. This new project, called MUNICS-Deep, will image one square degree to a depth two magnitudes fainter than MUNICS. While MUNICS is limited to studying galaxy evolution at $z \lesssim 1.2$, the new dataset will allow to probe the changes in the field galaxy population in the important redshift range $1 \lesssim z \lesssim 2$, thus building a bridge between medium-deep surveys and the regime of the Lyman-break galaxies (see Section 1.2 for an overview). Observations for MUNICS-Deep are still in progress, but promise exciting new results in observational cosmology.

Chapter 3

A Near-Infrared–Selected Galaxy Redshift Survey: Design and Observations

The main scientific results of my PhD thesis rely on a near-infrared selected spectroscopic redshift survey. This chapter describes how the targets for spectroscopy were selected and how the observations were carried out.

3.1 Selection of the Spectroscopic Sample

Objects for spectroscopic observations were chosen from the K -band selected photometric catalogue of MUNICS in ten survey fields, the details of which can be found in Table 2.2 (see Chapter 2 for a description of the field nomenclature). The K -magnitude selected field galaxy spectroscopy programme was carried out in the fields S2F1, S2F5, S5F1, S6F5 and S7F5, while the spectra available in the other fields originate from a dedicated search for faint red AGN.

Object selection for spectroscopy was based on two criteria. Firstly, we aimed at a K -band magnitude-limited sample. Due to the use of optical spectrographs, the appropriate K -band limit is determined by the typical colours of red galaxies (roughly $R-K \simeq 4$, see Figures 5.4 and 5.5) and the limits of the optical spectrographs at the telescopes we used. Trying to keep the K -band completeness of the spectroscopic sample as high as possible yields sample limits of $K \leq 17.5$ for spectroscopic observations at the Calar Alto 3.5-m telescope and $K \lesssim 19.0$ for observations at the Very Large Telescope (VLT). Obviously, a small fraction of very red objects will be lost, but their number density is comparatively small anyway (see, for instance, Martini (2001) and references therein). Results on the few very red objects identified spectroscopically can be found in Section 5.8.

Secondly, in selecting objects for spectroscopy, we have tried to exclude stars. This was done using the image-based classification of objects into point-like objects and extended sources as described in MUNICS I. For the classification the point-spread function (PSF) for each image and each filter is determined. Then the intensity distribution

Table 3.1: Summary of results of the test of the image-based classification method for a sample of objects with $K' \leq 16.5$ in two survey fields (upper part of table) and for the whole spectroscopic sample (lower part of table). The numbers quoted in the table give the number and fraction of objects with stellar or galactic spectrum among objects classified as point-like or extended, respectively.

Morphological classification	Spectral classification			
		Star	Galaxy	
Sparse sample with $K' \leq 16.5$:				
Point-like	39	100 per cent	0	0 per cent
Extended	11	20 per cent	44	80 per cent
Complete spectroscopic sample:				
Point-like	64	79 per cent	17	21 per cent
Extended	28	7 per cent	397	93 per cent

of every object in the images is compared to the PSF, and the objects are classified into stars (PSF-like sources) and galaxies (extended sources). Finally, this classification information, which is available for all objects in all six filters, is weighted by the signal-to-noise ratio of the object in each filter, and the final classification is done.

To test this classification procedure, we have built up a small spectroscopic test sample of bright objects which was purely magnitude selected and therefore contains both stars and galaxies. The results of the comparison between image-based and spectroscopic classification show that our morphological approach is able to distinguish stars and galaxies with reasonable reliability. The results of this test are summarised in Table 3.1.

On a purely magnitude-limited sample containing all objects with $K' \leq 16.5$, all objects classified as point-like are indeed stars, and the stellar contamination is 20 per cent only. On the other hand, we can also use the complete spectroscopic catalogue to investigate the reliability of our classification method, yielding also very good agreement between spectral and morphological classification.

Thus our method to classify objects into point-like or extended sources can reliably reduce stellar contamination of the spectroscopic catalogue as long as the objects are not too faint. Pre-selecting our spectroscopic sample by image morphology results in a loss of less than 4 per cent of all galaxies which are classified as point-like, and in a 7 per cent contamination by stars.

The quality of the classification procedure is also demonstrated in Figure 3.1, where one can see that the vast majority of all objects on the stellar sequence are indeed classified as point-like. In Chapter 5 we will show that the fraction of stars in our spectroscopic sample is indeed much lower than in comparable surveys.

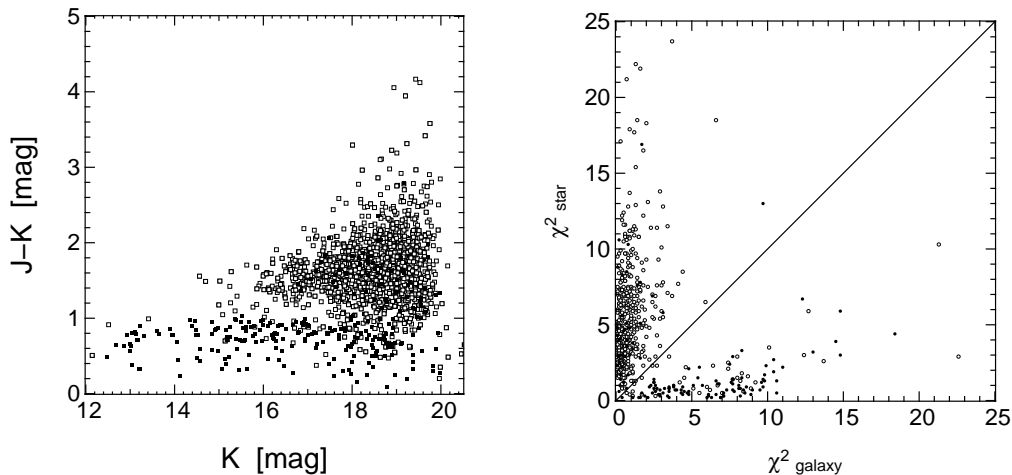


Figure 3.1: Illustration of resulting object classification in point-like (filled symbols) and extended sources (open symbols). *Left-hand panel:* The locus of objects in the $J - K$ vs. K diagram for two MUNICS mosaic fields. The sequence of stars at $J - K \simeq 1$ indeed contains mostly point-like sources. *Right-hand panel:* A comparison of the morphological classification to a χ^2 criterion based on fitting template spectral energy distributions of stars and galaxies to the broad-band photometry of the objects in the MUNICS field S2F1. Again, the agreement is very good.

3.2 Spectroscopic Observations

The largest part of the spectroscopic observations was carried out with the Multi-Object Spectrograph for Calar Alto (MOSCA) at the 3.5-m telescope at Calar Alto Observatory¹ (Spain), and with FOcal Reducer and low-dispersion Spectrograph (FORS) 1 and 2 (Seifert *et al.* 1994) at the European Southern Observatory’s Very Large Telescope (VLT)². Part of the sample was observed with the Low Resolution Spectrograph³ (LRS; Hill *et al.* 1998) at the Hobby-Eberly Telescope (HET) at McDonald Observatory, Texas, and with ESO Faint Object Spectrograph and Camera (EFOSC) 2 at the ESO 3.6-m telescope on La Silla (Chile). All observing runs are listed in Table 3.2.

MOSCA was used with the Green 500 grism⁴ and without any filter. MOSCA’s multi-object spectroscopy mode uses slit masks containing typically 20–25 slits of 1.5-arc-sec width. MOSCA is equipped with a 2048×4096 pixel CCD with 15- μ m pixel

¹The German-Spanish Astronomical Center at Calar Alto is operated by the Max-Planck-Institut für Astronomie, Heidelberg, jointly with the Spanish National Commission for Astronomy.

²ESO proposals number 66.A-0129 and 66.A-0123.

³The Marcario Low Resolution Spectrograph is a joint project of the Hobby-Eberly Telescope partnership and the Instituto de Astronomía de la Universidad Nacional Autónoma de México, and was partly funded by the Deutsche Forschungsgemeinschaft, grant number Be 1091/9–1. The Hobby-Eberly Telescope is operated by McDonald Observatory on behalf of The University of Texas at Austin, the Pennsylvania State University, Stanford University, Ludwig-Maximilians-Universität München, and Georg-August-Universität Göttingen.

⁴A “grism” is, as the name might suggest, a combination of a prism and a grating. The purpose of the device is to keep light of a certain central wavelength undeviated as it passes through the grism.

Table 3.2: Observing runs of spectroscopic follow-up observations for the MUNICS project. The runs in 2002 were mostly carried out in service mode.

Date	Telescope	Instrument	Comment
15.12.1999	ESO 3.6	EFOSC2	
26.–31.5.2000	Calar Alto 3.5	MOSCA	
27.5.2000	HET	LRS	
21.11.2000	VLT UT1 (Antu)	FORS1	
21.–22.11.2000	VLT UT2 (Kueyen)	FORS2	
24.–28.11.2000	Calar Alto 3.5	MOSCA	
17.–20.1.2001	Calar Alto 3.5	MOSCA	
26.3.–1.4..2001	Calar Alto 3.5	MOSCA	
18.–21.5.2001	Calar Alto 3.5	MOSCA	
15.–20.12.2001	Calar Alto 3.5	MOSCA	
9.–12.4.2002	Calar Alto 3.5	MOSCA	MUNICS-AGN
9.–17.5.2002	Calar Alto 3.5	MOSCA	
7.10.2002	Calar Alto 3.5	MOSCA	
4.–5.11.2002	Calar Alto 3.5	MOSCA	MUNICS-AGN
9.–10.11.2002	Calar Alto 3.5	MOSCA	
18./23./26.2.2003	HET	LRS	Cluster S6F1c11

size, yielding an effective area of 10×10 arcmin² usable for spectroscopy.

At the VLT, FORS1 offers 19 movable slit-lets, whereas FORS2 is equipped with a Mask Exchange Unit (MXU), which allows spectroscopy of a larger number of objects. For both instruments a slit width of 1 arc-sec was chosen. The CCD detectors are 2048×2048 pixel in size with $24\text{-}\mu\text{m}$ pixels, thus allowing a field of roughly 3×7 arcmin² to be used for spectroscopy. Grism 300 I and filter OG590 were used for the observations

In multi-object spectroscopy mode, the LRS at HET provides 13 slit-lets of 1.5-arc-sec width. The spectra were obtained through grism 300 and filter GG385.

Finally, EFOSC2 at the ESO 3.6-m telescope was equipped with grism 11 and a slit-width of 1.0 arc-sec. The technical characteristics of all instruments used for the spectroscopic observations are summarised in Table 3.3.

The objects selected for spectroscopy were sorted into bins according to their apparent R -band magnitude. The magnitude ranges, the typical number of mask setups for each MUNICS field (13×13 arcmin²), and the exposure times are given in Table 3.4. All objects with $R \leq 21.5$ (roughly corresponding to $K' \leq 17.5$) were observed at the Calar Alto 3.5-m telescope, the ESO 3.6-m telescope, and the HET, whereas spectroscopy of the fainter sample was carried out at the ESO VLT.

Table 3.3: Technical characteristics of the spectrographs used for the observations. The effective resolution of the resulting spectra is given for the gratings listed in the table and the appropriate slit-widths mentioned in the text (the seeing during the spectroscopic observations always was of the order of the slit-width).

Instrument	Grism & Filter	Spectral range (\AA)	Resolution (\AA)
MOSCA	Green 500	4300–8000	13.6
EFOSC2	G11	3380–7520	13.2
LRS	G300 + GG385	4000–8000	13.9
FORS1	G300I + OG590	6000–9500	13.0
FORS2	G300I + OG590	6000–9500	13.0

Table 3.4: R -band magnitude bins, typical number of masks per MUNICS field, and exposure times for the spectroscopic observations. Note that the faintest objects with $R > 21.5$ were observed at the ESO VLT, while all brighter objects were mainly observed at the 3.5-m telescope at Calar Alto, a few also at the ESO 3.6-m telescope, or at the HET.

Magnitude	Number of masks	Exposure time
$R \leq 18.5$	1	1×1800 s
$18.5 < R \leq 19.5$	2	2×2100 s
$19.5 < R \leq 20.5$	3	5×2400 s
$19.5 < R \leq 21.5$	4	5×5400 s
$R > 21.5$	9	3×3000 s

Chapter 4

Analysing Multi-Object Spectroscopy Data

The spectroscopic data for the redshift survey described in this thesis have to be treated in several ways before analysis. This ‘data reduction’ includes, for example, the subtraction of electronic noise, and the correction of sensitivity variations across the detector. Since these are crucial steps on the way to the final spectra, I will give a detailed account of the data reduction process in this chapter.

4.1 Motivation

Multi-object spectroscopy (MOS) is an efficient way of obtaining spectra for several objects at the same time. There are basically three different ways of doing this technically: with masks having slits cut into them at the place of the objects, with moving ‘slit-lets’, or with optical fibres. All spectra taken for the MUNICS redshift survey used either mask or slit-let spectroscopy. The astronomer who has to extract one-dimensional spectra from this kind of data faces several problems. Firstly, the mere number of spectra which have to be extracted from the two-dimensional frame. Secondly, the optics of the spectrograph bends the spectra, resulting in curved object spectra on the detector. Thirdly, the slits in MOS spectra are usually much shorter than in ‘long-slit’ spectroscopy, so special care has to be taken to ensure accurate subtraction of the night-sky emission. Some of the reduction steps can be done in an automatic manner, but many require interactive control, making the whole MOS data reduction process rather time-consuming.

This Chapter will describe the reduction of MOS data taken for the MUNICS redshift survey. Since no data for this project were taken with fibre spectrographs, the reduction procedure outlined in this Chapter does not apply to this kind of data. A specialised reduction software was developed. This ‘pipeline’ is based on IRAF¹ (Tody 1986, 1993) and makes use of standard IRAF reduction tools from the CCDRED and

¹IRAF, the Image Reduction and Analysis Facility, is distributed by the National Optical Astronomy Observatories, which are operated by the Association of Universities for Research in Astronomy, Inc, under cooperative agreement with the National Science Foundation.

SPECRED packages, but a number of additional tasks had to be developed within the IRAF Command Language (CL; Anderson 1989) environment for special problems like header correction, two-dimensional sky subtraction etc. Also, the pipeline was carefully designed to record all reduction steps and parameters to log files to make it easier for the user to trace potential problems. Another important part of the pipeline are applications to quickly control the quality of essential reduction steps like, for instance, the subtraction of the night-sky emission lines.

Since the reduction of MOS data is technically challenging, and since only very few detailed descriptions for MOS data reduction are available, I intend this chapter to serve as a guide to MOS data reduction for interested observers. Naturally, it is a rather technical chapter, so all readers interested in the scientific application of the MUNICS near-infrared selected redshift survey are advised to continue reading with Chapter 5.

4.2 Basic Data Reduction

4.2.1 Bias Correction and Cosmic-Ray Filtering

Data reduction was performed using IRAF, except for cosmic ray filtering. The data were obtained using charged-coupled devices (CCDs) as detectors, so firstly, a standard CCD reduction was performed within the IRAF CCDRED package (see Howell 2000 for technical details on CCDs and the basic principles of CCD reduction, and Massey 1997 for a guide to CCD reduction with IRAF).

To measure the two-dimensional noise pattern on the CCD, a number of ‘bias frames’, exposures with zero integration time, were taken and combined using ZERO-COMBINE. During visitor-mode observing runs, bias frames were taken on a daily basis. The bias pattern proved to be very stable, so that bias frames from different nights could be combined to achieve better statistics. The mean level and RMS of all bias frames was checked, and low and high pixels were rejected during the combining process. Note that the mean level of the bias frames was subtracted using the information from the ‘over-scan region’ yielding just the two-dimensional variations of the noise pattern with respect to the constant bias level. This bias image was then subtracted from all images, together with the mean noise level obtained from the over-scan region of each individual exposure in order to account for any variation of the bias level with temperature or time.

Bad pixels on the CCDs were corrected for by linear interpolation, and cosmic rays were identified by searching for narrow local maxima in the image and fitting a bivariate rotated Gaussian to each maximum. A locally deviant pixel is then replaced by the mean value of the surrounding pixels if the Gaussian obeys appropriate flux ratio and sharpness criteria (Gössl & Riffeser 2002). Note that this is a very time-consuming method, but produces excellent results. Emission lines on the galaxy spectra are not affected by this subtractions, since their width is considerably larger than the typical width of a cosmic-ray event. Note also that we prefer to remove the cosmic rays *before* the extraction of one-dimensional spectra, because the tracing of the curved spectra on the detector is a crucial step, and too many cosmic rays pose difficulties for the tracing algorithm, especially in case of faint objects.

4.2.2 Shifting, Weighting and Summing (Part 1)

Usually the total exposure for each mask was split into several shorter exposures. In many cases the objects were drifting a bit along the slits during the very long exposure times of up to 7.5 hours, so the individual exposures had to be shifted in order to make them aligned. To do this, the following method was adopted and implemented in an IRAF script: The positions of several spectra on the mask were measured by fitting Gaussian profiles perpendicular to the dispersion direction. Because of the curved spectra these positions have to be measured at the same position for each two-dimensional image. From the centres of the Gaussians the pixel shift was computed together with the RMS of the measurement for quality control. The two-dimensional images were then shifted with sub-pixel accuracy.

Before adding the individual images, optimum weights were computed from the signal of the spectra, their width (corresponding to the seeing for compact sources), and the sky background. The weighting scheme maximises the signal-to-noise ratio (SNR) for the faint objects (A. Gabasch, private communication; Heidt *et al.* 2003). Finally, after applying the weights, the two-dimensional images were added to a first image of the mask containing the information from all exposures.

4.3 MOS Reduction

4.3.1 Treatment of Tilted Slits

As described in Section `s:specobs`, part of the spectra were taken using the FORS2 instrument at the VLT. The mask preparation software for FORS2 allows to tilt slits in order to maximise the light received by the spectrograph. For elongated objects we have tried to align the slit along the major axis of the galaxies to reduce light loss at the mask.

While this procedure has some advantages, it does make MOS reduction a bit more complicated. In principle there are different ways of dealing with this, but to enable data reduction within the IRAF `SPECRED` package, we decided to rectify the spectra by rotating them in the two-dimensional image. For this purpose, I designed an IRAF programme which cuts out the appropriate slit section on the two-dimensional frame and rotates it according to the tilt angle given in the image header. After this correction, all slits were perfectly aligned and could be treated in the same manner.

4.3.2 Defining and Tracing the Spectra

The following reduction of the spectra was performed within the IRAF `SPECRED` package. The locations of the spectra on the two-dimensional image were defined at a given position along the dispersion axis (using `APEDIT`), and the spectra were followed using the `APTRACE` task. This task steps along the dispersion direction and determines the position of the spectrum at each position by fitting a Gaussian perpendicular to the dispersion direction (Ellingson 1989). To ensure accurate tracing also for faint objects, we took the sum of 50 pixels along the dispersion to construct the profile. Then the trace of the spectra produced by the distortion of the spectrograph was approximated

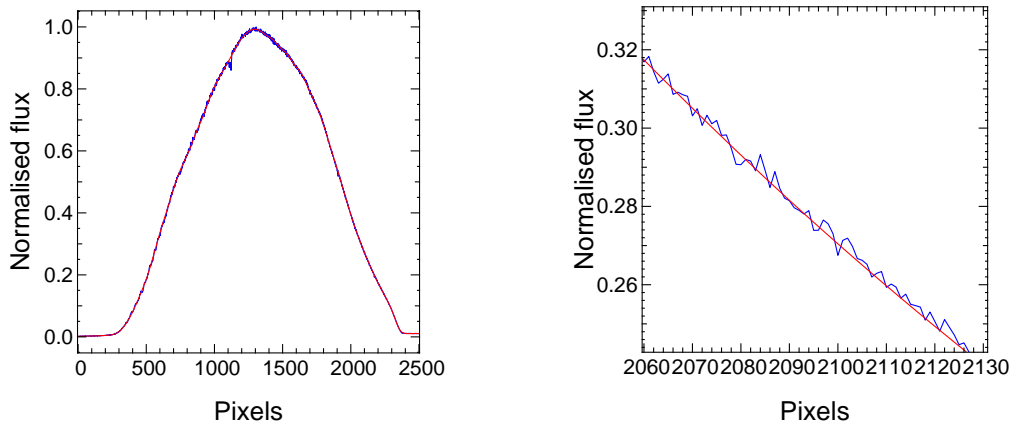


Figure 4.1: *Left-hand panel*: Typical slit illumination function of the MOSCA spectrograph with the Green 500 grism extracted from a continuum-lamp flat-field. The blue curve shows the illumination along the dispersion axis, and the red curve the fitted illumination function as described in the text. The *right-hand panel* shows an enlarged part of the curve, making the difference between the pixel-to-pixel variations (blue curve) and the smoothed illumination function (red curve) obvious.

by a fourth-order Legendre polynomial. To control the quality of the tracing process, the resulting trace functions were plotted on top of the two-dimensional image. An example for such a test image for one single slit is shown in the uppermost panel of Figure 4.5.

4.3.3 Flat-Fielding

Electronic detectors like the Charge-Coupled Devices (CCDs) used in optical astronomy show pixel-to-pixel variation of the detector sensitivity. For normal astronomical imaging this can be corrected using ‘flat-field’ images, normalised exposures of a uniformly lit surface, usually either the twilight sky or an appropriate screen in the telescope dome illuminated by an electric lamp. For spectroscopy, the detector records spectral information along one axis, so an internal continuum lamp within the spectrograph can be used as a source of uniform light. For this survey, flat-fields were constructed from typically 11...21 images of an internal continuum lamp. Dome flat-fields taken for comparison showed no marked difference to these continuum flats. The flat-fields were normalised by dividing the flat field of each slit by its ‘illumination function’. The illumination function is computed by fitting a set of 3rd-order splines to the pixel rows along the dispersion direction for each slit using the APNORMALIZE task. The number of spline pieces must not be too small in order to follow the illumination function properly, but not too large either in order not to follow the pixel-to-pixel sensitivity variations. The situation is illustrated in Figure 4.1, where we show a cut along the dispersion direction for one slit for the MOSCA spectrograph with the Green 500 grism (blue curve) and the corresponding illumination function (red curve).

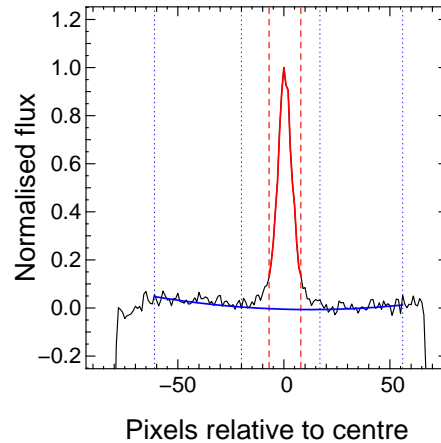


Figure 4.2: This figure shows how the apertures for the extraction of one-dimensional spectra were defined. The thin black line shows a typical profile of a spectrum across the slit. The flux is given in normalised units, the pixel coordinates are relative to the object position. The dashed lines and the thick part of the profile indicate the aperture used for profile fitting and object extraction, whereas the dotted lines show the sky apertures. The approximation of the sky background is also shown.

4.3.4 Shifting, Weighting and Summing (Part 2)

After dividing the individual un-shifted and un-weighted images by the normalised flat-field image (of course the pixel-to-pixel variations have to be corrected in the un-shifted images!), the flat-fielded images were shifted again with the pixel offsets recorded during the first shifting process, the weights were applied, and these images were summed to the final two-dimensional image of the mask.

4.3.5 Extraction of the One-Dimensional Spectra

After dividing the frames by the appropriate flat-field, the apertures for extracting one-dimensional spectra from the two-dimensional images as well as the apertures for subtraction of the night sky were defined. This was done manually in the APEDIT task for each object to ensure maximum signal-to-noise ratio and accurate sky subtraction. The extraction aperture was confined by the points where the profile of the spectrum perpendicular to the dispersion axis reaches the 10 per cent level. This particular value was chosen after extensive tests with different aperture widths. If possible, sky apertures on both sides of each object were used for the sky subtraction, and the variation of the night sky perpendicular to the spectrum of each object was approximated by a polynomial of second order. Note that we used lower-order polynomials in cases where there were only few pixels to define the sky region in order to prevent artefacts due to ill-defined approximations. Figure 4.2 illustrates the definition of extraction and sky-subtraction apertures.

After that the one-dimensional spectra were extracted by summing the pixel values for each wavelength bin within the manually defined apertures and subtracting the

appropriately scaled sky value from the fit perpendicular to the spectrum. Profile-weighted sums were used to maximise the signal-to-noise ratio (Horne 1986, Marsh 1989).

Additionally we produced two-dimensional sky-subtracted images to be able to check whether a feature seen in the one-dimensional spectrum is a real spectral feature or a residual, for example from the replacement of cosmic ray events or the subtraction of sky-lines. Note that check images like these are of paramount importance for quality control. Since the IRAF SPECRED package does not offer this possibility, a task had to be written which parses the appropriate IRAF database file containing the aperture definitions, extracts the important information and finally computes the two-dimensional sky-subtracted image in a way very similar to the one done during the actual extraction process. An example of one slit in a this kind of image is presented in Figure 4.5.

4.3.6 Wavelength Calibration

In the case of the MOSCA, EFOSC2 and LRS observations, spectra of internal lamps were used for wavelength calibration. Figure 4.3 shows as an example the spectrum of the Hg-Ar-Ne lamp in the MOSCA spectrograph. After identifying typically 10 lines in the calibration lamp spectra, the remaining lines were identified automatically using IDENTIFY, and the wavelength transformation was computed in form of a fourth order polynomial. The typical residuals from this approximation were of the order of 0.3\AA . Then the one-dimensional spectra were transformed to wavelength coordinates and re-binned using the appropriate resolution using the DISPCOR task. Note that we usually took only one wavelength calibration image per mask, either between two mask exposures or after finishing all mask exposures. Nevertheless, this does not affect the wavelength calibration, since the maximum shift of the spectral pattern of a calibration lamp, caused by the flexure of the instrument, was measured to be 1 pixel for MOSCA between two extreme orientations of the spectrograph. According to the manuals, the flexure of the other instruments should have a similar order of magnitude. Also, the accuracy of the wavelength calibration can be efficiently examined by measuring the positions of night-sky emission lines, and the comparison showed negligible deviations. The influence on the redshift determination will be discussed in Section 5.4. For the FORS data we used the lines of the night sky for the wavelength calibration, with the line data taken from Osterbrock *et al.* (1996, 1997), since the calibration frames taken with internal lamps were either over-exposed, or the lines did not cover the whole wavelength range. With night-sky emission lines there is the problem of line-broadening or mis-identification of lines (especially since many lines are actually doublets!), but the accuracy is still higher than the one which could be reached by using partly saturated lines or by extrapolation the wavelength solution over a large range in wavelength. The RMS of the night-sky emission line fits was of the order of 0.5\AA , slightly larger than with internal calibration lamps, but still very good. Moreover, for some objects we had independent measurements with MOSCA (where we could use internal lamps), and the agreement turned out to be very good, with no apparent systematics (see Section 5.4).

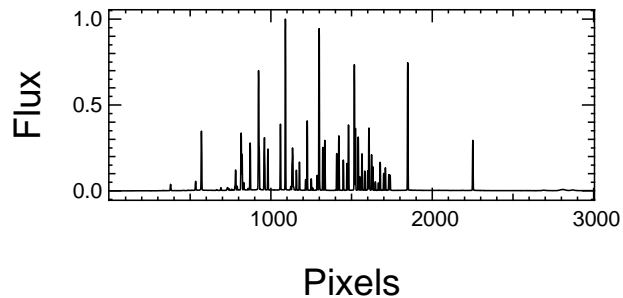


Figure 4.3: Wavelength calibration lamp spectrum as produced by the Hg-Ar-Ne lamp in the MOSCA spectrograph.

4.3.7 Flux calibration

Finally, the spectra were flux calibrated using spectro-photometric standard stars observed during each night. Both the relative flux calibration correction for the response function of the spectrograph and the absolute flux calibration to convert instrumental flux units to physical flux units were applied. The standard stars' one-dimensional spectrum, reduced in much the same way as outlined for the MOS data, was compared to the tabulated spectrum using the task `STANDARD`. From this, the 'sensitivity function' of the spectrograph was computed using `SENSFUNC`, and the flux calibration was applied (`CALIBRATE`). Extinction correction was based on average extinction curves either as published by the observatories (ESO for La Silla and Paranal Observatory, and McDonald Observatory) or by Hopp & Fernández (2002) for the Calar Alto observations. The accuracy of the flux calibration was tested by comparing the flux in individual broad-band photometry filters to the flux in the flux-calibrated spectrum. Figure 4.4 shows an example for this method. Clearly, the flux calibration is very good, with deviations visible only at the ends of the spectral range of the instrument, where the corrections due to the response function of the grism become large. Note that we do not apply corrections for light loss at the slit edges.

4.3.8 Redshift Determination

Redshifts were determined using the `RV` package within `IRAF`. Prominent absorption and emission features were identified in the spectra to obtain the corresponding redshift of a galaxy using the `RVIDLINES` tasks. The exact position of the lines is determined by fitting a Gaussian profile to the features.² We compared the one-dimensional spectrum with the two-dimensional sky-subtracted image to exclude features possibly affected by residuals from night-sky subtraction or cosmic filtering, see Figure 4.5 for an example of this kind of analysis image. Furthermore we ensured that the radial velocity displacement between different spectral features is not larger than the typical

²So far we have not applied cross-correlation techniques to determine redshifts, however we plan to do so in the future to reduce the fraction of galaxies without secure redshift due to low signal-to-noise ratios, although first tests show that we cannot significantly increase the number of securely measured redshifts by using correlation methods.

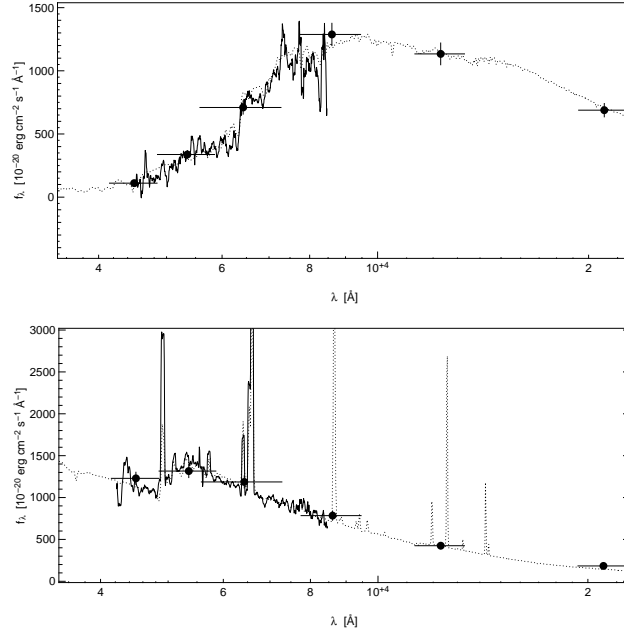


Figure 4.4: Comparison of the flux calibrated spectrum (solid line), the flux derived from MUNICS broad-band photometry in the filters *B*, *V*, *R*, *I*, *J* and *K* (filled circles with error bars), and a fit of a stellar population synthesis model to the photometric data (dotted line) for two objects in the spectroscopic MUNICS catalogue.

error expected from the measurement of the line centre and the wavelength calibration, i.e. typically $\Delta z \lesssim 5 \times 10^{-4}$. There were no significant differences observed between emission and absorption features, however, emission lines are usually much narrower and better defined than absorption lines yielding more precise redshift determination. For later control and object class selection all features identified in the spectra and used for the radial velocity measurement were recorded in the spectroscopic catalogue.

The measured redshifts were converted to heliocentric coordinates using the date of the observations and the observatory coordinates, but no corrections for the Sun's motion in the Milky Way was applied.

4.4 Catalogue Construction

The identification of the spectra with objects in the photometric catalogue is usually done using the files used to prepare the spectroscopic observations. During the definition of apertures for the trace the relative position of the spectrum in the slit is compared to a diagram showing the mask to ensure that the spectrum indeed corresponds to the desired object. In the case of additional objects on the slits, these are identified by measuring their distance to the main object in the slit and searching the photometric catalogue at the corresponding position.

All information is first entered into a mask-based catalogue. This catalogue is then processed by a script which produces the final catalogue sorted by right ascen-

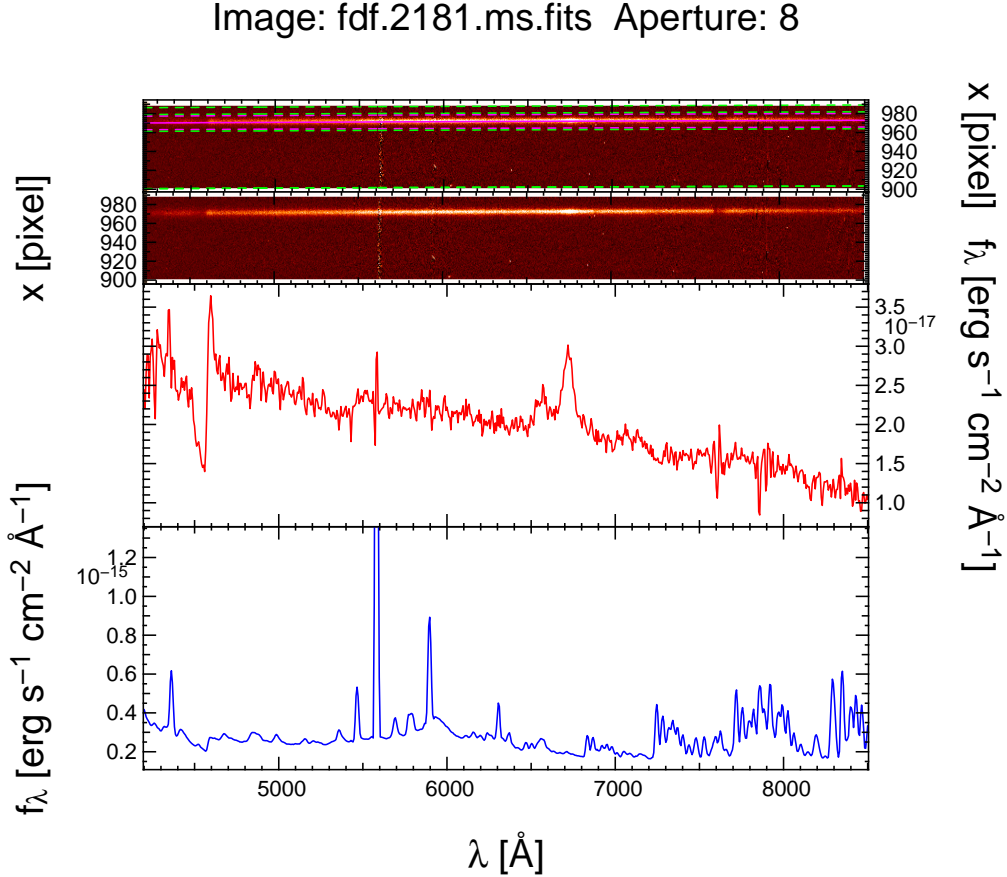


Figure 4.5: Example of an analysis plot used to control the quality of the reduction pipeline. The *first and second panel* show the region of the slit and its dispersion in the two-dimensional sky-subtracted image. Clearly, the sky subtraction is very good, only a few residuals from very strong lines are visible (e.g. the residual of the OI line at $\lambda = 5577\text{\AA}$). Additionally, the *first panel* shows the trace of the spectrum and the aperture limits for the extraction and sky-subtraction apertures. The extracted object spectrum and the sky spectrum are shown in the *third and fourth panel*, respectively. Note the difference in the flux scale for the last two panels, illustrating the importance of accurate subtraction of the night-sky lines which are much brighter than the object spectrum itself.

sion. During this processing, multiple observations are identified, and for each object with multiple spectroscopic observation the one with highest quality is identified and written to the final catalogue. All multiple observations are recorded in a special catalogue which can be used to check the agreement of these repeated observations (see Section 5.4).

The final spectroscopic catalogue contains the celestial coordinates, the pixel coordinates form the photometric catalogue, the instrumental identification (mask and slit number), the measured redshift, the object classification based on the observed spectrum (galaxy, AGN, star, or unidentified object), a confidence class for the redshift

Table 4.1: Description of the confidence classes for the redshift measurement used in the final spectroscopic catalogue.

Class	Description
1	Many spectral features securely identified, very high SNR
2	Many spectral features securely identified, high SNR
3	Many spectral features securely identified, intermediate SNR
4	Several spectral features identified, lower SNR
5	Tentative identification of only a few lines or single emission line, low SNR
6	no redshift measured (very low SNR or technical problem)

determination, and a list of spectral features used for measuring the object’s redshift. The confidence class assigned to each object ranges from “1” to “6”, where “1” means highest confidence, and “6” means that no redshift could be determined. Descriptions of the confidence classes can be found in Table 4.1, although these can give only a crude impression of the meaning of the confidence classes. For all further analysis objects with confidence classes “5” and “6” are excluded. To check the assignment of confidence classes, we have made use of the 131 repeat observations of 63 objects described in detail in Section 5.4. The agreement between confidence classes attributed to the same object from different observations is in general very good. Deviations can be explained by different signal-to-noise ratios due to weather conditions or technical reasons. Not a single object with confidence class “1” to “4” has got a deviant redshift from a repeat observation. Typical examples for spectra and the appropriate confidence classes are shown in Figure 4.6.

Table 4.2: The table shows a small section of the spectroscopic catalogue with the celestial coordinates, the field name, the pixel coordinates in the K -band image, the observational details (telescope, instrument, mask identification number and slit number), the redshift, the object type, the confidence class, and the (truncated) list of line features used for the redshift measurement, where ‘a’ and ‘e’ indicate absorption and emission lines, respectively, and the four-digit numbers give the approximate wavelength of the feature in \AA .

α	δ	Field	x_K	y_K	Tel.	Instr.	Run	Mask	Slit	z	T	C	Features
⋮													
10:24:00.75	+39:43:49.2	S5F1	902.90	435.84	CA35	MOSCA	112000	5202	10	0.176	G	1	a3934a3969a4300a4341a5175a5893 ...
10:24:01.71	+39:43:46.3	S5F1	874.72	428.94	CA35	MOSCA	112000	5301	15	0.177	G	1	e3727a3934a3969a4300e4341e4861...
10:24:02.22	+39:48:00.3	S5F1	871.26	1070.67	CA35	MOSCA	112000	5202	06	0.000	S	1	a
10:24:04.30	+39:48:30.8	S5F1	812.14	1148.69	CA35	MOSCA	122001	5402	12	0.351	G	1	e3727a3934a3969e4341e4861e4959...
10:24:04.74	+39:48:23.9	S5F1	798.89	1131.42	CA35	MOSCA	112000	5201	04	0.199	G	1	a3934a3969a4300a4341a4861a5175...
10:24:05.17	+39:45:57.9	S5F1	779.94	762.94	CA35	MOSCA	112000	5301	11	0.054	G	1	e4341e4861e4959e5007e6563e6717
10:24:05.95	+39:44:53.4	S5F1	754.38	600.48	CA35	MOSCA	112000	5201	08	0.175	G	3	a3934a3969a4341a4861a5893
10:24:06.07	+39:52:53.8	S5F1	772.57	1813.46	CA35	MOSCA	112000	5301	01	0.281	G	3	e3727a3934a3969a4300a4341a5893...
10:24:06.32	+39:45:04.4	S5F1	743.99	628.54	CA35	MOSCA	012001	5401	15	0.174	G	2	a3934a3969a4300a4861e5007a5175
10:24:06.60	+39:52:19.6	S5F1	755.57	1727.54	CA35	MOSCA	122001	5402	20	0.584	G	4	e3727a3934a3969a4300a4341a5175
10:24:06.84	+39:51:12.5	S5F1	745.57	1558.29	CA35	MOSCA	012001	5401	02	0.701	G	2	a3934a3969a4300a4341a4861a5175
10:24:07.99	+39:52:10.4	S5F1	714.64	1704.94	CA35	MOSCA	112000	5202	03	0.123	G	3	a3934a3969e4861a5175a6563a6583...
10:24:08.17	+39:46:15.2	S5F1	693.39	808.18	CA35	MOSCA	112000	5201	06	0.157	G	1	e3727a3934a3969e4341e4861e5007...
10:24:08.70	+39:49:40.4	S5F1	687.33	1326.60	CA35	MOSCA	012001	5401	05	0.473	G	2	e3727a3934a3969a4300e4861e5007
10:24:08.78	+39:49:59.3	S5F1	685.69	1374.42	CA35	MOSCA	112000	5301	06	0.474	G	1	e3727a3934a3969a4300a4341a4861...
10:24:08.95	+39:41:50.2	S5F1	658.53	139.46	CA35	MOSCA	112000	5201	12	0.263	G	1	e3727a3934a3969a4300e4861e5007...
10:24:09.72	+39:49:58.3	S5F1	658.35	1372.21	CA35	MOSCA	112002	5181	07	9.999	G	6	a
10:24:09.81	+39:53:09.4	S5F1	664.52	1854.85	CA35	MOSCA	112000	5202	01	0.153	G	2	e3727a3934a3969a4300a4341e5007...
10:24:10.18	+39:52:22.1	S5F1	651.63	1735.68	CA35	MOSCA	112000	5301	02	0.306	G	1	a3934a3969a4300a5175a5893a6563
10:24:10.22	+39:44:22.7	S5F1	628.65	525.02	CA35	MOSCA	012001	5401	17	0.217	G	1	e3727a3934a3969a4300e4341e4861...
10:24:12.63	+39:41:47.0	S5F1	551.26	133.09	CA35	MOSCA	012001	5401	24	0.027	G	4	e5007e6563
10:24:12.74	+39:45:20.7	S5F1	557.88	672.86	CA35	MOSCA	112000	5201	07	0.280	G	1	e3727a3934a3969a4300e4341e4861...
10:24:13.31	+39:44:08.3	S5F1	537.89	490.36	CA35	MOSCA	112002	5181	18	9.999	G	6	a
10:24:13.45	+39:47:37.6	S5F1	543.50	1018.90	CA35	MOSCA	012001	5401	09	0.469	G	2	e3727a3934a3969a4861a5175a5893
⋮													

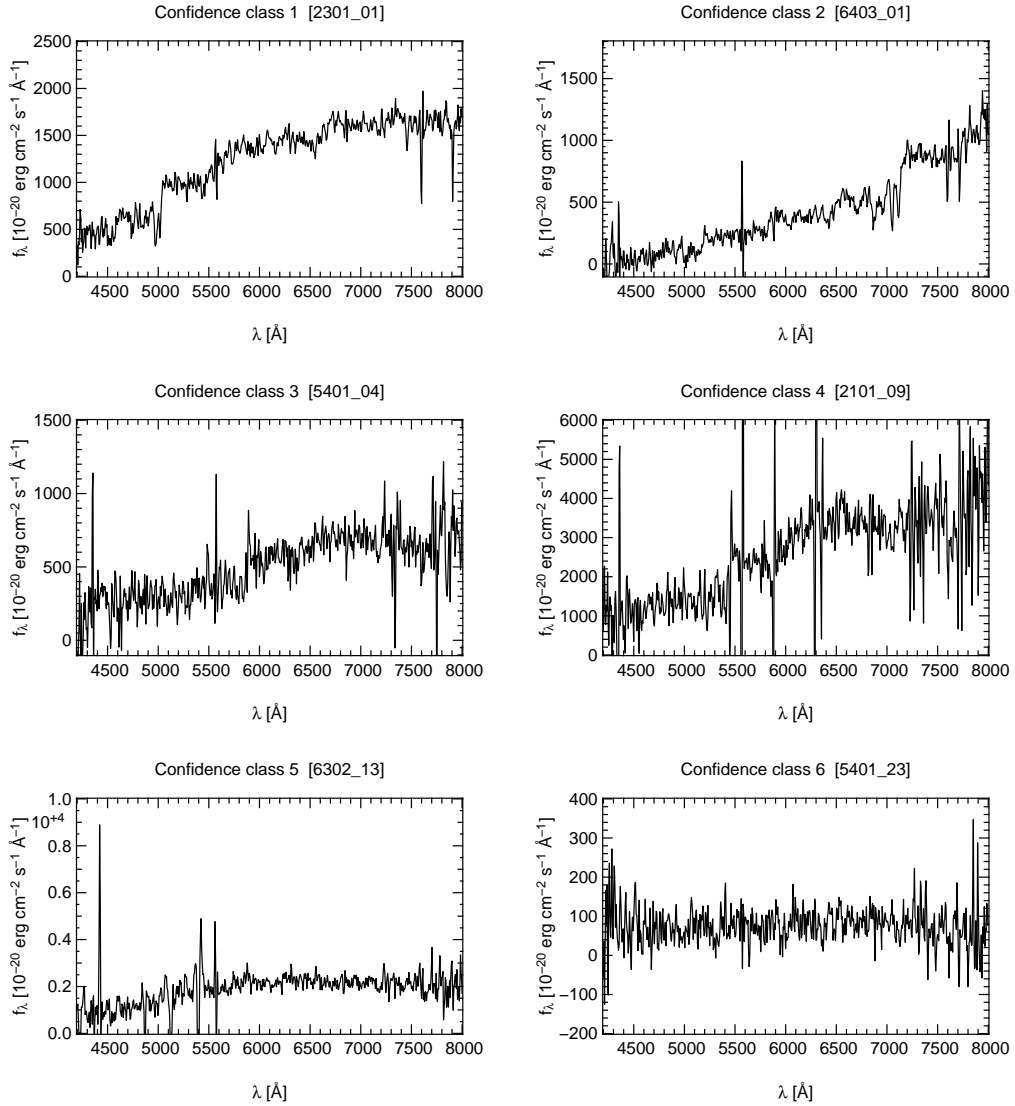


Figure 4.6: Examples for the assignment of confidence classes, ranging from “1” (upper left-hand panel) to “6” (lower right-hand panel). The numbers in square brackets denote the internal identification number of the object.

Chapter 5

The Spectroscopic Catalogue and its Properties

This Chapter discusses the characteristics of the spectroscopic catalogue, like the number of objects, their classification, the colour and redshift distributions, the completeness function, the redshift distribution and the error budget for the redshift measurements.

5.1 Number of Spectra and Object Classes

The final catalogue contains 1051 objects, 738 (or 70.2 per cent) of which could be successfully classified. Out of these 738 objects, 610 (or 82.7 per cent) are galaxies, 17 (2.3 per cent) are active galactic nuclei, and 111 (15.0 per cent) are stars. 328 objects remain unidentified due to bad quality of the spectra or a lack of prominent spectral features in the wavelength range covered by the spectra. Redshifts could be determined for 627 objects (confidence classes 1 to 4). The number of successfully classified galaxies, AGN and stars for all the fields are to be found in Table 5.1. It is obvious from these numbers that the *K*-band selected spectroscopic catalogue described here has a similar sample size as the *I*-band selected Canada–France Redshift Survey (CFRS; Lilly *et al.* 1995b) which provided important information on the evolution of galaxies. The MUNICS redshift survey is as large as the CFRS, but has all the advantages of *K*-band selection outlined in previous chapters.

The stellar content of the spectroscopic catalogue will be discussed in more detail in Section 5.10.

5.2 Confidence Classes

The number of objects in the confidence classes described above are given in Table 5.2. The first three confidence classes contain 57.3 per cent of all objects selected for spectroscopy; these objects have high-quality spectra. Redshifts could be determined for 66.6 per cent of the objects (confidence classes 1 to 4).

Table 5.1: The ten MUNICS survey fields for which spectroscopic data are available. The table gives the field name, the field coordinates for the equinox 2000, the limiting magnitudes for the spectroscopic observations, and the number of galaxies, active galactic nuclei, and stars with reliable spectroscopic classification in each field. The field named S2F1 contains the sparse sample observed with the ESO VLT. For statistical analysis, like the computation of the luminosity function in Chapter 6, only the five fields with highest completeness, *i.e.* S2F1, S2F5, S5F1, S6F5 and S7F5 are used. Fields for which no limiting magnitude is given were only observed in the course of the search for red AGN and thus have only few spectra. The last line shows the numbers for the Canada–France Redshift Survey (CFRS; Lilly *et al.* 1995b). The smaller fraction of stars in the MUNICS redshift survey is due to the pre-selection according to the morphological classification of the objects. On the other hand, the larger fraction of AGN is a result of the search program for faint red AGN.

Field	α	δ	Lim. mag.	Galaxies	AGN	Stars
	(2000.0)					
S2F1	03:06:41	+00:01:12	$K \leq 19.0$	186	5	28
S2F5	03:06:41	−00:13:30	$K \leq 17.5$	67	1	12
S3F1	09:04:38	+30:02:56		8	1	0
S3F5	09:03:44	+30:02:56		8	1	1
S4F1	03:15:00	+00:07:41		9	3	0
S5F1	10:24:01	+39:46:37	$K \leq 17.5$	107	1	2
S5F5	10:25:14	+39:46:37		13	1	1
S6F1	11:55:58	+65:35:55		6	1	2
S6F5	11:57:56	+65:35:55	$K \leq 17.5$	129	2	38
S7F5	13:34:44	+16:51:44	$K \leq 17.5$	60	1	27
All Fields				593	17	111
<i>CFRS</i>				591	6	200

Note that all objects with single emission lines are to be found in confidence class 5 which contains only about 1% of all objects. Therefore we do not include a separate analysis of this object class (as has been done, for example, for the CFRS, see Lilly *et al.* 1995a), since they do not contribute significantly to our database.

5.3 Redshift Distribution

The redshift distribution of the spectroscopic sample is shown in Figure 5.1. The histogram has the shape expected for a magnitude limited spectroscopic sample, except for the slight excess of objects with redshifts $z \gtrsim 0.6$ which, of course, are due to the sparse sample of faint objects observed at the VLT. The lack of objects with redshifts from VLT spectroscopy in the range $0.5 < z < 0.6$ is most likely due to the limits of

Table 5.2: Distribution of extragalactic objects into the 6 confidence classes used in the final spectroscopic catalogue.

Class	Number of objects	Percentage
1	299	30.45
2	135	13.75
3	129	13.14
4	91	9.27
5	11	1.12
6	317	32.28
Total	982	100.00

the instruments' spectral range. Objects with these redshifts have their 4000Å break¹ around the lower end of the spectral range and the H α line ($\lambda \simeq 6563\text{\AA}$) around the upper end of the spectral range. Thus redshifts of objects with low signal-to-noise ratio may be difficult to determine due to the absence of those prominent spectral features in the observed spectra. This kind of bias can be corrected for by looking at the fraction of galaxies with securely determined redshift as a function of two colours, as will be shown below.

It is also interesting to look for the signatures of large-scale structure in the redshift distribution. Obviously, this requires that the spectroscopic catalogue in a specific field is reasonably complete. As an example, Figure 5.2 shows the histogram of spectroscopic redshifts in the fields S2F1 and S6F5. In both cases peaks are clearly visible, for S2F1 at $z \simeq 0.11$, $z \simeq 0.24$, $z \simeq 0.36$, $z \simeq 0.42$ and $z \simeq 0.70$, for S6F5 at $z \simeq 0.25$, $z \simeq 0.30$, $z \simeq 0.39$ and $z \simeq 0.60$, with some less pronounced features in between. The strongest feature at $z \simeq 0.11$ in the field S2F1 is due to the galaxy cluster Abell 412 at $\alpha = 03 : 03 : 42$, $\delta = -00 : 22 : 00$ (2000.0; Abell *et al.* 1989). The centre of the cluster is lying well outside the MUNICS fields S2F1 and S2F5, but the cluster is very extended and thus contaminates the foreground in this area.

A comparison of this spectroscopic peaks with the results of a cluster finding algorithm using both angular coordinates and photometric redshifts (Botzler *et al.* 2004) shows that basically all of the peaks correspond to groups or clusters (Botzler 2004).

5.4 Accuracy of Redshift Determination

For objects with secure redshifts, where we consider all spectral features to be correctly identified, possible sources of error in the determination of redshift are firstly a

¹The spectral break at $\lambda \sim 4000\text{\AA}$ is caused by the combined efforts of hydrogen Balmer-continuum absorption in the spectra of B, A and F stars, and the Calcium II H & K absorption lines in the spectra of F, G and K stars. As these features are caused by early and late-type stars, respectively, the relative strength depends on a galaxy's stellar population: star-forming galaxies have stronger Balmer breaks, older galaxies have stronger 4000Å breaks.

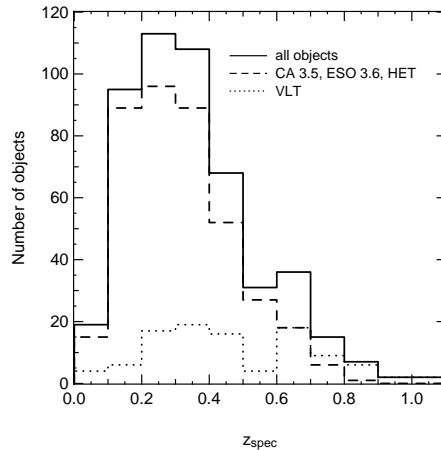


Figure 5.1: The overall redshift distribution of all galaxies and active galactic nuclei in the final spectroscopic catalogue (solid line), divided into objects with spectroscopy from the Calar Alto 3.5-m telescope, the ESO 3.6-m telescope or the HET (dashed line) and from the VLT (dotted line). Note the excess of objects at redshifts above 0.6 due to the VLT observations.

possible displacement between the object and the slit centre, secondly the error of the wavelength calibration, and finally the error in the measurement of the line centres.

1. An offset of the object with respect to the slit centre causes an error of the redshift measurement. We estimate the RMS error to be $0.5''$, corresponding to an inaccuracy of $\sigma \simeq 6 \times 10^{-4}$ in redshift space. This value is estimated from the accuracy of astrometry in the MUNICS catalogue (see MUNICS I), the typical errors of mask alignment and under the reasonable assumption that errors in the mechanical production of the masks (or in the slit-let positioning for FORS1 and the LRS) can be neglected.
2. The random errors of the wavelength calibration, the RMS of the residuals of the fit to the identified lines, are of the order 0.3\AA , or, in redshift, $\sigma \simeq 0.4 \times 10^{-4}$. Compared to the other sources of error, this inaccuracy can be neglected. For MOSCA, the maximum shift of the spectrum of the calibration lamp between zenith and airmass 2 was measured to be 1 pixel, corresponding to a systematic error of $\sigma \lesssim 4 \times 10^{-4}$ in redshift.
3. Typical errors of the measurement of the line centres for the redshift determination are $\sigma \lesssim 5 \times 10^{-4}$.

The overall limit to the accuracy estimated from these errors is $\sigma \simeq 8 \times 10^{-4}$ in redshift space.

We can also empirically determine the error of the redshift measurements from multiple observation of objects. A total of 63 galaxies – about 10 per cent of the sample – has been observed repeatedly, usually in order to fill gaps on the slit masks

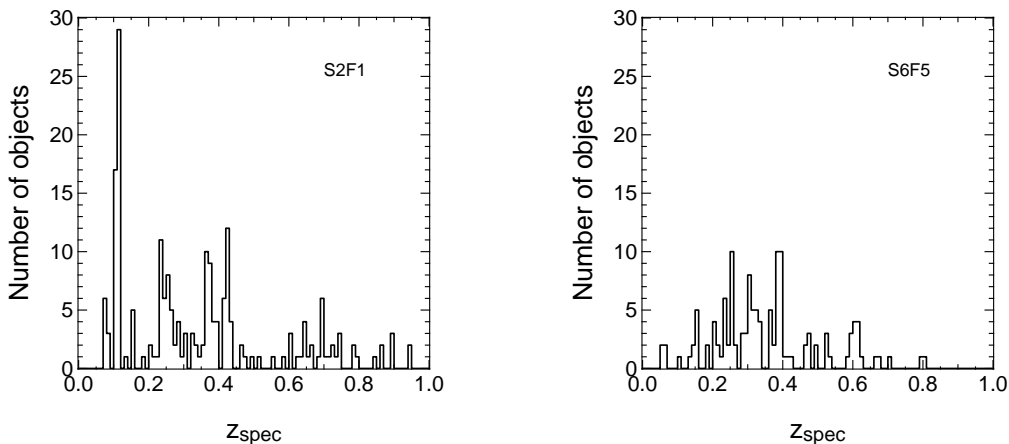


Figure 5.2: The redshift distribution of all galaxies in the MUNICS fields S2F1 (*left-hand panel*) and S6F5 (*right-hand panel*). Peaks caused by large-scale structure along the line of sight are clearly visible.

used for observation, thus enabling us to estimate typical errors of the redshift measurement by comparing the redshifts obtained from different observations. Note that some of these objects have been observed both with MOSCA and FORS, and some using MOSCA and the LRS. Thus it is possible to check for any systematics between redshift determinations with different spectrographs, and, in particular, for systematic offsets between different means of wavelength calibration, since we used the lines of the night sky for the FORS observations, whereas spectra from calibration lamps were used for the other spectrographs.

The histogram of the differences of the redshifts to the mean redshift for the 131 repeated redshift measurements of 63 objects is shown in the left-hand panel of Figure 5.3. Also shown is a Gaussian approximation to the histogram having a width characterised by $\sigma' = 5.6 \times 10^{-4}$, corresponding to an RMS error of single measurements of $\sigma = \sigma' \sqrt{2} = 7.9 \times 10^{-4}$, similar to the value we have derived from the formal error analysis. Furthermore, we do not find any systematical differences between redshift determinations achieved with data from different instruments or observing runs. The right-hand panel of the same Figure shows the same comparison for 8 objects where redshifts from other surveys is available. The data were retrieved from the NASA Extragalactic Database (NED) and originate from the Sloan Digital Sky Survey (SDSS) Early Data Release (Stoughton *et al.* 2002). In this case the error distribution has a width of $\sigma' = 4.3 \times 10^{-4}$ or $\sigma = 6.1 \times 10^{-4}$, close to the value expected from the error analysis discussed above.

5.5 Colours, Magnitudes, and Redshifts

To give a feeling for the distribution of objects in magnitudes, colours, and redshifts, we present diagrams for various combinations of these properties in Figures 5.4 and 5.5.

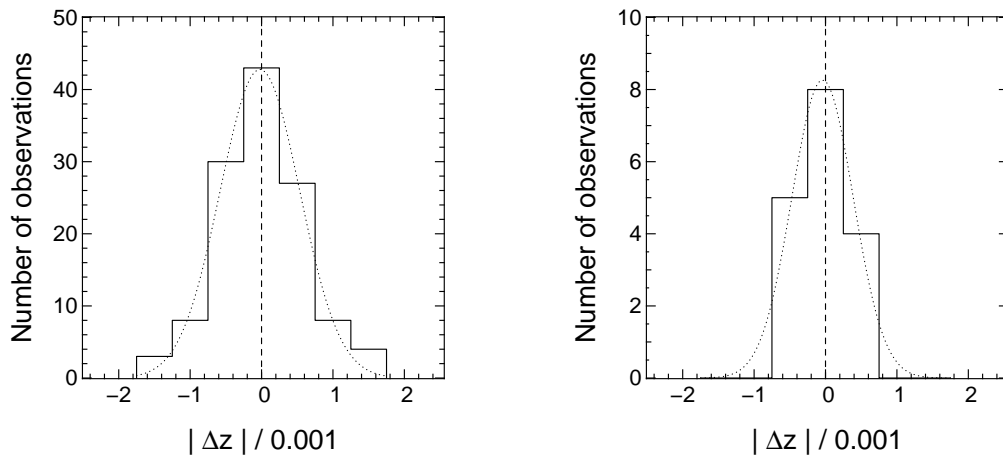


Figure 5.3: Histogram of the differences of redshifts to mean redshifts for objects with multiple spectroscopic observations (solid lines). *Left-hand panel*: Only for observations taken for the MUNICS redshift survey. *Right-hand panel*: Same as before, but for spectra where a redshift from the SDSS Early Data Release is available. The dotted lines show Gaussian approximations to the histograms for which $\sigma' = 5.6 \times 10^{-4}$ and $\sigma' = 4.3 \times 10^{-4}$, respectively, corresponding to an RMS error of single measurements of $\sigma = 7.9 \times 10^{-4}$ and $\sigma = 6.1 \times 10^{-4}$.

In Figure 5.4, we show distributions of the apparent K -, I - and B -band magnitudes as well as the $R-K$ colours versus redshift. The comparison of model spectral energy distributions from a combination of empirical spectra and stellar population synthesis models by Maraston (1998) for various Hubble types to the $R-K$ colours of the objects in the MUNICS spectroscopic catalogue (upper right-hand panel of Figure 5.4) shows good agreement, although we seem to miss blue objects at higher redshifts, a fact which must be accounted for in any analysis of this dataset.

Figure 5.5 shows the distribution of extended objects in the photometric catalogue together with the colour distribution of galaxies with spectroscopic redshifts. Comparison shows that the spectroscopic catalogue is a fair representation of the distribution of objects in the photometric sample. Clearly, there is some incompleteness for faint red objects, but this can be corrected for, as will be shown in the following Section.

5.6 Redshift Sampling Rate and Sky Coverage

Observations for the spectroscopy of objects from the photometric MUNICS catalogue are almost complete, and most of the fields have been observed with reasonable completeness. The fraction of galaxies with redshift among all galaxies in the photometric catalogue is usually called the *redshift sampling rate* (e.g. Lin *et al.* 1999). As an example, Figure 5.6 shows the redshift sampling rate of objects in all survey fields with spectroscopic data. The redshift sampling rate is the fraction of objects with successful redshift determination among all galaxies in the photometric catalogue, and, of course, is different from the *redshift success rate*, which is the fraction of all galaxies with

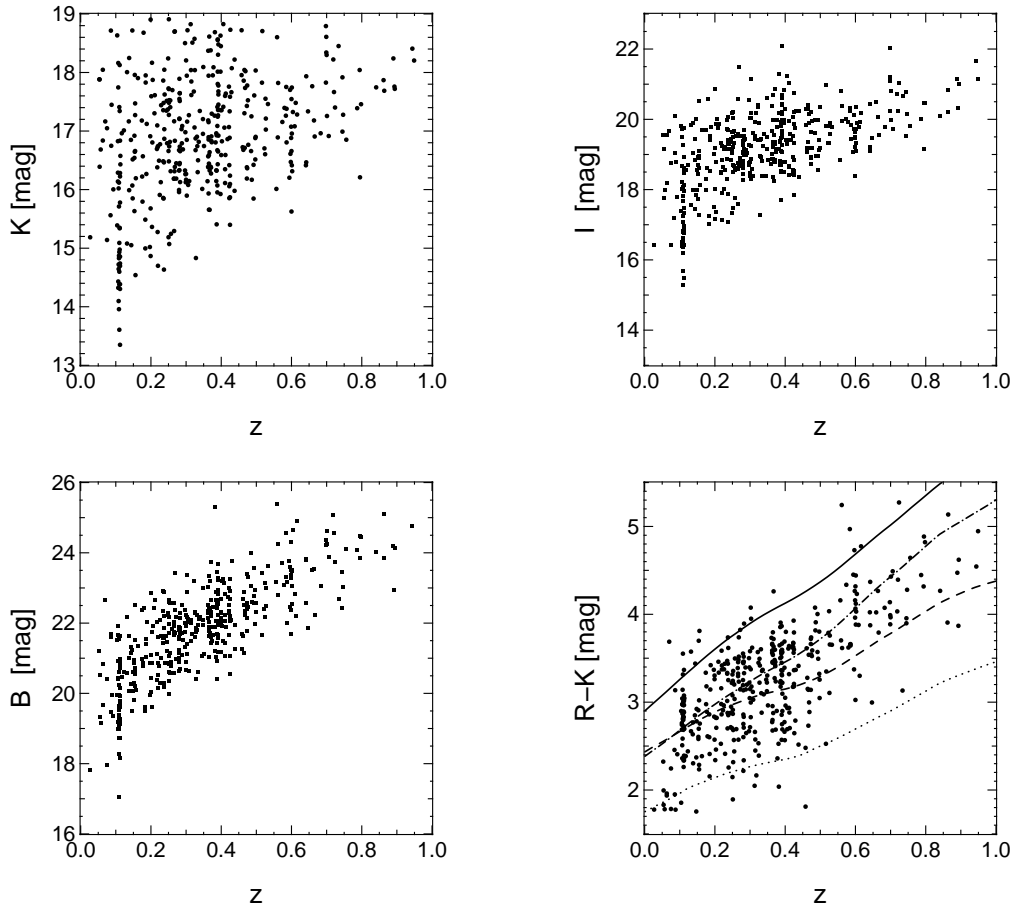


Figure 5.4: *Upper left-hand panel:* The distribution of apparent K -band magnitudes of galaxies versus redshift in the MUNICS spectroscopic sample. *Upper right-hand panel:* Same as before, but for I magnitudes. *Lower left-hand panel:* Same as before, but for B magnitudes. *Lower right-hand panel:* The $R-K$ -colour versus redshift diagram for galaxies with spectroscopic redshifts. Also shown are the redshift-tracks of model spectral energy distributions (Maraston 1998; see text for details), roughly corresponding to Hubble types E (solid line), Sa (dash-dotted line), Sb (dashed line), and Sc (dotted line).

redshift among all galaxies in the spectroscopic catalogue. The redshift success rate depending on apparent magnitude and colours is shown in Figure 5.7 and discussed in Section 5.7. These colour distribution should be compared to the distributions of objects from the photometric and spectroscopic catalogue shown in Figures 5.4 and 5.5.

Although a few of the masks for the fields still have to be observed, this does not necessarily inhibit the use of the sample for analysis of, e.g., the luminosity function, as long as the sample of objects with successful redshift determination is a fair representation of the total sample, and as long as any systematic incompleteness effects can be corrected for. We will show that this is the case for our catalogue because of

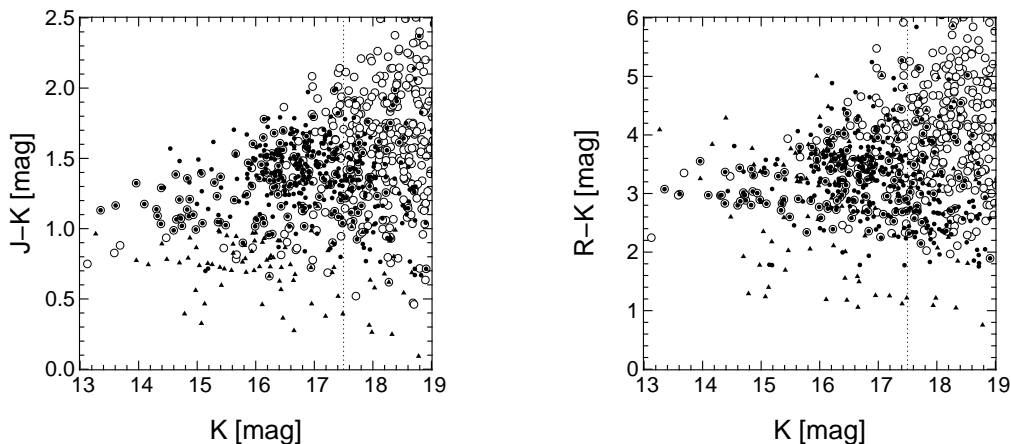


Figure 5.5: *Left-hand panel:* The $J-K$ versus K colour-magnitude diagram for galaxies (filled circles) and stars (filled triangles) with good-quality spectra. The open circles show the distribution of objects classified as extended in the photometric catalogue of one of the MUNICS fields (S2F1). Also indicated is the magnitude limit of the large and bright spectroscopic sample at $K = 17.5$ (dotted line). *Right-hand panel:* Same as before, but for the distribution of $R-K$ colours versus apparent K -band magnitude.

the procedure we followed during mask preparation and observation. Firstly, we have tried to select *all* objects with $K' \leq 17.5$ in five survey fields for spectroscopy at Calar Alto. Since the field of view of the spectrograph (MOSCA) is almost as large as the size of our survey field, and since we usually have several masks per magnitude bin (at least for the fainter objects), we are not limited by geometrical constraints from the arrangement of slits on each mask. For the brighter magnitude bins we sometimes had to drop a few objects during the preparation of a mask, but we have tried to include these objects in fainter mask setups. Hence we expect that the small fraction of objects on to which no slit could be put is statistically similar to the distribution of objects to the appropriate magnitude limit. Secondly, all masks which could be observed so far were selected randomly from the masks prepared for observations, so that we do not expect any selection bias here either. Figure 5.8 shows the distribution of objects with successful spectroscopy as compared to objects in the photometric catalogue for the survey patches called S2F1, S5F1, S6F5, and S7F5. These particular fields have highest completeness. The field S2F1 contains the sparse sample of fainter objects observed with the VLT. The figure nicely illustrates the statistically homogeneous distribution of the objects in the spectroscopic catalogue. The excess of objects with successful redshift determination visible in the lower half of the field S2F1 is due to foreground structure which can readily be seen in the image itself, showing again the influence of cosmic variance and the importance of having *several* fields with a relatively *large solid angle* for the analysis of statistical quantities, one of the huge advantages of the MUNICS project compared to smaller surveys.

The redshift sampling rate as a function of K -band magnitude for the individual fields is also shown in Figure A.1, in Appendix A.

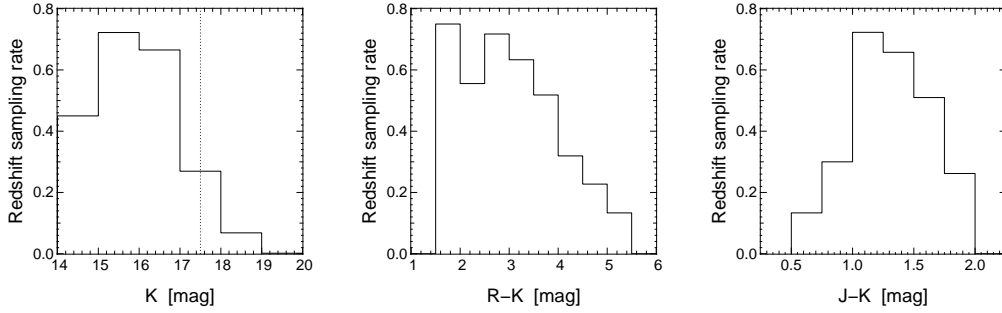


Figure 5.6: The *redshift sampling rate*, i.e. the fraction of successful redshift determinations among galaxies in the photometric catalogue, as a function of m_K (left-hand panel), $R-K$ (middle panel), and $J-K$ (right-hand panel) for all galaxies in the survey patches S2F1, S5F1, S6F5, and S7F5 (the field S2F5 has been excluded from further analysis because of the small number of available spectra). The dotted line in the left-hand panel indicates the formal limit of $K \leq 17.5$ of the main part of the spectroscopic survey. The colour distributions in the middle and the right-hand panel are those of objects brighter than this limit.

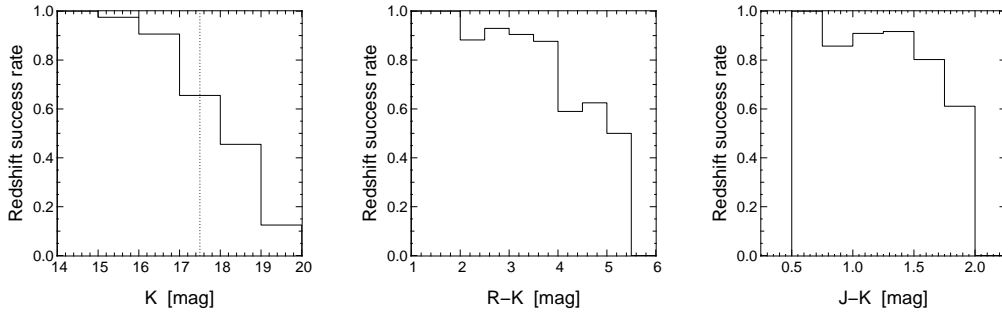


Figure 5.7: The *redshift success rate*, i.e. fraction of successful redshift determinations among all galaxies which were observed spectroscopically, as a function of m_K (without any colour constraint; left-hand panel), $R-K$ (middle panel), and $J-K$ (right-hand panel) for all galaxies in the survey patches S2F1, S5F1, S6F5, and S7F5). The dotted line in the left-hand panel indicates the formal limit of $K \leq 17.5$ of the main part of the spectroscopic survey. The colour distributions in the middle and the right-hand panel are those of objects brighter than this limit.

5.7 Redshift Success Rate

The efficiency of redshift determination of spectroscopic observations is described by the *redshift success rate* rather than the *redshift sampling rate*. The former is the fraction of objects with secure redshift among all galaxies which were observed spectroscopically and is shown in Figure 5.7. As expected, the redshift success rate drops off for very faint and very red objects, but is in general very high due to the good quality of the spectra.

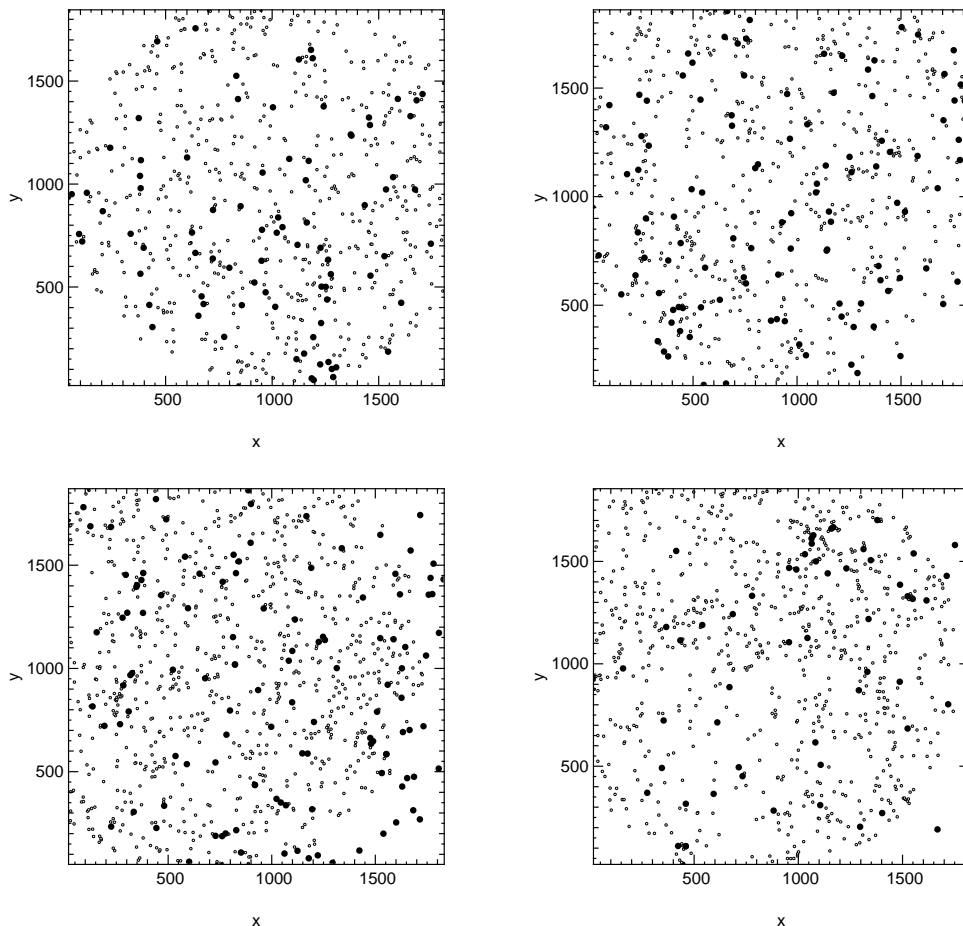


Figure 5.8: Sky coverage of spectroscopy in the MUNICS fields S2F1 (upper left-hand panel), S5F1 (upper right-hand panel), S6F5 (lower left-hand panel), and S7F5 (lower right-hand panel). The small open circles are objects in the photometric catalogue, the distribution of which is governed by the MUNICS field geometry (see MUNICS I). All galaxies with $K' \leq 17.5$ and successful redshift determination are marked by filled circles; they seem to be uniformly distributed on the sky. Note that spectroscopy of the galaxies in the field S7F5 is not complete yet. Coordinates are pixel coordinates in the K' -band MUNICS frame.

5.8 Extremely Red Objects

During the last years there has been a lot of research on ‘extremely red objects (EROs)’, usually defined in terms of their very red optical–near-infrared colour ($R-K > (5 \dots 6)$ mag; see, for instance, Martini (2001) and references therein). While the MUNICS catalogue obviously contains such objects, they are not aimed at with the spectroscopic observations described in this thesis, mainly because it is very difficult to obtain optical spectra of faint EROs. This is evident from Figures 5.6 and 5.7 showing the redshift sampling rate and the redshift success rate for the MUNICS spectroscopic ob-

servations. Nevertheless, there are 15 such objects in the spectroscopic catalogue, all having colours of $5.0 \text{ mag} \leq R-K \leq 5.5 \text{ mag}$. Among these we find 7 objects for which no redshift could be determined, 5 galaxies with redshifts $0.46 \leq z \leq 1.01$, all having a spectral energy distribution characteristic of early-type galaxies, as well as 3 stars of spectral type M.

First results of near-infrared spectroscopy of EROs selected from the MUNICS catalogue in the course of the ‘‘TNG EROs Spectroscopic Identification Survey (TESIS)’’ are described in Saracco *et al.* (2003). In the context of this project we have so far observed a total of 13 EROs with the low-resolution near-infrared spectrograph AMICI. For 10 objects we were able to derive a secure redshift. These spectra, together with the MUNICS photometry, allow a classification as early-type galaxies for 7 of these objects. Because of their different target selection we do not include these objects in the following statistical analysis.

5.9 Test of Object Classification

For the full photometric MUNICS dataset we cannot rely on spectroscopic information to classify objects as stars or galaxies. One way of doing this, a classification algorithm based on the objects’ shape in the images, has already been described in Section 3.1. However, this morphological classification might be problematic for very bright (saturated) objects, very faint (noisy) objects, or for compact high-redshift galaxies.

A more reliable way of doing this is a χ^2 -based criterion relying on fitting template spectral energy distributions of stars and galaxies to the broad-band photometry of the objects. We can test the accuracy of this classification method by comparing it to the spectroscopic classification (see Figure 5.9). It is obvious from the Figure that the χ^2 classification agrees very well with the spectroscopic information and thus provides an efficient method to discriminate between stars and galaxies in large photometric catalogues.

5.10 Stars in the Spectroscopic Catalogue

As shown above, the spectroscopic catalogue contains 111 stars. Although the main part of the objects selected for spectroscopy were morphologically classified as extended objects, a small part was purely magnitude selected to test the classification procedure. These observations yielded many stellar spectra, and, of course, some of the objects classified as extended turned out to be stars as well. In this section, we briefly discuss the properties of the stellar objects and their spectra. Note that only 99 out of the 111 stars are present in the final cleaned catalogue, as some lie outside the overlap area of the B , V , R , I , J and K images.

The distribution of $V - J$ colours of the stars in the sample is shown in Figure 5.10. The earliest spectral class present in the data are F stars. Blue stars are obviously missing in our K -selected spectroscopic sample. It is also clear from the Figure that M stars are dominating the stellar content of our spectroscopic survey.

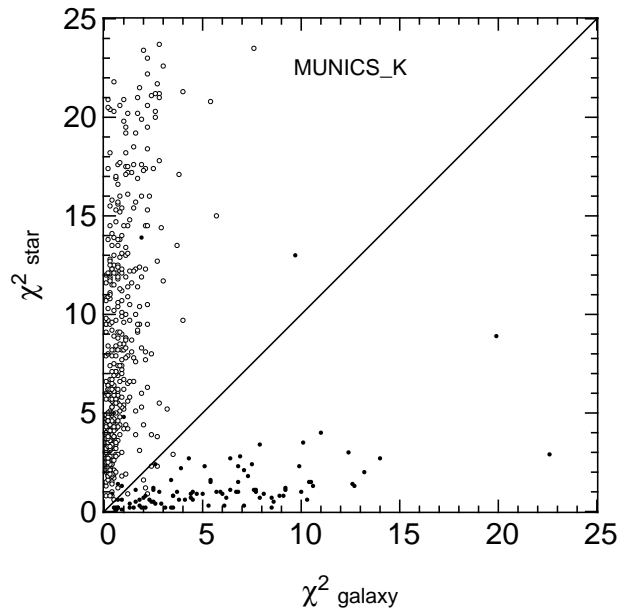


Figure 5.9: This diagram shows the loci of spectroscopically classified galaxies (open circles) and stars (crosses) in a plane defined by the χ^2 values of the best-fitting galactic and stellar spectral-energy distributions (SEDs) for the K -band selected MUNICS catalogue. The line used to discriminate the two classes is also indicated.

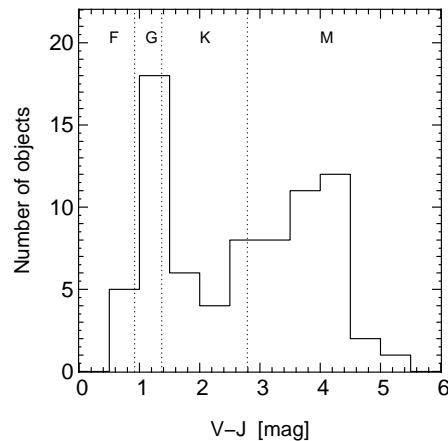


Figure 5.10: The histogram of $V - J$ colours of 99 stars in the spectroscopic MUNICS catalogue which also have photometric information in the six MUNICS filters. The dotted lines are the $V - J$ colours dividing the spectral types F, G, K and M (for dwarf stars) according to Binney & Merrifield (1998).

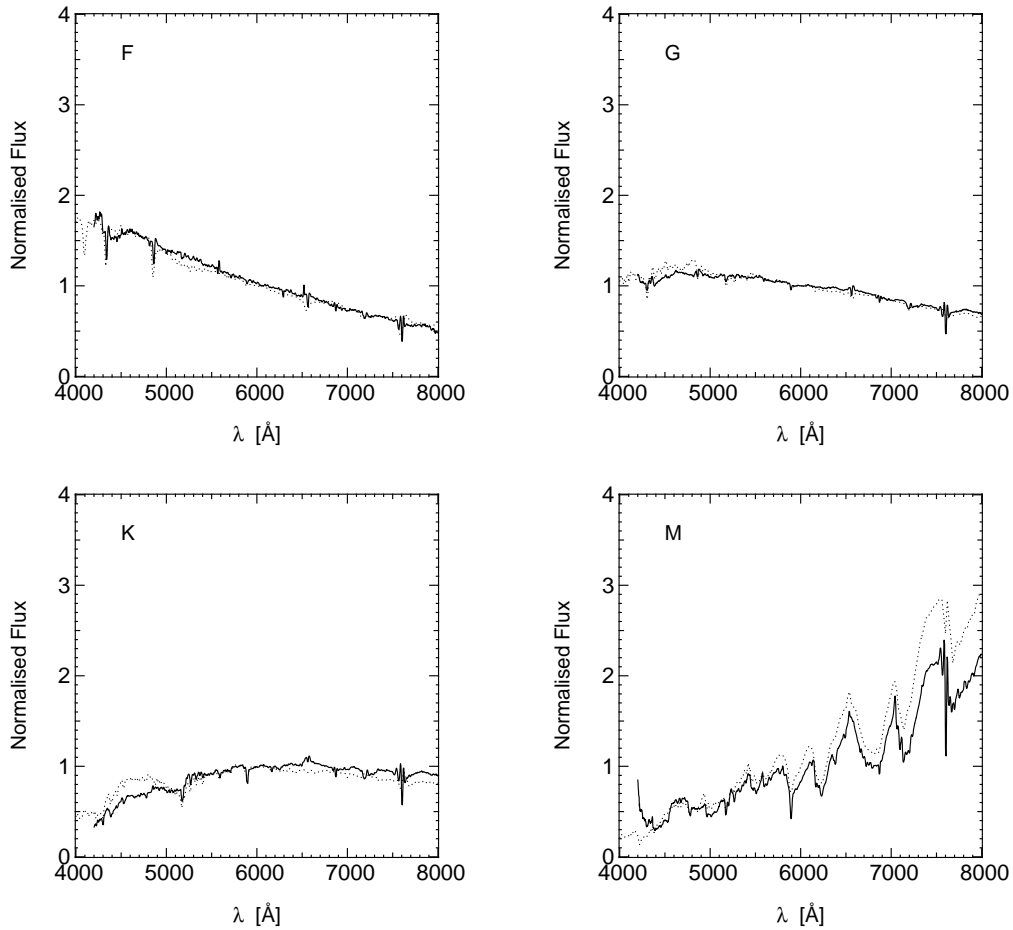


Figure 5.11: Composite spectra of stars roughly corresponding to spectral types F (*upper left-hand panel*), G (*upper right-hand panel*), K (*lower left-hand panel*) and M (*lower right-hand panel*). The stellar types have been pre-selected according to the colour criterion presented in Figure 5.10. Also shown are template spectral energy distributions for stars of type F4 V, G5 V, K4 V and M4 V (dotted lines) taken from the Bruzual–Persson–Gunn–Stryker library (Gunn & Stryker 1983).

More interesting than the colours are the spectra themselves. To illustrate the distribution of spectral types, we have taken all stars in each of the colour bins shown in Figure 5.10 and constructed a signal-to-noise weighted composite spectrum (see Figure 5.11).

Chapter 6

The Evolution of the Rest-Frame Near-Infrared Luminosity Function of Field Galaxies

This chapter, the first of two core Chapters of this thesis, describes the near-infrared luminosity function of galaxies and its evolution with redshift as derived from the near-infrared selected spectroscopic survey presented in the previous Chapters.

6.1 Introduction

The study of the luminosity function (LF) of galaxies at different wavelengths and at different cosmic epochs is one of the most important methods to address the problem of the formation and evolution of galaxies within observational cosmology.

As was already explained in Chapter 2, near-infrared selected galaxy surveys are an efficient tool for tracing the evolution of massive galaxies. The past ten years have seen a number of measurements of near-infrared LFs, all of which are summarised in Tables 6.5 and 6.6 below. The easiest way to determine the K -band LF of galaxies is by follow-up near-infrared photometry of existing, typically *optically* selected, galaxy redshift catalogues. Mobasher, Sharples, & Ellis (1993) and Szokoly *et al.* (1998) have chosen this approach, and later on Loveday (2000) has presented the LF at a median redshift $z = 0.051$ from K -band imaging of b_J -selected galaxies from the Stromlo-APM Redshift Survey (Maddox *et al.* 1990a, Loveday *et al.* 1996). Note that the use of optically-selected samples can lead to a bias against red (for example old or dusty) galaxies. Recently, Cohen (2002) derived LFs from the R -band selected Caltech Faint Galaxy Redshift Survey.

For *near-infrared* selected galaxy surveys, most measurements of the K -band LF so far were based on local ($z \lesssim 0.15$) samples. Gardner *et al.* (1997) have calculated the K -band luminosity function at a median redshift $z = 0.14$. Kochanek *et al.* (2001) have determined type-dependent LFs at median redshift $z = 0.023$ combining Two-Micron All Sky Survey (2MASS, Jarrett *et al.* 2000) and the CfA2 (Geller & Huchra 1989) and UZC (Falco *et al.* 1999) redshift databases. A similar strategy was adopted

by Cole *et al.* (2001) who combined the photometric 2MASS data with the 2dF Galaxy Redshift Survey (Folkes *et al.* 1999), and Balogh *et al.* (2001) who cross-correlate the 2MASS data with the Las Campanas Redshift Survey (Shectman *et al.* 1996). As will be shown below, there is good agreement between these determinations of the rest-frame K -band LF in the local universe. However, Huang *et al.* (2003) have presented a measurement of the local K -band LF from the Hawaii–AAO K -band Galaxy Redshift Survey, finding a slightly brighter M^* and a steeper faint-end slope, which they attribute to the influence of different redshift ranges of the local samples. They also note that their value for the faint-end slope is in better agreement with optical LFs. Kashikawa *et al.* (2003) used photometric redshifts on a deep K -band selected catalogue to construct the rest-frame K -band LF, finding almost no evolution to redshift $z = 3$.

At higher redshifts, Glazebrook *et al.* (1995) derived the K -band LF out to redshifts $z \leq 0.8$ and find evidence for a brightening of the characteristic luminosity at $z > 0.5$. Cowie *et al.* (1996) present the evolution of the K -band LF of galaxies in four redshift bins $z \in [0, 0.1]$, $z \in [0.1, 0.2]$, $z \in [0.2, 0.6]$, and $z \in [0.6, 1.0]$ based on a deep, but rather small spectroscopic sample, complemented by the shallower samples from Songaila *et al.* (1994). They find no evolution with redshift. Using our own, much larger sample of spectroscopically calibrated photometric redshifts from the MUNICS survey, we find mild evolution to redshift one, with a brightening of 0.5 to 0.7 mag, and a decrease in number density of about 25 per cent (Drory *et al.* 2003; hereafter MUNICS II).

The spectroscopic sample of K -band-selected galaxies described in Chapter 5 enables us to derive the rest-frame K -band LF of galaxies at redshifts $z = 0.2, 0.4$, and 0.7 from data based on a survey much larger in area than the Hawaii Deep Fields (Cowie *et al.* 1996), making the LF presented here much less affected by cosmic variance.

Furthermore, the rest-frame J -band LF at these redshifts is presented for the first time. So far, there are only two local measurements of the LF in this band (Balogh *et al.* 2001, Cole *et al.* 2001).

6.2 Computing the Luminosity Function

The LF is computed using the non-parametric V_{\max} formalism (Schmidt 1968). This method has been shown to yield an unbiased estimate of the LF if the sample is not affected by strong clustering (Takeuchi *et al.* 2000). Because of our field selection and the relatively large area of the survey, divided into several individual fields, we believe that this assumption is valid for our sample.

The V^{\max} formalism accounts for the fact that some fainter galaxies are not visible in the whole survey volume. In a perfect world with volume-limited redshift surveys, each galaxy i in a given redshift bin $[z_{\text{lower}}, z_{\text{upper}}]$ contributes to the number density an amount inversely proportional to the volume V_i in which the galaxy is detectable in the survey:

$$V_i = \int_{z_{\text{lower}}}^{z_{\text{upper}}} \frac{dV}{dz} dz, \quad (6.1)$$

where $dV = d\Omega r^2 dr$ is the comoving volume element and $d\Omega$ is the solid angle covered by the survey. However, due to the fact that in real life we have to deal with magnitude-limited surveys, a faint galaxy may not be visible in the whole survey volume. Assume that in a survey with given limiting magnitude galaxy i can be seen out to redshift z_{\max} . Then we have to correct the volume factor by V_i^{\max}/V_i , where

$$V_i^{\max} = \int_{z_{\text{lower}}}^{\min(z_{\text{upper}}, z_{\text{max}})} \frac{dV}{dz} dz. \quad (6.2)$$

Obviously, we have $z_{\max} \geq z_{\text{upper}}$ for a galaxy which is bright enough to be seen in the whole volume in investigation, and the correction factor is one. Otherwise, $z_{\max} < z_{\text{upper}}$, and the volume is smaller than the volume corresponding to the redshift range in which we compute the LF.

We have made sure that the effect of the volume correction is of importance only in the faintest bin in absolute magnitude, and that even in this case the correction is small.

Additionally, the contribution of each galaxy i is weighted by the inverse of the detection probability $P(m_{K,i})$ of the K' -band selected photometric catalogue, where we assume that the detection probability is independent of the galaxy type and can be approximated by that of point-like sources. Completeness simulations for realistic galaxy profiles at various redshifts have shown that this approximation is indeed sufficient for galaxies at redshifts $z < 1$ (Snigula *et al.* 2002, hereafter MUNICS IV). However, since the objects under consideration here are comparatively bright, the influence of this correction is negligible anyway.

In addition to the correction for the incompleteness of the *photometric* MUNICS catalogue described above, we have to correct for the incompleteness of the *spectroscopic* catalogue with respect to the photometric sample, described by the redshift sampling rate (see Section 5.6). In principle, this correction depends on the apparent magnitude of the objects (faint objects may produce a lower signal-to-noise ratio or might not have been considered for spectroscopy)¹, on their intrinsic type (it is easier to determine a redshift for objects showing prominent emission lines, for example) and on the redshift of the source (influencing the position of prominent spectral features with respect to the spectral range or bright night-sky emission lines, for example). However, it is difficult to determine a completeness ratio depending on spectral type and redshift, because this information is lacking for all objects without secure redshift measurement.

Hence the redshift sampling rate is often quantified in terms of its dependence on apparent magnitude and two colours instead of spectral type and redshift (see Lin *et al.* (1999), for example). In this work we compute the redshift sampling rate C_i ,

$$C_i = \frac{N_{z,i}}{N_i}, \quad (6.3)$$

¹Note that we can neglect any influence of the *size* of the objects (large objects might have larger losses of light at the slit of the spectrograph), since – especially at faint magnitudes – objects appear to be almost point-like.

depending on apparent K' -band magnitude m_K , and the colours $R-K$ and $J-K$. Specifically, for each galaxy i with a redshift, we determine the number N_i of galaxies in the photometric sample and the number $N_{z,i}$ of galaxies with successful redshift determination in joint bins of apparent magnitude and colours, where we count all galaxies j obeying

$$\begin{aligned} |m_{K,i} - m_{K,j}| &\leq 0.70 \text{ mag}, \\ |(R-K)_i - (R-K)_j| &\leq 0.70 \text{ mag}, \\ |(J-K)_i - (J-K)_j| &\leq 0.35 \text{ mag}. \end{aligned} \quad (6.4)$$

On the one hand, the size of the intervals should be large enough to contain a reasonable number of objects to avoid large fluctuations due to small-number statistics. On the other hand, the intervals should not be too large in order to be able to follow the change of the sampling rate. The numbers given in equation (6.4) have been chosen after careful tests. Note that we have used larger intervals for m_K and $R-K$ since these distributions are broader than the one for $J-K$. To illustrate the general behaviour of the redshift sampling rate, we show projections of the function in Figure 5.6. Note that we have to apply a correction factor of 0.93 to the sampling rate because of stellar contamination of the class of extended objects, a bias introduced by our image-based object classification algorithm, described in detail in Section 3.1.

The near-infrared LF $\Phi(M)$ is then computed according to the formula

$$\Phi(M) dM = \sum_i \frac{V_i}{V_i^{\max}} \frac{1}{V_i} \frac{1}{P(m_{K,i})} \frac{1}{C_i} dM, \quad (6.5)$$

where the sum runs over all objects i in the redshift range for which we want to calculate the LF. Naturally the volume terms can be simplified yielding $1/V_i^{\max}$.

6.3 Converting to Absolute Magnitudes

For the conversion of apparent magnitudes m into absolute magnitudes M we need $k(z)$ corrections for the galaxies, defined by

$$M = m - 5 \log \left(\frac{d_L(z)}{10 \text{ pc}} \right) - 2.5 \log(1+z) - k(z), \quad (6.6)$$

where $d_L(z)$ is the cosmological luminosity distance of the galaxy, and z is the redshift.

The $k(z)$ corrections for the objects in the spectroscopic catalogue are obtained by fitting the model spectral energy distributions shown in the left-hand panel of Figure 7.2 to the broad-band photometry of the objects. The template spectral energy distributions are constructed by combining empirical spectra and stellar population synthesis models by Maraston (1998). The detailed description of these models can

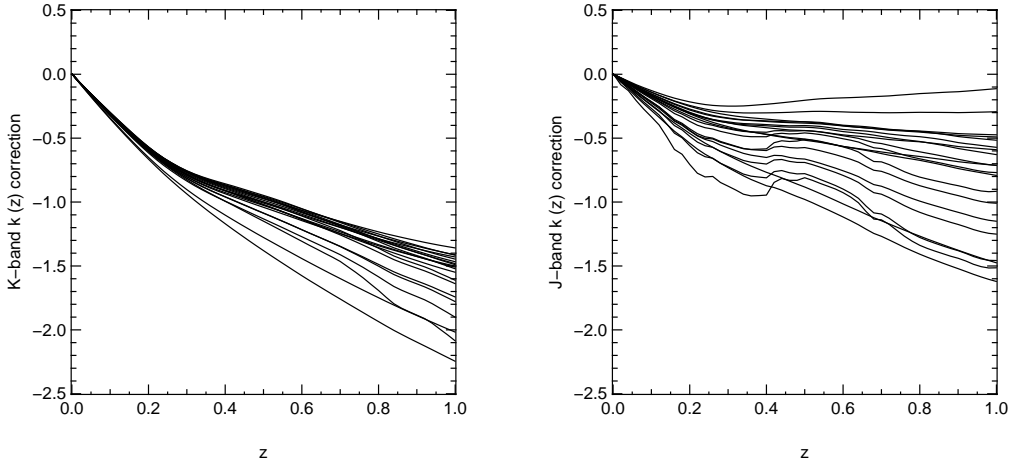


Figure 6.1: *Left-hand panel:* K -band $k(z)$ corrections as a function of redshift for the spectral energy distributions shown in Figure 7.2. *Right-hand panel:* Same as left-hand panel, but for the J band.

be found in MUNICS II. The $k(z)$ corrections for the K band and the J band are presented in the left-hand and right-hand panel of Figure 6.1, respectively, while Figure 4.4 shows a comparison of flux-calibrated spectrum, broad-band photometry, and fitted model spectral energy distribution for two objects in the spectroscopic catalogue.

We have also tested the influence of using only one intermediate-type model spectral energy distributions for deriving the $k(z)$ corrections. As is obvious from Figure 6.1, this should work well for the K band, where the spread between $k(z)$ corrections for different models is small, but a bit less so well for the J band with its larger variations. Indeed, we do see hardly any difference for the K -band LF, and only a small difference in the J band. However, it is important to note that in the following we do *not* use $k(z)$ corrections from one model, but those from the fitting of template spectral energy distributions to the six-filter broad-band photometry of the MUNICS catalogue.

6.4 The K -band Luminosity Function

The rest-frame K -band LF of galaxies drawn from the spectroscopic sample was constructed in the redshift intervals $0.1 \leq z \leq 0.3$ (median redshift $z = 0.2$), $0.3 \leq z \leq 0.6$ (median redshift $z = 0.4$), and $0.6 \leq z \leq 0.9$ (median redshift $z = 0.7$). The two lower redshift bins comprise the majority of objects in the sample, as can be seen in Figure 5.1.

The centres of the bins in absolute magnitude were chosen in a way which ensures a fair representation of the bright end of the LF, i.e. the bin centres at the bright end correspond roughly to the absolute magnitudes of the brightest objects in that bin.

The results for the K -band LF of galaxies in different redshift bins from spectroscopic observations can be found in Table 6.1 and Figure 6.2, where it is compared to the LFs determined from the local samples of Loveday (2000) and Kochanek *et al.*

(2001). Clearly there is a good general agreement between the LF measured at $z = 0.2$ and the ones from local galaxy samples, although our data seem to suggest a somewhat smaller value for M_K^* . Fitting a Schechter function (Schechter 1976; see also equations (6.7) and (6.8) for the parametrisation of the function) to the LF yields the parameters $M_K^* - 5 \log h = (-23.79 \pm 0.24)$ mag and $\Phi_K^* = (1.11 \pm 0.12) \times 10^{-2} h^3 \text{Mpc}^{-3}$. We used a fixed value of $\alpha_K = -1.10$, close to the values derived for local galaxies by Loveday (2000) and Kochanek *et al.* (2001). Contrary to the J -band LF discussed below, our normalisation also nicely agrees with the Cole *et al.* (2001) measurement, although they derive a considerably shallower faint-end slope of $\alpha = -0.93 \pm 0.04$. The errors were derived by running Monte-Carlo simulations with 100 000 iterations, taking into account the errors due to the binning in absolute magnitudes. Excluding the faintest magnitude bin does not change the result of the fit significantly.

Note that the agreement between our measurement and the local Schechter functions is also very good at the faint end, although with poor statistics and large correction factors due to the incompleteness. From this we draw the conclusion that our method to correct for incompleteness yields reliable estimates.

At redshifts $0.3 \leq z \leq 0.6$, we find a mild evolution of the LF, with a higher characteristic luminosity and a lower normalisation, yielding Schechter parameters of $M_K^* - 5 \log h = (-24.04 \pm 0.26)$ mag and $\Phi_K^* = (0.71 \pm 0.25) \times 10^{-2} h^3 \text{Mpc}^{-3}$. The error contours for the Schechter parameters for the LF in the two lower redshift bins are shown in the same figure. These contours were computed from the χ^2 distribution. Finally, we show a comparison of the measurements of the K -band LF in all three redshift bins. Although the statistics becomes rather poor in the highest redshift bin with median redshift $z = 0.7$, it confirms the trend for the evolution of the LF. However, it is evident that the total evolution out to redshifts around 0.7 is not dramatically large.

Comparison of our result with the measurements by Cowie *et al.* (1996) who derived the K -band LF at various redshifts $0 < z < 1$ from a spectroscopic sample in two small fields shows good agreement with our results. Their values for the Schechter parameters M_K^* , Φ_K^* , and α_K are similar to measurements for local samples. Again, our data favour a slightly larger characteristic luminosity, but the trend of a falling normalisation with redshift is found both in the MUNICS and in the Cowie *et al.* measurements of the LF.

6.5 The J -band Luminosity Function

The results for the rest-frame J -band LF of galaxies from our spectroscopic catalogue are shown in Figure 6.3 and summarised in Table 6.2. Note that this is the first determination of the J -band LF at higher redshifts following the local measurements by Balogh *et al.* (2001) and Cole *et al.* (2001).

The Schechter parameters (see equations (6.7) and (6.8) for the definition of the Schechter function) derived in the lowest redshift bin ($0.1 \leq z \leq 0.3$, median redshift $z = 0.2$) are $M_J^* - 5 \log h = (-22.45 \pm 0.24)$ mag, $\Phi_J^* = (1.49 \pm 0.22) \times 10^{-2} h^3 \text{Mpc}^{-3}$ with the faint-end slope α_J set to $\alpha_J = -1.00$. The errors were derived by running Monte-Carlo simulations with 100 000 iterations, taking into account the errors due to

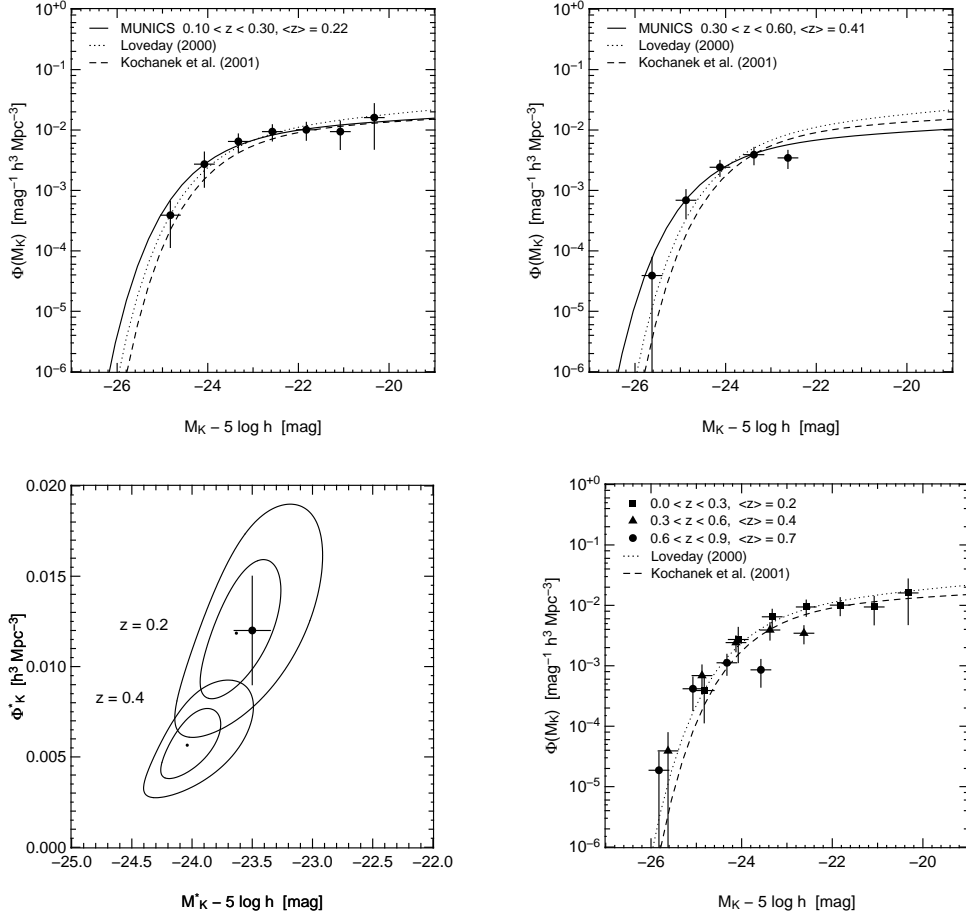


Figure 6.2: The K -band LF of galaxies from spectroscopic observations of MUNICS galaxies. *Upper left panel:* The LF in the redshift range $0.1 \leq z \leq 0.3$ (median redshift $z = 0.2$; filled symbols). The vertical error bars give the Poissonian error, while the binning error was estimated as $b/\sqrt{12}$ with the size b of the bin. Also shown are the measurements of the local K -band LF by Loveday (2000; dotted line) and Kochanek *et al.* (2001; dashed line), as well as a Schechter approximation to the MUNICS data (solid line). The parameters of the Schechter fit are $M_K^* - 5 \log h = (-23.79 \pm 0.24)$ mag, $\Phi_K^* = (1.11 \pm 0.12) \times 10^{-2} h^3 \text{Mpc}^{-3}$, and $\alpha_K = -1.10$ (fixed). *Upper right panel:* The same as before, but in the redshift range $0.3 \leq z \leq 0.6$ (median redshift $z = 0.4$), with Schechter parameters $M_K^* - 5 \log h = (-24.04 \pm 0.26)$ mag, $\Phi_K^* = (0.71 \pm 0.25) \times 10^{-2} h^3 \text{Mpc}^{-3}$, and $\alpha_K = -1.10$ (fixed). *Lower left-hand panel:* Error contours (1σ and 2σ) for the Schechter parameters M_K^* and Φ_K^* from the χ^2 distribution. The filled circle indicates the average value of local measurements from Table 6.5; the “error bars” give an idea of the variation between different authors’ measurements. *Lower right-hand panel:* The LF in the interval $0.6 \leq z \leq 0.9$ (median redshift $z = 0.70$; filled circles), compared to the results from the two lower redshift ($z = 0.2$, squares; $z = 0.4$, triangles) as well as the local measurements.

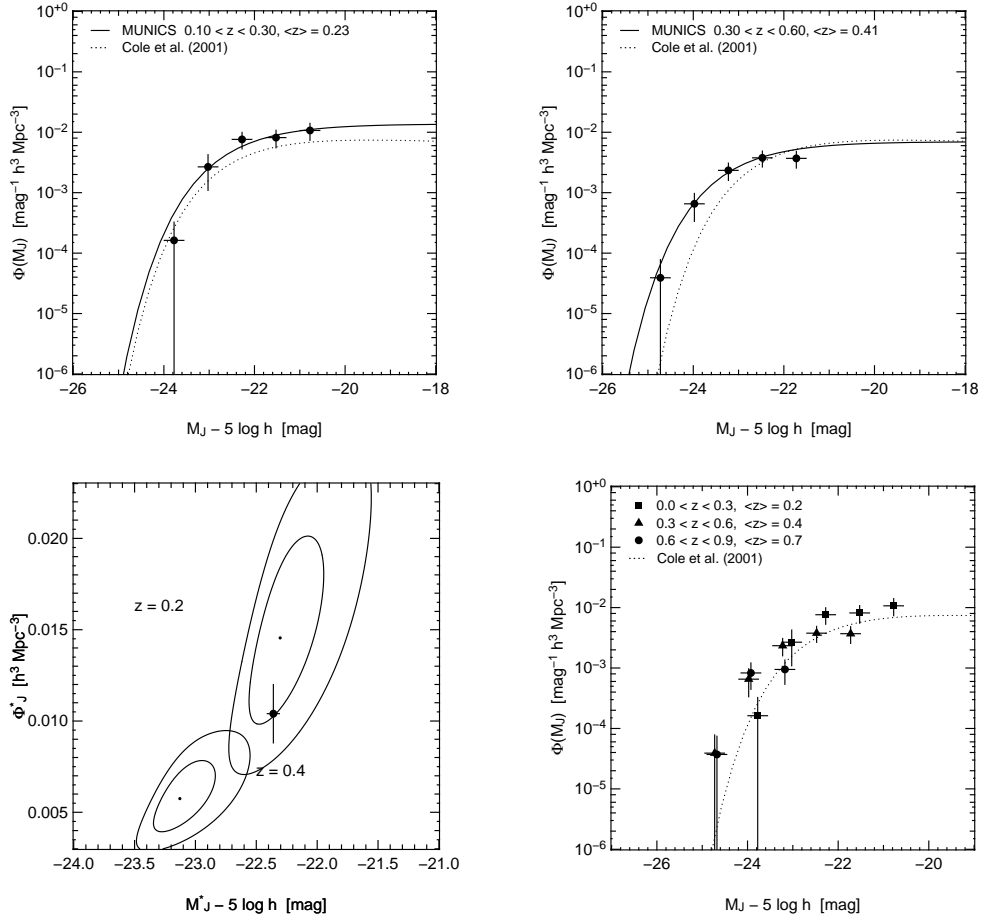


Figure 6.3: The J -band LF of galaxies from spectroscopic observations of MUNICS galaxies. *Upper left panel:* The LF in the redshift range $0.1 \leq z \leq 0.3$ (median redshift $z = 0.2$; filled symbols). The vertical error bars give the Poissonian error, while the binning error was estimated from $b/\sqrt{12}$ with the size b of the bin. Also shown are the measurement of the local J -band LF by Cole *et al.* (2001) as well as a Schechter approximation to the MUNICS data (solid line). The parameters of the Schechter fit are $M_J^* - 5 \log h = (-22.45 \pm 0.24)$ mag, $\Phi_J^* = (1.49 \pm 0.22) \times 10^{-2} h^3 \text{ Mpc}^{-3}$, and $\alpha_J = -1.00$ (fixed). *Upper right-hand panel:* The same as before, but in the redshift range $0.3 \leq z \leq 0.6$ (median redshift $z = 0.4$), with Schechter parameters $M_J^* - 5 \log h = (-23.06 \pm 0.24)$ mag, $\Phi_J^* = (0.76 \pm 0.25) h^3 \text{ Mpc}^{-3}$, and $\alpha_J = -1.00$ (fixed). *Lower left panel:* Error contours (1σ and 2σ) for the Schechter parameters M_J^* and Φ_J^* in the two lower redshift bins from the χ^2 distribution. The filled circle indicates the value of the local measurement by Cole *et al.* (2001) with the appropriate error bar. *Lower right-hand panel:* The LF in the interval $0.6 \leq z \leq 0.9$ (median redshift $z = 0.70$; filled circles) compared to the LF in the two lower redshift bins ($z = 0.2$, squares; $z = 0.4$, triangles) and the measurements of the local J -band LF by Cole *et al.* (2001).

the binning in absolute magnitudes. Compared to the Cole *et al.* (2001) sample, our measurement seems to favour a similar characteristic magnitude M_J^* , but a somewhat larger value of the normalisation Φ_K^* . Unfortunately, Balogh *et al.* (2001), the only other work on the J -band LF available so far, do not derive the normalisation, thus the reason for the discrepancy remains unclear. In the K -band, the value of the normalisation derived by Cole *et al.* (2001) is in good agreement with other measurements, although maybe a bit on the low side.

For the intermediate redshift bin $0.3 \leq z \leq 0.6$ (median redshift $z = 0.4$), the Schechter parameters derived from our data are $M_J^* - 5 \log h = (-23.06 \pm 0.24)$ mag, $\Phi_J^* = (0.76 \pm 0.25) h^3 \text{Mpc}^{-3}$, where α_J was again set to a value of -1.00 . Thus, similar to the K -band, we see a mild evolution of the LF with a higher characteristic luminosity and a smaller normalisation. The error contours for the Schechter parameters of the LF in the two lower redshift bins are shown in the same Figure. These contours were derived from the χ^2 distribution. At the highest redshifts probed by our sample, the evolution of the J -band LF seems to be confirmed, although the statistics becomes rather poor in this case.

6.6 Kolmogorov-Smirnov Tests of Luminosity Function Evolution

One method to compare the measurements of the near-infrared LFs at various redshifts is to apply the Kolmogorov-Smirnov test to the cumulative distribution of objects in absolute magnitudes. Of course, completeness and $1/V_{\text{max}}$ corrections have to be applied to each individual object entering the distribution. The advantage of this method is that it uses the absolute magnitudes as measured in the sample *without binning*. Furthermore, it is independent of the *relative* normalisation of the samples one wants to compare.

We firstly have run this test by comparing the cumulative luminosity distributions from our data in the three redshift bins to the local measurements of the LF. The results are shown in Table 6.3 for the K -band, and Table 6.4 for the J -band, respectively. Furthermore, we show the resulting cumulative distributions in Figures 6.4 and 6.5 for the K band and the J band, respectively.

While the cumulative distributions are in fair agreement for the lower redshift bin ($0.1 < z < 0.3$), they are significantly different for the two higher redshift bins ($0.3 < z < 0.6$ and $0.6 < z < 0.9$, respectively), confirming the result found from the fitting of Schechter parameters M^* and Φ^* .

As an additional test we have applied the Kolmogorov-Smirnov test to the cumulative distributions from the two lower redshift bins. The results of this test are shown in Figure 6.6, where one can see that the probabilities that both distributions are drawn from the same parent population are very small.

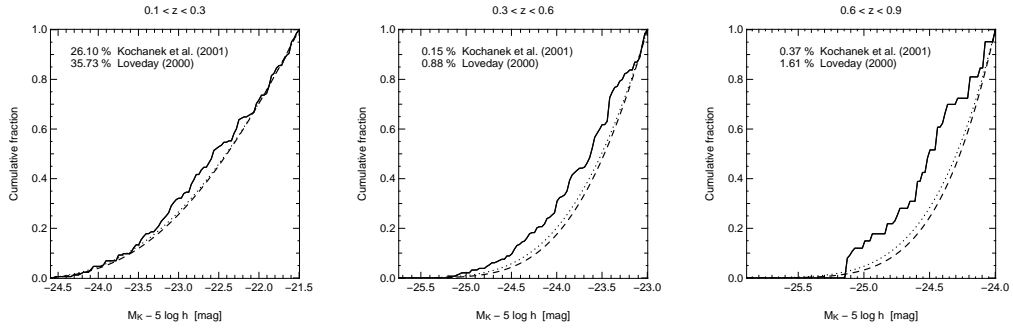


Figure 6.4: Resulting cumulative distribution functions for the absolute K -band magnitudes from the MUNICS spectroscopic catalogue (solid line) as compared to the local measurements by Loveday (2000; dotted line) and Kochanek *et al.* (2001; dashed line). The diagram on the left-hand side compares the $0.1 < z < 0.3$ redshift bin to the local one, the middle diagram shows the same for the $0.3 < z < 0.6$ redshift interval, and the diagram on the right-hand side compares the distributions in the $0.6 < z < 0.9$ interval to the local ones. The values quoted in the diagrams give the probabilities that both cumulative distributions are drawn from the same population.

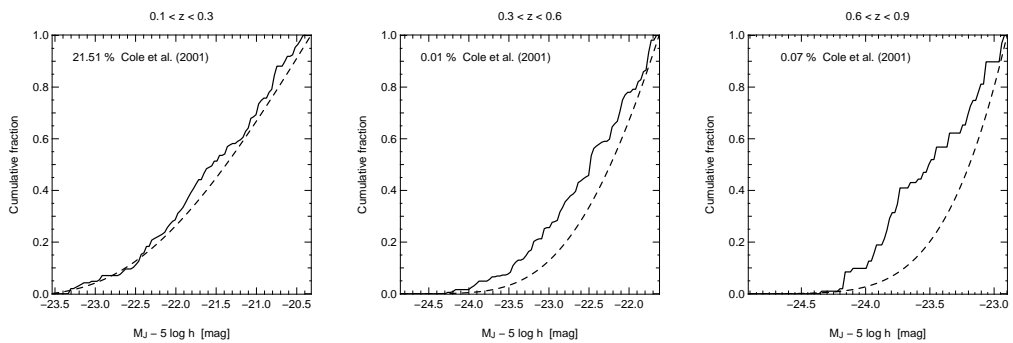


Figure 6.5: Resulting cumulative distribution functions for the absolute J -band magnitudes from the MUNICS spectroscopic catalogue (solid line) as compared to the local measurements by Cole *et al.* (2001; dashed line). The diagram on the left-hand side compares the $0.1 < z < 0.3$ redshift bin to the local one, the middle diagram shows the same for the $0.3 < z < 0.6$ redshift interval, and the diagram on the right-hand side compares the distribution in the $0.6 < z < 0.9$ interval to the local one. The values quoted in the plots give the probabilities that both cumulative distributions are drawn from the same population.

Table 6.1: The uncorrected values $\Phi_u(M_K)$ of the K -band LF, the completeness-corrected values $\Phi(M_K)$, and their errors $d\Phi(M_K)$ for the individual redshift intervals and magnitude bins. Here, ‘completeness correction’ refers to the correction of incompleteness of the photometric catalogue, the incompleteness of the spectroscopic sample with respect to the photometric one, and to the V/V_{\max} correction.

$M_K - 5 \log h$ (mag)	$\Phi_u(M_K)$	$\Phi(M_K)$ ($\text{mag}^{-1} h^3 \text{Mpc}^{-3}$)	$d\Phi(M_K)$
Median redshift $\langle z \rangle = 0.2$:			
-24.825	3.25×10^{-4}	3.89×10^{-4}	2.75×10^{-4}
-24.075	1.63×10^{-3}	2.56×10^{-3}	1.55×10^{-3}
-23.325	5.69×10^{-3}	6.78×10^{-3}	2.22×10^{-3}
-22.575	7.64×10^{-3}	9.68×10^{-3}	2.88×10^{-3}
-21.825	5.85×10^{-3}	1.05×10^{-2}	3.49×10^{-3}
-21.075	3.25×10^{-3}	1.01×10^{-2}	4.97×10^{-3}
-20.325	1.14×10^{-3}	1.75×10^{-2}	1.22×10^{-2}
Median redshift $\langle z \rangle = 0.4$:			
-25.625	2.93×10^{-5}	3.90×10^{-5}	3.90×10^{-5}
-24.875	4.69×10^{-4}	6.91×10^{-4}	3.42×10^{-4}
-24.125	1.41×10^{-3}	2.44×10^{-3}	7.14×10^{-4}
-23.375	1.50×10^{-3}	4.12×10^{-3}	1.32×10^{-3}
-22.625	8.51×10^{-4}	3.86×10^{-3}	1.27×10^{-3}
Median redshift $\langle z \rangle = 0.7$:			
-25.825	1.50×10^{-5}	1.87×10^{-5}	1.87×10^{-5}
-25.075	1.65×10^{-4}	4.20×10^{-4}	2.37×10^{-4}
-24.325	2.84×10^{-4}	1.14×10^{-3}	4.42×10^{-4}
-23.575	1.35×10^{-4}	9.63×10^{-4}	4.59×10^{-4}

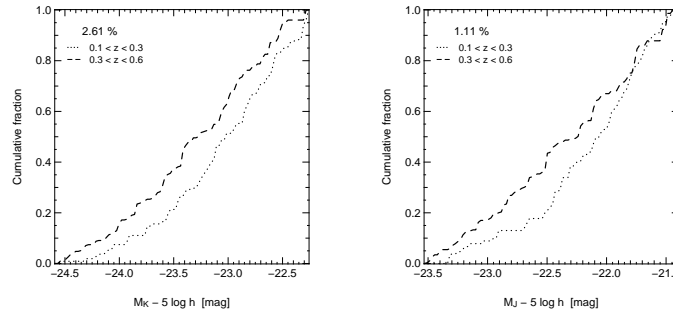


Figure 6.6: Cumulative distributions in absolute magnitude for the two lower redshift bins and results from a Kolmogorov-Smirnov test applied to these data, both for the K band (left-hand panel) and the J band (right-hand panel).

Table 6.2: The uncorrected values $\Phi_u(M_J)$ of the J -band LF, the completeness-corrected values $\Phi(M_J)$, and their errors $d\Phi(M_J)$ for the individual redshift intervals and magnitude bins. Here, ‘completeness correction’ refers to the correction of incompleteness of the photometric catalogue, the incompleteness of the spectroscopic sample with respect to the photometric one, and to the V/V_{\max} correction.

$M_J - 5 \log h$ (mag)	$\Phi_u(M_J)$	$\Phi(M_J)$ ($\text{mag}^{-1} h^3 \text{Mpc}^{-3}$)	$d\Phi(M_J)$
Median redshift $\langle z \rangle = 0.2$:			
-23.775	1.63×10^{-4}	1.63×10^{-4}	1.63×10^{-4}
-23.025	1.95×10^{-3}	2.88×10^{-3}	1.70×10^{-3}
-22.275	6.34×10^{-3}	7.55×10^{-3}	2.30×10^{-3}
-21.525	6.50×10^{-3}	8.26×10^{-3}	2.68×10^{-3}
-20.775	6.50×10^{-3}	1.13×10^{-2}	3.55×10^{-3}
Median redshift $\langle z \rangle = 0.4$:			
-24.725	2.93×10^{-5}	3.90×10^{-5}	3.90×10^{-5}
-23.975	4.40×10^{-4}	6.58×10^{-4}	3.21×10^{-4}
-23.225	1.20×10^{-3}	2.37×10^{-3}	7.57×10^{-4}
-22.475	1.61×10^{-3}	3.94×10^{-3}	1.16×10^{-3}
-21.725	9.68×10^{-4}	4.02×10^{-3}	1.24×10^{-3}
Median redshift $\langle z \rangle = 0.7$:			
-24.675	2.99×10^{-5}	3.67×10^{-5}	3.67×10^{-5}
-23.925	2.84×10^{-4}	8.41×10^{-4}	3.89×10^{-4}
-23.175	2.24×10^{-4}	9.72×10^{-4}	4.21×10^{-4}

Table 6.3: Probabilities for compatible cumulative distributions of absolute magnitudes derived from a Kolmogorov-Smirnov test. The comparison distributions are derived from the local LF measurements by Loveday (2000) and Kochanek *et al.* (2001). The magnitudes in the second column are upper limits to the range of absolute magnitudes for which the distribution has been computed.

Redshift	M_K (mag)	Loveday (2000)	Kochanek <i>et al.</i> (2001)
$\langle z \rangle = 0.2$	-21.5	35.73 %	26.10 %
$\langle z \rangle = 0.4$	-23.0	0.88 %	0.15 %
$\langle z \rangle = 0.7$	-24.0	1.61 %	0.37 %

Table 6.4: Probabilities for compatible cumulative distributions of absolute magnitudes derived from a Kolmogorov-Smirnov test. The comparison distribution is derived from the local LF measurement by Cole *et al.* (2001). The magnitudes in the second column are upper limits to the range of absolute magnitudes for which the distribution has been computed.

Redshift	M_J (mag)	Cole <i>et al.</i> (2001)
$\langle z \rangle = 0.2$	-20.3	21.51 %
$\langle z \rangle = 0.4$	-21.6	0.01 %
$\langle z \rangle = 0.7$	-22.9	0.07 %

6.7 Likelihood Analysis of Luminosity Function Evolution

In this Section we will describe a χ^2 analysis of the redshift evolution of the near-infrared LFs. This test uses the Schechter parametrisation

$$\Psi(L) = \frac{\Phi^*}{L^*} \left(\frac{L}{L^*} \right)^\alpha \exp\left(-\frac{L}{L^*}\right) \quad (6.7)$$

of the LF, where L^* is the characteristic luminosity, α the faint-end slope, and Φ^* the normalisation of the LF (Schechter 1976). The corresponding equation in absolute magnitudes reads

$$\Psi(M) = \frac{2}{5} \Phi^* \ln 10 10^{0.4(M^*-M)(1+\alpha)} \exp\left(-10^{0.4(M^*-M)}\right). \quad (6.8)$$

To estimate the rate of evolution of the parameters with redshift, we define evolution parameters μ and ν as follows:

$$\begin{aligned} \Phi^*(z) &= \Phi^*(0) (1 + \mu z), \\ M^*(z) &= M^*(0) + \nu z, \text{ and} \\ \alpha(z) &= \alpha(0) \equiv \alpha. \end{aligned} \quad (6.9)$$

Note that the faint end of the LF cannot be determined very well from our data, thus we leave the faint-end slope α of the Schechter LF fixed, as we have also done during the fitting of a Schechter function to our data.

To quantify the redshift evolution of Φ^* and M^* we now compare our LF data in *all* redshift bins with the local Schechter function evolved according to equation (6.9) to the appropriate redshift. We do this for a grid of values for ν and μ , and calculate the value of χ^2 for each grid point according to

$$\chi^2(\nu, \mu) = \frac{1}{n} \sum_i \sum_j \frac{\left(\Phi(M_i, z_j) - \Psi(M_i, \nu, \mu, z_j) \right)^2}{\sigma_{ij}^2}, \quad (6.10)$$

where $\Phi(M_i, z_j)$ is the measurement of the LF at median redshift z_j in the magnitude bin centred on M_i , $\Psi(M_i, \nu, \mu, z_j)$ is the local Schechter function evolved according to the evolution model defined in equation (6.9) to the redshift z_j , σ_{ij} is the RMS error of the LF value in the appropriate redshift bin, and n is the number of free parameters of the approximation, i.e. the number of data points used minus the number of parameters derived from the fitting.

We want to compare our measurement of the K -band LF with the Schechter approximations to the local determinations. We use the measurements by Loveday (2000) and Kochanek *et al.* (2001) for the K -band (since the LF parameters derived from local samples are very similar anyway), and the local J -band LF is the one by Cole *et al.* (2001). The Schechter parameters derived by those authors are shown in Tables 6.5 and 6.6. Choosing a shallower faint-end slope in the K band, similar to the one derived by Cole *et al.* (2001), changes the result slightly, but – within the errors – not significantly.

To avoid that data points with large completeness correction factors affect the result, we exclude all LF measurements with a total correction factor (photometric incompleteness, spectroscopic incompleteness, and V/V_{\max} correction) larger than three.

The result of the likelihood analysis is shown in Figure 6.7. For the K -band, we compare our measurements at redshifts 0.2, 0.4, and 0.7 to the local measurements by Loveday (2000) and Kochanek *et al.* (2001), and to the average of their Schechter parameters. We detect a brightening of $\Delta M_K^*/\Delta z \simeq -0.70$ magnitudes, and a decline of the number density of objects to redshift one. The decrease of Φ_K^* with redshift is obviously quite strongly dependent on the parameters of the local LF, however, for the average value we derive $\Delta\Phi_K^*/(\Phi_K^*\Delta z) \simeq -0.35$. These results also give quantitative estimates of the evolution which can already be seen in the Schechter parameters derived from our data, see Table 6.1 for details. Note that Huang *et al.* (2003) derive a significantly brighter M^* , a slightly larger normalisation, and a steeper faint-end slope, which they ascribe to redshift selection effects. If their measurements are valid, the brightening to redshift one would be smaller, whereas the evolution in number density would be even larger.

Within the errors, the results found in this work agree nicely with the measurements of the K -band LF derived from the full MUNICS sample based on photometric redshifts. First results are shown in MUNICS III and show the same trend for the evolution of the LF with redshift. A more detailed analysis is presented in MUNICS II, where the evolutionary trend with a brightening of 0.5 to 0.7 mag and a decrease in number density of roughly 25 per cent to redshift one is confirmed.

Very recently, Pozzetti *et al.* (2003) used about 500 spectroscopic redshifts to derive very similar values for the evolution of the K -band LF from the K 20 survey (Cimatti *et al.* 2002b).

In the case of the J -band (right-hand panel of Figure 6.7), the evolution of the LF is obviously not very well constrained. This is also apparent from the error contours of the Schechter parameters shown in Figure 6.3 (lower left-hand panel), where one can see that the local measurement by Cole *et al.* (2001) has a characteristic magnitude similar to the one derived in our lowest redshift bin, but a normalisation *in between* the ones derived from our two lower redshift intervals, thus making any conclusions about

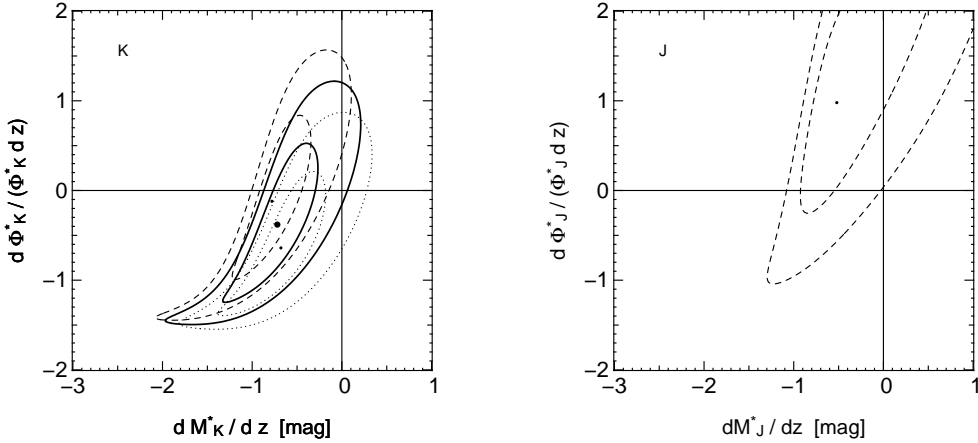


Figure 6.7: *Left-hand panel:* Result of the estimation of the redshift evolution of the Schechter parameters M_K^* and Φ_K^* between $z = 0.4$ (MUNICS LF) and the local universe from Loveday (2000; dotted line), Kochanek *et al.* (2001; dashed line), and for an average of these two local measurements (solid line) as derived from a χ^2 approach (see text for details). The contours correspond to 1σ and 2σ confidence level. The $d\Phi^*/dz = 0$ and $dM^*/dz = 0$ lines indicate the non-evolution values. *Right-hand panel:* The same for the J -band LF. In this case, the local measurement is taken from Cole *et al.* (2001, dotted line), with the appropriate Schechter parameters from Table 6.6, and the evolution is very badly constrained.

evolution with respect to the local sample difficult. However, we note that the evolution in brightness seems to be similar to the one seen in the K band. We will also show in Section 6.8 that measurements from the 6dFGS indicate that the normalisation of the J -band LF measured by Cole *et al.* might be too low.

Furthermore, we note that our J -band LF data seem to confirm the trend seen for the K band, which is also evident from the Kolmogorov-Smirnov tests presented in Section 6.6.

6.8 Improved Local Luminosity Functions from the 6dFGS

It is obvious from the analysis above that the local comparison LFs are of great importance for the study of LF evolution, because the redshift range covered by MUNICS alone is not really sufficient, and the local volume probed by MUNICS is too small to derive a local LF from MUNICS. It has also been pointed out that the local J -band LF by Cole *et al.* (2001) seems to be in disagreement with our measurement as far as the normalisation is concerned.

Hence we tried to improve this situation by searching for a large local comparison sample to derive near-infrared LFs. This became possible recently with the release of the First Data Release of the 6dF Galaxy Survey (6dFGS; Jones *et al.* 2004).

The 6dFGS is a large spectroscopic survey, primarily based on objects drawn from the 2MASS near-infrared imaging survey (Jarrett *et al.* 2000). Thus 6dFGS is a near-

Table 6.5: Summary of samples used for deriving the K -band field-galaxy luminosity function (see Table 6.6 for more details).

Source	Limit (mag)	Area (arcmin ²)	No	z	$M_K^* - 5 \log h$ (mag)	α_K	Φ_K^* ($10^{-2} h^3 \text{Mpc}^{-3}$)
Mobasher <i>et al.</i> (1993) ¹	$B_J \leq 17, K \leq 13$		181	0.0–0.1	-23.37 ± 0.30	-1.00 ± 0.30	1.12 ± 0.16
Songaila <i>et al.</i> (1994) ²	$K \leq 14.5 - 20$	5544–5					
Glazebrook <i>et al.</i> (1995) ³	$K \leq 17.0$	552	124	0.0–0.8	-23.14 ± 0.23	-1.04	2.22 ± 0.53
Cowie <i>et al.</i> (1996) ⁴	$K \leq 19.5$	26	254	0.2–1.0	-23.49 ± 0.10	-1.25 ± 0.15	0.80 ± 0.20
Gardner <i>et al.</i> (1997) ⁵	$K \leq 15.0$	15840	567	0.14	-23.30 ± 0.17	-1.00 ± 0.24	1.44 ± 0.20
Szokoly <i>et al.</i> (1998) ⁶	$R_F \leq 18.5, K \leq 16.5$	2160	175	0.0–0.4	-23.80 ± 0.30	-1.30 ± 0.20	0.86 ± 0.29
Loveday (2000) ⁷	$K \leq 12.0$		363	0.05	-23.58 ± 0.42	-1.16 ± 0.19	1.20 ± 0.08
Kochanek <i>et al.</i> (2001) ⁸	$K_{20} \leq 11.25$		4192	0.02	-23.43 ± 0.05	-1.09 ± 0.06	1.16 ± 0.10
Cole <i>et al.</i> (2001) ⁹	$b_J \leq 19.5, K \leq 13$	$2.2 \cdot 10^6$	17173	0.05	-23.36 ± 0.02	-0.93 ± 0.04	1.16 ± 0.17
Balogh <i>et al.</i> (2001) ¹⁰	$R_c \leq 15 - 17, K \leq 13$			0.0–0.18	-23.48 ± 0.08	-1.10 ± 0.14	
Huang <i>et al.</i> (2003) ¹¹	$K \leq 15$		1065	0.138	-23.70 ± 0.08	-1.39 ± 0.09	1.30 ± 0.20
6dFGS (this work)	$K \leq 12.75$		~ 35000	0.05	-23.83 ± 0.10	-1.11 ± 0.04	1.35 ± 0.11
MUNICS (this work)	$K \leq 17.5 - 19.0$	649	157	0.1–0.3	-23.79 ± 0.24	-1.10	1.11 ± 0.12
			145	0.3–0.6	-24.04 ± 0.26	-1.10	0.71 ± 0.25

¹ Based on the optically-selected Anglo-Australian Redshift Survey (Peterson *et al.* 1986). A correction of +0.22 magnitudes is sometimes applied to their result because of their method of calculating $k(z)$ corrections (Glazebrook *et al.* 1995). ² The area of the Songaila *et al.* (1994) sample actually continuously decreases with K magnitude. The values in the table are intended to give a rough impression of the parameters of the catalogue. No LF is derived by the authors, however, the sample has been used by Cowie *et al.* (1996) in combination with their deep sample to study the evolution of the K -band LF. ³ A correction of -0.30 magnitudes is often applied to their result due to the use of fixed-aperture photometry (Glazebrook *et al.* 1995). ⁴ Cowie *et al.* (1996) determine the LF in four redshift bins from a combination of their deep sample with the shallower samples from Songaila *et al.* (1994). The values for the Schechter parameters given in the table are from their fit to the LF over the whole redshift range, with errors estimated from the dispersion of the values for different redshift intervals. ⁵ The spectroscopic catalogue of Gardner *et al.* (1997) is sparsely selected on the large photometric sample with the parameters given in the table due to geometric limitations imposed by the fibre spectrograph used for the observations. ⁶ Based on redshift from the optically-selected Kitt-Peak Galaxy Redshift Survey (Munn *et al.* 1997). ⁷ Based on K -band imaging of galaxies from the optically-selected Stromlo-APM galaxy survey (Maddox *et al.* 1990a, Loveday *et al.* 1996). ⁸ Based on a combination of the 2MASS catalogue (Jarrett *et al.* 2000) with the CfA2 (Geller & Huchra 1989) and UZC (Falco *et al.* 1999) surveys. ⁹ Based on a combination of the 2MASS catalogue (Jarrett *et al.* 2000) with the 2dFGRS (Folkes *et al.* 1999). ¹⁰ Based on a combination of the 2MASS catalogue (Jarrett *et al.* 2000) with the Las Campanas Redshift Survey (Shectman *et al.* 1996). ¹¹ Hawaii-AA0 K -band Galaxy Redshift Survey.

Table 6.6: Summary of samples used for deriving the J -band field-galaxy luminosity function, giving the source for the data, the approximate limiting magnitude (either in the optical or in the near-infrared), the approximate area, the number of objects, the redshift range of the survey (either as interval or as median redshift), and the parameters of the Schechter function derived from the data. Parameters without error estimate were kept fixed during the fitting procedure. This information is also valid for Table 6.5.

Source	Limit (mag)	Area (arcmin ²)	No	z	$M_J^* - 5 \log h$ (mag)	α_J	Φ_J^* ($10^{-2} h^3 \text{Mpc}^{-3}$)
Cole <i>et al.</i> (2001) ¹	$b_J \leq 19.5, K \leq 13$	$2.2 \cdot 10^6$	17173	0.05	-22.36 ± 0.02	-0.93 ± 0.04	1.08 ± 0.16
Balogh <i>et al.</i> (2001) ²	$R_c \leq 15 - 17, K \leq 13$			0.0–0.18	-22.23 ± 0.07	-0.96 ± 0.12	
6dFGS (this work)	$K \leq 12.75$		~ 35000	0.05	-22.83 ± 0.09	-1.12 ± 0.03	1.33 ± 0.11
MUNICS (this work)	$K \leq 17.5 - 19.0$	649	132	0.1–0.3	-22.45 ± 0.24	-1.00	1.49 ± 0.22
			145	0.3–0.6	-23.06 ± 0.24	-1.00	0.76 ± 0.25

¹ Based on a combination of the 2MASS catalogue (Jarrett *et al.* 2000) with the 2dFGRS (Folkes *et al.* 1999). ² Based on a combination of the 2MASS catalogue (Jarrett *et al.* 2000) with the Las Campanas Redshift Survey (Shectman *et al.* 1996).

Table 6.7: Summary of samples used for deriving the H -band field-galaxy luminosity function (see Table 6.6 for more details).

Source	Limit (mag)	Area (arcmin ²)	No	z	$M_H^* - 5 \log h$ (mag)	α_H	Φ_H^* ($10^{-2} h^3 \text{Mpc}^{-3}$)
6dFGS (this work)	$K \leq 12.75$		~ 35000	0.05	-23.56 ± 0.08	-1.11 ± 0.03	1.36 ± 0.13

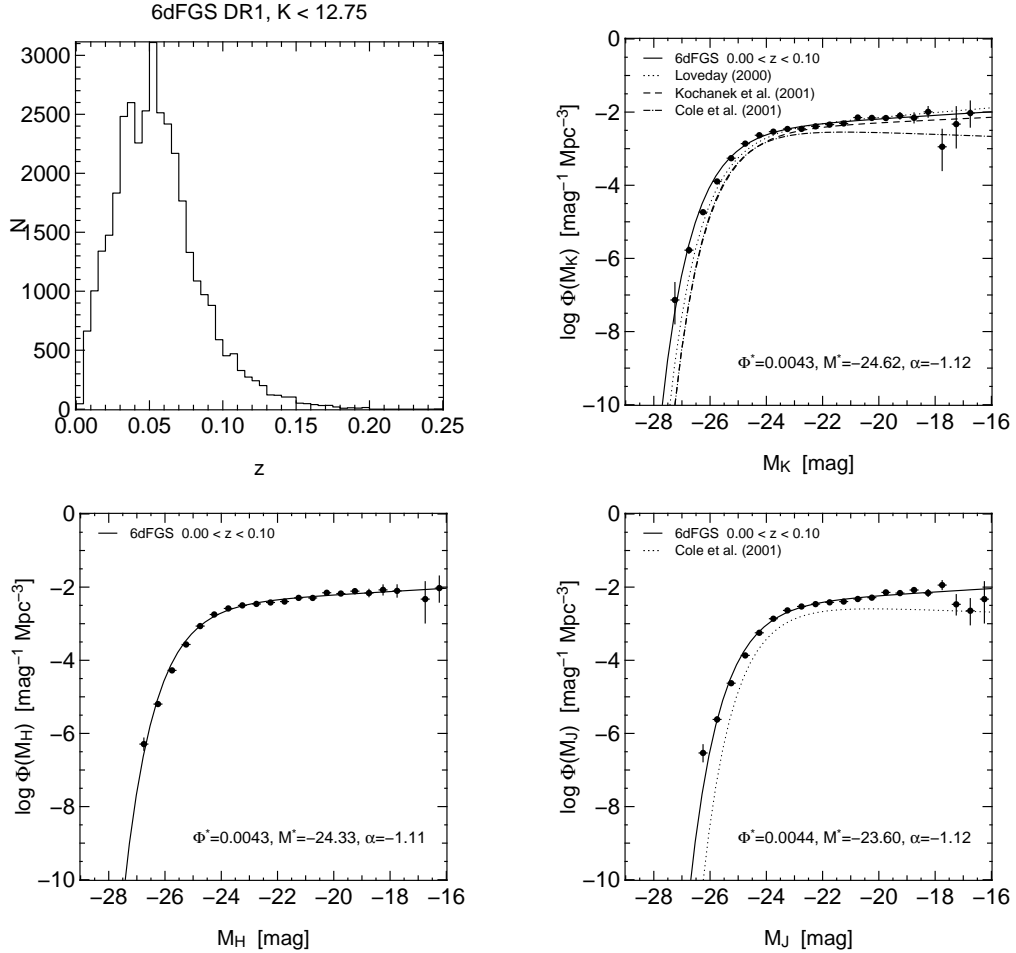


Figure 6.8: *Top left-hand panel:* Histogram of roughly 35 000 spectroscopic redshifts of 2MASS galaxies with $K < 12.75$ from the First Data Release of the 6dF Galaxy Survey (Jones *et al.* 2004). The *other panels* show field galaxy LFs in the rest-frame near-infrared bands K (top right-hand panel), H (bottom left-hand panel) and J (bottom right-hand panel). Note that these LFs are computed from the K -selected catalogue using $h = 0.7$.

infrared selected galaxy catalogue, making it an ideal local complement for MUNICS. The First Data Release contains roughly 35 000 galaxies with secure redshifts. The histogram of redshifts for a sub-sample of 2MASS galaxies in the 6dFGS-DR1 with $K \leq 12.75$ is shown in the top left-hand panel of Figure 6.8. The median redshift is $z \approx 0.05$, with a tail out to $z \approx 0.15$.

We used this sample to derive K -band selected LF in the near-infrared filters K , H and J in the same way as we derived the MUNICS LFs. In brief, we used the V_{\max} method and applied all sampling and incompleteness corrections as described in Jones *et al.* (2004). The resulting LFs are shown in Figure 6.8. Schechter functions were fitted to all LF bins with small errors, the parameters of which are shown in Figure 6.8.

Figure 6.9: New determination of the evolution of near-infrared LFs based on the local measurement derived from the 6dFGS.

In the K band, there is rather good agreement between most of the local samples, with the exception of the Cole *et al.* (2001) measurement which has a different faint-end slope. Also, the characteristic absolute magnitude M_K^* derived from the 6dFGS LF seems to be brighter than other measurements (see also Table 6.5). In the H band this is the first measurement of the LF, so no comparison with existing data can be given. However, it is clear that the H -band LF does not behave vastly different from the ones in the K and J band which, of course, is not surprising. The most interesting result is the one for the J band. Here there is clearly a significant difference with the only literature measurement by Cole *et al.* (2001). Not only is the faint-end slope much steeper than given by them, but the number density of galaxies seems to be higher than suggested by Cole *et al.* (2001). Moreover, the 6dFGS LF is again shifted to brighter luminosities.

The influence of this new determination of the local near-infrared LFs has some impact on the evolution of M^* and Φ^* as discussed above. In the case of the K band, the normalisation of the 6dFGS is very similar to other local measurements, but the characteristic luminosity is somewhat brighter, thus reducing the brightness evolution. In the J band, the effect concerning the luminosity is similar. However, there is some improvement for the density: The 6dFGS suggests a considerably higher local density than the Cole *et al.* (2001) measurement, thus allowing a better constraint than previously possible. This helps to the problem with the evolution of the J -band LF apparent from Figure 6.7. The updated results for the evolution of the near-infrared LFs is presented in Figure 6.9. We will present improved estimates of LF evolution in Chapter 8 where we estimate the LF evolution from the large photometric MUNICS catalogs selected both at near-infrared and at optical wavelengths.

6.9 Luminosity Functions: The Connection to Theory

How can the characteristic shape of the galaxy luminosity function be explained theoretically? Clearly, the formation and evolution of structure is a very complicated story (Peebles 1980, 1993, Peacock 1999): Initial fluctuations in the density field grow by gravitational attraction, mainly driven by the ‘cold dark matter’ (CDM) assumed to present in the universe.

So much for the easy part. The formation and evolution of real galaxies with their gas and stars is even more complicated: The baryonic matter component then falls into these ‘dark matter haloes’, stars are formed and die, and their metal production and energy release affects the surrounding material, an effect known as ‘feedback’ (see the introduction of the paper by Adelberger *et al.* 2003 for an illuminating and amusing description of why we need feedback). Not only is the dynamics of the gaseous component very complicated, but also our understanding of star formation is far from complete (see Evans 1999 for a review).

It is clearly very difficult to numerically assess this physical processes in a com-

plete way, although modern hydrodynamical simulations try to proceed along this line. Hence only simplified numerical models for galaxy formation are available. The basic principle of these ‘semi-analytic models’ (e.g. Kauffmann *et al.* 1999, Somerville & Primack 1999, Cole *et al.* 2000) is as follows: The growth of dark matter haloes, their merging and mass assembly are taken from cosmological simulations or constructed from Monte-Carlo techniques. The complicated hydrodynamical processes within the haloes, i.e. the gas cooling and heating, star formation, supernova explosions and their feedback on their environment etc., are parametrised with simple models. Although these simplified models are physically motivated, it is important to note that many of the processes they describe are only poorly understood.

Another problem with the models is their ‘normalisation’. The free parameters of the models can be adjusted within a range of values to fit certain observed characteristics of the galaxy population. Some modelers prefer to fit the local Tully–Fisher relation for spirals (Tully & Fisher 1977), a correlation between the B -band luminosity of spiral galaxies and their rotation velocity, while others prefer to make their models fit the local luminosity function. Apparently, for many models there seems to be a problem with fitting both at the same time.

But what is the special challenge for these models when trying to reproduce the shape of the luminosity function? The problem is the conversion of the halo mass function to the galaxy luminosity function. The halo mass function in CDM theory has a different shape than the luminosity function: At small masses, it rises steeper than the luminosity function, while at high masses it lacks the sharp cut-off seen at the bright end of the luminosity function (Jenkins *et al.* 2001). Thus the theorists face the problem of suppressing star formation in low and high mass haloes. In Figure 6.10 this is illustrated by comparing a halo mass function from Benson *et al.* (2003), converted to a K -band galaxy luminosity function by assuming a constant mass-to-light ratio of $\mathcal{M}/L_K = 11 \mathcal{M}_\odot/L_{K,\odot}$, to the Schechter parametrisations of the field-galaxy luminosity functions by Loveday (2000), Kochanek *et al.* (2001) and my determination based on the 6dFGS (see Section 6.8).

The standard picture of galaxy formation assumes that the in-falling gas heats to the virial temperature of the dark-matter halo’s potential well and later cools down (Rees & Ostriker 1977, White & Rees 1978). For a thermally supported gas cloud, the minimum mass required for collapse, the *Jeans mass* \mathcal{M}_J (Jeans 1928), is a function of the mean particle density n and the kinetic temperature T of the gas,

$$\mathcal{M}_J \propto T^{3/2} n^{-1/2}. \quad (6.11)$$

Thus, since stars can only form from cool gas, the only possibilities to circumvent star formation in a dark-matter halo are either to remove the gas, or to heat it.

For low-mass haloes, it is generally assumed that the energetic feedback from massive stars (a) might drive gas out of the system (Dekel & Silk 1986), and (b) efficiently re-heats the cold gas in the system, thus preventing the formation of more stars (e.g. Benson *et al.* 2003). In fact, star formation in these galaxies could have been delayed by the ultraviolet background until $z \lesssim 1$ (Babul & Rees 1992); as “boojums”² (“blue

²The fantasy word is taken from Lewis Carroll’s famous poem “The Hunting of the Snark” (Carroll

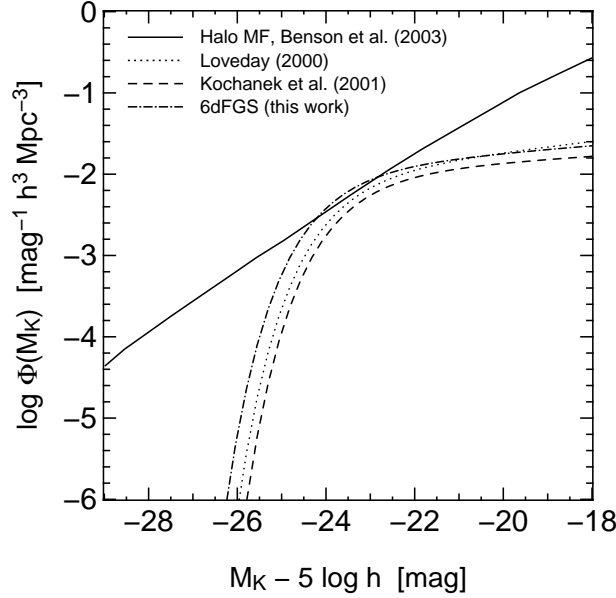


Figure 6.10: Comparison of the mass function of dark matter halos in CDM simulations (solid line) and two examples for local K -band field-galaxy luminosity functions (dotted and dashed lines). The halo mass function has been normalised to the knee of the luminosity function, thus illustrating the prediction of models with *constant mass-to-light ratio* $\mathcal{M}/L_K = 11 \mathcal{M}_\odot/L_{K,\odot}$ and *without feedback* (modified version of Figure 1 in Benson *et al.* 2003).

objects observed just undergoing moderate starburst”) they could make up the major part of the faint blue galaxy counts (Babul & Ferguson 1996). However, inhibiting star formation in high-mass haloes presents a more difficult problem.

Benson *et al.* (2003) investigate the influence of different feedback mechanisms on the faint and bright end of the galaxy luminosity function. They find that it is rather difficult to obtain a good match for both faint and bright galaxies. While they succeed in suppressing cooling in high-mass haloes, they conclude that this would require either thermal conduction or the expulsion of gas from haloes in super-winds at temperatures high enough to prevent recapture. However, the conduction rates needed for the former process are rather high, and the energy needed for the latter is likely larger than the one available from supernovae. They also find better agreement for lower values of $\sigma_8 \sim 0.7$, the normalisation of the power spectrum of density fluctuations on scales of $8 h^{-1}$ Mpc. However, according to measurements of the fluctuations in the cosmic microwave background by the WMAP satellite, $\sigma_8 = 0.84 \pm 0.04$ (Spergel *et al.* 2003), lower than the value that was used in the Benson *et al.* model ($\sigma_8 = 0.93$), but not as low as $\sigma_8 = 0.7$.

Binney (2004), on the other hand, disagrees with the generally agreed conception that all of the in-falling gas heats to the virial temperature of the halo. Based on X-ray observations indicating that very little, if any, gas is cooling in galaxy clusters (Tamura

et al. 2001, Peterson *et al.* 2003), he assumes that a fraction f of the gas fails to heat to the virial temperature, where f decreases as the halo mass increases. The gravitationally heated fraction of the gas is then further heated by supernova feedback and the central black hole. Nuclear black holes have been found in all galaxies with bulges investigated so far (Kormendy & Richstone 1995, Kormendy 2004). For small-mass halos, the hot gas is heated sufficiently to flow out of the system, whereas in high-mass systems the gas is either retained in the system or pushed up so high in the halo that it takes several Gyr to fall back after the energy output by type-II supernovae has decreased (D’Ercole *et al.* 1989). At some point this hot material may densify sufficiently to heat any in-falling cold gas, thus ‘calling a halt to star formation’ (Binney 2004).

6.10 Comparison to Galaxy Formation Models

It is interesting to compare the near-infrared selected LFs presented here to theoretical predictions as made by semi-analytic models described in Section 6.9.

To demonstrate some of the failures of these models we compare the K -band LF and its redshift evolution with some of the semi-analytic models available (Figure 6.11). The models were taken from Kauffmann *et al.* (1999), the Durham group (Baugh *et al.* 2003) and the GALICS group (Hatton *et al.* 2003). Clearly one of the largest difficulties of the models is the bright end of the LF at low redshift, where many models over-predict the number of bright galaxies. This is a general problem of the models (Benson *et al.* 2003): The mass function of dark matter haloes has a power-law shape, thus the processes acting during galaxy formation and evolution decrease the numbers of galaxies both at the faint end and at the bright end, effectively resulting in the Schechter-like form of the LF. The methods by which semi-analytic models achieve the high-luminosity cut-off observed in the galaxy LF are often rather crude: in some cases an upper mass limit for star formation in dark matter haloes is defined. Clearly, a lot of theoretical work remains to be done, and the discrepancies between the models and the observations tell more about deficiencies in the models than about the physics of galaxy formation.

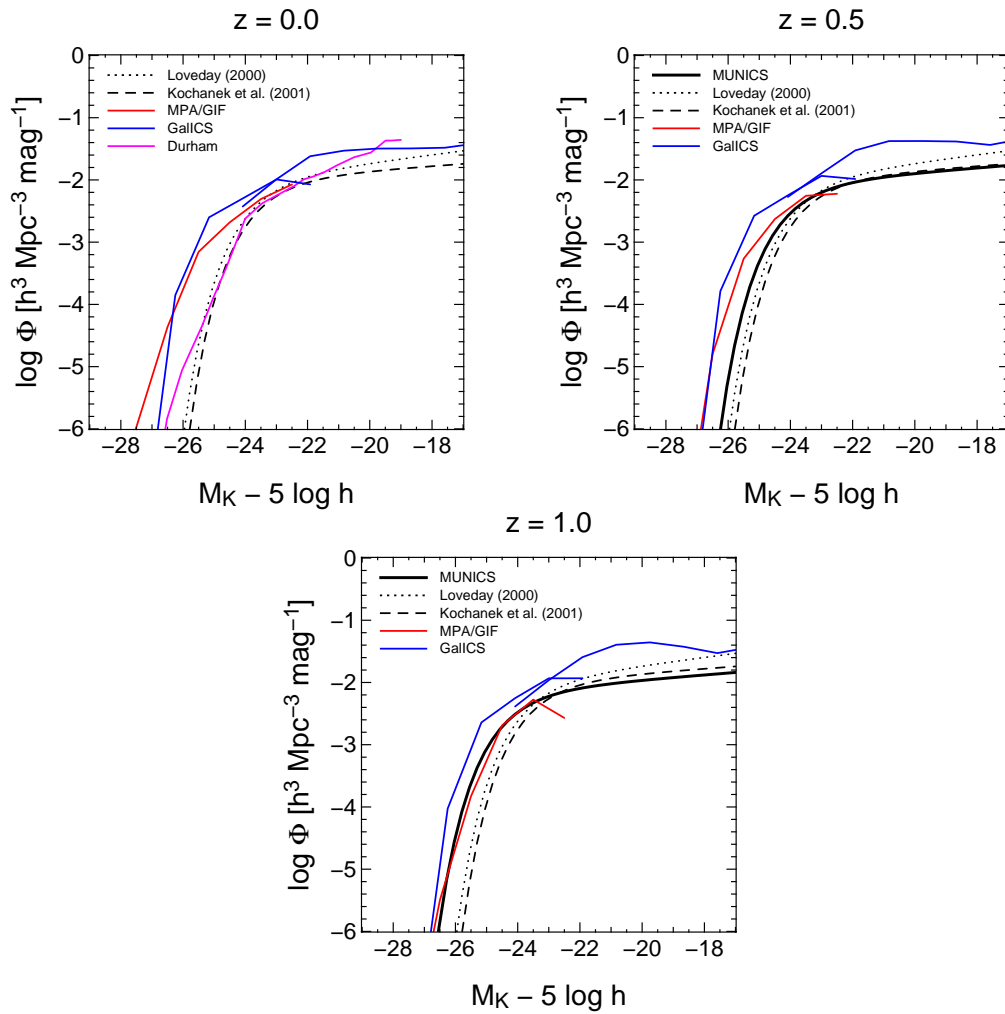


Figure 6.11: Comparison of K -band LF to semi-analytic models for redshift $z = 0.0$ (upper left-hand panel), $z = 0.5$ (upper right-hand panel) and $z = 1.0$ (bottom panel). The dotted and dashed line refer to local measurements of the LF, the thick solid line to the local LF evolved according to the MUNICS measurements. Clearly, these models fail to reproduce the observed LF (see the text for a detailed discussion).

Chapter 7

The Construction of Optically Selected MUNICS Catalogues

In the following we want to present optically selected MUNICS catalogues. These contain many more objects than the spectroscopic sample (and than many previous surveys!) and can thus be used to study the evolution of the galaxy population with high statistical accuracy. Furthermore, they can be used to investigate the influence of colour selection effects on galaxy surveys. While most of the surveys done until the 1980's were optically selected (either in the B band or in the I band), Chapter 6 has presented results from a near-infrared selected galaxy catalogue. The I -band and B -band selected galaxy samples from the MUNICS survey presented in the following two Chapters can be used for comparison with previous work and to study selection effects. Since the MUNICS spectroscopic sample was pre-selected on the K -band photometric catalogue, we have to rely on photometric redshifts to determine distances to galaxies.

In this chapter we want to discuss the construction and the properties of the I -band and B -band selected photometric catalogues as well as the measurement and reliability of photometric redshifts. We will often refer to the different catalogues as MUNICS_K, MUNICS_I and MUNICS_B for short.

7.1 Catalogue Construction

Object detection was performed on the I -band and B -band images using the YODA source extraction software (Drory 2003). Sources are detected by requiring a minimum number N_{pix} of consecutive pixels to lie above a certain threshold t expressed in units of the local RMS σ of the background noise. To ensure secure detection of faint sources, the images are convolved with a Gaussian of FWHM similar to the seeing in the image. The choice of the number of consecutive pixels N_{pix} and the threshold t is a compromise between limiting magnitude at some completeness fraction, say 50 per cent, and the number of tolerable spurious detections per unit image area (Saha 1995, see also the discussion in MUNICS I).

For the K -band selected catalogue, Drory *et al.* (2001b) chose to fix the threshold $t = 3\sigma$ and the convolution kernel to have the same FWHM as the seeing in the

images. To find reasonable values for N_{pix} and t they performed simulations with varying minimum number of consecutive pixels on the K -band image of one of our mosaic fields (S6F5). Accepting 1 per cent contamination by false detections, they fixed the minimum number of consecutive pixels at 2 times the seeing disk area, $N_{pix} = \pi(1.4FWHM/2)^2$, (10 pixels at $1''$, 16 pixels at $1.5''$ seeing for the MUNICS pixel scale) and performed object detection using these parameters on all K -band images.

However, optical images have different characteristics than near-infrared images, so we decided to run new simulations to ensure best detection on the I -band and B -band images. Instead of fixing two parameters (the threshold and the convolution kernel) and keeping only one free parameter (as with the K -band detection), we chose only one fixed parameter: The size of the convolution kernel was set to be equal to the (Gaussian) PSF of the images. Thus we kept both the threshold and the number of consecutive pixels as free parameters in our simulations. Choosing a PSF-like Gaussian kernel for the image convolution is necessary to ensure secure detection of faint, compact objects in the images. The number of false detections was measured by running the detection algorithm on the same images multiplied by -1 .

From these simulations, the best choice of parameters is $t = 4\sigma$ for the detection threshold, and $N_{pix} = \pi(FWHM/2)^2$ for the minimum number of consecutive pixels required for an object. Thus, compared to the near-infrared detection, the threshold was changed from 3σ to 4σ of the local background, but the number of consecutive pixels was reduced from twice the equivalent area of the seeing disk to the equivalent area of the seeing disk, which seems a reasonable choice of parameters. With these settings, the contamination rate (the rate of false detections) is actually below 1 per cent.

Since one of the ideas of this Chapter is a comparison of properties of the K -band and the optically selected galaxies, we have convinced ourselves that this change of detection parameters does not influence the results presented here. The reason is that different detection parameter choices mostly affect the object statistics at the very faintest apparent magnitudes. Since these objects also have large photometric errors, they are usually excluded from any further analysis and thus cannot influence the results of our work.

In Figure 7.1 we show the completeness functions for the I -band images of the ten MUNICS mosaic fields, based on Monte-Carlo simulations of artificial point-sources placed at random in the images. After running the object detection algorithm on the images, the fraction of re-detected artificial objects as a function of magnitude is computed.

Photometry was done in elliptical apertures the shape of which was determined from the first and second moments of the light distribution in the detection image, as described in Drory (2003), and additionally in fixed size circular apertures of 5 and 7 arc seconds diameter. To ensure measurement at equal physical scales in every pass-band, the individual frames were convolved to the same seeing FWHM, namely that of the image with the worst seeing in each field.

Aperture fluxes and magnitudes were computed for each object present in the I -band and B -band catalogues irrespective of a detection in any other band. For this

Table 7.1: The number of detected objects in the ten MUNICS mosaic fields, both for the K -band, I -band and the B -band selected catalogue, together with the effective area. The fields S3F1 and S4F1 have inadequate data quality and are not used in the analysis presented below. The last line shows averages for the eight fields with good quality data.

Field	N_{det} (K band)	N_{det} (I band)	N_{det} (B band)	Area [arcmin ²]
S2F1	646	1186	1418	119.1
S2F5	836	1478	1496	123.7
S3F1	487	932	1174	116.6
S3F5	743	1146	1248	107.6
S4F1	557	1184	894	105.6
S5F1	608	842	1441	115.7
S5F5	468	631	1202	105.3
S6F1	529	1041	1376	117.1
S6F5	826	830	1402	116.5
S7F5	749	996	1161	119.1
All	6449	10267	12812	1146.3
Average	676	1064	1343	115.5

purpose the centroid coordinates of the sources found in the detection images were transformed to the other frames using full astrometric transformations between the image coordinate systems. For this purpose, the images in the other five filters of each field were registered against the image in the detection band by matching the positions of ~ 200 bright homogeneously distributed objects in the frames and determining the coordinate transform from the detection system to each image in the other four pass-bands using the tasks `XYXYMATCH` and `GEOMAP` within `IRAF`. The scatter in the determined solutions is less than 0.1 pixels RMS in the transformation from I or B to the other optical bands, and less than 0.2 pixels RMS from I or B to the near-infrared frames. Note that the frames themselves are not transformed to avoid artefacts from the re-sampling. We only determine accurate transformations and apply these later to the apertures in the photometry process, where the shapes of the apertures were transformed using only the linear terms of the transformation.

The raw photometric catalogues were then cleaned of objects which are not located in the overlap area of all six filter images. To do this, we constructed the exact overlap area by measuring the circular apertures in the optical images and the polygons resulting from the 2-by-2 mosaics in the near infrared. To avoid problems with the photometry of objects close to image borders we excluded objects closer than 10 arc-sec to the image border. The resulting numbers of objects in the cleaned catalogue as well as the effective image areas are listed in Table 7.1.

The agreement between the photometry of I -selected and K -selected objects present in both catalogues is very good (see Figure B.1 in Appendix B). The same

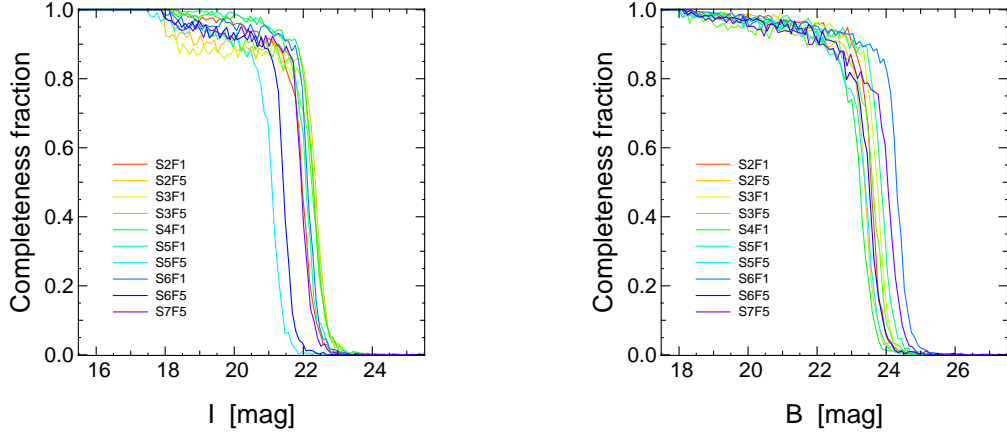


Figure 7.1: Result of Monte-Carlo simulations with artificial point sources placed in the I -band (*left-hand panel*) and B -band images (*right-hand panel*) of MUNICS.

is true for the comparison of photometry between MUNICS_I and MUNICS_B (see Figure B.2 in Appendix B). The scatter is due to the fact that photometry is performed in elliptical apertures the shape of which is determined in the respective detection image. Thus, the apertures for the K -band and the I -band selected photometry can be different, thus producing the observed scatter.

Morphological object classification in either PSF-like or extended objects was performed in a manner similar to the K -band selected catalogue (see MUNICS I), but was improved in two ways.

Firstly, as for the K -selected catalogue the morphological information in all filters was used. Already for that catalogue it was intended to weight the classification information for each object by the signal-to-noise in all six filters. However, due to a bug in the code the object classification in MUNICS I was always based on the objects' morphology in K and J . This bug was fixed, hence classification is now based on the information in all filters.

More specifically, an objects is classified as PSF-like, if it is classified as non-extended in the two filters with highest signal-to-noise ratio.

Secondly, we improved our method to select stars for the determination of the PSF. For the old catalogues (MUNICS I), this was done by hand, but we have now implemented a semi-automatic algorithm:

1. On the detection catalogue, select relatively bright objects (to avoid contamination with very faint, i.e. noisy objects), but exclude very bright objects (to avoid saturated stars).
2. Do κ - σ clipping to get the mean asymmetry of stellar objects (e.g. to account for telescope tracking problems).
3. Select objects with asymmetry parameter smaller than some limit.
4. Do Gaussian fits to all these objects to measure their FWHM.

5. Do κ - σ clipping on FWHM measurements to get the seeing.
6. Use stars within 3σ around the mean seeing for PSF measurement.

In some cases, this automatic algorithm required interaction. Firstly, the asymmetry limit should not be larger than the intrinsic asymmetry. Secondly, for some high galactic latitude fields the number of stars is so small that the stellar sequence is not well defined. However in most cases the selection of PSF stars is very stable. Diagrams showing the objects selected for PSF determination can be found in Appendix C.

7.2 Photometric Redshifts

Photometric redshifts are derived using the method presented in Bender *et al.* (2001). We only briefly outline the procedure in this section. The method is a template matching algorithm rooted in Bayesian statistics closely resembling the method presented by Benítez (2000). However, instead of relying on a predetermined set of template SEDs, semi-empirical templates matching the photometric properties of the sample are used. The templates are derived by fitting stellar population models of Maraston (1998) of different age and dust extinction and Kinney-Calzetti (Kinney *et al.* 1996) spectra to combined broad-band energy distributions of MUNICS and FDF (Heidt *et al.* 2003) galaxies having spectroscopic redshifts. In this way, representative galaxy templates of mixed stellar populations (variable age, metallicity, and dust extinction) optimised for the MUNICS dataset are obtained.

The total spectroscopic sample is divided into two groups of objects. The first subsample (all objects with redshifts in the field S2F1) is used for constructing SED templates, the second subsample (all other objects with spectroscopic redshifts) is used for comparing spectroscopic and photometric redshifts and thereby calibrating the SED library.

The observed-frame apparent magnitudes of objects in the first subsample are transformed to rest-frame redshift zero, and fitted by an initial set of stellar population synthesis models. Objects best fitting the same model are grouped together. Since each group will contain objects from a variety of redshifts, a densely sampled SED from the broad band photometry of these objects is obtained.

This initial set of SEDs is used to determine photometric redshifts for the total sample of objects having spectroscopic redshifts. The photometric redshifts are compared to the spectroscopic ones, and, additionally, the same de-redshifting procedure is applied to the spectroscopic sub-sample not used for the initial construction of the SEDs, only that now we group the objects by the SED that gave the best fit during the determination of the photometric redshift. Using this comparison, deficiencies in the set of SEDs can be identified as those become apparent through systematic offsets between the de-redshifted magnitudes and the SED templates. This is the case since such deficiencies lead to a wrongly determined photometric redshift and therefore to the assignment of a wrong SED.

This procedure is repeated with a refined set of SEDs, by changing SEDs, abolishing some and adding others, until a satisfactory library of template SEDs is found.

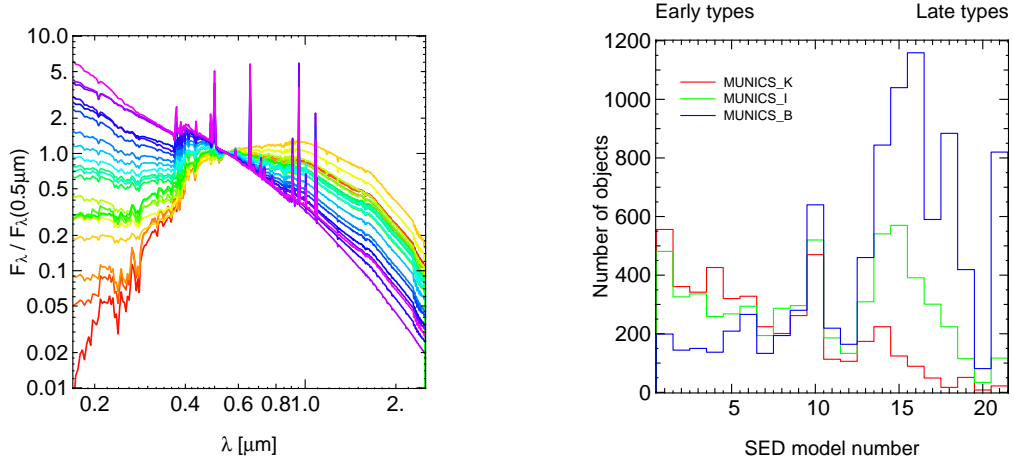


Figure 7.2: *Left-hand panel:* Template SEDs for galaxies used in the computation of photometric redshifts for the *K*-, *I*- and *B*-selected samples (see the text for details). *Right-hand panel:* The distribution of SED types in the three MUNICS catalogues. The SED number is an internal SED identification. Small numbers refer to redder (early-type) galaxies, higher numbers to bluer (late-type) galaxies.

The left-hand panel of Figure 7.2 shows the final template SED library used to derive photometric redshifts in what follows. It is the same set of SEDs also used for the *K*-band selected catalogue, since the SEDs anyway cover a wide range from very red old models to young star-bursting models. As we show in the right-hand panel of Figure 7.2, the difference between the differently selected catalogue lies then only in the distribution of selected SEDs: While in the *K*-selected sample the algorithm picks preferentially red galaxy types (and only very few heavily star-forming objects), the distribution for the *I*-selected sample is more balanced, and indeed reversed for the *B*-selected sample.

Finally, Figure 7.5 compares photometric and spectroscopic redshifts for all ~ 500 objects within five MUNICS Mosaic Fields and shows the distribution of redshift errors. The typical scatter in the relative redshift error $\Delta z / (1 + z)$ is 0.056. The mean redshift bias is negligible. The distribution of the errors is roughly Gaussian. There is no visible difference between the distributions among the survey fields. Although this performance is encouraging, it is important to say that the spectroscopic data become sparse at $z \gtrsim 0.6$ and there are only very few spectroscopic redshifts at $z > 1$.

To illustrate the use of photometric redshifts, we show two instructive examples of photometric redshift determinations of galaxies and the identification of an M-star in Figure 7.3. These examples help to understand how the technique works and the uncertainties involved.

Firstly, a spiral-like system at redshift $z \simeq 0.90$. Here the Balmer break is redshifted beyond the *R*-band filter, and only one SED contributes significantly to the global peak in the redshift probability distribution. The rather broad probability distribution in redshift is due to the fact that the Balmer break is in the rather large sampling gap between the *R* and *I* bands, and therefore its position is not very well determined. Note

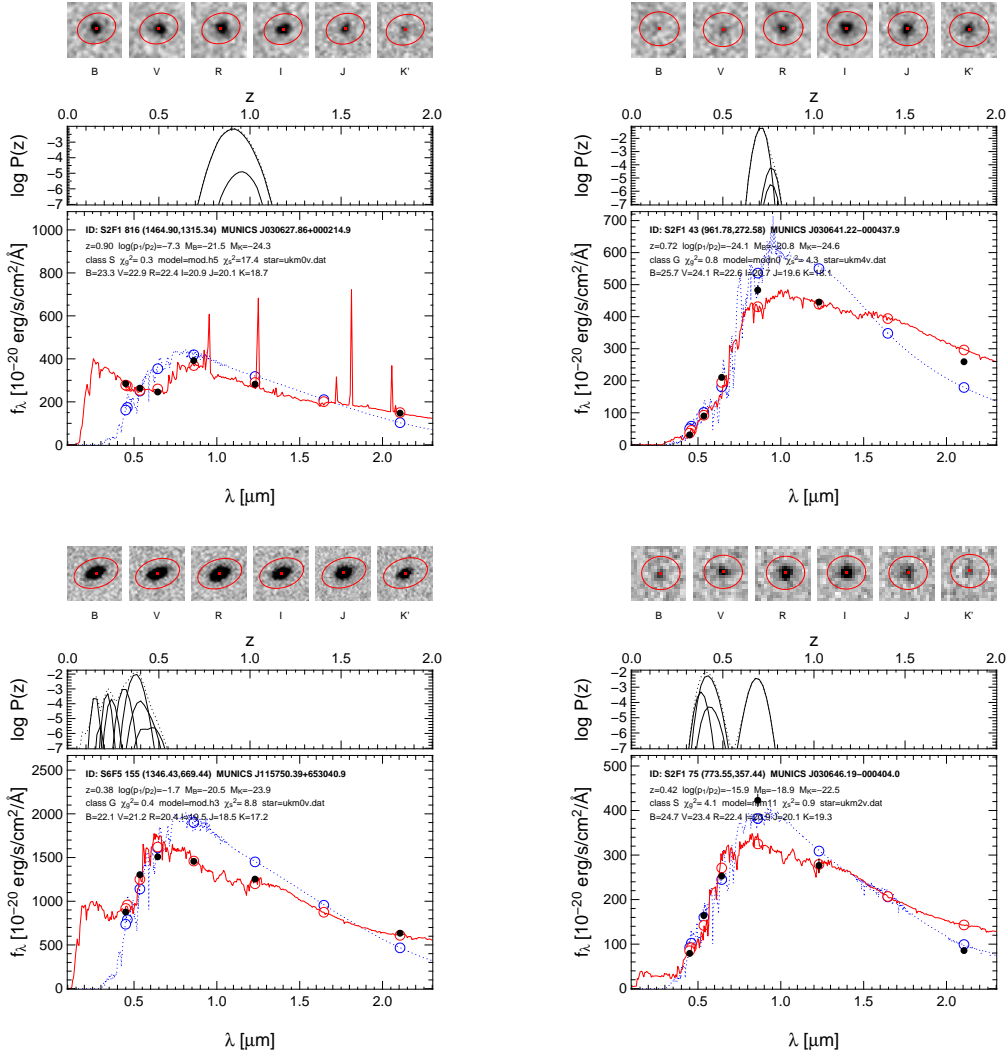


Figure 7.3: Four examples for photometric redshift fits (see text for details). For each example object, the uppermost panel shows cut-outs from the MUNICS images in all six filters together with the photometry aperture. In the middle panel we show the photometric redshift probability distributions of different galaxy template SEDs (solid lines) and the total probability distribution (dotted line). In the bottom panel we show the photometric measurements in *B*, *V*, *R*, *I*, *J* and *K* as filled circles, the best-fitting galaxy template SED in red, and the best-fitting stellar SED as a blue dotted line. For both SEDs the expected photometric measurements are indicated by the open circles.

that this object, although very bright in the optical, is very faint in the K band, and therefore probably a rather low-mass system.

Secondly, an early-type object at redshift $z \simeq 0.72$. The redshift determination can be regarded as quite secure although there are competing SEDs around the global peak of the redshift probability function. In this case, the redshift is determined by the 4000\AA break and the steep decline in flux bluer thereof. Because the object is undetected in B and only barely detected in V , the rest-frame ultraviolet and blue slopes of the spectrum are not firmly determined and hence slightly differing effective ages are giving reasonable fits. This uncertainty in age or type translates into an uncertainty in redshift. Therefore there are competing SEDs at similar but not identical redshifts contributing to the total redshift probability distribution.

Common to both above examples is that the position in redshift of the global maximum of the total redshift probability distribution is always compatible with the redshift one would derive by looking at the probability distribution of the most likely SED.

Thirdly, an early-type object at low redshift ($z \simeq 0.38$). In this case the ultraviolet part of the SED is even less constrained, yielding a larger number of competing template SEDs.

The fourth panel in Figure 7.3 shows an object best fit by the SED of an M2 star. We have used a criterion based on a comparison of the best χ^2 for redshifted galaxy template SEDs and stellar SEDs to discriminate between star and galaxies, to test the robustness of the morphological and colour based star-galaxy separation presented in MUNICS I, hoping to be able to improve the procedure at faint magnitudes. The main problem hereby is the lack of reliable SEDs for cool stars with the necessary broad wavelength coverage. Using only this SED based star-galaxy separation instead of the morphological method does not change the results of this work. Note that we present an independent measure of the reliability of our star-galaxy separation in Chapter 3, where we test it against blind spectroscopy.

The photometric redshift histograms for MUNICS_K, MUNICS_I and MUNICS_B can be found in Figure 7.4. Note the high redshift tails in the distributions for MUNICS_K and MUNICS_B, caused by luminous red galaxies at $1 \lesssim z \lesssim 2$ and the ultraviolet emission of blue galaxies shifted into the B band, respectively. In contrast to these distributions the redshift histogram for MUNICS_I shows a rather sharp redshift cut-off at $z \sim 1.25$. A comparison with the deeper I -selected catalog for the FORS Deep Field (FDF; Heidt *et al.* 2003, Gabasch *et al.* 2004a) cut at the limiting I -band magnitude of MUNICS_I shows a similar distribution (upper right-hand panel in Figure 7.4). The reason for this is that at $m_{\text{lim}}^I \simeq 23$ mag, the limiting magnitude of MUNICS_I, we miss red galaxies at $z \lesssim 1$. These are present in MUNICS_K ($m_{\text{lim}}^K \simeq 19$ mag), but have $I - K$ colours up to 5. Obviously, these objects are too faint in the I band to be detected in MUNICS_I. On the other hand, the high-redshift population of blue galaxies escapes detection because their emission peak in the ultraviolet is still blue ward of the I band.

The redshift distributions presented in Figure 7.4 can be fitted by an analytic function as shown by Brainerd *et al.* (1996). For a normalised redshift distribution, this formula reads:

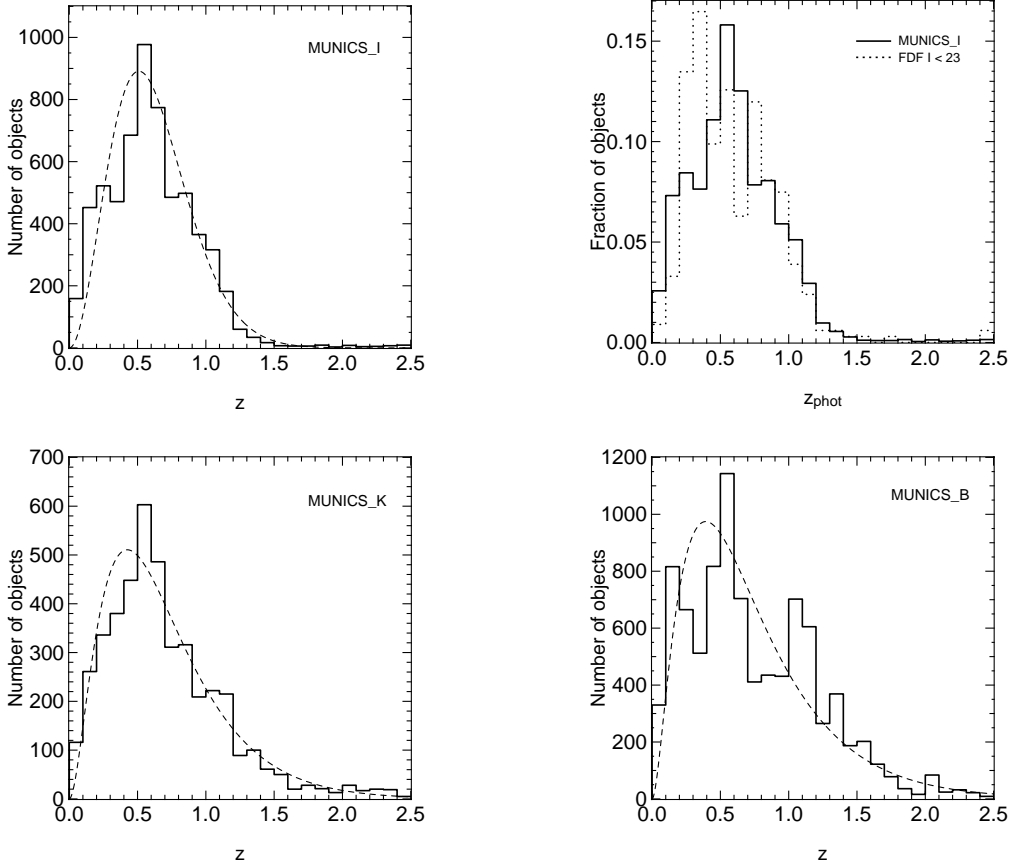


Figure 7.4: *Upper left-hand panel:* Histogram of photometric redshifts for MUNICS_I. *Upper right-hand panel:* Comparison of the redshift distribution in the I -band selected MUNICS catalogue to the one of a $I < 23$ sample from the FORS Deep Field (FDF; Heidt *et al.* 2003, Gabasch *et al.* 2004a). *Lower left-hand panel:* Histogram of photometric redshifts in MUNICS_K. *Lower right-hand panel:* Histogram of photometric redshifts in MUNICS_B.

$$f(z) = \frac{dN}{dz} = \frac{\beta z^2}{\Gamma(3/\beta)z_0^3} \exp\left(-\left(\frac{z}{z_0}\right)^\beta\right) \quad (7.1)$$

The parameters β and z_0 of the best-fitting function for the redshift distributions of the K , I and B selected catalogues can be found in Table 7.2, while the corresponding functions are shown in comparison to the redshift distributions in Figure 7.4.

It is also interesting to compare the photometric redshift of an object in the I -selected (B -selected) catalogue to its photometric redshift in the K -selected (I -selected) catalogue. In a perfect world, the two should be the same, but small differences in object centring and differences in the object's shape in the K and the I image lead to slightly different photometry. Hence the result is a scatter around the one-to-one relation, as shown in Figure 7.6. However, the general agreement is extremely good,

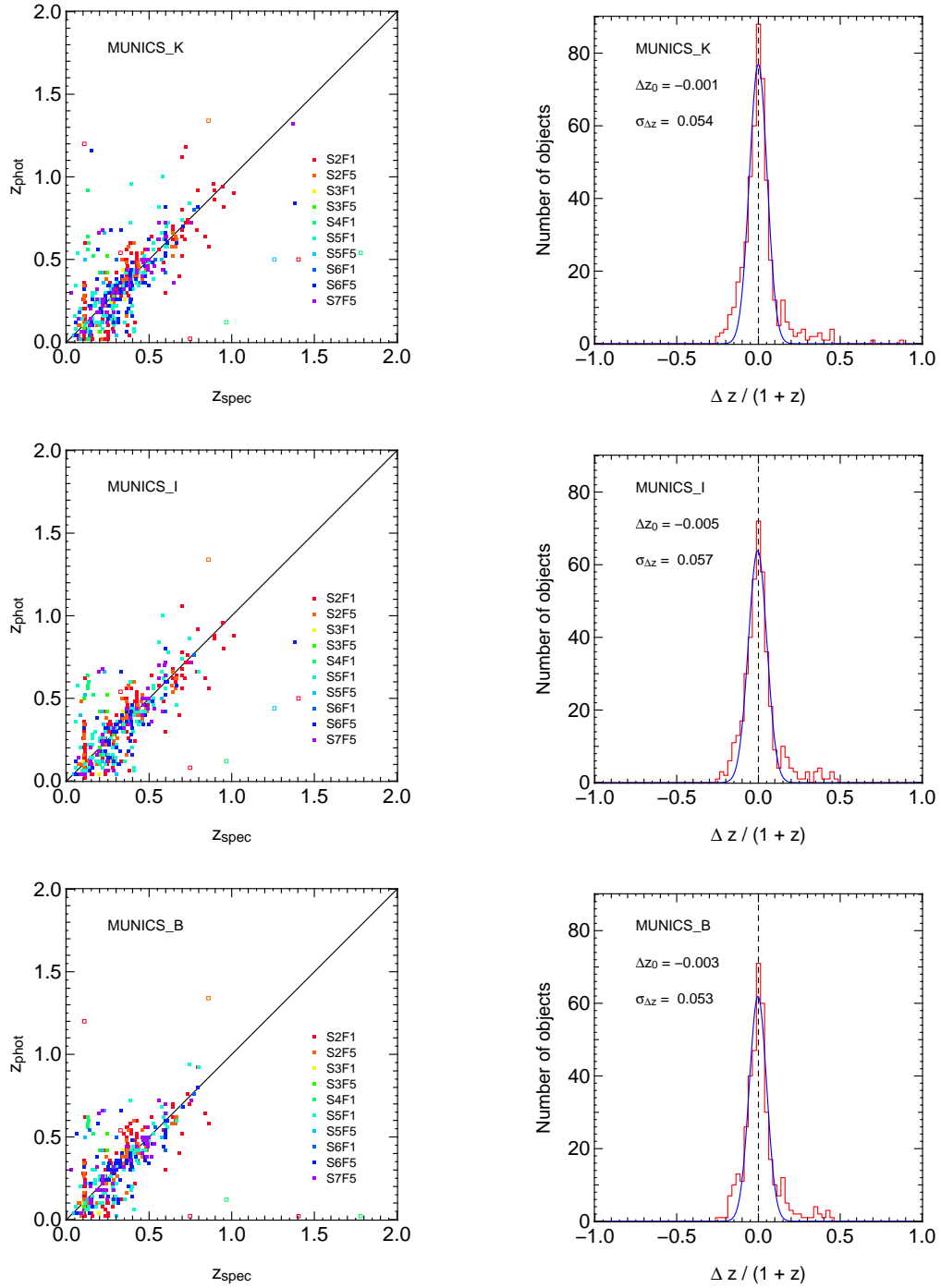


Figure 7.5: *Left-hand panels:* A comparison of photometric and spectroscopic redshifts MUNICS_K (*top*), MUNICS_I (*middle*) and MUNICS_B (*bottom*). Filled symbols are galaxies, open symbols quasars. *Right-hand panels:* The corresponding histogram of the redshift differences together with a Gaussian fit showing the quality of the photometric redshifts.

Table 7.2: Parameters z_0 and β of the best-fitting analytic approximation to the redshift histogram using the functional form described by Brainerd *et al.* (1996), as well as the number of galaxies N_{galaxies} in each catalogue and the first $M_1 = \bar{z} \equiv \sum z f(z)$, second $M_2 \equiv \sum (z - \bar{z})^2 f(z)$ and third $M_3 \equiv \sum (z - \bar{z})^3 f(z)$ moments of the redshift distribution, essentially characterising the mean, the width and the skewness of the distribution.

Catalogue	N_{galaxies}	z_0	β	M_1	M_2	M_3
MUNICS_K	4467	0.159	0.859	0.700	0.191	0.111
MUNICS_I	6180	0.445	1.617	0.613	0.080	0.015
MUNICS_B	9064	0.094	0.717	0.738	0.257	0.207

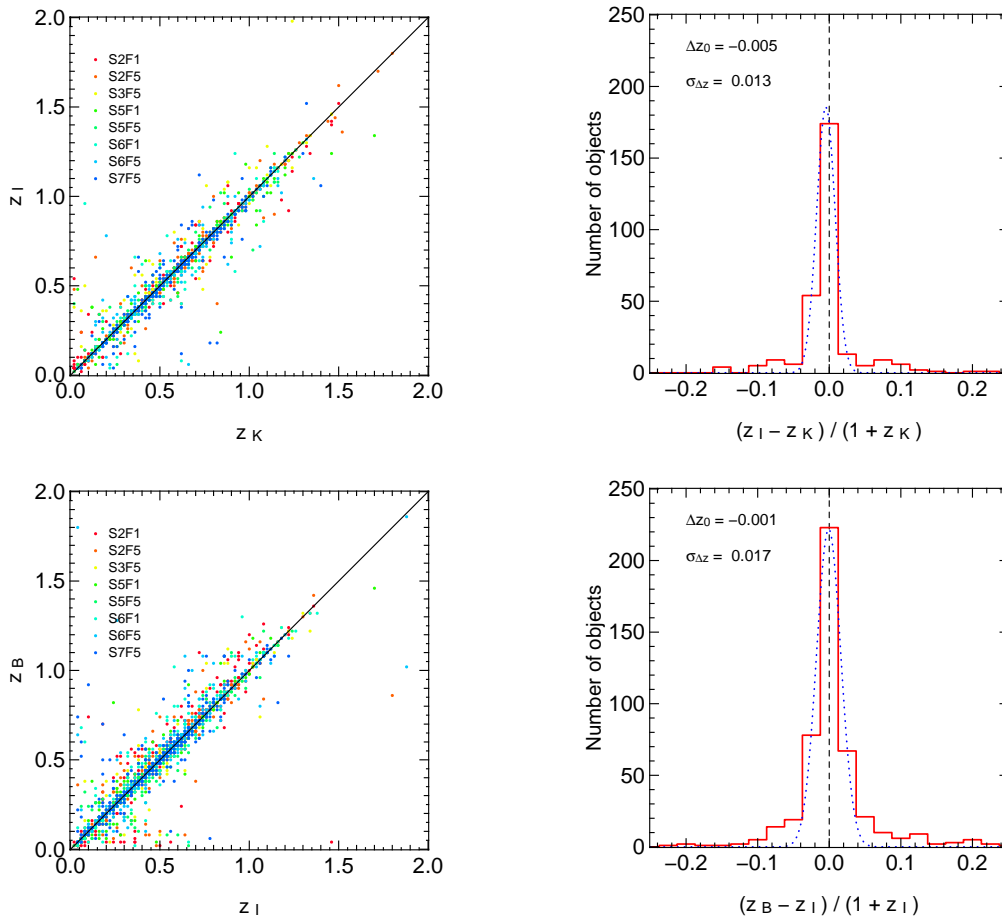


Figure 7.6: *Upper left-hand panel:* A comparison of photometric redshifts from the I -selected MUNICS catalogue to those from the K -selected MUNICS sample ($K \leq 19$). *Upper right-hand panel:* The histogram of the redshift differences together with a Gaussian fit showing the quality of the photometric redshifts. *Lower left-hand panel:* Comparison of photometric redshifts from MUNICS_I and MUNICS_B. *Lower right-hand panel:* The corresponding histogram.

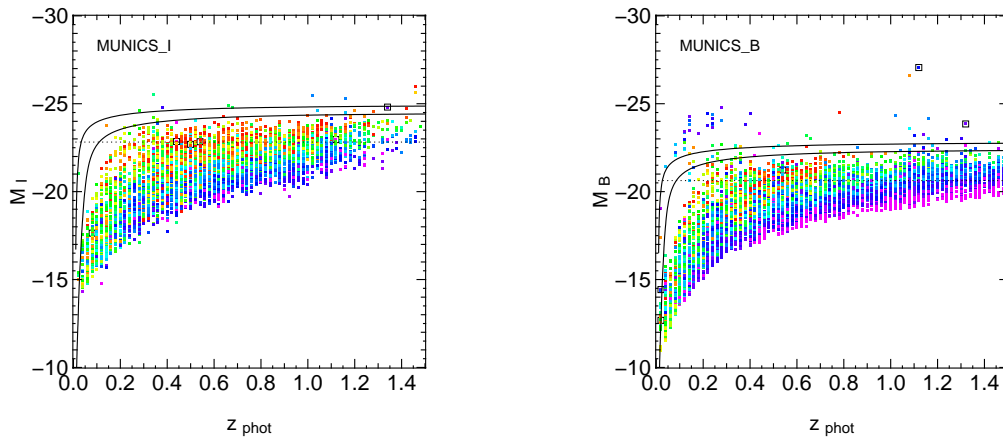


Figure 7.7: Plot of the absolute magnitude M_I versus the photometric redshift z_{phot} for MUNICS_I (left-hand panel) and of M_B versus z_{phot} for MUNICS_B (right-hand panel). The different colours denote the different model SEDs, where the colour corresponds roughly to the model colour, i.e. early-type galaxies are shown in red, late-type galaxies in blue. The dotted line indicates the local value of M^* . The solid lines are the contours corresponding to 1 and 10 expected objects (see text for details). Objects spectroscopically classified as active galactic nuclei (AGN) are additionally marked as open squares

as can be seen from the histogram of redshift differences also shown in the Figure.

Finally, in Figure 7.7 we show the distribution of absolute I magnitude versus photometric redshift for different model SEDs, ranging from early types (redder colours) to late types (bluer colours). The distribution of objects is caused by three effects:

1. The more or less horizontal cut-off at high luminosities represents the sharp drop of the Schechter luminosity function for luminous objects. We can test whether this is in agreement with expectations using the following method. The number of expected objects $N_{\text{obj}}(M, z)$ as a function of absolute magnitude M and redshift z is the product of the survey's solid angle A , the comoving volume element dV/dz and the luminosity function $\Phi(M)$:

$$N_{\text{obj}} = A \frac{dV}{dz} \Phi(M) dz dM \quad (7.2)$$

Using the local Schechter parameters from Blanton *et al.* (2001) and converting them to Vega magnitudes and a standard cosmology ($\Omega_M = 0.3$, $\Omega_\Lambda = 0.7$, $H_0 = 70 \text{ km s}^{-1} \text{ Mpc}^{-1}$), we can derive these expected numbers. In the Figure, we show the contours of 1 and 10 expected objects in intervals of 1 in M and 0.1 in z , respectively, and it is obvious that there is reasonable agreement with the actual distribution of objects.

It is also clear from these diagrams that the characteristic luminosity M^* must become brighter with redshift since one can clearly see a tilt in the high-luminosity cut-off of the object distribution.

2. The curved edge at low luminosities is due to the fact that we have a magnitude-limited sample.
3. The depleted region at low redshifts and medium to high luminosities is a volume effect. At these redshifts, the volume is small, and since luminous objects are very rare, we do not see them in our survey.

The objects with very high B -band luminosity in MUNICS_B (see right-hand panel of Figure 7.7) are likely to be active galactic nuclei (AGN). Indeed, spectroscopically identified AGN are marked in the Figure, and they are found in this region of the diagram. Note that the number of spectroscopic AGN is small, and they are mostly drawn from a sample of AGN selected for their red colour. One would expect a larger number of AGN in a B -selected sample because of their blue colours.

7.3 Star–Galaxy Separation

For computing statistical properties of the field-galaxy population like its luminosity function, it is necessary to remove all stars from the analysis. In a photometric catalogue, this can be done in two ways. Either by looking at an object’s morphology in the image, i.e. whether it appears to be similar to the point-spread function (PSF) of the image or extended, or by looking at the spectral energy distribution (SED), in this case as traced by the six-filter photometry, and comparing it to template spectra of stars and galaxies. The disadvantage of the morphological approach is clearly its tendency to fail at fainter magnitudes (because of the lower signal-to-noise ratio and because distant galaxies look more and more compact), while it works reasonably well at brighter magnitudes (see, e.g., MUNICS I).

For this investigation, we decided to take the second route. The photometric redshift technique as described in Section 7.2 compares the photometry in the six MUNICS filters to template SEDs of stars and galaxies. Each fit is assigned a χ^2 value, and we can simply discriminate between stars and galaxies by comparing the χ^2 values of the best-fitting stellar and the best-fitting galactic SED. More specifically, we classify all objects as stars for which $\chi_{\text{star}}^2 < \chi_{\text{galaxy}}^2$.

This procedure can be tested by checking against the spectroscopic sample described in Chapter 5. This is illustrated in Figure 7.8, where we show the χ^2 values of objects spectroscopically classified as stars or galaxies, respectively, both for the I and the B -selected catalogue. Clearly, the SED classifier does work very well.

Note that in all comparisons between MUNICS_K, MUNICS_I and MUNICS_B presented in this Chapter we have used the same χ^2 -based classification method. The corresponding diagram for the K -selected sample can be found in Figure 5.9.

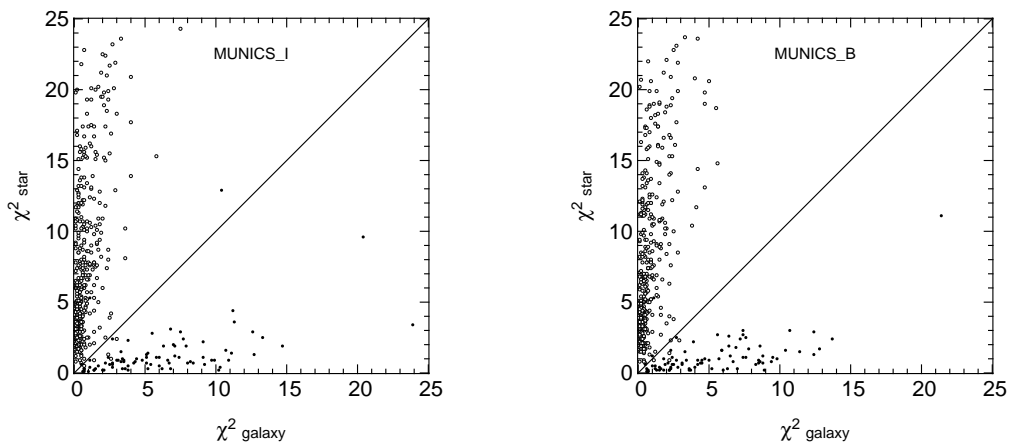


Figure 7.8: This diagram shows the loci of spectroscopically classified galaxies (open circles) and stars (crosses) in a plane defined by the χ^2 values of the best-fitting galactic and stellar spectral-energy distributions (SEDs) for the I -band selected MUNICS catalogue (*left-hand panel*) and the B -band selected sample (*right-hand panel*). The line used to discriminate the two classes is also indicated.

Chapter 8

Galaxy Evolution From Optically Selected MUNICS Catalogues

In the following we want to present optically selected MUNICS catalogues. These contain many more objects than the spectroscopic sample (and than many previous surveys!) and can thus be used to study the evolution of the galaxy population with high statistical accuracy. Furthermore, they can be used to investigate the influence of colour selection effects on galaxy surveys. While most of the surveys done until the 1980's were optically selected (either in the B band or in the I band), we have presented results from a near-infrared selected galaxy catalogue. The I -band and B -band selected galaxy samples from the MUNICS survey presented in this Chapter can be used for comparison with previous work and to study selection effects. Since the MUNICS spectroscopic sample was pre-selected on the K -band photometric catalogue, we have to rely on photometric redshifts to determine distances to galaxies.

In this chapter, the second of the two main science chapters of this thesis, we want to discuss differences between the galaxy populations drawn from the K -band, the I -band and the B -band selected samples. Furthermore, we present measurements of the evolution of luminosity functions, the luminosity density and the star formation rate density. Finally we show an investigation of the connection between star formation and mass for field galaxies at different redshifts. As in the previous chapter, we will often refer to the different catalogues as MUNICS_K, MUNICS_I and MUNICS_B for short.

8.1 Comparison of I - and K -Band Selected Galaxies

We want to investigate the differences of the galaxy populations in K and I -selected samples. One way of doing this is to study rest-frame colour distributions. Cole *et al.* (2001) divided their K -selected sample of local galaxies into three luminosity classes and looked at the distribution of rest-frame $b_J - K_s$ and $J - K_s$ colours. Note that the K -band luminosity is a measure of a galaxy's stellar mass. Their main finding is – not surprising in a way – that at smaller K -luminosities (i.e. smaller masses) there is a more and more prominent population of blue, star forming galaxies. It is interesting to

test this also for higher redshifts and different selection bands.

The red line in the upper left-hand panel of Figure 8.1 shows the $B - K$ rest-frame colour distributions of K -selected MUNICS galaxies at $0 \leq z \leq 1$, confirming the result of Cole *et al.* (2001). Moreover, we present in this Figure the same distributions for I -band selected MUNICS galaxies (green line), showing clearly that the main difference between near-infrared and optically selected samples are the bluer colours of low-luminosity (low-mass) galaxies. This is even more pronounced for the B -selected sample shown as a blue line.

Four conclusions can be immediately drawn from this distributions. Firstly, as already noted by Cole *et al.* (2001), a population of blue, star forming galaxies contributes more strongly at fainter luminosities. Secondly, this populations becomes more numerous at bluer selection wavelengths. Thirdly, the colour distribution seems to be wider at fainter absolute K -band magnitudes (although part of this effect may be attributed to the larger errors in the rest-frame $B - K$ colour for these objects). Fourthly, and maybe most importantly, the colour distributions of high-mass galaxies change very little as a function of redshift. Hence one would not expect much variation of the bright end of the galaxy luminosity function in different *selection* bands like K and I . We will test this in Section 8.2.2.

In the other three panels of Figure 8.1 we present the rest-frame $B - K$ colour distributions in the two redshift intervals $[0.0, 0.5]$ and $[0.5, 1.0]$ for MUNICS_K (upper right-hand panel), MUNICS_I (lower left-hand panel) and MUNICS_B (lower right-hand panel). First, it is very interesting that the colour distributions agree so well for the highest luminosity objects (irrespective of the selection filter). Furthermore, there is a clear trend with redshift in the sense that lower-luminosity objects get bluer. That means that even at redshift $z \sim 1$ the increased star-formation rate is dominated by low-luminosity (low-mass) systems. Finally, it is worth noting that this evolutionary trend with redshift is barely visible in the K -selected sample, clearly evident in the I -selected sample, but gets very large in the B -selected sample: Indeed, for the low-mass objects with $-21.75 > M_K > -23.00$, the shift between redshift $z \sim 0.25$ and $z \sim 0.75$ is $\Delta(B - K) \sim 0.3$ for MUNICS_K, $\Delta(B - K) \sim 0.7$ for MUNICS_I, but as large as $\Delta(B - K) \sim 1.0$ for MUNICS_B!

How can this be interpreted? The rest-frame colour of a galaxy is governed by the age of its stellar population, its star-formation activity, the metallicity and the dust content. Let us neglect the influence of metallicity and dust for the moment. The lack of redshift evolution of the rest-frame colours of high K -band luminosity galaxies over $0 \lesssim z \lesssim 1$ means that these objects must have built up their stellar mass at earlier times. The fact that also at lower K luminosities galaxies of similar rest-frame colour can be found even in the higher redshift bin indicates that also part of the lower mass objects formed early, although the majority of them had (or has) major star-formation activity at $z \lesssim 1$. It is also clear from these colour distributions that the rise of the star-formation rate to redshift unity is mostly driven by lower-mass galaxies.

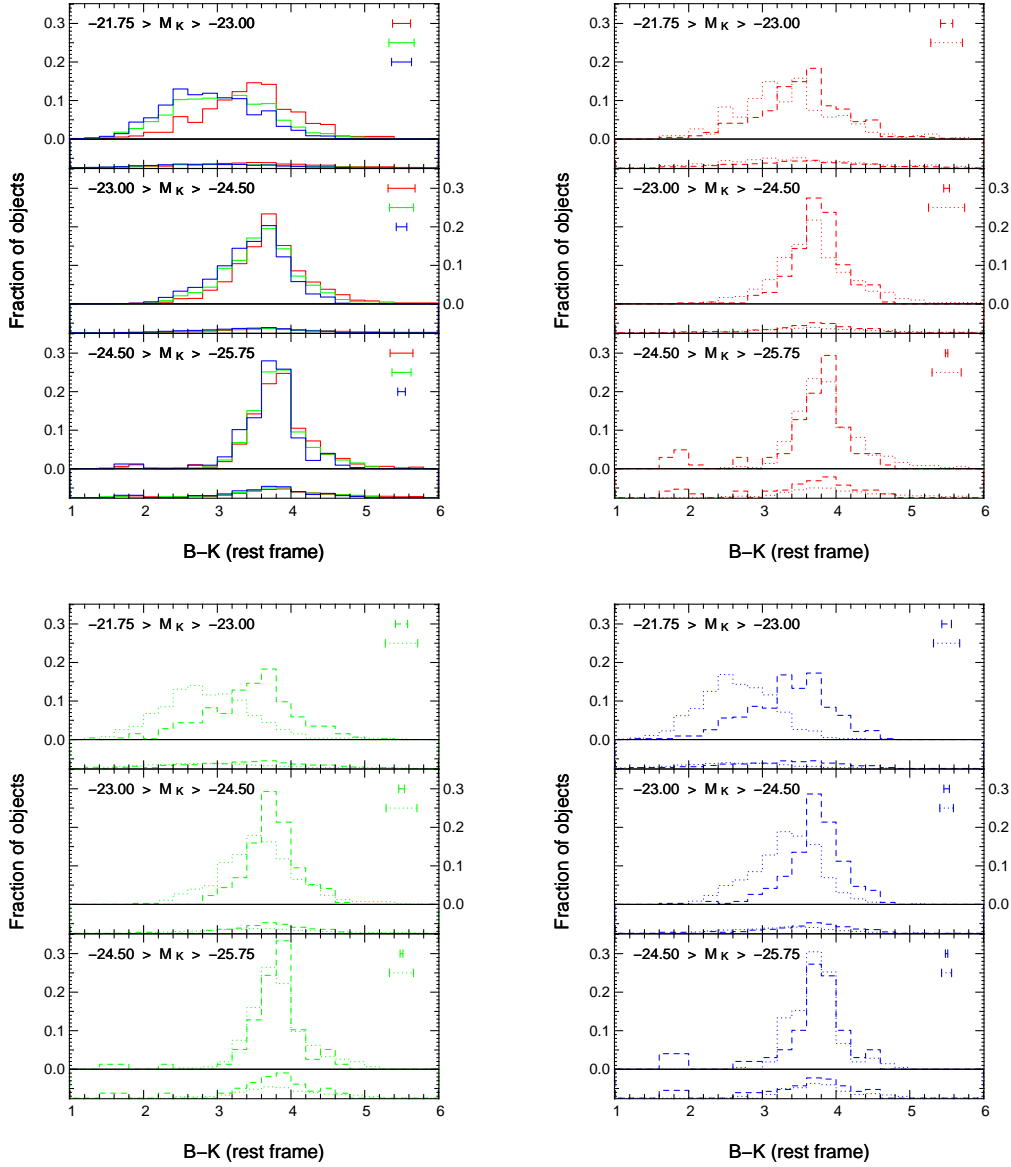


Figure 8.1: Distribution of rest-frame $B - K$ colours for K -selected (red), I -band selected (green) and B -band selected (blue) MUNICS galaxies, divided into three different K -band luminosity classes. *Upper left-hand panel*: All galaxies with $0 \leq z \leq 1$. *All other panels*: Sub-divided into galaxies with $0 \leq z \leq 0.5$ (dashed line) and $0.5 \leq z \leq 1.0$ (dotted line). In each plot, the distribution of Poisson errors is also shown below the object histograms. Furthermore, typical $B - K$ error bars are also indicated in every plot.

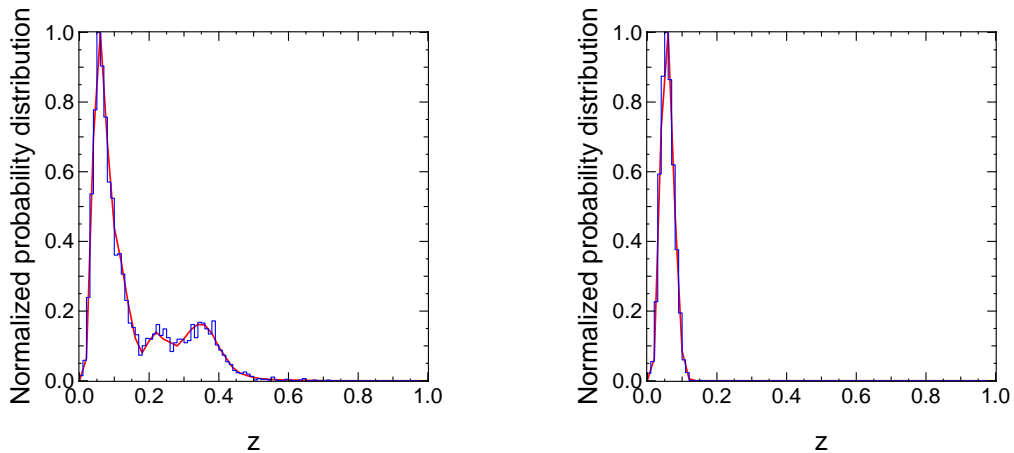


Figure 8.2: Example of a total redshift probability distribution (left-hand panel) and for the probability distribution of the best-fitting galaxy model (right-hand panel) for an object in the I -selected MUNICS catalogue. The histograms in both panels show Monte-Carlo approximations to these distributions after 5000 realisations.

8.2 Luminosity Functions

8.2.1 Computing the Luminosity Function

As for the spectroscopic LF presented in Chapter 6, the LF is computed using the non-parametric V_{\max} formalism (see Section 6.2, Schmidt 1968). In brief, the V^{\max} formalism accounts for the fact that some fainter galaxies are not visible in the whole survey volume. In a volume-limited redshift survey, each galaxy i in a given redshift bin $[z_{\text{lower}}, z_{\text{upper}}]$ contributes to the number density an amount inversely proportional to the volume V_i of the survey:

$$V_i = \int_{z_{\text{lower}}}^{z_{\text{upper}}} \frac{dV}{dz} dz, \quad (8.1)$$

where $dV = d\Omega r^2 dr$ is the comoving volume element and $d\Omega$ is the solid angle covered by the survey. However, due to the fact that we have to deal with magnitude-limited surveys, a faint galaxy may not be visible in the whole survey volume. Assuming that in a survey with given limiting magnitude galaxy i can be seen out to redshift z_{\max} , we have to correct the volume factor by V_i^{\max}/V_i , where

$$V_i^{\max} = \int_{z_{\text{lower}}}^{\min(z_{\text{upper}}, z_{\max})} \frac{dV}{dz} dz. \quad (8.2)$$

Obviously, we have $z_{\max} \geq z_{\text{upper}}$ for a galaxy which is bright enough to be seen in the whole volume in investigation, and the correction factor is one. Otherwise, $z_{\max} < z_{\text{upper}}$, and the volume is smaller than the volume corresponding to the redshift range in which we compute the LF.

We have made sure that the effect of the volume correction is of importance only in the faintest bin in absolute magnitude, and that even in this case the correction is small.

Additionally, the contribution of each galaxy i is weighted by the inverse of the detection probability $P(m_{\text{det},i})$ of the parent catalogue. The LF $\Phi(M)$ is then computed according to the formula

$$\Phi(M) dM = \sum_i \frac{V_i}{V_i^{\text{max}}} \frac{1}{V_i} \frac{1}{P(m_{\text{det},i})} dM, \quad (8.3)$$

where the sum runs over all objects i in the redshift range for which we want to calculate the LF. Naturally the volume terms can be simplified to $1/V_i^{\text{max}}$.

We include two effects in the total error budget of the luminosity function. Firstly, the limited number of objects in each magnitude bin produces statistical uncertainties. Secondly, the errors in the photometric redshift estimates have some influence on the luminosity function.

The statistical errors are derived using Poissonian statistics, following the approximations by Gehrels (1986) and Ebeling (2003)¹ for approximation of Poissonian errors for small numbers.

To investigate the influence of photometric redshift errors on the luminosity function, we perform Monte-Carlo simulations. In these simulations, we take the original input catalogue used for deriving the luminosity function, and assign to each object a redshift within the redshift error distribution given by the photometric-redshift algorithm. The shape of this probability distribution is taken into account as shown in Figure 8.2. In principle, there are two ways of doing this. Either one uses the redshift probability distribution of the best-fitting SED (right-hand panel in Figure 8.2, or the sum of the probability distributions of all SEDs (the total probability distribution) as shown in the left-hand panel of the figure. One might expect the total probability distribution to have the advantage that it accounts better for systematic uncertainties in the SED fitting. However, we have carried out careful tests which show that the errors derived from the total distribution are not significantly different from the ones for the best distribution. This is most likely due to the fact that the probability distribution for the best-fitting SED usually dominates the total distribution. Since the total distribution also takes more Monte-Carlo realisations to converge, we decided to use the probability distribution of the best-fitting SED for our simulations.

The errors are then computed as follows. The Poisson error and the standard deviation around the mean derived from the Monte-Carlo simulations are summed quadratically. In addition, any difference between the measured value for the LF in a magnitude bin and the mean from the Monte-Carlo simulations is considered a measure of systematic errors. This is also added quadratically, but only in one direction, i.e. if the Monte-Carlo mean is higher than the measured value the upper error bar is enlarged,

¹Note that MNRAS managed to mess up Table 1 in Ebeling (2003), where, for the positive coefficients, the exponent was replaced by the leading digit. However, the correct values can be obtained from the preprint version `astro-ph/0301285` (Ebeling, private communication), or now from an Erratum (Ebeling 2004).

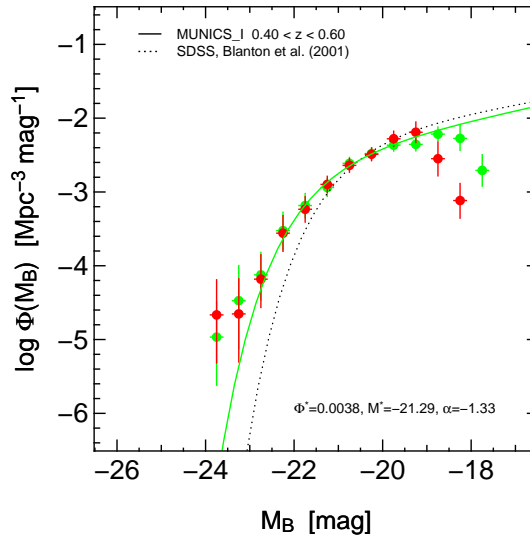


Figure 8.3: The influence of the selection band on the LF. We compare the B -band LF at redshift $z = 0.5$ derived from the I -selected MUNICS catalogue (green symbols and green line) to the one derived from the K -selected catalogue (red symbols). The agreement is obviously very good. As a reference we also show the local SDSS B -band LF (Blanton *et al.* 2001, dotted line).

but not the lower one. All our χ^2 fitting routines, both for the Schechter parameters and for the LF evolution, can handle asymmetric errors.

8.2.2 The Influence of the Selection Band

One important application of catalogues selected in different wavelength regimes is a test of the influence of selection effects on statistical quantities like the luminosity function (LF). To illustrate these effects, we show in Figure 8.3 as a typical example the comparison of B -band LFs at redshift $z = 0.5$ from the K and I -band selected catalogues. It is evident that the LFs agree very well at the bright end. At the faint end, the agreement is still very good, but it is also clear that the I -selected data reach to fainter B -band luminosities than the K -band data. Thus, to the MUNICS depths, the influence of the detection band even on optical LFs is not dramatic. This is in agreement with our expectations from the rest-frame colour distributions presented in Section 8.1.

8.2.3 Luminosity Function from the I -Selected Sample

In this Section we present luminosity functions from the I -selected MUNICS sample at redshifts $z \simeq 0.5$, $z \simeq 0.7$, $z \simeq 0.9$ and $z \simeq 1.1$. The B -band luminosity function results are presented in Figures 8.4 and 8.5, the I -band LF in Figures 8.6 and 8.7, and the K -band LF in Figures 8.8 and 8.9.

We summarise the parameters Φ^* , M^* and α of the Schechter fits in Table 8.1.

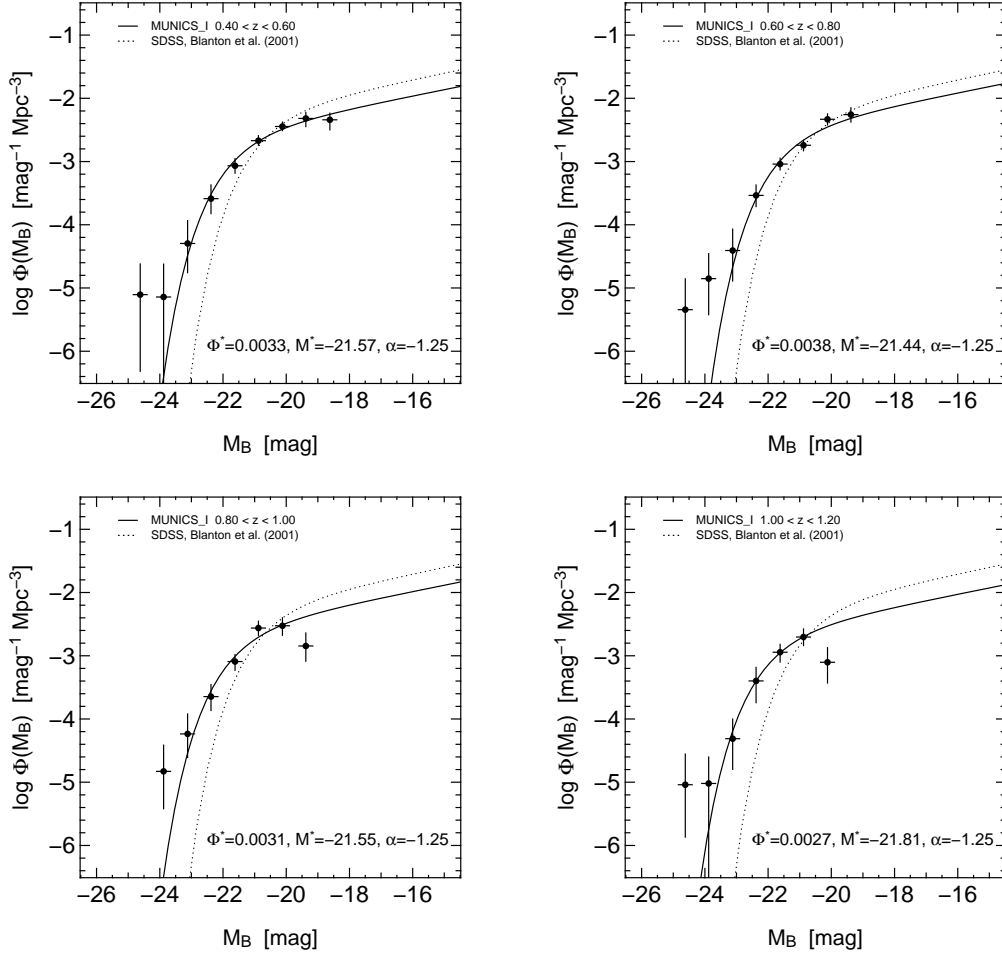


Figure 8.4: The B -band LF from the I -selected catalogue at redshifts $z = 0.5$ (*upper left-hand panel*), $z = 0.7$ (*upper right-hand panel*), $z = 0.9$ (*lower left-hand panel*) and $z = 1.1$ (*lower right-hand panel*). One can clearly see the effect of brightening and decreasing number density with increasing redshift z .

Note that we have kept the faint-end slope α fixed to the local value during the fitting process since the MUNICS data do not constrain the slope very well.

8.2.4 Luminosity Function Evolution

To estimate the rate of evolution of the Schechter parameters Φ^* and M^* with redshift, we define evolution parameters π and μ as follows:²

²Our parametrisation is identical to the one chosen in Gabasch *et al.* (2004a) (with parameters a and b) and equivalent to the form $\Phi \propto (1+z)^P$, $L \propto (1+z)^Q$ sometimes found in the literature (especially in the context of radio-source evolution). The parameters translate as follows:

$$\pi = b = P \quad \text{and} \quad \mu = a = -\frac{2.5Q}{\ln 10}. \quad (8.4)$$

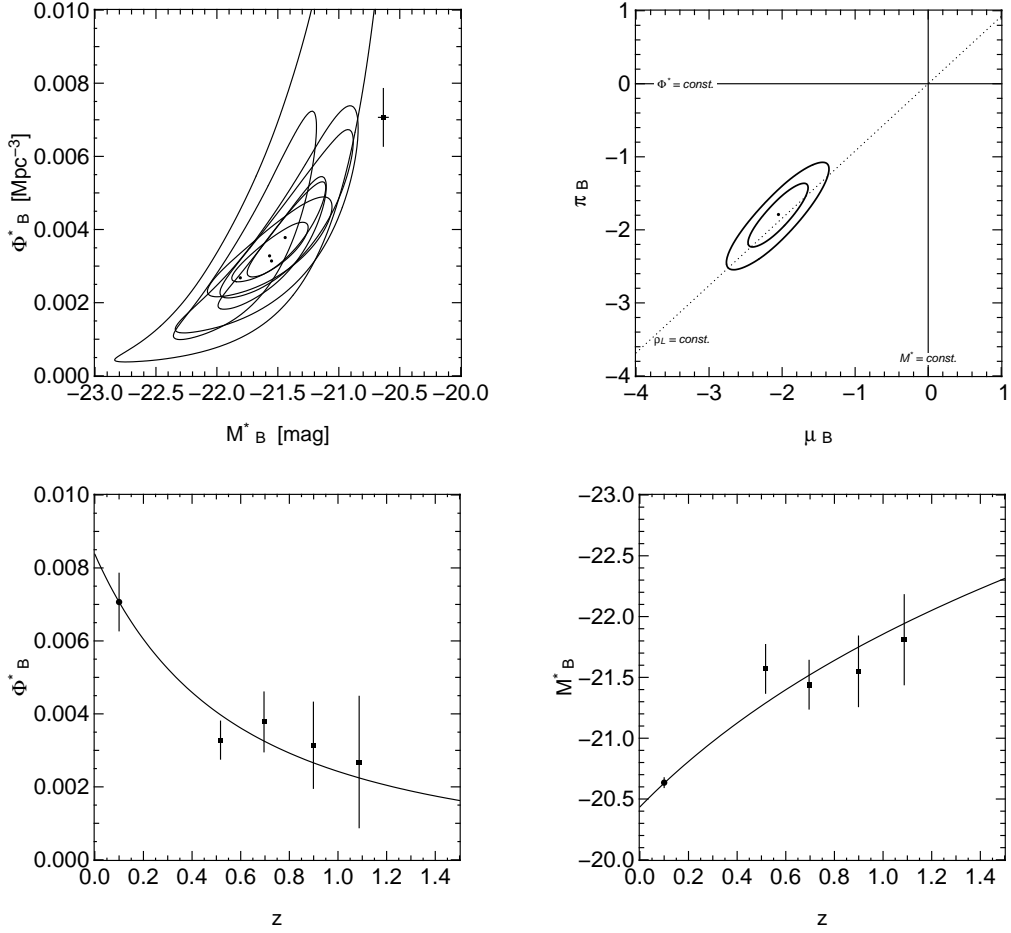


Figure 8.5: The B -band LF from the I -selected catalogue: Schechter contours (*upper left-hand panel*), evolutionary parameters (*upper right-hand panel*), Φ^* versus z (*lower left-hand panel*) and M^* versus z (*lower right-hand panel*).

$$\begin{aligned}
 \Phi^*(z) &= \Phi^*(0) (1+z)^\pi, \\
 M^*(z) &= M^*(0) + \mu \ln(1+z), \text{ and} \\
 \alpha(z) &= \alpha(0) \equiv \alpha.
 \end{aligned}
 \tag{8.5}$$

As local comparison we use the LFs from the Sloan Digital Sky Survey (SDSS; York *et al.* 2000) presented in Blanton *et al.* (2001). (We do not use the LFs presented in Blanton *et al.* (2003).) We show the resulting evolutionary estimates for the I -selected MUNICS catalogue and the LF in the rest-frame B , I and K filter in Figure 8.10. The corresponding values for the evolutionary parameters π and μ can be found in Table 8.2.

We find 2σ evidence for evolution in Φ^* for all filters, and the same for evolution in M^* except for the K band, where the M^* is compatible with no evolution within 2σ .

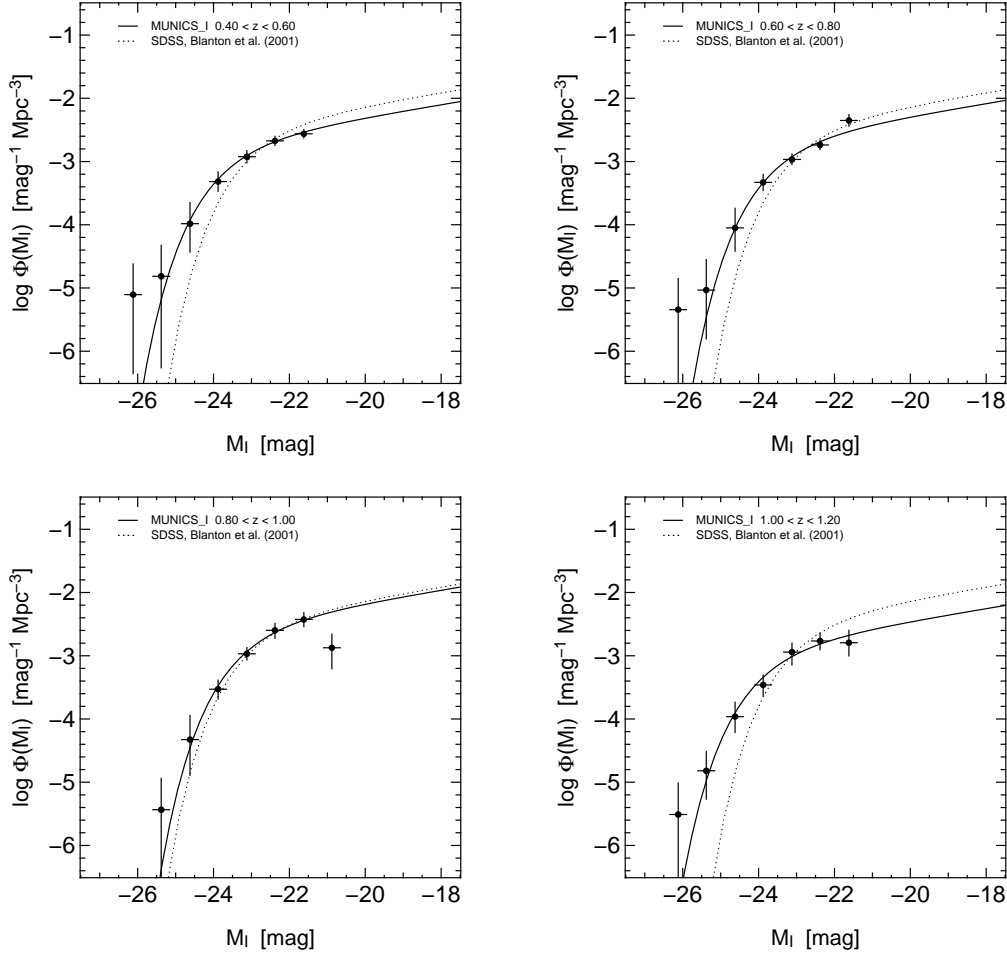


Figure 8.6: The I -band LF from the I -selected catalogue at redshifts $z = 0.5$ (*upper left-hand panel*), $z = 0.7$ (*upper right-hand panel*), $z = 0.9$ (*lower left-hand panel*) and $z = 1.1$ (*lower right-hand panel*). One can clearly see the effect of brightening and decreasing number density with increasing redshift z .

Also, there is a clear trend in the sense that the evolution becomes stronger in bluer pass-bands. In the Figure we also show the line of constant luminosity density ρ_L . The evolution of the LF parameters seems to follow this relation rather closely, however, the luminosity density (as derived from the Schechter function!) in the B band seems to increase slightly with redshift while the one in the K band decreases mildly.

We would like to compare our results for the redshift evolution of the LF to other studies in a qualitative way. At the lowest redshifts, Loveday (2004) used the SDSS (York *et al.* 2000) data to study the evolution of the optical LF from $z = 0$ to $z = 0.3$. He claims to see strong evolution over this redshift interval with an increase of the number density of bright galaxies by a factor of ≈ 3 . Unfortunately, our survey's volume at low redshifts is too small to study this in more detail.

Other authors have studied the evolution of the LF from optically selected, al-

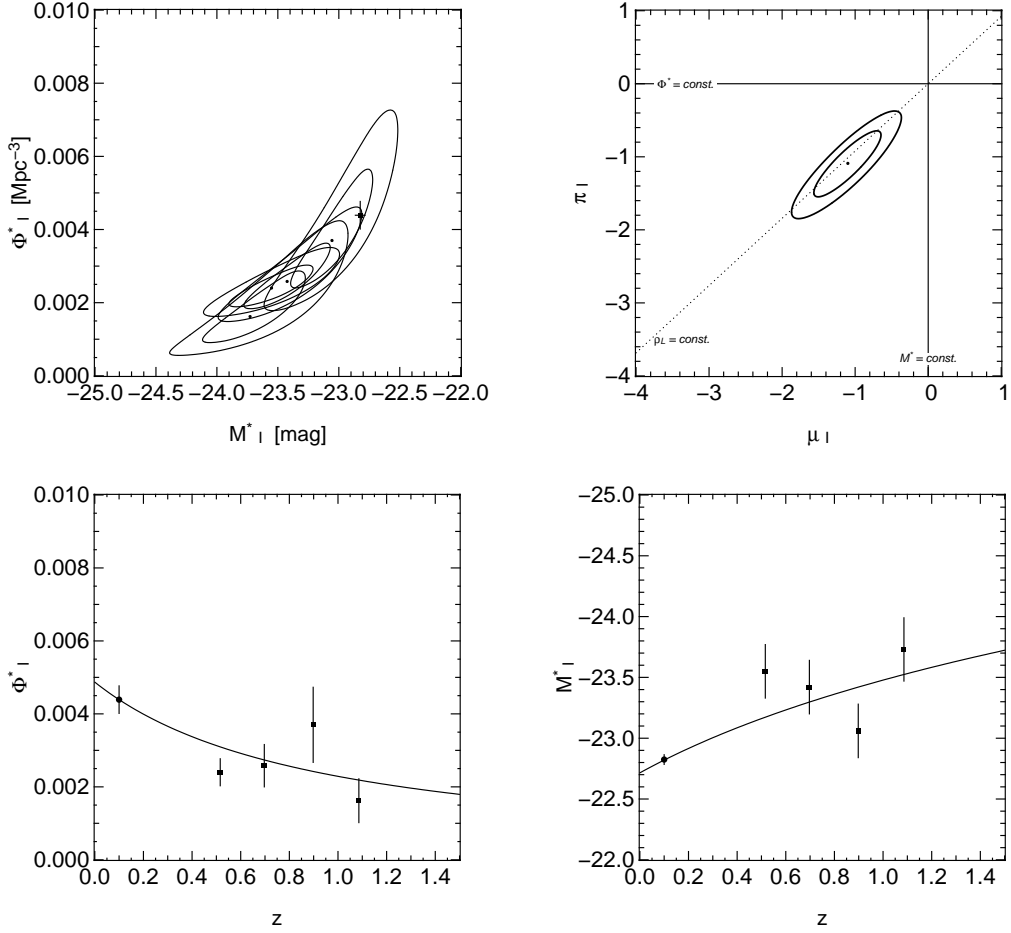


Figure 8.7: The I -band LF from the I -selected catalogue: Schechter contours (*upper left-hand panel*), evolutionary parameters (*upper right-hand panel*), Φ^* versus z (*lower left-hand panel*) and M^* versus z (*lower right-hand panel*).

though much smaller samples to $z \sim 1$, most notably Lilly *et al.* (1995c) from an I -band selected spectroscopic survey, showing reasonable agreement with our results. Type-dependent LF estimates were presented by, e.g., Lin *et al.* (1999), Wolf *et al.* (2003).

The same evolutionary trend for the LF can be seen out to higher redshifts: Gabasch *et al.* (2004a, b), Gabasch (2004) use the deep I -band selected FORS Deep Field (FDF; Heidt *et al.* 2003) to trace the evolution of the LF from the ultraviolet to the near-infrared out to redshifts $z \sim 5$ finding similar results to the ones presented here. That dataset is complimentary to our catalogue, since the FDF lacks the large local volume of MUNICS which allows us to study the lower redshift part of the evolution with high statistical accuracy. Ilbert *et al.* (2004) studied optical LFs from the VIMOS-VLT Deep Survey (Le Fèvre *et al.* 2004) and found similar results.

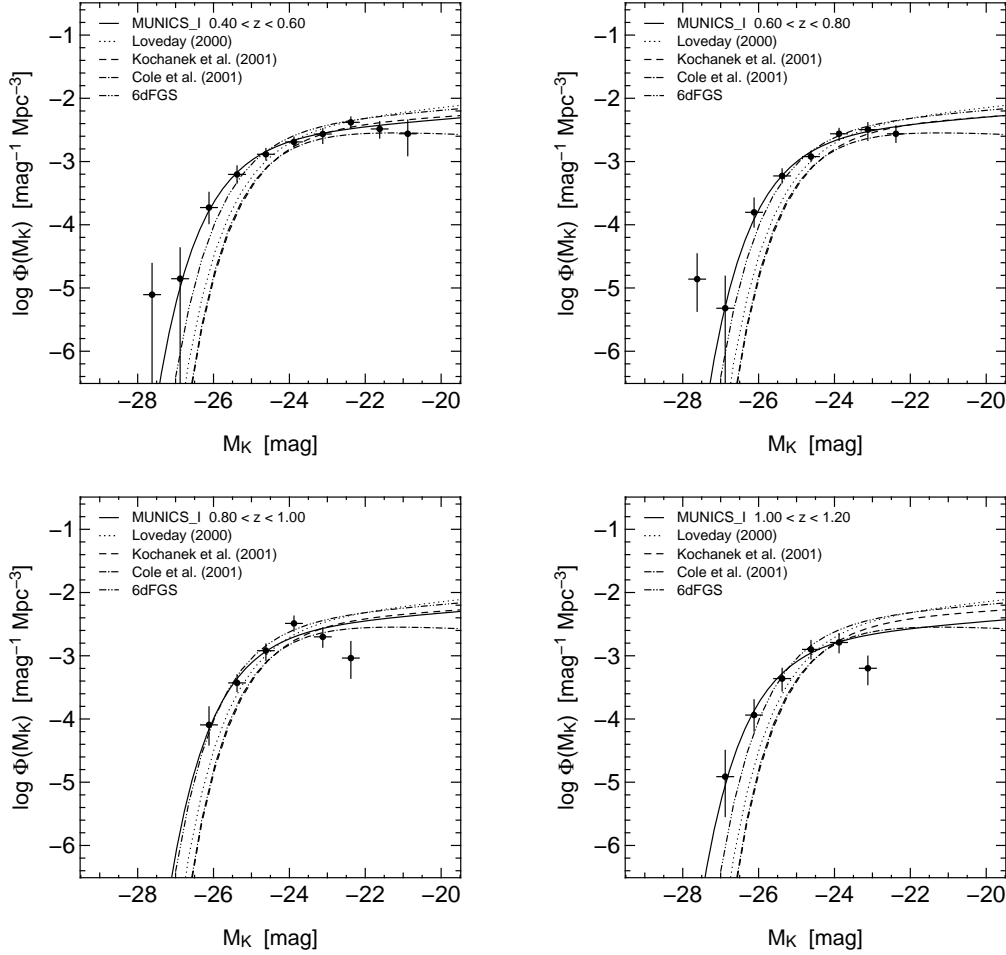


Figure 8.8: The K -band LF from the I -selected catalogue at redshifts $z = 0.5$ (*upper left-hand panel*), $z = 0.7$ (*upper right-hand panel*), $z = 0.9$ (*lower left-hand panel*) and $z = 1.1$ (*lower right-hand panel*). One can clearly see the effect of brightening and decreasing number density with increasing redshift z .

8.3 The Galaxy Luminosity Density

It is also interesting to follow the redshift evolution of the luminosity density in different wavebands. The luminosity density ρ_L is defined as the integral of the luminosity function $\Phi(L)$, i.e.

$$\rho_L = \int_0^{\infty} L \Phi(L) dL. \quad (8.6)$$

For a Schechter-type luminosity function as defined in equation (1.22) with parameters Φ^* , M^* and α the luminosity density can be simply computed from

$$\rho_L = \Phi^* L^* \Gamma(\alpha + 2) \quad (8.7)$$

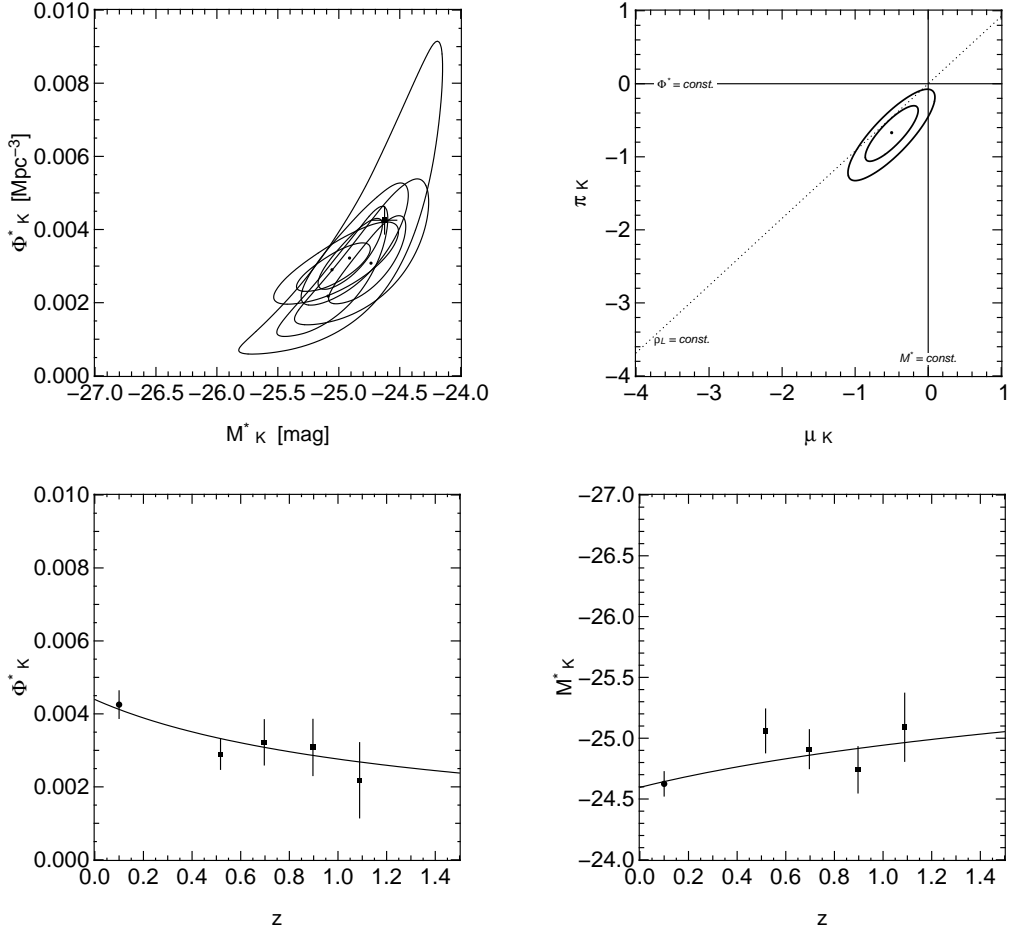


Figure 8.9: The K -band LF from the I -selected catalogue: Schechter contours (*upper left-hand panel*), evolutionary parameters (*upper right-hand panel*), Φ^* versus z (*lower left-hand panel*) and M^* versus z (*lower right-hand panel*).

where Γ is the gamma function. Hence there are two different ways for computing ρ_L . One could either fit a Schechter function to the measured luminosity function data and then calculate the luminosity density following equation (8.7), or one can simply sum up the binned luminosity function values. For the second case one has to correct for incomplete sampling of the LF at the faint end: Assume that we can measure the LF reliably for luminosities larger than L_{lim} . Then we would add up all the LF values with $L \geq L_{\text{lim}}$ and correct the measured luminosity density by a factor based on the Schechter fit to the LF:

$$\rho_L = \left(\frac{\int_0^\infty L \Phi(L) dL}{\int_{L_{\text{lim}}}^\infty L \Phi(L) dL} \right) \sum_{L \geq L_{\text{lim}}} \Phi(L) \Delta L. \quad (8.8)$$

We have performed both calculations and show both the ‘directly summed’ and

Table 8.1: Schechter parameters Φ^* and M^* and α for the LFs in the B , I and K band derived from MUNICS_I.

$\langle z \rangle$	Φ^* [10^{-3} Mpc^{-3}]	M^* [mag]	α	M_{lim} [mag]	$\min(\chi_{\text{red}}^2)$
<i>B</i> -band LF:					
0.5	3.28 ± 0.52	-21.57 ± 0.20	-1.25	-18.0	0.60
0.7	3.78 ± 0.82	-21.44 ± 0.20	-1.25	-19.0	1.16
0.9	3.14 ± 1.18	-21.55 ± 0.29	-1.25	-20.0	1.17
1.1	2.68 ± 1.80	-21.81 ± 0.37	-1.25	-21.0	0.71
<i>I</i> -band LF:					
0.5	2.40 ± 0.37	-23.55 ± 0.22	-1.25	-20.0	0.27
0.7	2.58 ± 0.58	-23.42 ± 0.22	-1.25	-21.0	1.10
0.9	3.70 ± 1.03	-23.06 ± 0.22	-1.25	-21.0	0.31
1.1	1.62 ± 0.60	-23.73 ± 0.26	-1.25	-22.0	0.52
<i>K</i> -band LF:					
0.5	2.90 ± 0.42	-25.06 ± 0.18	-1.12	-22.0	0.45
0.7	3.22 ± 0.62	-24.91 ± 0.16	-1.12	-23.0	0.83
0.9	3.08 ± 0.77	-24.74 ± 0.19	-1.12	-23.0	1.24
1.1	2.18 ± 1.03	-25.09 ± 0.28	-1.12	-24.0	0.28

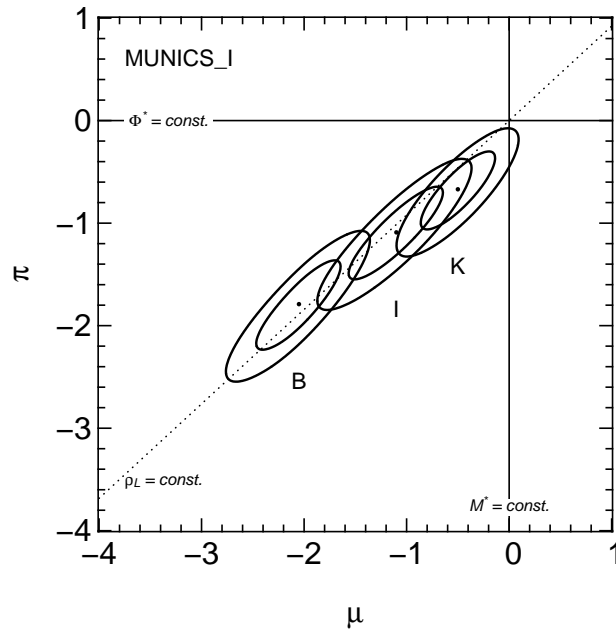


Figure 8.10: Estimates for the evolutionary parameters π and μ (1σ and 2σ contours) for the B -, I - and K -band LFs computed on MUNICS_I. The solid lines show constant Φ^* and M^* , respectively, the dotted line indicates constant luminosity density, i.e. $\pi = \frac{\ln 10}{2.5} \mu \simeq 0.921 \mu$.

Table 8.2: Parameters π and μ for the evolution of the LFs in the B , I and K band derived from MUNICS_I.

Filter	π	μ	$\min(\chi_{\text{red}}^2)$
B	-1.76 ± 0.24	-2.03 ± 0.23	1.24
I	-1.00 ± 0.27	-1.05 ± 0.28	1.07
K	-0.62 ± 0.20	-0.48 ± 0.20	1.07

the ‘LF derived’ value for the luminosity density ρ_L . Our results are presented in Figure 8.11

In the ultraviolet, there is a marked increase in the luminosity density to redshift one, and a slightly slower increase thereafter. In the B band the trend is very similar with clearly shallower slope at $z < 1$ and a plateau at $z \simeq 1$. The luminosity density in the I filter is then more or less flat, and in K there might even be a small decrease in ρ_L . The behaviour observed in B , I and K agrees with the evolutionary trend of the luminosity function as shown in Figure 8.10, where the most likely evolutionary parameters for B , I and K are slightly above, just on and slightly below the line of constant ρ_L , respectively.

8.4 The Star-Formation Rate Density as a Function of Redshift

The star formation rate density (SFRD) as a function of redshift has developed into a powerful tool to investigate the build-up of stellar mass in galaxies. Defined as the integrated star formation rate (SFR) per unit comoving volume, the SFRD $\dot{\rho}_*$ has been used to study star formation activity in galaxy populations out to $z \sim 6$ (e.g. Lilly *et al.* 1996, Madau *et al.* 1996, 1998, Steidel *et al.* 1999b, Bouwens *et al.* 2004, Gabasch *et al.* 2004c). In all these studies, the SFR is determined either from the UV continuum luminosity (Madau *et al.* 1998) or from emission line fluxes (Kennicutt 1992, Rosa-González *et al.* 2002).

There has been some debate in the literature about the slope of the SFRD at low redshifts which can be described as

$$\dot{\rho}_*(z) = \sigma (1+z)^\zeta \quad (\text{power-law model}) \quad (8.9)$$

where σ , the SFRD at $z = 0$, and ζ are free parameters. While some argue for a steep rise as $\zeta \simeq 4$ (Lilly *et al.* 1996, Tresse *et al.* 2002), others find a much shallower slope of $\zeta \simeq 1.7$ (Cowie *et al.* 1999, Sullivan *et al.* 2000) (see the summary in Table 8.3). We will try to answer this question with our large sample of galaxies, combined with galaxies from the FORS Deep Field project (Heidt *et al.* 2003).

The low-redshift slope of the SFRD is also important as a test of galaxy formation models. Recently, Hernquist & Springel (2003) (HS2003 hereafter) have proposed an analytical model for the SFRD based on hydrodynamic simulations. They identify two

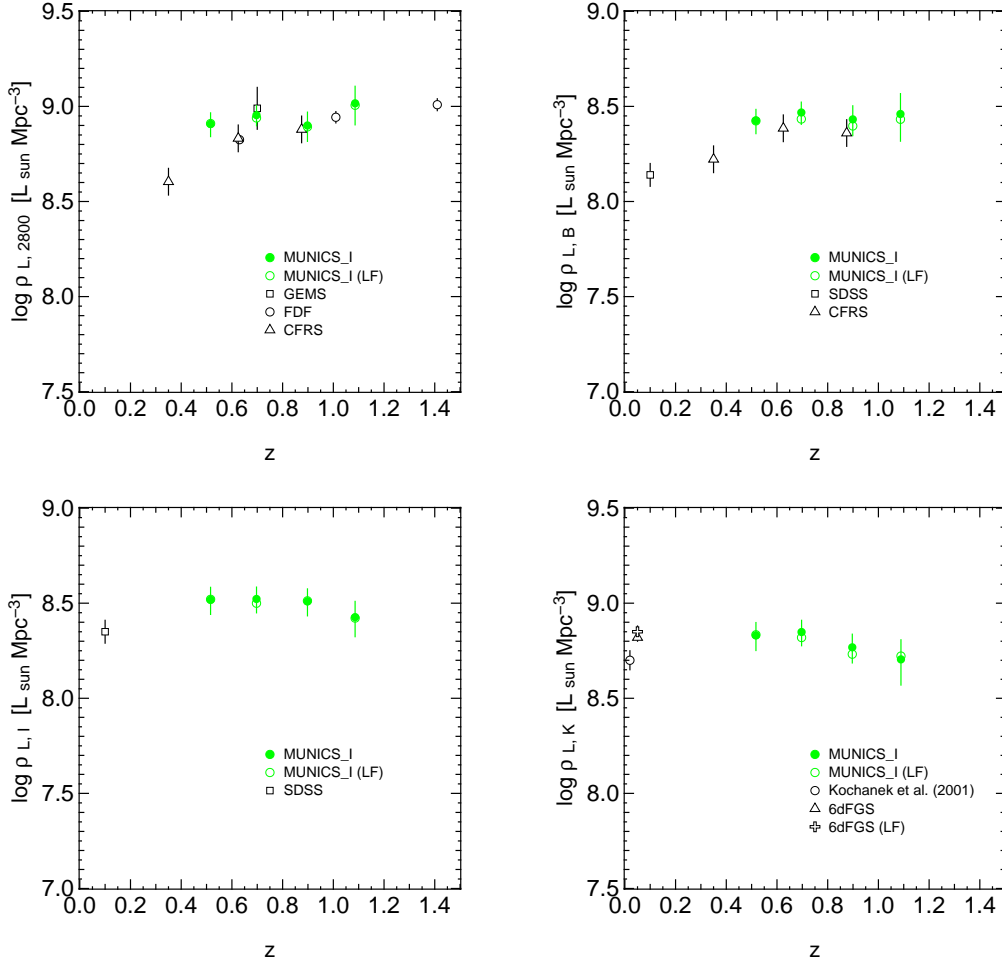


Figure 8.11: The luminosity density of galaxies at $\lambda \simeq 2800\text{\AA}$ (*upper left-hand panel*), in the *B* band (*upper right-hand panel*), in the *I* band (*lower left-hand panel*) and in the *K* band (*lower right-hand panel*). The MUNICS_I measurements are shown as green filled and open circles for the directly summed and the LF integrated luminosity density, respectively. Literature values (open symbols) were taken from Lilly *et al.* (1996), Gabasch *et al.* (2004a), Blanton *et al.* (2001), Kochanek *et al.* (2001), Wolf *et al.* (2004) and my own measurement from the 6dFGS (see Section 6.8).

regimes: While the SFRD at high redshift is dominated by the gravitational growth of the halo mass function, its low-redshift behaviour scales with the cooling rate of the gas in the haloes. HS2003 propose a simple approximation to the SFRD at low redshifts

$$\dot{\rho}_{\star}(z) = \sigma \left(\frac{H(z)}{H_0} \right)^q \quad (\text{HS2003 model}). \quad (8.10)$$

From their simulations they derive $q \approx 4/3$, only weakly dependent on details of the gas physics, and propose this slope as a test for their galaxy models. We will test this prediction for the low-redshift slope of the SFRD in this Section.

Table 8.3: Summary of results concerning the slope of the SFRD at low redshift.

Reference	Tracer	ζ
Lilly <i>et al.</i> (1996)	L_{2800}	3.9 ± 0.75
Hogg <i>et al.</i> (1998)	[OII]	$\simeq 4$
Cowie <i>et al.</i> (1999)	L_{2500}	$\simeq 1.5$
Sullivan <i>et al.</i> (2000)	L_{2000}	$\simeq 1.7$
Tresse <i>et al.</i> (2002)	H α	4.1 ± 0.3
Teplitz <i>et al.</i> (2003)	[OII]	$\simeq 4$

To measure the SFRD, star-formation rates (SFRs) were derived from the ultraviolet luminosity at $\lambda \sim 2800\text{\AA}$ as described in Madau *et al.* (1998):

$$\frac{\text{SFR}}{M_{\odot} \text{ yr}^{-1}} = \text{const.} \frac{L_{2800}}{\text{erg s}^{-1} \text{ Hz}^{-1}}, \quad (8.11)$$

where L_{2800} is the galaxy's luminosity at 2800\AA , $\text{const.} = 1.266 \cdot 10^{-28}$ for a Salpeter initial mass function (IMF; Salpeter 1955), and $\text{const.} = 1.961 \cdot 10^{-28}$ for a Scalo IMF (Scalo 1986). In the following we will assume a Salpeter IMF. The ultraviolet luminosity for the MUNICS galaxies was computed from the spectral energy distributions fitted to the photometry by the photometric redshift code. Literature data were taken from the compilation of Somerville *et al.* (2001).

The SFRD is then computed by summing the luminosities of all galaxies brighter than some minimum luminosity in the redshift interval in consideration. We then correct for incompleteness by fitting Schechter functions to the luminosity functions in the redshift bins, and correcting for the lost flux fainter than the luminosity limit. Note that we do not correct for dust extinction, but since we are interested in the *slope* of the SFRD rather than its absolute values this should not affect our results.

We combine our MUNICS data with measurements of the SFRD in the FORS Deep Field (FDF, Heidt *et al.* 2003, Gabasch *et al.* 2004a, c).

Our measurement of the SFRD is presented in Figure 8.12, together with previously published determinations of the SFRD derived from the luminosity at $\lambda \simeq 2800\text{\AA}$. It is clear from this Figure that our measurement of the SFRD has a much shallower slope at low redshifts than previously suggested. Indeed, the SFRD seems to drop by a factor of ≈ 2 rather than by ≈ 10 between redshifts $z = 1$ and $z = 0$.

We estimate the parameters (σ, ζ) of the power-law model and (σ, q) of the model by HS2003 by minimising χ^2 taking into account the statistical errors of the MUNICS and FDF measurements. We exclude all FDF data points with $z < 0.3$ (where we cannot sample the bright end of the luminosity function) and $z > 1.5$ (where the SFRD reaches its peak or flattens). The best-fitting models are shown in the left-hand panels of Figure 8.12, and their parameters are listed in Table 8.4.

We find that the SFRD increases essentially linear with $(1+z)$ over the redshift range $0.5 \leq z \leq 1.5$. This is in reasonable agreement with the measurements by Cowie *et al.* (1999) and Sullivan *et al.* (2000) (both of which do not give error estimates),

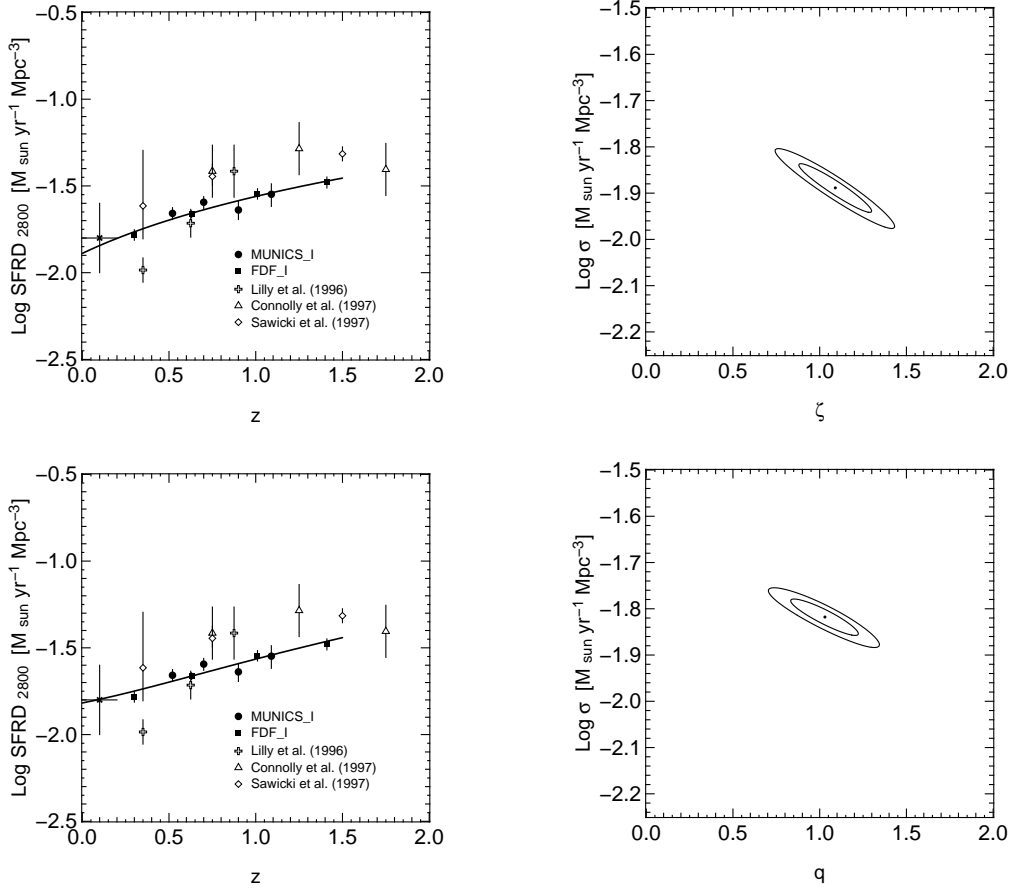


Figure 8.12: *Left-hand panels:* The SFRD at redshifts $z < 2$ as derived from L_{2800} . MUNICS and FDF measurements are shown as filled circles and squares, respectively, while literature data are indicated by open symbols for comparison. Note the considerably smaller error bars on the MUNICS and FDF data. The \times symbol at $z = 0.1$ with its error bars gives an idea of the range and scatter of local measurements (see text for details). The solid lines represent our best-fitting models for the low-redshift SFRD, once for the power-law model (*upper panel*) and for the HS2003 model (*lower panel*). The *right-hand panels* show the 1σ and 2σ error contours of our χ^2 fits.

but inconsistent with the $(1+z)^4$ evolution reported by Lilly *et al.* (1996), Hogg *et al.* (1998), Tresse *et al.* (2002) and Teplitz *et al.* (2003).

A fit of the HS2003 model yields an exponent q of $q = 1.03 \pm 0.13$. This is only marginally shallower than their prediction of $q \approx 4/3$: Their prediction deviates roughly 2σ from our measurement. As described in Hernquist & Springel (2003), the SFRD is mostly governed by gas cooling, with the slope mainly determined by cosmology. The fact that we measure a marginally shallower slope could indicate some influence of the cooling rate on the slope. Indeed, the cooling rate might decrease slower than in their model, or metal enrichment might play a role during that epoch, as discussed in their paper.

Table 8.4: Best-fitting parameters for the power-law and the HS2003 models. σ is measured in units of $M_{\odot} \text{yr}^{-1} \text{Mpc}^{-3}$.

Model	$\log \sigma$	ζ/q	$\min \chi_{\text{red}}^2$
Power-law:	-1.89 ± 0.03	1.09 ± 0.14	0.70
HS2003:	-1.82 ± 0.02	1.03 ± 0.13	0.94

Comparing this to the range of local measurements for the SFRD (indicated by the point with error bars at $z = 0.1$ in Figure 8.12, shows good agreement between with the values extrapolated from our fits. The estimate of the local value is based on the measurements by Gallego *et al.* (1995), Gronwall (1999) and Sullivan *et al.* (2000), using the values given in Table A2 of Somerville *et al.* (2001) for the first two.

8.5 Downsizing: Connecting Star Formation and Stellar Mass

Cowie *et al.* (1996) noticed that with increasing redshift the locus of galaxies with large rest-frame [OII] equivalent width (a measure of star formation activity) moved to higher absolute K -band luminosities (a measure of stellar mass). We show their original plot in Figure 1.9. This effect, which they called “downsizing”, can be interpreted in the sense that the most massive galaxies had their epoch of major star formation at earlier times (see also Section 1.3.4).

We want to verify this effect with the K and I -selected MUNICS samples. As in Section 8.4 we use the ultraviolet continuum around $\lambda = 2800\text{\AA}$ to derive star-formation rates for the MUNICS galaxies. We investigate the connection between star-formation rate and stellar mass by correlating the SFR with the absolute K -band magnitude at various redshifts. Furthermore, we also estimate the stellar masses of the MUNICS galaxies by fitting stellar population synthesis models by Bruzual & Charlot (2003) to the MUNICS broad-band photometric data (N. Drory, private communication).

In Figure 8.13 we show a variation of Cowie *et al.*’s original diagram replacing the [OII] ($\lambda = 3727\text{\AA}$) equivalent width by the SFR derived from the UV continuum. In this Figure we show both the K and the I -selected MUNICS galaxies as magenta and red symbols, respectively. First of all we note that there is no marked difference between the two catalogues. Secondly, it is obvious that there is clear evolution with redshift. While at low z the distribution is rather narrow with a small fraction of galaxies with much higher star-formation rates, it gets much broader with increasing redshift. In contrast to Cowie *et al.*’s finding there does not seem to be a lack of high-mass star-forming galaxies at low redshift. It rather seems that there is a general rise in the average star-formation rate with redshift, in agreement with the findings of Section 8.4.

The difference between our result and the findings by Cowie *et al.* (1996) may be

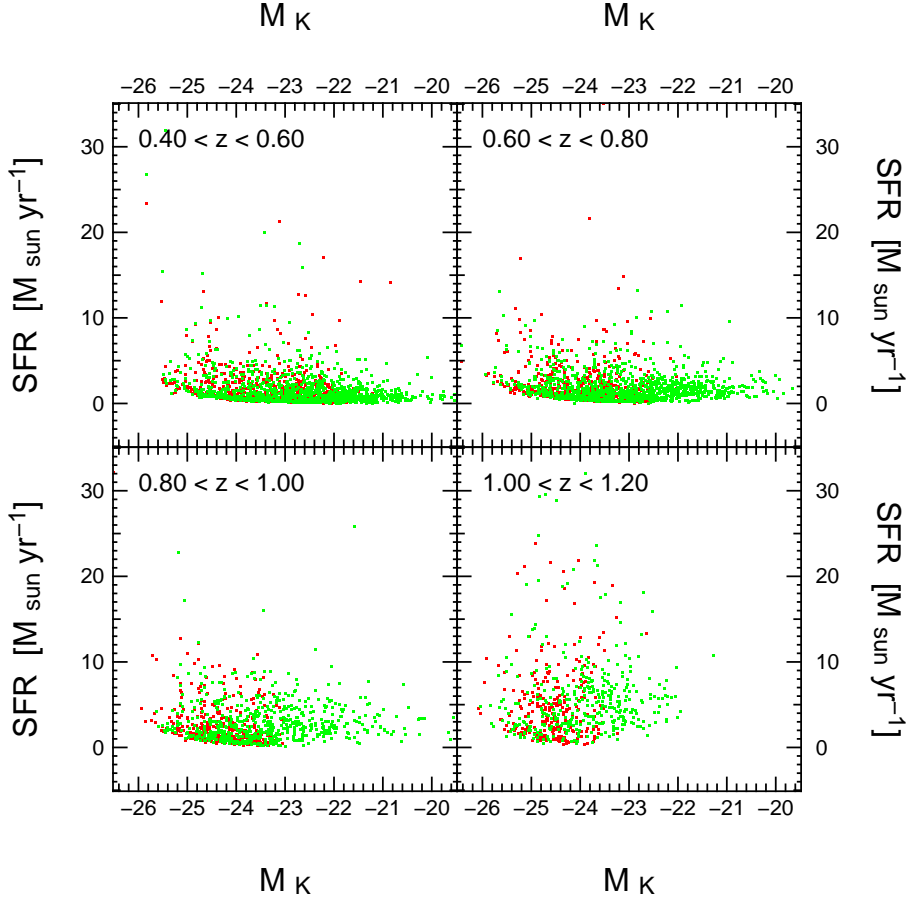


Figure 8.13: SFR *versus* absolute *K*-band magnitude for MUNICS_K (red symbols) and MUNICS_I (green symbols). See the text for details.

due to two effects. First, their sample is rather small so that they might have missed the rare high-mass star-forming galaxies in their tiny local volume. Secondly, they plot the [OII] equivalent width instead of the SFR. While this reduces uncertainties from the conversion of line flux to SFR, it also may make the effect of downsizing look more pronounced because the SFR of a galaxy is computed from the [OII] equivalent width according to

$$\text{SFR} \simeq 7 \cdot 10^{-12} \text{EW}_{[\text{OII}]} \frac{L_B}{L_{B,\odot}} \quad (8.12)$$

(Kennicutt 1992, Rosa-González *et al.* 2002). I.e. the SFR is proportional to the product of the equivalent width and the (*B*-band) *luminosity* of a galaxy. Now for the majority of galaxies L_B and L_K will be correlated, so that for the high-mass (large L_K) galaxies the SFR might be high even if the [OII] equivalent width is not extreme. On the other hand, low-luminosity galaxies with large equivalent widths may not produce much mass. We can test this by converting our SFRs as derived from the ultraviolet continuum to [OII] equivalent widths according to equation (8.12). The result is shown

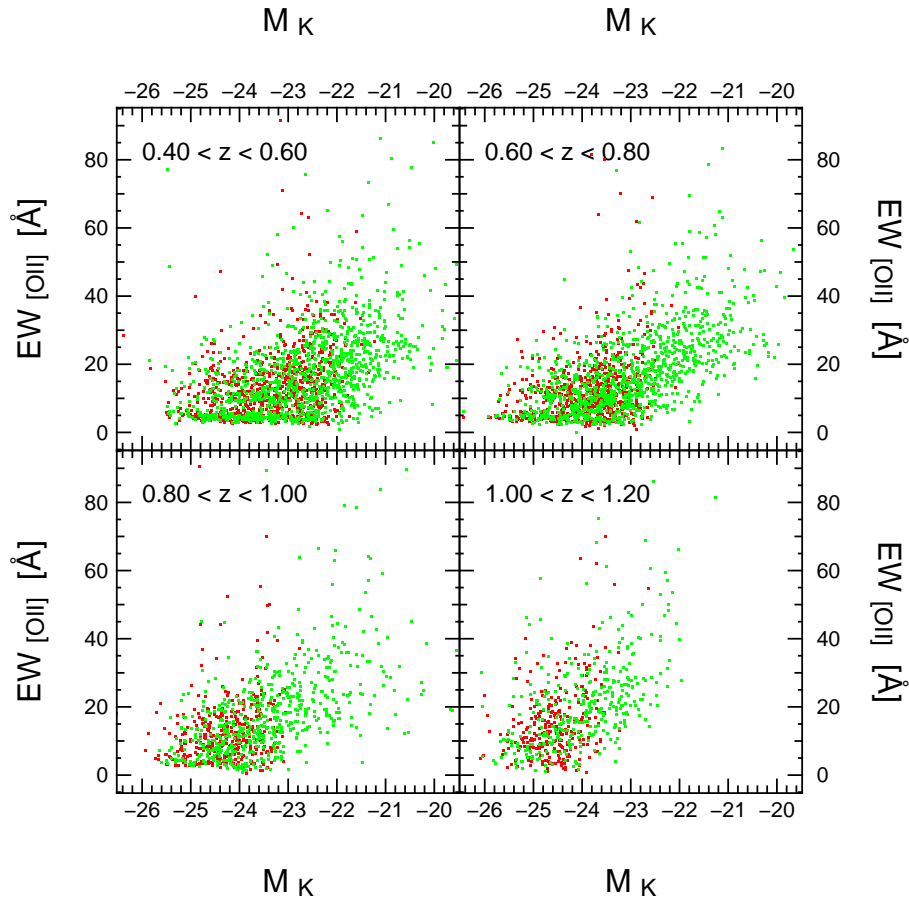


Figure 8.14: [OII] equivalent width *versus* absolute K -band magnitude for MUNICS_K (red symbols) and MUNICS_I (green symbols). See the text for details.

in Figure 8.14. The distribution of galaxies now looks completely different, and indeed much more similar to Figure 1.9 from Cowie *et al.* (1996).

Another way to look at this is the “specific SFR” (SSFR, Brinchmann & Ellis 2000), which is defined as the SFR per unit stellar mass.

Stellar masses are computed from the multi-colour photometry using a method similar to the one used in Drory *et al.* (2004a). It is described in detail and tested against spectroscopic and dynamical mass estimates in Drory, Bender & Hopp (2004b). In brief, we derive stellar masses by fitting a grid of stellar population synthesis models by Bruzual & Charlot (2003) with a range of star formation histories (SFHs), ages, metallicities and dust attenuations to the broad-band photometry. We describe star formation histories (SFHs) by a two-component model consisting of a main component with a smooth SFH $\propto \exp(-t/\tau)$ and a burst. We allow the SFH timescale to vary in $\tau \in [0.1, \infty]$ Gyr, the metallicity in $-0.6 \leq [\text{Fe}/\text{H}] \leq 0.3$, the age between 0.5 Gyr and the age of the universe at the objects redshift and the extinction in $0 \leq A_V \leq 1.5$.

In Figure 8.15 we show the SSFR as a function of stellar mass for four different

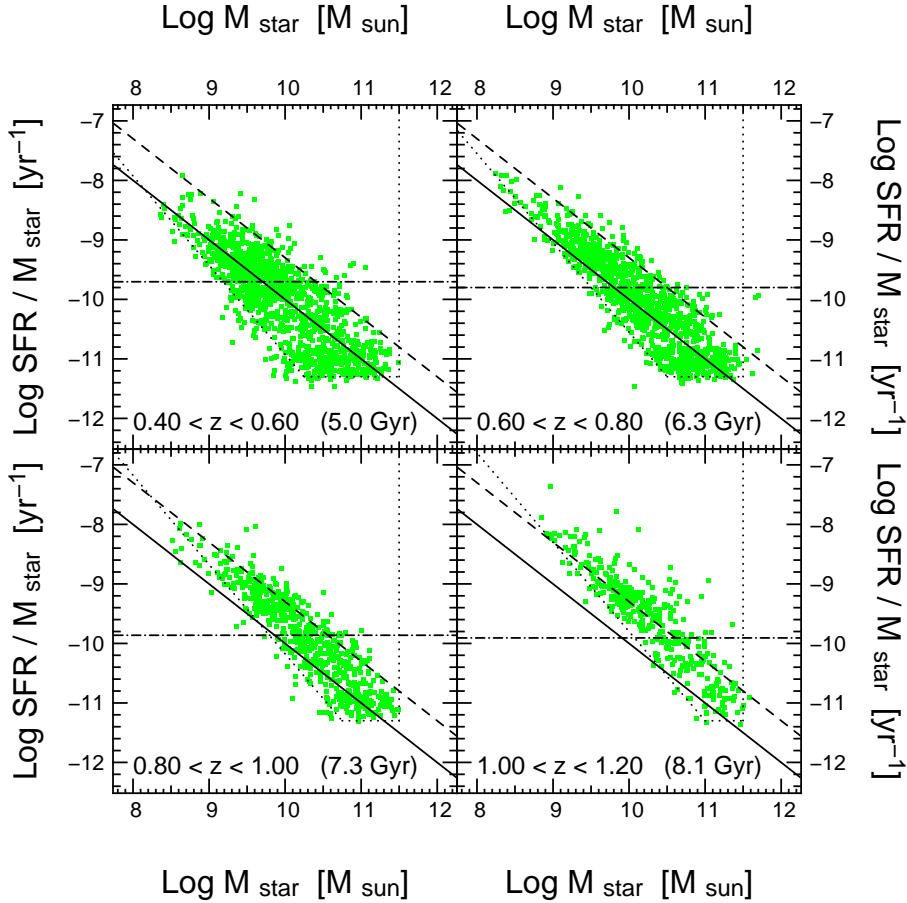


Figure 8.15: The specific SFR (i.e. the SFR per unit stellar mass) as a function of stellar mass for MUNICS_I. The solid line corresponds to a SFR of $1 M_{\odot} \text{ yr}^{-1}$. A SFR of $5 M_{\odot} \text{ yr}^{-1}$ is depicted by the dashed line. While this is a good measure of the upper envelope of the majority of objects at $z \sim 0.5$, the point distribution shifts to higher SSFRs with increasing redshift. The dotted lines indicate the limits of the point distribution due to magnitude limits, the model SED set and the mass function. See the text for details. The dash-dotted line is the SSFR required to double a galaxy’s mass between each redshift epoch and today (assuming constant SFR); the corresponding look-back time is indicated in each panel.

redshift bins. A number of observations can be made in this plot, but let us first discuss the limits of the point distribution as indicated by the dotted lines.

- The sharp cut-off at the high mass end at $\log M_{\text{star}}/M_{\odot} \simeq 11.5$ is likely to be produced by the high-mass cut-off of the stellar mass function (see also Figure 1.7). As expected, the location of this cut-off does not vary strongly with redshift over the redshift range we are sampling with MUNICS_I.
- The lower limit at $\log \text{SSFR} \simeq -11.3$ is due to the fact that data points fit by the same model spectral energy distribution (SED) occupy horizontal slices in

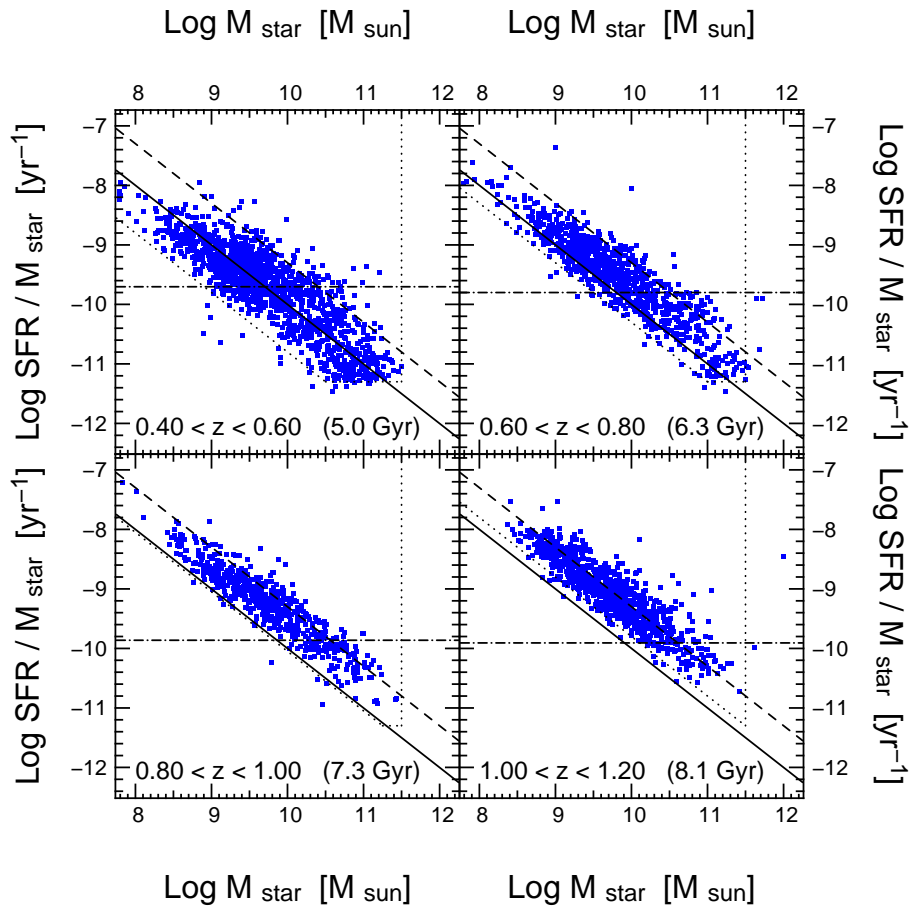


Figure 8.16: Same as Figure 8.15, but for MUNICS_B.

the diagram, with the reddest (oldest, least active) galaxies at the bottom and subsequently bluer models along the distribution to higher values of $\log \text{SSFR}$ (this can be also seen in the distribution of model ages in Figure 8.18). Thus the lower part of the point distribution always corresponds to one (comparatively old) SED, yielding a horizontal cut-off since for one particular SED there is a linear correlation between the ultraviolet luminosity ($\propto \text{SFR}$) and the near-infrared luminosity ($\propto M_{\text{star}}$).

- Finally, the limit of the point distribution to the left of the diagram is due to the limiting magnitudes in all filters of the MUNICS survey. This is apparent from Figures 8.16 and 8.17, where we show the same diagram for the MUNICS_B and MUNICS_K samples, respectively. For MUNICS_B the limit of the distribution runs parallel to a line of constant star-formation rate (B -band selection *is* indeed equivalent to a selection in SFR!), but we obviously miss high-mass, low-SFR objects at higher redshifts (they are very red and thus too faint in B). The selection line then becomes gradually steeper going from MUNICS_B to MUNICS_I and MUNICS_K, with the K band coming closest to a selection in

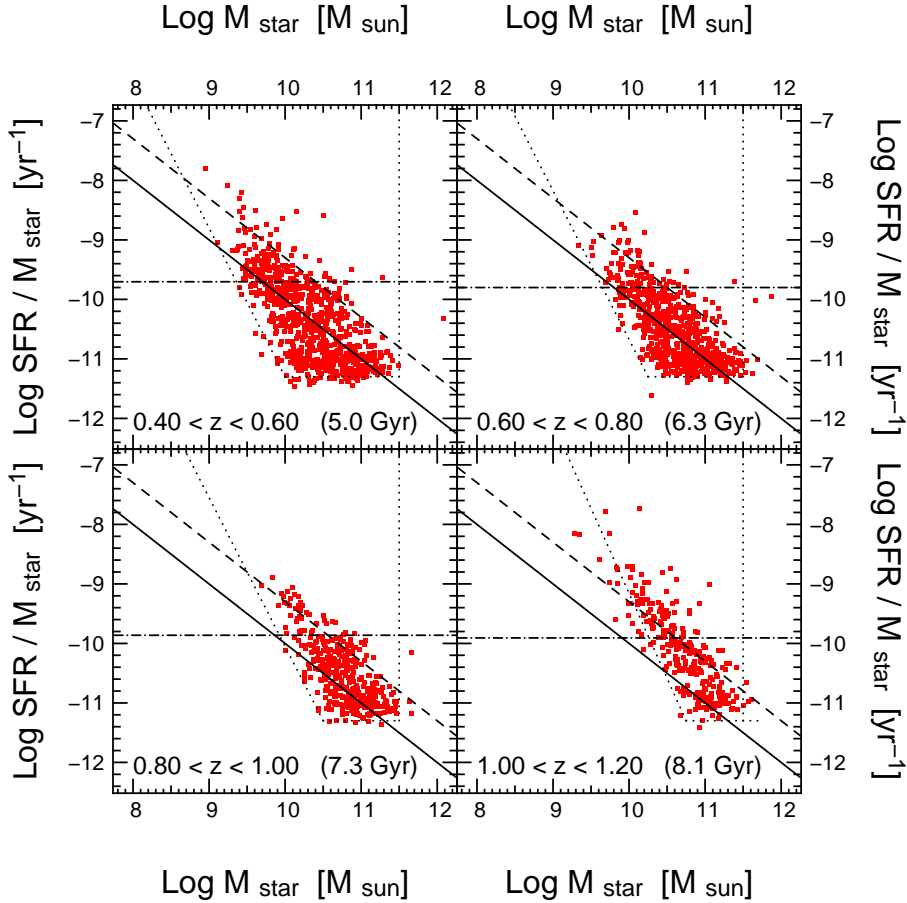


Figure 8.17: Same as Figure 8.15, but for MUNICS_K.

stellar mass.

The first and maybe most important result which can be derived from this diagram is that there is an upper bound on the SSFR (with a few galaxies with even higher SFRs which are likely starburst galaxies or AGN). It runs parallel to lines of constant star-formation over a wide range of masses $M \gtrsim 10^9 M_\odot$ and at all redshifts, meaning that this upper limit of the SFR does not depend on galaxy mass. Furthermore, this maximum SFR is generally increasing with increasing redshift for all stellar masses, from $\text{SFR} \simeq 5 M_\odot \text{yr}^{-1}$ at $z \simeq 0.5$ to $\text{SFR} \simeq 10 M_\odot \text{yr}^{-1}$ at $z \simeq 1.1$. Note that, while the lower part of the SSFR in the diagram is affected by incompleteness, the constraints on the upper envelope are robust. This is evident from Figure 8.19 where we show the histogram of the SFR for the four different redshift bins, clearly showing the increase of the maximum SFR with redshift.

Hints for a shift of this upper envelope to higher SSFRs with redshift were already noted by Brinchmann & Ellis (2000) and Bauer *et al.* (2004) from smaller galaxy samples, but our large sample of more than 6000 galaxies allows to constrain this change in a much more robust way.

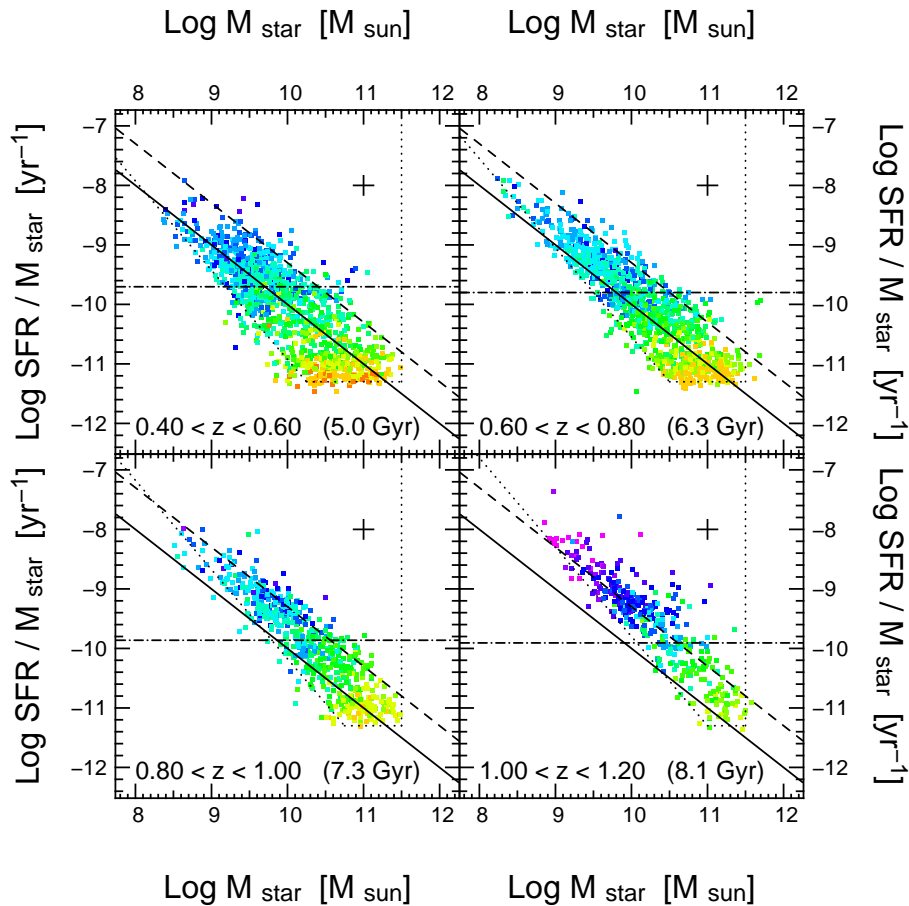


Figure 8.18: Same as Figure 8.15, but objects coloured according to the age of the CSP model fit to the photometry, ranging from 9 Gyr (red) to 0.05 Gyr (purple). The error cross in each panel gives an idea of the typical errors.

Finally we indicate the SSFR needed to double a galaxy's stellar mass between the epoch of observation and today (assuming a constant SFR). Clearly, the most massive galaxies are well below this line at all redshifts, indicating that they formed the bulk of their stars at earlier times, in agreement with the age distribution discussed above. This also means that star formation contributes much more to the mass build-up of less massive galaxies than to high-mass systems. While between redshifts $z = 1$ and $z = 0$ the mass of a $10^{11} M_{\odot}$ system would typically change by $\sim 40\%$ due to star formation, the mass of $10^{10} M_{\odot}$ galaxies would grow by a factor of ~ 5 and that of $10^9 M_{\odot}$ systems by a factor of ~ 40 . This example assumes a constant SFR of $\dot{\rho}_{*} = 5 M_{\odot} \text{ yr}^{-1}$ over a period of 7.7 Gyr which, as will be shown below, is likely to be unrealistic (at least for the lower-mass systems).

The same diagram, also for the *I*-band selected MUNICS catalogue, is shown in Figure 8.18 for different ages of the CSP model fitted to the broad-band photometry. It is clear from this Figure that the most massive galaxies contain the oldest and also the least active stellar populations.

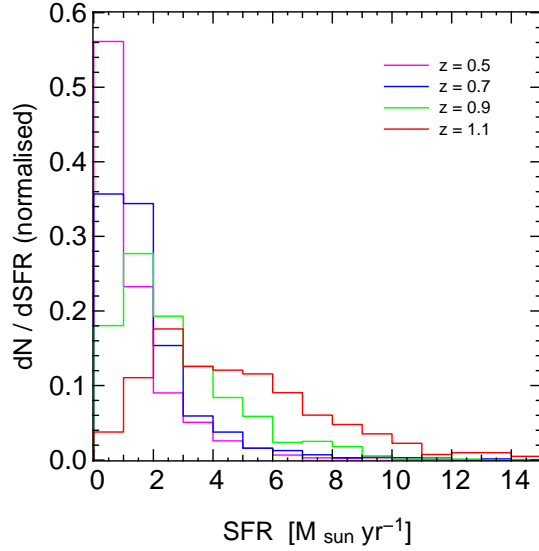


Figure 8.19: Normalised histogram of the SFR for the four different redshift bins used. The shift of the maximum to higher SFRs with increasing redshift is clearly visible.

We can also infer from Figure 8.18 that star formation in lower mass galaxies cannot proceed at constant SFR for a long time: All galaxies above the dot-dashed line in the diagram have the potential to double their stellar mass between the epoch of observation and today (assuming a constant SFR). While lower mass galaxies at low redshift tend to be gas rich, there is a large spread in measured gas-to-stellar-mass fractions (Mateo 1998, Pérez-González *et al.* 2003, Kannappan 2004). However, very gas-rich systems are rare (Davies *et al.* 2001), i.e. the majority of these galaxies does not have huge gas supplies, which might lead us to believe that low-mass galaxies cannot exhibit constant star formation over longer time-scales, but show variable star formation histories, as they are derived for dwarf galaxies in the Local Group (see e.g. Mateo 1998, Tosi 2001, Grebel 2004 for reviews). It is not possible to say from our data whether we see these galaxies in the process of formation or during one of multiple episodes of active star formation. However, it is likely that we pick them up during an active phase of star formation. Also, it is clear from the completeness limits that we cannot detect low-mass galaxies with low SSFR.

Considering the high-mass end, we can try to draw some conclusions about the contributions of star formation and merging to the change of stellar mass. Between redshifts $z \simeq 1.1$ and $z \simeq 0.5$, the characteristic mass of the cut-off of the galaxies' stellar mass function changes by $\Delta \log M \simeq 0.15$ dex (Drory *et al.* 2004a, Fontana *et al.* 2004, Conselice *et al.* 2004). For a $M_{\star} = 10^{11} M_{\odot}$ stellar mass galaxy, a constant SFR of $\dot{\rho}_{\star} = 5 M_{\odot} \text{ yr}^{-1}$ over a period of time of $\Delta t = 3.1$ Gyr (the difference in time between these redshift values), yields a growth in stellar mass of $\Delta M_{\star} \simeq 2 \cdot 10^{10} M_{\odot}$, or $\Delta \log M_{\star} \simeq 0.1$ dex. Considering the uncertainty of the results and our lack of knowledge about the star formation histories of these galaxies, we cannot really decide about the relative importance of star formation and merging. We note, however, that our re-

sults on the growth of stellar mass does not require a substantial contribution of merging over the redshift range $0 \lesssim z \lesssim 1$.

Chapter 9

Summary and Conclusions

In this Chapter we will summarise our results and discuss them in the context of our ideas of galaxy formation and evolution.

9.1 Summary of Results

This thesis presented work on galaxy evolution from a near-infrared selected galaxy redshift survey and much larger optically selected galaxy catalogues where distances were derived from photometric redshifts. All this work is based on the data of the Munich Near-Infrared Cluster Survey (MUNICS) described in Chapter 2. I presented details of the selection of objects for spectroscopy, the spectroscopic observations and the data reduction in Chapters 3 and 4. Chapter 5, on the other hand, discusses properties of objects in the spectroscopic catalogue like the redshift distribution, the redshift accuracy and the stellar content. Technical details for the optically selected photometric samples are summarised in Chapter 7.

More important than the technical aspects of this work are, of course, the scientific results presented in Chapters 6 and 8. In this thesis I have derived the following results concerning the evolution of galaxies in the range $0 \lesssim z \lesssim 1$:

- The **Luminosity Function** changes with increasing redshift in the sense that the characteristic luminosity increases but the number density decreases. This effect is smaller at rest-frame near-infrared wavelengths (see Chapter 6) and gets more pronounced at shorter wavelengths (see Section 8.2). This evolutionary trend continues to higher redshifts (Gabasch *et al.* 2004a, b, Gabasch 2004). Furthermore we could show that luminosity functions derived from catalogues based on different selection bands do not differ at the bright end: The brightest galaxies are sampled by all selection methods, however, differences may arise at the fainter part of the luminosity function.
- The **Luminosity Density** rises from $z \sim 0$ to $z \sim 1$. The slope of this increase is steepest in the ultraviolet regime, gets shallower at optical bands and is slightly falling in the near-infrared (see Section 8.3). This is in agreement with the results on the evolution of the luminosity function (Section 8.2). It is also consistent

with the evolution of the Star Formation Rate (usually measured in solar masses per year, see below): At $z \gtrsim 1$, the star-formation rate is high, and thus the K -band luminosity density increases with time. The drop of the star-formation rate at $z \lesssim 1$, on the other hand, yields a less pronounced increase of the K -band luminosity density with time. Since the K -band luminosity is a measure of a galaxy's stellar mass, this can be understood as a slightly rising mass density due to star formation (assuming a constant mass-to-light ratio over this redshift range).

- A study of **rest-frame $B - K$ colour distributions** for the three different selection bands and different redshifts allows important conclusions about selection effects and the evolution of galaxy populations. First, we could show that the selection band influences the colour distributions only for objects with low K -band luminosities (small stellar masses), while the distributions look remarkably similar for high-mass galaxies. Secondly, the colour distributions get wider and bluer with decreasing K luminosity, indicating a higher average star-formation rate and a wider distribution of star-formation rates for less massive galaxies. Thirdly, there is strong colour evolution with redshift for the redshift interval $0 \lesssim z \lesssim 1$ in the sense that with increasing redshift galaxies become bluer (i.e. have larger star-formation activity). This can hardly be seen for the most massive galaxies, but becomes more and more so for the lowest mass galaxies. Also, the trend becomes stronger going from K -band selection to B -band selection. This means that the increase in star formation rate from redshift zero to one is largely driven by lower mass galaxies, and that the most massive galaxies have assembled the bulk of their stellar mass before redshift unity.
- From our large photometric catalogue, in combination with data from the FORS Deep Field (FDF, Heidt *et al.* 2003), we could determine the **Star Formation Rate Density** from the ultraviolet luminosity at $\lambda \simeq 2800\text{\AA}$ in the redshift range $0 \lesssim z \lesssim 1$ with very high accuracy. We see evidence for a shallow rise of the star formation rate density from the local universe to redshift one, with an increase of a factor ≈ 2 rather than the often quoted factor of ≈ 10 . The slope can be well approximated by a function of the form $\dot{\rho}_* \propto (1+z)^\zeta$ with $\zeta = 1.09 \pm 0.14$, close to a linear relation with redshift. Previously reported results according to which the star formation rate density rises steeply as $(1+z)^4$ are inconsistent with our measurement. The local value extrapolated from this relation is in good agreement with previously measured values of the star formation rate density at $z \simeq 0$.
- We also compare the slope of the star formation rate density at low redshift to the model by Hernquist & Springel (2003), an analytic approximation to hydrodynamic simulations of galaxy formation. They predict a value of $q \approx 4/3$ for the exponent in their model. We show that their model is in good agreement with the data. Our measurement of $q = 1.03 \pm 0.13$ is slightly shallower than their prediction, but agrees within roughly 2σ . As described in Hernquist & Springel (2003), the star formation rate density is mostly governed by gas cool-

ing, with the slope mainly determined by cosmology. The fact that we measure a marginally shallower slope could indicate some influence of the cooling rate on the slope. Indeed, the cooling rate might decrease more slowly than in their model, or metal enrichment might play a role during that epoch, as discussed in their paper.

- In the 1990s, Cowie *et al.* (1996) investigated a small, near-infrared selected spectroscopic sample of galaxies and saw evidence that at higher redshifts progressively more massive galaxies are undergoing rapid star formation, an effect they called **downsizing**. We investigated this effect using our large MUNICS sample based on photometric redshifts and deriving star-formation rates from the ultraviolet continuum emission of the galaxies. We could not fully confirm the observations by Cowie *et al.* (1996): The presence of strongly star-forming galaxies with high K -band luminosities at higher redshifts is due to a general increase of star-formation activity *at all masses* rather than a shift of the locus of these galaxies to higher K -band luminosities (see Section 8.5). We think that their interpretation was biased by their small sample probing only a small volume of space at low redshifts (massive galaxies are rare!) and the use of the [OII] emission line equivalent width as a measure for star-formation. Nevertheless it remains true that massive galaxies had their epoch of major star formation at earlier times than less massive galaxies (see below).
- Downsizing, as explained in the previous item, is a way to explore the connection between star-formation activity and stellar mass already assembled in galaxies. We further explored this connection by looking at the **specific star-formation rate**, defined as the current star-formation rate of a galaxy normalised by its stellar mass. The specific star-formation rate as a function of redshift reveals a number of remarkable properties (see Section 8.5). First, the specific star-formation rate is distributed parallel to lines of constant star-formation rate for a wide range of masses, i.e. galaxies of different masses do not show markedly different star-formation rates (in solar masses per year). Secondly, the specific star formation rate is decreasing with mass. Hence star formation does contribute significantly only to the growth of low-mass galaxies. We could also show that these lower mass systems cannot sustain their high star-formation rates over extended periods of time. Thirdly, the high star-formation rate envelope of the specific star-formation rate is shifted to higher formation rates with increasing redshift. This means that star formation is stronger at higher redshift for all masses as we already pointed out above. Fourthly, we could also show that the most massive galaxies at all epoch contain the oldest and least active stellar populations, and that we do not require a substantial contribution of merging to the growth of stellar mass over the redshift range probed. These results give a more detailed view on the interpretation of the rest-frame $B - K$ colour distributions discussed above. Finally we could show that our results do not require a significant contribution of galaxy merging to the growth of stellar mass over this redshift range.

9.2 Interpretation

Our studies of the evolution of the galaxy population presented in this thesis are focused on the universe at redshifts $z \lesssim 1$, i.e. the second half of the life of the universe at its present age. Our observations of the star formation rate density show that the universe has entered a quieter phase of existence: The star formation rate density decreases with time (i.e. with decreasing redshift), although not as steeply as previously thought, reflected in a decrease of the ultraviolet and optical blue luminosity density with time, and a slower build-up of stellar mass of galaxies. This trend is also confirmed by our results on the evolution of luminosity functions during this cosmic epoch: The typical luminosity gets gradually fainter, while the normalisation, the number density, increases with time. This effect is the more pronounced the bluer the wavelength regime in which the luminosity function is studied.

Although not a critical test, most of this can, indeed, be reconciled with the standard scenario of hierarchical galaxy formation. In this model, galaxies form from low-mass building blocks which merge in time and gradually form larger galaxies. However, some things remain puzzling, especially the fact that the most massive galaxies seem to contain the oldest stellar populations and have formed the bulk of their stars at earlier times. Some sort of anti-hierarchical component might have to be included in the hierarchical models after all, but it is not clear how this works in detail.

More detailed comparison of our data with predictions within the framework of hierarchical galaxy formation yield a somewhat ambivalent picture. While a comparison of the Hernquist & Springel (2003) approximation for the low-redshift evolution of the star formation rate density based on hydrodynamic simulations shows good agreement with our measurements, semi-analytic predictions of luminosity functions fail to reproduce the observations. However, it remains unclear how much of this failure can be attributed to the foundations of the theoretical model and how much to their rather primitive descriptions of poorly understood physical phenomena like gas cooling, star formation and feedback. Maybe it is also not surprising that an integrated quantity like the ultraviolet luminosity density (from which the star formation rate density is derived) is more readily reproduced than the luminosity function itself.

It is clear that much remains to be done – both observationally and theoretically – to gain a better understanding of the formation and evolution of galaxies in our universe.

Bibliography

- Abell, G. O., Corwin, H. G., & Olowin, R. P. 1989: *A catalog of rich clusters of galaxies*, ApJS, 70, 1
- Abraham, R. G., Tanvir, N. R., Santiago, B. X., Ellis, R. S., Glazebrook, K., & van den Bergh, S. 1996: *Galaxy morphology to $I=25$ mag in the Hubble Deep Field*, MNRAS, 279, L47
- Adelberger, K. L., Steidel, C. C., Giavalisco, M., Dickinson, M., Pettini, M., & Kellogg, M. 1998: *A Counts-in-Cells Analysis Of Lyman-break Galaxies At Redshift $z \sim 3$* , ApJ, 505, 18
- Adelberger, K. L., Steidel, C. C., Shapley, A. E., Hunt, M. P., Erb, D. K., Reddy, N. A., & Pettini, M. 2004: *Optical Selection of Star-forming Galaxies at Redshifts $1 < z < 3$* , ApJ, 607, 226
- Adelberger, K. L., Steidel, C. C., Shapley, A. E., & Pettini, M. 2003: *Galaxies and Intergalactic Matter at Redshift $z \sim 3$: Overview*, ApJ, 584, 45
- Ajiki, M., Taniguchi, Y., Murayama, T., Nagao, T., Veilleux, S., Shioya, Y., Fujita, S. S., Kakazu, Y., *et al.* 2002: *A New High-Redshift Ly α Emitter: Possible Superwind Galaxy at $z = 5.69$* , ApJ, 576, L25
- Anderson, E. 1989: *An Introductory User's Guide to IRAF Scripts*, revised by R. Seaman, available at <http://iraf.noao.edu/>
- Aragón-Salamanca, A., Ellis, R. S., Couch, W. J., & Carter, D. 1993: *Evidence for systematic evolution in the properties of galaxies in distant clusters*, MNRAS, 262, 764
- Arnouts, S., D'Odorico, S., Cristiani, S., Zaggia, S., Fontana, A., & Giallongo, E. 1999: *The NTT SUSI deep field*, A&A, 341, 641
- Arnouts, S., Vandame, B., Benoist, C., Groenewegen, M. A. T., da Costa, L., Schirmer, M., Mignani, R. P., Slijkhuis, R., *et al.* 2001: *ESO imaging survey. Deep public survey: Multi-color optical data for the Chandra Deep Field South*, A&A, 379, 740
- Baade, W. 1944: *The Resolution of Messier 32, NGC 205, and the Central Region of the Andromeda Nebula.*, ApJ, 100, 137

- Babul, A. & Ferguson, H. C. 1996: *Faint Blue Galaxies and the Epoch of Dwarf Galaxy Formation*, ApJ, 458, 100
- Babul, A. & Rees, M. J. 1992: *On dwarf elliptical galaxies and the faint blue counts*, MNRAS, 255, 346
- Balogh, M. L., Christlein, D., Zabludoff, A. I., & Zaritsky, D. 2001: *The Environmental Dependence of the Infrared Luminosity and Stellar Mass Functions*, ApJ, 557, 117
- Bauer, A., Drory, N., Hill, G. J., & Feulner, G. 2004: *Specific star formation rates to redshift 1.5*, ApJ, submitted
- Baugh, C. M., Benson, A. J., Cole, S., Frenk, C. S., & Lacey, C. 2003: *The Evolution of Galaxy Mass in Hierarchical Models*, in: The Mass of Galaxies at Low and High Redshift. Proceedings of the ESO Workshop held in Venice, Italy, 24-26 October 2001., 91
- Baum, W. A. 1962: *Photoelectric Magnitudes and Red-Shifts*, in: IAU Symp. 15: Problems of Extra-Galactic Research, Vol. 15., 390
- Bell, E. F., McIntosh, D. H., Katz, N., & Weinberg, M. D. 2003a: *A First Estimate of the Baryonic Mass Function of Galaxies*, ApJ, 585, L117
- Bell, E. F., McIntosh, D. H., Katz, N., & Weinberg, M. D. 2003b: *The Optical and Near-Infrared Properties of Galaxies. I. Luminosity and Stellar Mass Functions*, ApJS, 149, 289
- Bender, R., Appenzeller, I., Böhm, A., Drory, N., Fricke, K. J., Gabasch, A., Heidt, J., Hopp, U., *et al.* 2001: *The FORS Deep Field: Photometric Data and Photometric Redshifts*, in: Deep Fields, ed. S. Cristiani, A. Renzini, & R. E. Williams, Springer, 96
- Bender, R., Saglia, R. P., Ziegler, B., Belloni, P., Greggio, L., Hopp, U., & Bruzual, G. 1998: *Exploring Cluster Elliptical Galaxies as Cosmological Standard Rods*, ApJ, 493, 529
- Benítez, N. 2000: *Bayesian Photometric Redshift Estimation*, ApJ, 536, 571
- Benson, A. J., Bower, R. G., Frenk, C. S., Lacey, C. G., Baugh, C. M., & Cole, S. 2003: *What Shapes the Luminosity Function of Galaxies?*, ApJ, 599, 38
- Bertin, E. & Dennefeld, M. 1997: *Galaxy evolution at low redshift? I. Optical counts*, A&A, 317, 43
- Binney, J. 2004: *On the origin of the galaxy luminosity function*, MNRAS, 347, 1093
- Binney, J. & Merrifield, M. 1998: *Galactic Astronomy*, Princeton University Press
- Blain, A. W. & Longair, M. S. 1993: *Submillimetre Cosmology*, MNRAS, 264, 509

- Blanton, M. R., Dalcanton, J., Eisenstein, D., Loveday, J., Strauss, M. A., SubbaRao, M., Weinberg, D. H., Anderson, J. E., *et al.* 2001: *The Luminosity Function of Galaxies in SDSS Commissioning Data*, AJ, 121, 2358
- Blanton, M. R., Hogg, D. W., Bahcall, N. A., Brinkmann, J., Britton, M., Connolly, A. J., Csabai, I., Fukugita, M., *et al.* 2003: *The Galaxy Luminosity Function and Luminosity Density at Redshift $z = 0.1$* , ApJ, 592, 819
- Boesgaard, A. M. & Steigman, G. 1985: *Big bang nucleosynthesis - Theories and observations*, ARA&A, 23, 319
- Botzler, C. S. 2004: *Finding Structures in Photometric Redshift Surveys*, PhD thesis, Ludwig-Maximilians-Universität München
- Botzler, C. S., Snigula, J., Bender, R., & Hopp, U. 2004: *Finding structures in photometric redshift galaxy surveys: an extended friends-of-friends algorithm*, MNRAS, 349, 425
- Bouwens, R., Broadhurst, T., & Illingworth, G. 2003: *Cloning Dropouts: Implications for Galaxy Evolution at High Redshift*, ApJ, 593, 640
- Bouwens, R. J., Illingworth, G. D., Thompson, R. I., Blakeslee, J. P., Dickinson, M. E., Broadhurst, T. J., Eisenstein, D. J., Fan, X., *et al.* 2004: *Star Formation at $z \sim 6$: The Hubble Ultra Deep Parallel Fields*, ApJ, 606, L25
- Bower, R., Lucey, J. R., & Ellis, R. S. 1992: *Precision photometry of early-type galaxies in the Coma and Virgo clusters: a test of the universality of the colour-magnitude relation — II. Analysis*, MNRAS, 254, 601
- Brainerd, T. G., Blandford, R. D., & Smail, I. 1996: *Weak Gravitational Lensing by Galaxies*, ApJ, 466, 623
- Brinchmann, J. & Ellis, R. S. 2000: *The Mass Assembly and Star Formation Characteristics of Field Galaxies of Known Morphology*, ApJ, 536, L77
- Bromm, V. & Larson, R. B. 2004: *The First Stars*, Annual Reviews of Astronomy and Astrophysics, 10.1146/annurev.astro.42.053102.134034, First published online as a Review in Advance on May 19, 2004
- Bruzual, G. & Charlot, S. 2003: *Stellar population synthesis at the resolution of 2003*, MNRAS, 344, 1000
- Bunker, A. J., Stanway, E. R., Ellis, R. S., McMahon, R. G., & McCarthy, P. J. 2003: *A star-forming galaxy at $z = 5.78$ in the Chandra Deep Field South*, MNRAS, 342, L47
- Carroll, L. 1876: *The Hunting of the Snark*, Macmillan & Co.
- Carroll, S. M., Press, W. H., & Turner, E. L. 1992: *The cosmological constant*, ARA&A, 30, 499

- Casertano, S., de Mello, D. ., Dickinson, M., Ferguson, H. C., Fruchter, A. S., Gonzalez-Lopezlira, R. A., Heyer, I., Hook, R. N., *et al.* 2000: *WFPC2 Observations of the Hubble Deep Field South*, AJ, 120, 2747
- Cimatti, A., Andreani, P., Rottgering, H., & Tilanus, R. 1998: *Vigorous star formation hidden by dust in a galaxy at a redshift of 1.4*, Nature, 392, 895
- Cimatti, A., Daddi, E., Cassata, P., Pignatelli, E., Fasano, G., Vernet, J., Fomalont, E., Kellermann, K., *et al.* 2003: *The manifold spectra and morphologies of EROs*, A&A, 412, L1
- Cimatti, A., Daddi, E., di Serego Alighieri, S., Pozzetti, L., Mannucci, F., Renzini, A., Oliva, E., Zamorani, G., *et al.* 1999: *New clues on the nature of extremely red galaxies*, A&A, 352, L45
- Cimatti, A., Daddi, E., Mignoli, M., Pozzetti, L., Renzini, A., Zamorani, G., Broadhurst, T., Fontana, A., *et al.* 2002a: *The K20 survey. I. Disentangling old and dusty star-forming galaxies in the ERO population*, A&A, 381, L68
- Cimatti, A., Mignoli, M., Daddi, E., Pozzetti, L., Fontana, A., Saracco, P., Poli, F., Renzini, A., *et al.* 2002b: *The K20 survey. III. Photometric and spectroscopic properties of the sample*, A&A, 392, 395
- Cohen, J. G. 2002: *Caltech Faint Galaxy Redshift Survey. XVI. The Luminosity Function for Galaxies in the Region of the Hubble Deep Field-North to $z=1.5$* , ApJ, 567, 672
- Cole, S., Lacey, C. G., Baugh, C. M., & Frenk, C. S. 2000: *Hierarchical galaxy formation*, MNRAS, 319, 168
- Cole, S., Norberg, P., Baugh, C. M., Frenk, C. S., Bland-Hawthorn, J., Bridges, T., Cannon, R., Colless, M., *et al.* 2001: *The 2dF galaxy redshift survey: near-infrared galaxy luminosity functions*, MNRAS, 326, 255
- Coles, P. & Lucchin, F. 1995: *Cosmology. The origin and evolution of cosmic structure*, Chichester: Wiley
- Colless, M. 1997: *Wide Field Spectroscopy and the Universe*, in: ASSL Vol. 212: Wide-field spectroscopy,, 227
- Connolly, A. J., Szalay, A. S., Dickinson, M., Subbarao, M. U., & Brunner, R. J. 1997: *The Evolution of the Global Star Formation History as Measured from the Hubble Deep Field*, ApJ, 486, L11
- Conselice, C. J. *et al.* 2004: *The Luminosity, Stellar Mass, and Number Density Evolution of Field Galaxies of Known Morphology from $z = 0.5 - 3$* , ApJ, submitted, astro-ph/0405001,
- Couch, W. J. & Newell, E. B. 1984: *Distant clusters of galaxies. I - Uniform photometry of 14 rich clusters*, ApJS, 56, 143

- Couch, W. J. & Sharples, R. M. 1987: *A spectroscopic study of three rich galaxy clusters at $Z = 0.31$* , MNRAS, 229, 423
- Cowie, L. L., Gardner, J. P., Hu, E. M., Songaila, A., Hodapp, K.-W., & Wainscoat, R. J. 1994: *The Hawaii K-band galaxy survey. I. Deep K-band imaging*, ApJ, 434, 114
- Cowie, L. L., Songaila, A., & Barger, A. J. 1999: *Evidence for a Gradual Decline in the Universal Rest-Frame Ultraviolet Luminosity Density for $z < 1$* , AJ, 118, 603
- Cowie, L. L., Songaila, A., Hu, E. M., & Cohen, J. G. 1996: *New Insight on Galaxy Formation and Evolution From Keck Spectroscopy of the Hawaii Deep Fields*, AJ, 112, 839
- Cuby, J.-G., Le Fèvre, O., McCracken, H., Cuillandre, J.-C., Magnier, E., & Meneux, B. 2003: *Discovery of a $z = 6.17$ galaxy from CFHT and VLT observations*, A&A, 405, L19
- Daddi, E., Cimatti, A., Broadhurst, T., Renzini, A., Zamorani, G., Mignoli, M., Saracco, P., Fontana, A., *et al.* 2002: *The K20 survey. II. The different spatial clustering of $z \sim 1$ old and dusty star-forming EROs*, A&A, 384, L1
- Davies, J. I., de Blok, W. J. G., Smith, R. M., Kambas, A., Sabatini, S., Linder, S. M., & Salehi-Reyhani, S. A. 2001: *Gas-rich galaxies and the HI mass function*, MNRAS, 328, 1151
- Dawson, S., Stern, D., Bunker, A. J., Spinrad, H., & Dey, A. 2001: *Serendipitously Detected Galaxies in the Hubble Deep Field*, AJ, 122, 598
- de Vaucouleurs, G. 1948: *Recherches sur les nébuleuse extragalactiques. II. Analyse des nébuleuses NGC 3115, 3379, 4649 et 4594. Observation et discussion*, Annales d'Astrophysique, 11, 247
- Dekel, A. & Silk, J. 1986: *The origin of dwarf galaxies, cold dark matter, and biased galaxy formation*, ApJ, 303, 39
- D'Ercole, A., Renzini, A., Ciotti, L., & Pellegrini, S. 1989: *X-ray evolution of model elliptical galaxies*, ApJ, 341, L9
- Dey, A., Graham, J. R., Ivison, R. J., Smail, I., Wright, G. S., & Liu, M. C. 1999: *Observations of a $z = 1.44$ Dusty, Ultraluminous Galaxy and Implications for Deep Submillimeter Surveys*, ApJ, 519, 610
- Dey, A., Spinrad, H., Stern, D., Graham, J. R., & Chaffee, F. H. 1998: *A Galaxy at $z = 5.34$* , ApJ, 498, L93
- Dicke, R. H., Peebles, P. J. E., Roll, P. G., & Wilkinson, D. T. 1965: *Cosmic Black-Body Radiation.*, ApJ, 142, 414
- Dickinson, M., Papovich, C., Ferguson, H. C., & Budavári, T. 2003: *The Evolution of the Global Stellar Mass Density at $0 < z < 3$* , ApJ, 587, 25

- Dickinson, M., Stern, D., Giavalisco, M., Ferguson, H. C., Tsvetanov, Z., Chornock, R., Cristiani, S., Dawson, S., *et al.* 2004: *Color-selected Galaxies at $z \sim 6$ in the Great Observatories Origins Deep Survey*, ApJ, 600, L99
- Djorgovski, S. & Davis, M. 1987: *Fundamental Properties of Elliptical Galaxies*, ApJ, 313, 59
- Dressler, A. & Gunn, J. E. 1983: *Spectroscopy of galaxies in distant clusters. II - The population of the 3C 295 cluster*, ApJ, 270, 7
- Dressler, A., Lynden-Bell, D., Burstein, D., Roger Davies, R. L., M., F. S., Terlevich, R. J., & G., W. 1987: *Spectroscopy and photometry of elliptical galaxies. I. A new Distance Estimator*, ApJ, 313, 42
- Drory, N. 2002: *A Near-IR Selected Photometric Survey of Distant Galaxies*, PhD thesis, Ludwig-Maximilians-Universität München
- Drory, N. 2003: *Yet another object detection application (yoda)*, A&A, 397, 371
- Drory, N., Bender, R., Feulner, G., Hopp, U., Maraston, C., Snigula, J., & Hill, G. J. 2003: *The Munich Near-Infrared Cluster Survey. II. The K-Band Luminosity Function of Field Galaxies to $z \sim 1.2$* , ApJ, 595, 698 (MUNICS II)
- Drory, N., Bender, R., Feulner, G., Hopp, U., Maraston, C., Snigula, J., & Hill, G. J. 2004a: *The Munich Near-Infrared Cluster Survey: The stellar masses of K-band selected galaxies to $z \sim 1.2$* , ApJ, 608, 742 (MUNICS VI)
- Drory, N., Bender, R., & Hopp, U. 2004b: *Comparing Spectroscopic and Photometric Stellar Mass Estimates*, ApJ, 616, L103
- Drory, N., Bender, R., Snigula, J., Feulner, G., Hopp, U., Maraston, C., Hill, G. J., & Mendes de Oliveira, C. 2001a: *The Munich Near-Infrared Cluster Survey: Number Density Evolution of Massive Field Galaxies to $z \sim 1.2$ as Derived from the K-Band-selected Survey*, ApJ, 562, L111 (MUNICS III)
- Drory, N., Feulner, G., Bender, R., Botzler, C. S., Hopp, U., Maraston, C., Mendes de Oliveira, C., & Snigula, J. 2001b: *The Munich Near-Infrared Cluster Survey – I. Field selection, object extraction, and photometry*, MNRAS, 325, 550 (MUNICS I)
- Ebeling, H. 2003: *Improved approximations of Poissonian errors for high confidence levels*, MNRAS, 340, 1269
- Ebeling, H. 2004: *Erratum: Improved approximations of Poissonian errors for high confidence levels*, MNRAS, 349, 768
- Einstein, A. 1916: *Die Grundlage der allgemeinen Relativitätstheorie*, Annalen der Physik, 49, 769
- Ellingson, E. 1989: *A User's Guide to Multislit Spectroscopic Reductions with IRAF*, available at <http://iraf.noao.edu/>

- Ellis, R., Santos, M. R., Kneib, J., & Kuijken, K. 2001: *A Faint Star-forming System Viewed through the Lensing Cluster Abell 2218: First Light at $z \simeq 5.6$?*, ApJ, 560, L119
- Ellis, R. S. 1997: *Faint Blue Galaxies*, ARA&A, 35, 389
- Ellis, R. S., Colless, M., Broadhurst, T., Heyl, J., & Glazebrook, K. 1996: *Autofib Redshift Survey - I. Evolution of the galaxy luminosity function*, MNRAS, 280, 235
- Ellis, R. S., Smail, I., Dressler, A., Couch, W. J., Oemler, A. J., Butcher, H., & Sharples, R. M. 1997: *The Homogeneity of Spheroidal Populations in Distant Clusters*, ApJ, 483, 582
- Elston, R., Rieke, G. H., & Rieke, M. J. 1988: *Deep 2 micron imaging of the sky - Evidence for a new extragalactic population*, ApJ, 331, L77
- Elston, R., Rieke, M. J., & Rieke, G. H. 1989: *Observations of deep 2 micron survey galaxies - Primeval galaxy candidates*, ApJ, 341, 80
- Evans, N. J. 1999: *Physical Conditions in Regions of Star Formation*, ARA&A, 37, 311
- Falco, E. E., Kurtz, M. J., Geller, M. J., Huchra, J. P., Peters, J., Berlind, P., Mink, D. J., Tokarz, S. P., *et al.* 1999: *The Updated Zwicky Catalog (UZC)*, PASP, 111, 438
- Fan, X., Narayanan, V. K., Lupton, R. H., Strauss, M. A., Knapp, G. R., Becker, R. H., White, R. L., Pentericci, L., *et al.* 2001: *A Survey of $z > 5.8$ Quasars in the Sloan Digital Sky Survey. I. Discovery of Three New Quasars and the Spatial Density of Luminous Quasars at $z \sim 6$* , AJ, 122, 2833
- Fan, X., Strauss, M. A., Schneider, D. P., Becker, R. H., White, R. L., Haiman, Z., Gregg, M., Pentericci, L., *et al.* 2003: *A Survey of $z > 5.7$ Quasars in the Sloan Digital Sky Survey. II. Discovery of Three Additional Quasars at $z > 6$* , AJ, 125, 1649
- Fanson, J. L., Fazio, G. G., Houck, J. R., Kelly, T., Rieke, G. H., Tenerelli, D. J., & Whitten, M. 1998: *Space Infrared Telescope Facility (SIRTF)*, in: Proc. SPIE Vol. 3356, p. 478-491, Space Telescopes and Instruments V, Pierre Y. Bely; James B. Breckinridge; Eds., 478-491
- Ferguson, H. C., Dickinson, M., Giavalisco, M., Kretchmer, C., Ravindranath, S., Idzi, R., Taylor, E., Conselice, C. J., *et al.* 2004: *The Size Evolution of High-Redshift Galaxies*, ApJ, 600, L107
- Ferguson, H. C., Dickinson, M., & Williams, R. 2000: *The Hubble Deep Fields*, ARA&A, 38, 667
- Ferrarese, L. & Merritt, D. 2000: *A Fundamental Relation between Supermassive Black Holes and Their Host Galaxies*, ApJ, 539, L9

- Feulner, G. 2000: *Optische Komplementärbeobachtungen zur Suche nach Galaxienhaufen im Infraroten*, Diplomarbeit, Ludwig–Maximilians–Universität München
- Feulner, G., Bender, R., Drory, N., Hopp, U., Snigula, J., & Hill, G. J. 2003: *The Munich Near-Infrared Cluster Survey - V. The evolution of the rest-frame K- and J-band galaxy luminosity functions to $z \sim 0.7$* , MNRAS, 342, 605 (MUNICS V)
- Fixsen, D. J., Cheng, E. S., Gales, J. M., Mather, J. C., Shafer, R. A., & Wright, E. L. 1996: *The Cosmic Microwave Background Spectrum from the Full COBE FIRAS Data Set*, ApJ, 473, 576
- Flores, H., Hammer, F., Thuan, T. X., Césarsky, C., Desert, F. X., Omont, A., Lilly, S. J., Eales, S., *et al.* 1999: *15 Micron Infrared Space Observatory Observations of the 1415+52 Canada-France Redshift Survey Field: The Cosmic Star Formation Rate as Derived from Deep Ultraviolet, Optical, Mid-Infrared, and Radio Photometry*, ApJ, 517, 148
- Folkes, S., Ronen, S., Price, I., Lahav, O., Colless, M., Maddox, S., Deeley, K., Glazebrook, K., *et al.* 1999: *The 2dF Galaxy Redshift Survey: spectral types and luminosity functions*, MNRAS, 308, 459
- Fontana, A., Pozzetti, L., Donnarumma, I., Renzini, A., Cimatti, A., Zamorani, G., Menci, N., Daddi, E., *et al.* 2004: *The K20 survey. VI. The distribution of the stellar masses in galaxies up to $z \simeq 2$* , A&A, 424, 23
- Franx, M., Labbé, I., Rudnick, G., van Dokkum, P. G., Daddi, E., Förster Schreiber, N. M., Moorwood, A., Rix, H., *et al.* 2003: *A Significant Population of Red, Near-Infrared-selected High-Redshift Galaxies*, ApJ, 587, L79
- Friedmann, A. 1922: *Über die Krümmung des Raumes*, Zeitschrift für Physik, 10, 377
- Frye, B., Broadhurst, T., & Benítez, N. 2002: *Spectral Evidence for Widespread Galaxy Outflows at $z > 4$* , ApJ, 568, 558
- Gabasch, A. 2004: *Galaxy Evolution in the FORS Deep Field*, PhD thesis, Ludwig–Maximilians–Universität München
- Gabasch, A., Bender, R., Seitz, S., Hopp, U., Saglia, R. P., Feulner, G., Snigula, J., Drory, N., *et al.* 2004a: *The evolution of the luminosity functions in the FORS Deep Field from low to high redshift: I. The blue bands*, A&A, 421, 41
- Gabasch, A., Bender, R., Seitz, S., Hopp, U., Saglia, R. P., Feulner, G., Snigula, J., Drory, N., *et al.* 2004b: *The evolution of the luminosity functions in the FORS Deep Field from low to high redshift: I. The red bands*, A&A, in preparation
- Gabasch, A., Salvato, M., Saglia, R. P., Bender, R., Hopp, U., Seitz, S., Feulner, G., Pannella, M., *et al.* 2004c: *The Star Formation Rate History in the FORS Deep and GOODS-South Fields*, ApJ, 616, L83

- Gallego, J., Zamorano, J., Aragon-Salamanca, A., & Rego, M. 1995: *The Current Star Formation Rate of the Local Universe*, ApJ, 455, L1
- Gardner, J. P., Sharples, R. M., Frenk, C. S., & Carrasco, B. E. 1997: *A Wide-Field K-band Survey: The Luminosity Function of Galaxies*, ApJ, 480, L99
- Gebhardt, K., Bender, R., Bower, G., Dressler, A., Faber, S. M., Filippenko, A. V., Green, R., Grillmair, C., *et al.* 2000: *A Relationship between Nuclear Black Hole Mass and Galaxy Velocity Dispersion*, ApJ, 539, L13
- Gebhardt, K., Faber, S. M., Koo, D. C., Im, M., Simard, L., Illingworth, G. D., Phillips, A. C., Sarajedini, V. L., *et al.* 2003: *The DEEP Groth Strip Survey. IX. Evolution of the Fundamental Plane of Field Galaxies*, ApJ, 597, 239
- Gehrels, N. 1986: *Confidence limits for small numbers of events in astrophysical data*, ApJ, 303, 336
- Geller, M. J. & Huchra, J. P. 1989: *Mapping the universe*, Science, 246, 897
- Giavalisco, M. 2002: *Lyman-Break Galaxies*, ARA&A, 40, 579
- Giavalisco, M. & Dickinson, M. 2001: *Clustering Segregation with Ultraviolet Luminosity in Lyman Break Galaxies at $z \sim 3$ and Its Implications*, ApJ, 550, 177
- Giavalisco, M., Ferguson, H. C., Koekemoer, A. M., Dickinson, M., Alexander, D. M., Bauer, F. E., Bergeron, J., Biagetti, C., *et al.* 2004: *The Great Observatories Origins Deep Survey: Initial Results from Optical and Near-Infrared Imaging*, ApJ, 600, L93
- Giavalisco, M., Steidel, C. C., Adelberger, K. L., Dickinson, M. E., Pettini, M., & Kellogg, M. 1998: *The Angular Clustering of Lyman-Break Galaxies at Redshift $z \sim 3$* , ApJ, 503, 543
- Giavalisco, M., Steidel, C. C., & Macchetto, F. D. 1996: *Hubble Space Telescope Imaging of Star-forming Galaxies at Redshifts $z > 3$* , ApJ, 470, 189
- Glazebrook, K., Abraham, R. G., McCarthy, P. J., Savaglio, S., Chen, H., Crampton, D., Murowinski, R., Jørgensen, I., *et al.* 2004: *A high abundance of massive galaxies 3-6 billion years after the Big Bang*, Nature, 430, 181
- Glazebrook, K., Peacock, J. A., Miller, L., & Collins, C. A. 1995: *An Imaging K-band survey – II. The redshift survey and galaxy evolution in the infrared*, MNRAS, 275, 169
- Gössl, C. A. & Riffeser, A. 2002: *Image reduction pipeline for the detection of variable sources in highly crowded fields*, A&A, 381, 1095
- Graham, J. R. & Dey, A. 1996: *The Redshift of an Extremely Red Object and the Nature of the Very Red Galaxy Population*, ApJ, 471, 720

- Grebel, E. K. 2004: *The Evolutionary History of Local Group Irregular Galaxies*, in: *Origin and Evolution of the Elements*, 237
- Gronwall, C. 1999: *The Star Formation Rate Density of the Local Universe from the KPNO International Spectroscopic Survey*, in: *AIP Conf. Proc. 470: After the Dark Ages: When Galaxies were Young (the Universe at $2 \leq z \leq 5$)*, 335
- Gunn, J. E. & Stryker, L. L. 1983: *Stellar spectrophotometric atlas, wavelengths from 3130 to 10800 Å*, *ApJS*, 52, 121
- Guth, A. H. 1981: *Inflationary universe: A possible solution to the horizon and flatness problems*, *Phys. Rev. D*, 23, 347
- Hammer, F., Crampton, D., Le Fèvre, O., & Lilly, S. J. 1995: *The Canada-France Redshift Survey. IV. Spectroscopic Selection Effects and 0300+00 Field Spectroscopic Data*, *ApJ*, 455, 88
- Hatton, S., Devriendt, J. E. G., Ninin, S., Bouchet, F. R., Guiderdoni, B., & Vibert, D. 2003: *GALICS- I. A hybrid N-body/semi-analytic model of hierarchical galaxy formation*, *MNRAS*, 343, 75
- Heidt, J., Appenzeller, I., Gabasch, A., Jäger, K., Seitz, S., Bender, R., Böhm, A., Snigula, J., *et al.* 2003: *The FORS Deep Field: Field selection, photometric observations and photometric catalog*, *A&A*, 398, 49
- Hernquist, L. & Springel, V. 2003: *An analytical model for the history of cosmic star formation*, *MNRAS*, 341, 1253
- Heydon-Dumbleton, N. H., Collins, C. A., & MacGillivray, H. T. 1989: *The Edinburgh/Durham Southern Galaxy Catalogue. II - Image classification and galaxy number counts*, *MNRAS*, 238, 379
- Heyl, J., Colless, M., Ellis, R. S., & Broadhurst, T. 1997: *Autofib Redshift Survey - II. Evolution of the galaxy luminosity function by spectral type*, *MNRAS*, 285, 613
- Hill, G. J., Nicklas, H. E., MacQueen, P. J., Tejada, C., Cobos Duenas, F. J., & Mitsch, W. 1998in: *Proc. SPIE, Optical Astronomical Instrumentation*, ed. Sandro D'Odorico, Vol. 3355,, 375
- Hinshaw, G., Spergel, D. N., Verde, L., Hill, R. S., Meyer, S. S., Barnes, C., Bennett, C. L., Halpern, M., *et al.* 2003: *First-Year Wilkinson Microwave Anisotropy Probe (WMAP) Observations: The Angular Power Spectrum*, *ApJS*, 148, 135
- Hogg, D. W., Cohen, J. G., Blandford, R., & Pahre, M. A. 1998: *The O II Luminosity Density of the Universe*, *ApJ*, 504, 622
- Holden, B. P., Stanford, S. A., Eisenhardt, P., & Dickinson, M. 2004: *Evolution in the Color-Magnitude Relation of Early-Type Galaxies in Clusters of Galaxies at $z \simeq 1$* , *AJ*, 127, 2484

- Holland, W. S., Robson, E. I., Gear, W. K., Cunningham, C. R., Lightfoot, J. F., Jenness, T., Ivison, R. J., Stevens, J. A., *et al.* 1999: *SCUBA: a common-user submillimetre camera operating on the James Clerk Maxwell Telescope*, MNRAS, 303, 659
- Hopp, U. & Fernández, M. 2002: *Extinction coefficients for Calar Alto*, Calar Alto Newsletter, No. 4, available online at <http://www.caha.es/newsletter/news02a/hopp/paper.pdf>
- Horne, K. 1986: *An optimal extraction algorithm for CCD spectroscopy*, PASP, 98, 609
- Howell, S. B. 2000: *Handbook of CCD Astronomy*, Cambridge University Press
- Hu, E. M., Cowie, L. L., & McMahon, R. G. 1998: *The Density of Ly alpha Emitters at Very High Redshift*, ApJ, 502, L99
- Hu, E. M., Cowie, L. L., McMahon, R. G., Capak, P., Iwamuro, F., Kneib, J.-P., Maihara, T., & Motohara, K. 2002: *A Redshift $z = 6.56$ Galaxy behind the Cluster Abell 370*, ApJ, 568, L75
- Hu, E. M., McMahon, R. G., & Cowie, L. L. 1999: *An Extremely Luminous Galaxy at $z = 5.74$* , ApJ, 522, L9
- Hu, E. M. & Ridgway, S. E. 1994: *Two extremely red galaxies*, AJ, 107, 1303
- Hu, W. & Dodelson, S. 2002: *Cosmic Microwave Background Anisotropies*, ARA&A, 40, 171
- Huang, J.-S., Glazebrook, K., Cowie, L. L., & Tinney, C. 2003: *The Hawaii+Anglo-Australian Observatory K-Band Galaxy Redshift Survey. I. The Local K-Band Luminosity Function*, ApJ, 584, 203
- Hubble, E. 1929: *A Relation between Distance and Radial Velocity among Extragalactic Nebulae*, Proceedings of the National Academy of Science, 15, 168
- Hubble, E. P. 1926: *Extragalactic nebulae*, ApJ, 64, 321
- Hughes, D. H., Serjeant, S., Dunlop, J., Rowan-Robinson, M., Blain, A., Mann, R. G., Ivison, R., Peacock, J., *et al.* 1998: *High-redshift star formation in the Hubble Deep Field revealed by a submillimetre-wavelength survey*, Nature, 394, 241
- Ilbert, O. *et al.* 2004: *The VIMOS-VLT Deep Survey: Evolution of the galaxy luminosity function up to $z = 2$ in first epoch data*, A&A, submitted, astro-ph/0409134
- Infante, L., Pritchet, C., & Quintana, H. 1986: *Galaxy counts and colors in a South Galactic Pole field*, AJ, 91, 217
- Jarrett, T. H., Chester, T., Cutri, R., Schneider, S., Skrutskie, M., & Huchra, J. P. 2000: *2MASS Extended Source Catalog: Overview and Algorithms*, AJ, 119, 2498

- Jarvis, J. F. & Tyson, J. A. 1981: *FOCAS - Faint Object Classification and Analysis System*, AJ, 86, 476
- J Jeans, J. H. 1928: *Astronomy and cosmogony*, Cambridge University Press
- Jenkins, A., Frenk, C. S., White, S. D. M., Colberg, J. M., Cole, S., Evrard, A. E., Couchman, H. M. P., & Yoshida, N. 2001: *The mass function of dark matter haloes*, MNRAS, 321, 372
- Jones, D. H., Saunders, W., Colless, M., Read, M. A., Parker, Q. A., Watson, F. G., Campbell, L. A., Burkey, D., *et al.* 2004: *The 6dF Galaxy Survey: samples, observational techniques and the first data release*, MNRAS, 355, 747
- Jones, L. R., Fong, R., Shanks, T., Ellis, R. S., & Peterson, B. A. 1991: *Galaxy number counts. I - Photographic observations to $B = 23.5$ mag*, MNRAS, 249, 481
- Jørgensen, I., Franx, M., Hjorth, J., & van Dokkum, P. G. 1999: *The evolution of cluster E and S0 galaxies measured from the Fundamental Plane*, MNRAS, 308, 833
- Kajisawa, M. & Yamada, T. 2001: *When Did the Hubble Sequence Appear?: Morphology, Color, and Number-Density Evolution of the Galaxies in the Hubble Deep Field North*, PASJ, 53, 833
- Kannappan, S. J. 2004: *Linking Gas Fractions to Bimodalities in Galaxy Properties*, ApJ, 611, L89
- Kashikawa, N., Takata, T., Ohyama, Y., Yoshida, M., Maihara, T., Iwamuro, F., Motohara, K., Totani, T., *et al.* 2003: *Subaru Deep Survey. III. Evolution of Rest-Frame Luminosity Functions Based on the Photometric Redshifts for a K'-Band-Selected Galaxy Sample*, AJ, 125, 53
- Kauffmann, G. & Charlot, S. 1998: *The K-band luminosity function at $z=1$: a powerful constraint on galaxy formation theory*, MNRAS, 297, L23
- Kauffmann, G., Colberg, J. M., Diaferio, A., & White, S. D. M. 1999: *Clustering of galaxies in a hierarchical universe - I. Methods and results at $z=0$* , MNRAS, 303, 188
- Kelson, D. D., Illingworth, G. D., van Dokkum, P. G., & Franx, M. 2000: *The Evolution of Early-Type Galaxies in Distant Clusters. III. M/L_V Ratios in the $z = 0.33$ Cluster CL 1358+62*, ApJ, 531, 184
- Kennicutt, R. C. 1992: *The integrated spectra of nearby galaxies - General properties and emission-line spectra*, ApJ, 388, 310
- Kinney, A. L., Calzetti, D., Bohlin, R. C., McQuade, K., Storchi-Bergmann, T., & Schmitt, H. R. 1996: *Template Ultraviolet to Near-Infrared Spectra of Star-forming Galaxies and Their Application to K-Corrections*, ApJ, 467, 38

- Kochanek, C. S., Pahre, M. A., Falco, E. E., Huchra, J. P., Mader, J., Jarrett, T. H., Chester, T., Cutri, R., *et al.* 2001: *The K-Band Galaxy Luminosity Function*, ApJ, 560, 566
- Kodaira, K., Taniguchi, Y., Kashikawa, N., Kaifu, N., Ando, H., Karoji, H., Ajiki, M., Akiyama, M., *et al.* 2003: *The Discovery of Two Lyman α Emitters beyond Redshift 6 in the Subaru Deep Field*, PASJ, 55, L17
- Kodama, T., Yamada, T., Akiyama, M., Aoki, K., Doi, M., Furusawa, H., Fuse, T., Imanishi, M., *et al.* 2004: *Down-sizing in galaxy formation at $z \sim 1$ in the Subaru/XMM-Newton Deep Survey (SXDS)*, MNRAS, 350, 1005
- Kolb, E. W. & Turner, M. S. 1990: *The early universe*, Frontiers in Physics, Addison-Wesley, Reading, MA
- Koo, D. C. 1985: *Optical multicolors - A poor person's Z machine for galaxies*, AJ, 90, 418
- Koo, D. C. 1986: *Multicolor photometry of field galaxies to $B = 24$* , ApJ, 311, 651
- Kormendy, J. 2004: *The Stellar-Dynamical Search for Supermassive Black Holes in Galactic Nuclei*, in: *Coevolution of Black Holes and Galaxies*, 1
- Kormendy, J. & Richstone, D. 1995: *Inward Bound—The Search For Supermassive Black Holes In Galactic Nuclei*, ARA&A, 33, 581
- Kron, R. G. 1978: *Photometry of a complete sample of faint galaxies*, PhD thesis, California University, Berkeley
- Kurk, J. D., Cimatti, A., di Serego Alighieri, S., Vernet, J., Daddi, E., Ferrara, A., & Ciardi, B. 2004: *A Lyman α emitter at $z = 6.5$ found with slitless spectroscopy*, A&A, 422, L13
- Landolt, A. U. 1992: *UBVRI Photometric Standard Stars in the Magnitude Range $11.5 < V < 16.0$ Around the Celestial Equator*, AJ, 104, 340
- Le Fèvre, O., Crampton, D., Lilly, S. J., Hammer, F., & Tresse, L. 1995: *The Canada-France Redshift Survey. II. Spectroscopic Program: Data for the 0000-00 and 1000+25 Fields*, ApJ, 455, 60
- Le Fèvre, O. *et al.* 2004: *First epoch VVDS-Deep survey: 11564 spectra with $17.5 \leq I_{AB} \leq 24$, and the redshift distribution over $0 \leq z \leq 5$* , A&A, submitted, astro-ph/0409133
- Lehnert, M. D. & Bremer, M. 2003: *Luminous Lyman Break Galaxies at $z > 5$ and the Source of Reionization*, ApJ, 593, 630
- Lilly, S. J., Cowie, L. L., & Gardner, J. P. 1991: *A deep imaging and spectroscopic survey of faint galaxies*, ApJ, 369, 79

- Lilly, S. J., Hammer, F., Le Fèvre, O., & Crampton, D. 1995a: *The Canada-France Redshift Survey. III. "Single Emission-Line" Objects, Analysis of Repeat Observations, and Spectroscopic Identifications in the 1415+52 and 2215+00 Fields*, ApJ, 455, 75
- Lilly, S. J., Le Fèvre, O., Crampton, D., Hammer, F., & Tresse, L. 1995b: *The Canada-France Redshift Survey. I. Introduction to the Survey, Photometric Catalogs, and Surface Brightness Selection Effects*, ApJ, 455, 50
- Lilly, S. J., Le Fèvre, O., Hammer, F., & Crampton, D. 1996: *The Canada-France Redshift Survey: The Luminosity Density and Star Formation History of the Universe to $z \sim 1$* , ApJ, 460, L1
- Lilly, S. J., Tresse, L., Hammer, F., Crampton, D., & Le Fèvre, O. 1995c: *The Canada-France Redshift Survey. VI. Evolution of the Galaxy Luminosity Function to $z \sim 1$* , ApJ, 455, 108
- Lin, H., Yee, H. K. C., Carlberg, R. G., Morris, S. L., Sawicki, M., Patton, D. R., Wirth, G., & Shepherd, C. W. 1999: *The CNOC2 Field Galaxy Luminosity Function. I. A Description of Luminosity Function Evolution*, ApJ, 518, 533
- Longair, M. S. 1998: *Galaxy Formation*, Springer Verlag
- Loveday, J. 2000: *The K-band luminosity function of nearby field galaxies*, MNRAS, 312, 557
- Loveday, J. 2004: *Evolution of the galaxy luminosity function at $z < 0.3$* , MNRAS, 347, 601
- Loveday, J., Peterson, B. A., Maddox, S. J., & Efstathiou, G. 1996: *The Stromlo-APM Redshift Survey. IV. The Redshift Catalog*, ApJS, 107, 201
- Lowenthal, J. D., Koo, D. C., Guzman, R., Gallego, J., Phillips, A. C., Faber, S. M., Vogt, N. P., Illingworth, G. D., *et al.* 1997: *Keck Spectroscopy of Redshift $z \sim 3$ Galaxies in the Hubble Deep Field*, ApJ, 481, 673
- Madau, P., Ferguson, H. C., Dickinson, M. E., Giavalisco, M., Steidel, C. C., & Fruchter, A. 1996: *High-redshift galaxies in the Hubble Deep Field: colour selection and star formation history to $z \sim 4$* , MNRAS, 283, 1388
- Madau, P., Pozzetti, L., & Dickinson, M. 1998: *The Star Formation History of Field Galaxies*, ApJ, 498, 106
- Maddox, S. J., Efstathiou, G., Sutherland, W. J., & Loveday, J. 1990a: *The APM galaxy survey. I - APM measurements and star-galaxy separation*, MNRAS, 243, 692
- Maddox, S. J., Sutherland, W. J., Efstathiou, G., Loveday, J., & Peterson, B. A. 1990b: *Galaxy Evolution at Low Redshift*, MNRAS, 247, 1

- Maraston, C. 1998: *Evolutionary synthesis of stellar populations: a modular tool*, MNRAS, 300, 872
- Marleau, F. R. & Simard, L. 1998: *Quantitative Morphology of Galaxies in the Hubble Deep Field*, ApJ, 507, 585
- Marsh, T. R. 1989: *The extraction of highly distorted spectra*, PASP, 101, 1032
- Martini, P. 2001: *A Deep Multicolor Survey. VII. Extremely Red Objects and Galaxy Formation*, AJ, 121, 2301
- Massey, P. 1997: *A User's Guide to CCD Reductions with IRAF*, available at <http://iraf.noao.edu/>
- Mateo, M. L. 1998: *Dwarf Galaxies of the Local Group*, ARA&A, 36, 435
- McCarthy, P. J. 2004: *EROs and Faint Red Galaxies*, Annual Reviews of Astronomy and Astrophysics, 10.1146/annurev.astro.42.053102.134032, First published online as a Review in Advance on June 1, 2004
- McCarthy, P. J., Carlberg, R. G., Chen, H.-W., Marzke, R. O., Firth, A. E., Ellis, R. S., Persson, S. E., McMahon, R. G., *et al.* 2001: *The Las Campanas Infrared Survey: Early-Type Galaxy Progenitors beyond $z=1$* , ApJ, 560, L131
- Metcalf, N., Fong, R., & Shanks, T. 1995a: *CCD galaxy photometry and the calibration of photographic surveys*, MNRAS, 274, 769
- Metcalf, N., Ratcliffe, A., Shanks, T., & Fong, R. 1998: *UBVRI photometry of the Durham-AAT redshift survey*, MNRAS, 294, 147
- Metcalf, N., Shanks, T., Campos, A., McCracken, H. J., & Fong, R. 2001: *Galaxy number counts - V. Ultradeep counts: the Herschel and Hubble Deep Fields*, MNRAS, 323, 795
- Metcalf, N., Shanks, T., Fong, R., & Jones, L. R. 1991: *Galaxy number counts. II - CCD observations to $B = 25$ mag*, MNRAS, 249, 498
- Metcalf, N., Shanks, T., Fong, R., & Roche, N. 1995b: *Galaxy number counts - III. Deep CCD observations to $B=27.5$ mag*, MNRAS, 273, 257
- Mobasher, B., Sharples, R. M., & Ellis, R. S. 1993: *A Complete Galaxy Redshift Survey - Part Five - Infrared Luminosity Functions for Field Galaxies*, MNRAS, 263, 560
- Moriondo, G., Cimatti, A., & Daddi, E. 2000: *The morphology of extremely red objects*, A&A, 364, 26
- Moustakas, L. A., Casertano, S., Conselice, C. J., Dickinson, M. E., Eisenhardt, P., Ferguson, H. C., Giavalisco, M., Grogin, N. A., *et al.* 2004: *Morphologies and Spectral Energy Distributions of Extremely Red Galaxies in the GOODS-South Field*, ApJ, 600, L131

- Munn, J. A., Koo, D. C., Kron, R. G., Majewski, S. R., Bershad, M. A., & Smetanka, J. J. 1997: *The Kitt Peak Galaxy Redshift Survey with Multicolor Photometry: Basic Data*, ApJS, 109, 45
- Nagao, T., Taniguchi, Y., Kashikawa, N., Kodaira, K., Kaifu, N., Ando, H., Karoji, H., Ajiki, M., *et al.* 2004: *A Strong Ly α Emitter at $z = 6.33$ in the Subaru Deep Field Selected as an i' -Dropout*, ApJ, 613, L9
- Narlikar, J. V. & Padmanabhan, T. 1991: *Inflation for astronomers*, ARA&A, 29, 325
- Odehahn, S. C., Windhorst, R. A., Driver, S. P., & Keel, W. C. 1996: *Automated Morphological Classification in Deep Hubble Space Telescope UBVI Fields: Rapidly and Passively Evolving Faint Galaxy Populations*, ApJ, 472, L13
- Osterbrock, D. E., Fulbright, J. P., & Bida, T. A. 1997: *Night-Sky High-Resolution Spectral Atlas of OH Emission Lines for Echelle Spectrograph Wavelength Calibration. II*, PASP, 109, 614
- Osterbrock, D. E., Fulbright, J. P., Martel, A. R., Keane, M. J., Trager, S. C., & Basri, G. 1996: *Night-Sky High-Resolution Spectral Atlas of OH and O2 Emission Lines for Echelle Spectrograph Wavelength Calibration*, PASP, 108, 277
- Pérez-González, P. G., Gil de Paz, A., Zamorano, J., Gallego, J., Alonso-Herrero, A., & Aragón-Salamanca, A. 2003: *Stellar populations in local star-forming galaxies - II. Recent star formation properties and stellar masses*, MNRAS, 338, 525
- Papovich, C., Dickinson, M., & Ferguson, H. C. 2001: *The Stellar Populations and Evolution of Lyman Break Galaxies*, ApJ, 559, 620
- Partridge, R. B. & Peebles, P. J. E. 1967: *Are Young Galaxies Visible?*, ApJ, 147, 868
- Pascarelle, S. M., Lanzetta, K. M., & Fernández-Soto, A. 1998: *The Ultraviolet Luminosity Density of the Universe from Photometric Redshifts of Galaxies in the Hubble Deep Field*, ApJ, 508, L1
- Peacock, J. A. 1999: *Cosmological physics*, Cambridge University Press
- Peebles, P. J. E. 1980: *The large-scale structure of the universe*, Princeton University Press
- Peebles, P. J. E. 1993: *Principles of physical cosmology*, Princeton University Press
- Peebles, P. J. E. 2002: *When did the Large Elliptical Galaxies Form?*, in: ASP Conf. Ser. 283: A New Era in Cosmology, 351
- Penzias, A. A. & Wilson, R. W. 1965: *A Measurement of Excess Antenna Temperature at 4080 Mc/s.*, ApJ, 142, 419
- Peterson, B. A., Ellis, R. S., Efstathiou, G., Shanks, T., Bean, A. J., Fong, R., & Zen-Long, Z. 1986: *A complete galaxy redshift sample. III - Methods and catalogue*, MNRAS, 221, 233

- Peterson, J. R., Kahn, S. M., Paerels, F. B. S., Kaastra, J. S., Tamura, T., Bleeker, J. A. M., Ferrigno, C., & Jernigan, J. G. 2003: *High-Resolution X-Ray Spectroscopic Constraints on Cooling-Flow Models for Clusters of Galaxies*, ApJ, 590, 207
- Pettini, M., Shapley, A. E., Steidel, C. C., Cuby, J., Dickinson, M., Moorwood, A. F. M., Adelberger, K. L., & Giavalisco, M. 2001: *The Rest-Frame Optical Spectra of Lyman Break Galaxies: Star Formation, Extinction, Abundances, and Kinematics*, ApJ, 554, 981
- Planck, M. 1899: *Über irreversible Strahlungsvorgänge: Fünfte Mittheilung (Schluss)*, Sitzungsberichte der Königlich Preußischen Akademie der Wissenschaften zu Berlin, 1899 (I), 440
- Poggianti, B. M., Bridges, T. J., Komiyama, Y., Yagi, M., Carter, D., Mobasher, B., Okamura, S., & Kashikawa, N. 2004: *A Comparison of the Galaxy Populations in the Coma and Distant Clusters: The Evolution of $k+a$ Galaxies and the Role of the Intracluster Medium*, ApJ, 601, 197
- Porciani, C. & Giavalisco, M. 2002: *The Clustering Properties of Lyman Break Galaxies at Redshift $z \sim 3$* , ApJ, 565, 24
- Pozzetti, L., Cimatti, A., Zamorani, G., Daddi, E., Menci, N., Fontana, A., Renzini, A., Mignoli, M., *et al.* 2003: *The K20 survey. V. The evolution of the near-IR Luminosity Function*, A&A, 402, 837
- Pozzetti, L. & Mannucci, F. 2000: *Extremely red galaxies: age and dust degeneracy solved?*, MNRAS, 317, L17
- Rees, M. J. & Ostriker, J. P. 1977: *Cooling, dynamics and fragmentation of massive gas clouds - Clues to the masses and radii of galaxies and clusters*, MNRAS, 179, 541
- Rhoads, J. E., Dey, A., Malhotra, S., Stern, D., Spinrad, H., Jannuzi, B. T., Dawson, S., Brown, M. J. I., *et al.* 2003: *Spectroscopic Confirmation of Three Redshift $z \sim 5.7$ Ly α Emitters from the Large-Area Lyman Alpha Survey*, AJ, 125, 1006
- Rix, H. & Rieke, M. J. 1993: *Tracing the Stellar Mass in M51*, ApJ, 418, 123
- Robertson, H. P. 1935: *Kinematics and World-Structure*, ApJ, 82, 284
- Robertson, H. P. 1936a: *Kinematics and World-Structure II.*, ApJ, 83, 187
- Robertson, H. P. 1936b: *Kinematics and World-Structure III.*, ApJ, 83, 257
- Roche, N. D., Almaini, O., Dunlop, J., Ivison, R. J., & Willott, C. J. 2002: *The clustering, number counts and morphology of extremely red ($R - K > 5$) galaxies to $K < 21$* , MNRAS, 337, 1282
- Rosa-González, D., Terlevich, E., & Terlevich, R. 2002: *An empirical calibration of star formation rate estimators*, MNRAS, 332, 283

- Rudnick, G., Rix, H., Franx, M., Labbé, I., Blanton, M., Daddi, E., Förster Schreiber, N. M., Moorwood, A., *et al.* 2003: *The Rest-Frame Optical Luminosity Density, Color, and Stellar Mass Density of the Universe from $z = 0$ to $z = 3$* , *ApJ*, 599, 847
- Sachs, R. K. & Wolfe, A. M. 1967: *Perturbations of a Cosmological Model and Angular Variations of the Microwave Background*, *ApJ*, 147, 73
- Saha, P. 1995: *On Magnitude Limits for Point Source Detections*, *AJ*, 110, 916
- Salpeter, E. E. 1955: *The Luminosity Function and Stellar Evolution*, *ApJ*, 121, 161
- Saracco, P., Longhetti, M., Severgnini, P., Della Ceca, R., Mannucci, F., Bender, R., Drory, N., Feulner, G., *et al.* 2003: *Massive $z \sim 1.3$ evolved galaxies revealed*, *A&A*, 398, 127 (TESIS I)
- Sawicki, M. J., Lin, H., & Yee, H. K. C. 1997: *Evolution of the Galaxy Population Based on Photometric Redshifts in the Hubble Deep Field*, *AJ*, 113, 1
- Scalo, J. M. 1986: *The stellar initial mass function*, *Fundamentals of Cosmic Physics*, 11, 1
- Schechter, P. 1976: *An analytic expression for the luminosity function for galaxies*, *ApJ*, 203, 297
- Schmidt, B. 1931: *Ein lichtstarkes komafreies Spiegelsystem*, *Centralzeitung für Optik und Mechanik*, 52, 25
- Schmidt, M. 1968: *Space Distribution and Luminosity Functions of Quasi-Stellar Radio Sources*, *ApJ*, 151, 393
- Scott, D. & Smoot, G. F. 2004: *Cosmic Background Radiation Mini-Review*, S. Eidelmann *et al.* (eds.): 'The Review of Particle Physics', *Physics Letters B*, 592, 1
- Seifert, W., Mitsch, W., Nicklas, H., & Rupprecht, G. 1994in: *Proc. SPIE, Instrumentation in Astronomy VIII*, ed. David L. Crawford, Eric R. Craine, Vol. 2198,, 213
- Severgnini, P., Della Ceca, R., Braito, V., Saracco, P., Longhetti, M., Bender, R., Drory, N., Feulner, G., *et al.* 2004: *X-ray Emitting EROs: A Key Population for Type-2 QSOs*, *A&A*, in press, astro-ph/0410434 (TESIS II)
- Shapley, A. E., Steidel, C. C., Adelberger, K. L., Dickinson, M., Giavalisco, M., & Pettini, M. 2001: *The Rest-Frame Optical Properties of $z \simeq 3$ Galaxies*, *ApJ*, 562, 95
- Shectman, S. A., Landy, S. D., Oemler, A., Tucker, D. L., Lin, H., Kirshner, R. P., & Schechter, P. L. 1996: *The Las Campanas Redshift Survey*, *ApJ*, 470, 172
- Silk, J. 1968: *Cosmic Black-Body Radiation and Galaxy Formation*, *ApJ*, 151, 459

- Smail, I., Ivison, R. J., & Blain, A. W. 1997: *A Deep Sub-millimeter Survey of Lensing Clusters: A New Window on Galaxy Formation and Evolution*, ApJ, 490, L5
- Smail, I., Ivison, R. J., Blain, A. W., & Kneib, J.-P. 2002a: *The nature of faint submillimetre-selected galaxies*, MNRAS, 331, 495
- Smail, I., Ivison, R. J., Kneib, J.-P., Cowie, L. L., Blain, A. W., Barger, A. J., Owen, F. N., & Morrison, G. 1999: *The discovery of ERO counterparts to faint submillimetre galaxies*, MNRAS, 308, 1061
- Smail, I., Owen, F. N., Morrison, G. E., Keel, W. C., Ivison, R. J., & Ledlow, M. J. 2002b: *The Diversity of Extremely Red Objects*, ApJ, 581, 844
- Smith, G. P., Smail, I., Kneib, J.-P., Czoske, O., Ebeling, H., Edge, A. C., Pelló, R., Ivison, R. J., *et al.* 2002: *A Hubble Space Telescope lensing survey of X-ray-luminous galaxy clusters - II. A search for gravitationally lensed EROs*, MNRAS, 330, 1
- Snigula, J. 2001: *Analyse der Galaxienverteilung in den Quasarfeldern des MUNICS-Surveys*, Diplomarbeit, Ludwig-Maximilians-Universität München
- Snigula, J., Drory, N., Bender, R., Botzler, C. S., Feulner, G., & Hopp, U. 2002: *The Munich Near-Infrared Cluster Survey – IV. Biases in the Completeness of Deep Near-Infrared Imaging Data*, MNRAS, 336, 1329 (MUNICS IV)
- Soifer, B. T., Matthews, K., Djorgovski, S., Larkin, J., Graham, J. R., Harrison, W., Jernigan, G., Lin, S., *et al.* 1994: *Deep imaging of the field of the $Z = 4.9$ quasar PC 1247+3406, and faint galaxy counts in the K band with the Keck telescope*, ApJ, 420, L1
- Somerville, R. S. & Primack, J. R. 1999: *Semi-analytic modelling of galaxy formation: the local Universe*, MNRAS, 310, 1087
- Somerville, R. S., Primack, J. R., & Faber, S. M. 2001: *The nature of high-redshift galaxies*, MNRAS, 320, 504
- Songaila, A., Cowie, L. L., Hu, E. M., & Gardner, J. P. 1994: *The Hawaii K-band galaxy survey. 3: Spectroscopy of K less than 20 galaxies*, ApJS, 94, 461
- Spergel, D. N., Verde, L., Peiris, H. V., Komatsu, E., Nolta, M. R., Bennett, C. L., Halpern, M., Hinshaw, G., *et al.* 2003: *First-Year Wilkinson Microwave Anisotropy Probe (WMAP) Observations: Determination of Cosmological Parameters*, ApJS, 148, 175
- Spinrad, H. 2004: *The Most Distant Galaxies*, in: *Astrophysics Update*, ed. J. W. Mason, Springer, 155
- Spinrad, H., Stern, D., Bunker, A., Dey, A., Lanzetta, K., Yahil, A., Pascarelle, S., & Fernández-Soto, A. 1998: *A $z = 5.34$ Galaxy Pair in the Hubble Deep Field*, AJ, 116, 2617

- Stanford, S. A., Eisenhardt, P. R., & Dickinson, M. 1998: *The Evolution of Early-Type Galaxies in Distant Clusters*, ApJ, 492, 461
- Stanford, S. A., Eisenhardt, P. R. M., & Dickinson, M. 1995: *Evolution of Infrared-Selected Galaxies in $z \sim 0.4$ Clusters*, ApJ, 450, 512
- Steidel, C., Adelberger, K., Giavalisco, M., Dickinson, M., Pettini, M., & Kellogg, M. 1999a: *Galaxy clustering at $z \sim 3$* , in: Large-Scale Structure in the Universe, edited by G. Efstathiou *et al.*, Philosophical Transactions of the Royal Society London, Volume 357., 153
- Steidel, C. C., Adelberger, K. L., Dickinson, M., Giavalisco, M., Pettini, M., & Kellogg, M. 1998: *A Large Structure of Galaxies at Redshift $z \sim 3$ and Its Cosmological Implications*, ApJ, 492, 428
- Steidel, C. C., Adelberger, K. L., Giavalisco, M., Dickinson, M., & Pettini, M. 1999b: *Lyman-Break Galaxies at $z \gtrsim 4$ and the Evolution of the Ultraviolet Luminosity Density at High Redshift*, ApJ, 519, 1
- Steidel, C. C., Giavalisco, M., Dickinson, M., & Adelberger, K. L. 1996a: *Spectroscopy of Lyman Break Galaxies in the Hubble Deep Field*, AJ, 112, 352
- Steidel, C. C., Giavalisco, M., Pettini, M., Dickinson, M., & Adelberger, K. L. 1996b: *Spectroscopic Confirmation of a Population of Normal Star-forming Galaxies at Redshifts $z > 3$* , ApJ, 462, L17
- Steidel, C. C. & Hamilton, D. 1992: *Deep imaging of high redshift QSO fields below the Lyman limit. I - The field of Q0000-263 and galaxies at $Z = 3.4$* , AJ, 104, 941
- Steidel, C. C. & Hamilton, D. 1993: *Deep imaging of high redshift QSO fields below the Lyman limit. II - Number counts and colors of field galaxies*, AJ, 105, 2017
- Steidel, C. C., Pettini, M., & Hamilton, D. 1995: *Lyman Imaging of High-Redshift Galaxies. III. New Observations of Four QSO Fields*, AJ, 110, 2519
- Steidel, C. C., Shapley, A. E., Pettini, M., Adelberger, K. L., Erb, D. K., Reddy, N. A., & Hunt, M. P. 2004: *A Survey of Star-forming Galaxies in the $1.4 \lesssim z \lesssim 2.5$ Redshift Desert: Overview*, ApJ, 604, 534
- Stern, D. & Spinrad, H. 1999: *Search Techniques for Distant Galaxies*, PASP, 111, 1475
- Stern, D. *et al.* 2004: *A Galaxy at $z = 6.545$ and Constraints on the Epoch of Reionization*, ApJ, submitted, astro-ph/0407409
- Stevenson, P. R. F., Shanks, T., & Fong, R. 1986: *New observations of galaxy number counts*, in: Spectral Evolution of Galaxies., 439–445
- Stoughton, C., Lupton, R. H., Bernardi, M., Blanton, M. R., Burles, S., Castander, F. J., Connolly, A. J., Eisenstein, D. J., *et al.* 2002: *Sloan Digital Sky Survey: Early Data Release*, AJ, 123, 485

- Sullivan, M., Treyer, M. A., Ellis, R. S., Bridges, T. J., Milliard, B., & Donas, J. 2000: *An ultraviolet-selected galaxy redshift survey - II. The physical nature of star formation in an enlarged sample*, MNRAS, 312, 442
- Szokoly, G. P., Subbarao, M. U., Connolly, A. J., & Mobasher, B. 1998: *The Near-Infrared Number Counts and Luminosity Functions of Local Galaxies*, ApJ, 492, 452
- Takeuchi, T. T., Yoshikawa, K., & Ishii, T. T. 2000: *Tests of Statistical Methods for Estimating Galaxy Luminosity Function and Applications to the Hubble Deep Field*, ApJS, 129, 1
- Tamura, T., Kaastra, J. S., Peterson, J. R., Paerels, F. B. S., Mittaz, J. P. D., Trudolyubov, S. P., Stewart, G., Fabian, A. C., *et al.* 2001: *X-ray spectroscopy of the cluster of galaxies Abell 1795 with XMM-Newton*, A&A, 365, L87
- Taniguchi, Y., Ajiki, M., Murayama, T., Nagao, T., Veilleux, S., Sanders, D. B., Komiyama, Y., Shioya, Y., *et al.* 2003a: *The Discovery of a Very Narrow Line Star-forming Object at a Redshift of 5.66*, ApJ, 585, L97
- Taniguchi, Y., Shioya, Y., Ajiki, M., Fujita, S. S., Nagao, T., & Murayama, T. 2003b: *Lyman α Emitters Beyond Redshift 5: The Dawn of Galaxy Formation*, Journal of Korean Astronomical Society, 36, 123
- Teplitz, H. I., Collins, N. R., Gardner, J. P., Hill, R. S., & Rhodes, J. 2003: *Emission-Line Galaxies in the STIS Parallel Survey. II. Star Formation Density*, ApJ, 589, 704
- Terlevich, A. I., Caldwell, N., & Bower, R. G. 2001: *The colour-magnitude relation for galaxies in the Coma cluster*, MNRAS, 326, 1547
- Thomas, D., Greggio, L., & Bender, R. 1999: *Constraints on galaxy formation from α -enhancement in luminous elliptical galaxies*, MNRAS, 302, 537
- Thompson, D., Beckwith, S. V. W., Fockenbrock, R., Fried, J., Hippelein, H., Huang, J. ., von Kuhlmann, B., Leinert, C., *et al.* 1999: *The Surface Density of Extremely Red Objects*, ApJ, 523, 100
- Tody, D. 1986: *The IRAF Data Reduction and Analysis System*, in: Instrumentation in astronomy VI; Proceedings of the Meeting, Tucson, AZ, Mar. 4-8, 1986. Part 2 (A87-36376 15-35). Bellingham, WA, Society of Photo-Optical Instrumentation Engineers, 1986, p. 733., 733
- Tody, D. 1993: *IRAF in the Nineties*, in: ASP Conf. Ser. 52: Astronomical Data Analysis Software and Systems II., 173
- Tosi, M. 2001: *Stellar Populations and Chemical Evolution of Late-Type Dwarf Galaxies*, in: Dwarf galaxies and their environment., 67

- Tran, K. H., Franx, M., Illingworth, G., Kelson, D. D., & van Dokkum, P. 2003: *The Nature of E+A Galaxies in Intermediate-Redshift Clusters*, ApJ, 599, 865
- Tresse, L. & Maddox, S. J. 1998: *The H α Luminosity Function and Star Formation Rate at $z \sim 0.2$* , ApJ, 495, 691
- Tresse, L., Maddox, S. J., Le Fèvre, O., & Cuby, J.-G. 2002: *The H α luminosity function and star formation rate up to $z \sim 1$* , MNRAS, 337, 369
- Treu, T., Stiavelli, M., Casertano, S., Møller, P., & Bertin, G. 2002: *The Evolution of Field Early-Type Galaxies to $z \sim 0.7$* , ApJ, 564, L13
- Treu, T., Stiavelli, M., Walker, A. R., Williams, R. E., Baum, S. A., Bernstein, G., Blacker, B. S., Carollo, C. M., *et al.* 1998: *An extremely red $r^{1/4}$ galaxy in the test image of the Hubble Deep Field South*, A&A, 340, L10
- Treyer, M. A., Ellis, R. S., Milliard, B., Donas, J., & Bridges, T. J. 1998: *An ultraviolet-selected galaxy redshift survey: new estimates of the local star formation rate*, MNRAS, 300, 303
- Tully, R. B. & Fisher, J. R. 1977: *A new method of determining distances to galaxies*, A&A, 54, 661
- Tyson, J. A. 1988: *Deep CCD survey - Galaxy luminosity and color evolution*, AJ, 96, 1
- Tytler, D., O'Meara, J. M., Suzuki, N., & Lubin, D. 2000: *Review of Big Bang Nucleosynthesis and Primordial Abundances*, Physica Scripta Volume T, 85, 12
- Väisänen, P. & Johansson, P. H. 2004: *Number counts of bright extremely red objects: Evolved massive galaxies at $z \sim 1$* , A&A, 421, 821
- van den Bergh, S., Abraham, R. G., Ellis, R. S., Tanvir, N. R., Santiago, B. X., & Glazebrook, K. G. 1996: *A Morphological Catalog of Galaxies in the Hubble deep Field*, AJ, 112, 359
- van den Bergh, S., Cohen, J. G., Hogg, D. W., & Blandford, R. 2000: *Caltech Faint Galaxy Redshift Survey. XIV. Galaxy Morphology in the Hubble Deep Field (North) and Its Flanking Fields to $z = 1.2$* , AJ, 120, 2190
- van der Wel, A., Franx, M., van Dokkum, P. G., & Rix, H.-W. 2004: *The Fundamental Plane of Field Early-Type Galaxies at $z = 1$* , ApJ, 601, L5
- van Dokkum, P. G. & Ellis, R. S. 2003: *On the Assembly History of Early-Type Galaxies in the Hubble Deep Field-North*, ApJ, 592, L53
- van Dokkum, P. G., Förster Schreiber, N. M., Franx, M., Daddi, E., Illingworth, G. D., Labbé, I., Moorwood, A., Rix, H., *et al.* 2003: *Spectroscopic Confirmation of a Substantial Population of Luminous Red Galaxies at Redshifts $z \gtrsim 2$* , ApJ, 587, L83

- van Dokkum, P. G., Franx, M., Förster Schreiber, N. M., Illingworth, G. D., Daddi, E., Knudsen, K. K., Labbé, I., Moorwood, A., *et al.* 2004: *Stellar Populations and Kinematics of Red Galaxies at $z > 2$: Implications for the Formation of Massive Galaxies*, ApJ, 611, 703
- van Dokkum, P. G., Franx, M., Kelson, D. D., & Illingworth, G. D. 1998: *Luminosity Evolution of Early-Type Galaxies to $Z = 0.83$: Constraints on Formation Epoch and Omega*, ApJ, 504, L17
- van Dokkum, P. G., Franx, M., Kelson, D. D., & Illingworth, G. D. 2001: *Luminosity Evolution of Field Early-Type Galaxies to $Z=0.55$* , ApJ, 553, L39
- van Dokkum, P. G. & Stanford, S. A. 2003: *The Fundamental Plane at $z = 1.27$: First Calibration of the Mass Scale of Red Galaxies at Redshifts $z > 1$* , ApJ, 585, 78
- Walker, A. G. 1935: *On the formal comparison of Milne's kinematical system with the systems of general relativity*, MNRAS, 95, 263
- Weinberg, S. 1972: *Gravitation and Cosmology: Principles and Applications of the General Theory of Relativity*, John Wiley & Sons
- Weymann, R. J., Stern, D., Bunker, A., Spinrad, H., Chaffee, F. H., Thompson, R. I., & Storrie-Lombardi, L. J. 1998: *Keck Spectroscopy and NICMOS Photometry of a Redshift $Z = 5.60$ Galaxy*, ApJ, 505, L95
- White, S. D. M. & Rees, M. J. 1978: *Core condensation in heavy halos - A two-stage theory for galaxy formation and clustering*, MNRAS, 183, 341
- Williams, R. E., Baum, S., Bergeron, L. E., Bernstein, N., Blacker, B. S., Boyle, B. J., Brown, T. M., Carollo, C. M., *et al.* 2000: *The Hubble Deep Field South: Formulation of the Observing Campaign*, AJ, 120, 2735
- Williams, R. E., Blacker, B., Dickinson, M., Dixon, W. V. D., Ferguson, H. C., Fruchter, A. S., Giavalisco, M., Gilliland, R. L., *et al.* 1996: *The Hubble Deep Field: Observations, Data Reduction, and Galaxy Photometry*, AJ, 112, 1335
- Wilson, G., Huang, J.-S., Pérez-González, P. G., Egami, E., Ivison, R. J., Rigby, J. R., Alonso-Herrero, A., Barmby, P., *et al.* 2004: *Extremely Red Objects in the Lockman Hole*, ApJS, 154, 107
- Wilson, R. N. 2004: *Reflecting Telescope Optics I: Basic Design Theory and its Historical Development*, Springer
- Wolf, C., Meisenheimer, K., Rix, H.-W., Borch, A., Dye, S., & Kleinheinrich, M. 2003: *The COMBO-17 survey: Evolution of the galaxy luminosity function from 25 000 galaxies with $0.2 < z < 1.2$* , A&A, 401, 73
- Wolf, C. *et al.* 2004: *GEMS: In what type of galaxies do most stars form at $z \sim 0.7$?*, ApJ, submitted, astro-ph/0408289

- Wuyts, S., van Dokkum, P. G., Kelson, D. D., Franx, M., & Illingworth, G. D. 2004: *The Detailed Fundamental Plane of Two High-Redshift Clusters: MS 2053-04 at $z = 0.58$ and MS 1054-03 at $z = 0.83$* , ApJ, 605, 677
- Yan, H. *et al.* 2004a: *High-Redshift Extremely Red Objects in the HST Ultra Deep Field REvealed by the GOODS IRAC Observations*, ApJ, in press, astro-ph/0408070,
- Yan, L., Choi, P. I., Fadda, D., Marleau, F. R., Soifer, B. T., Im, M., Armus, L., Frayer, D. T., *et al.* 2004b: *Spitzer 24 Micron Observations of Optical/Near-Infrared-Selected Extremely Red Galaxies: Evidence for Assembly of Massive Galaxies at $z \sim 1 - 2?$* , ApJS, 154, 75
- Yan, L., McCarthy, P. J., Weymann, R. J., Malkan, M. A., Teplitz, H. I., Storrie-Lombardi, L. J., Smith, M., & Dressler, A. 2000: *Extremely Red Objects from the Hubble Space Telescope NICMOS Parallel Imaging Survey*, AJ, 120, 575
- Yan, L. & Thompson, D. 2003: *Hubble Space Telescope WFPC2 Morphologies of K-selected Extremely Red Galaxies*, ApJ, 586, 765
- Yan, L., Thompson, D., & Soifer, B. T. 2004c: *Optical Spectroscopy of K-Selected Extremely Red Galaxies*, AJ, 127, 1274
- Yang, J., Turner, M. S., Schramm, D. N., Steigman, G., & Olive, K. A. 1984: *Primordial nucleosynthesis - A critical comparison of theory and observation*, ApJ, 281, 493
- Yasuda, N., Fukugita, M., Narayanan, V. K., Lupton, R. H., Strateva, I., Strauss, M. A., Ivezić, Ž., Kim, R. S. J., *et al.* 2001: *Galaxy Number Counts from the Sloan Digital Sky Survey Commissioning Data*, AJ, 122, 1104
- York, D. G., Adelman, J., Anderson, J. E., Anderson, S. F., Annis, J., Bahcall, N. A., Bakken, J. A., Barkhouser, R., *et al.* 2000: *The Sloan Digital Sky Survey: Technical Summary*, AJ, 120, 1579

Appendix A

Completeness of the Magnitude-Selected Spectroscopic Programme

In this appendix, I present magnitude-dependent completeness fractions for the five MUNICS fields with magnitude-selected spectroscopy (S2F1, S2F5, S5F1, S6F5, and S7F5). More precisely, we show K -band magnitude histograms of objects with successful spectroscopic redshift determination as compared to extended objects in the photometric catalogue.

The field with highest completeness, S2F1, also contains the sparse sample of faint objects observed spectroscopically at the VLT, thus its comparatively large number of objects fainter than $K' = 17.5$. In all other fields, objects fainter than this formal magnitude limit of the spectroscopic observations result from gaps in the slit masks having been filled with these objects.

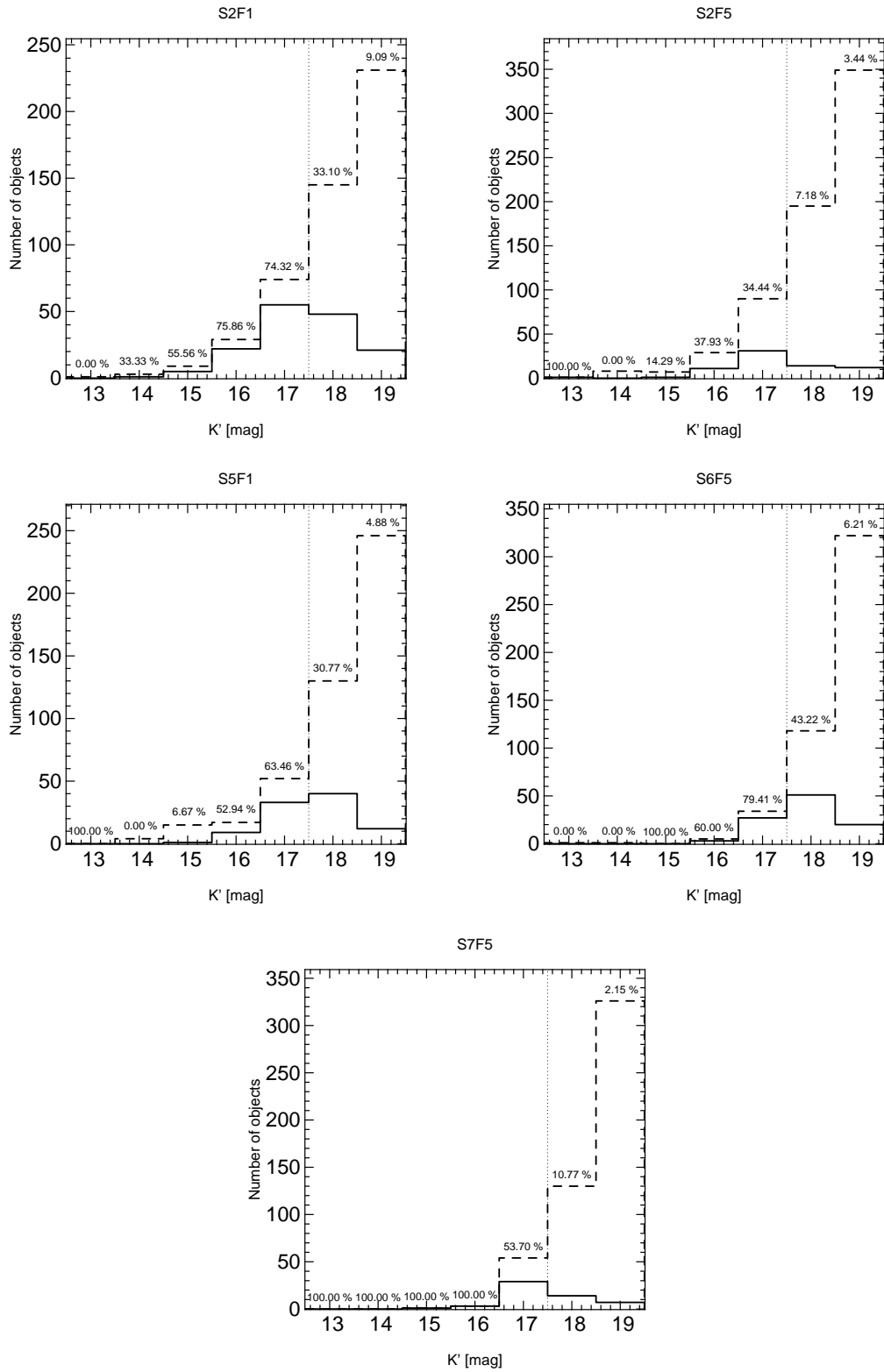


Figure A.1: Completeness of magnitude-selected spectroscopy in MUNICS. The dashed line shows the histogram of galaxies classified as extended in the photometric catalogue, the solid line the galaxies in the spectroscopic catalogue. The dotted line indicates the formal magnitude limit of $K' = 17.5$ of the spectroscopic observations.

Appendix B

Comparison of Photometry of K , I and B -Selected Objects

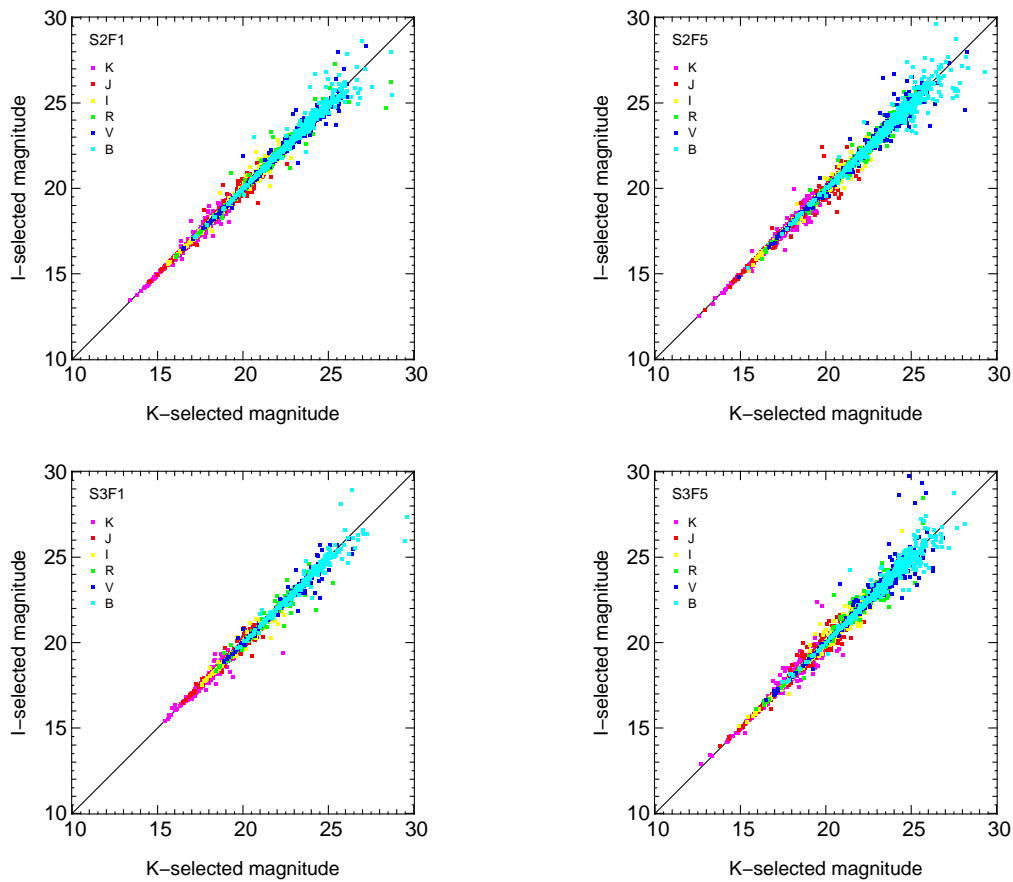


Figure B.1: Comparison of magnitudes of objects in the K -band and I -band selected catalogues for all ten MUNICS fields and for all six filters.

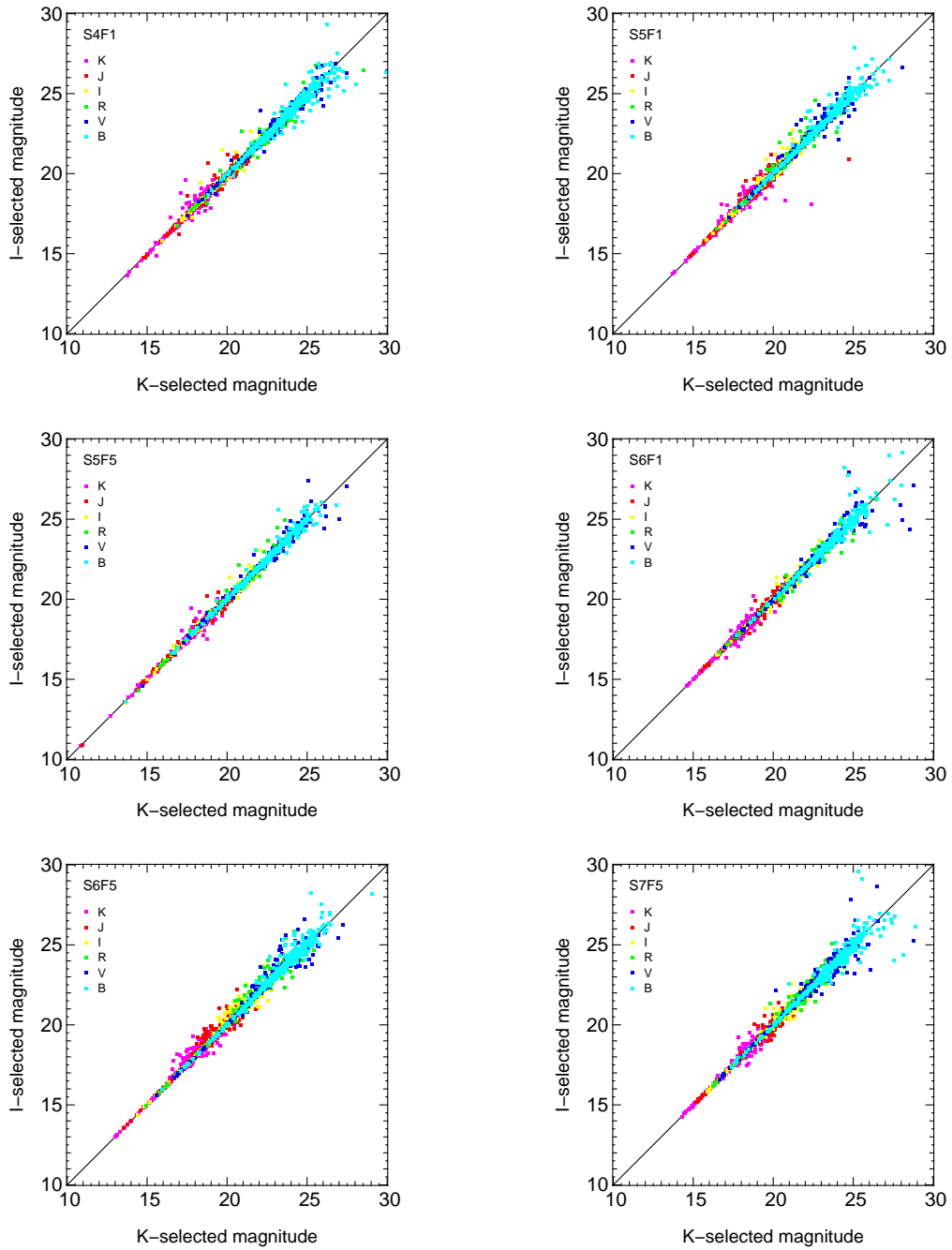


Figure B.1: Continued

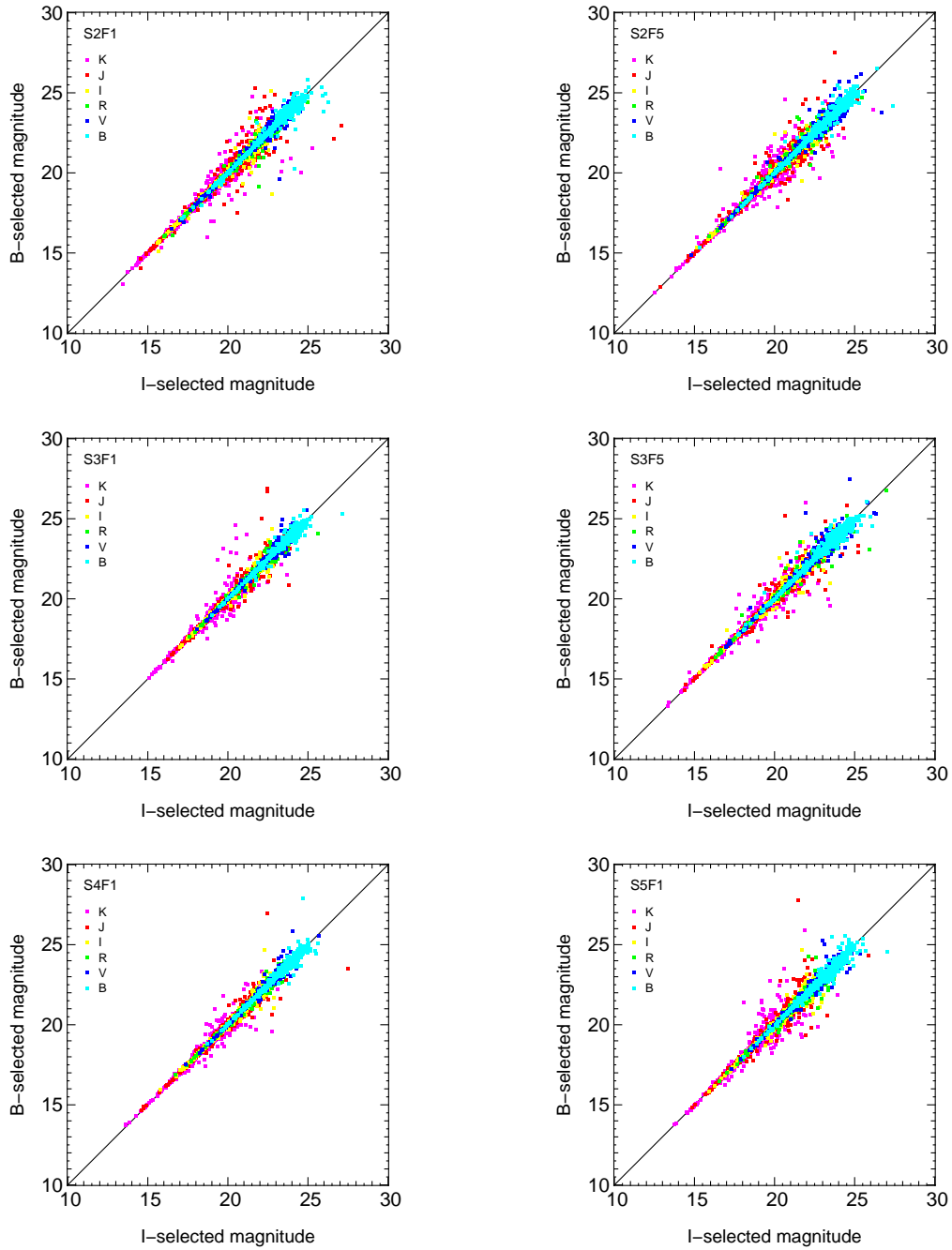


Figure B.2: Comparison of magnitudes of objects in the *I*-band and *B*-band selected catalogues for all ten MUNICS fields and for all six filters.

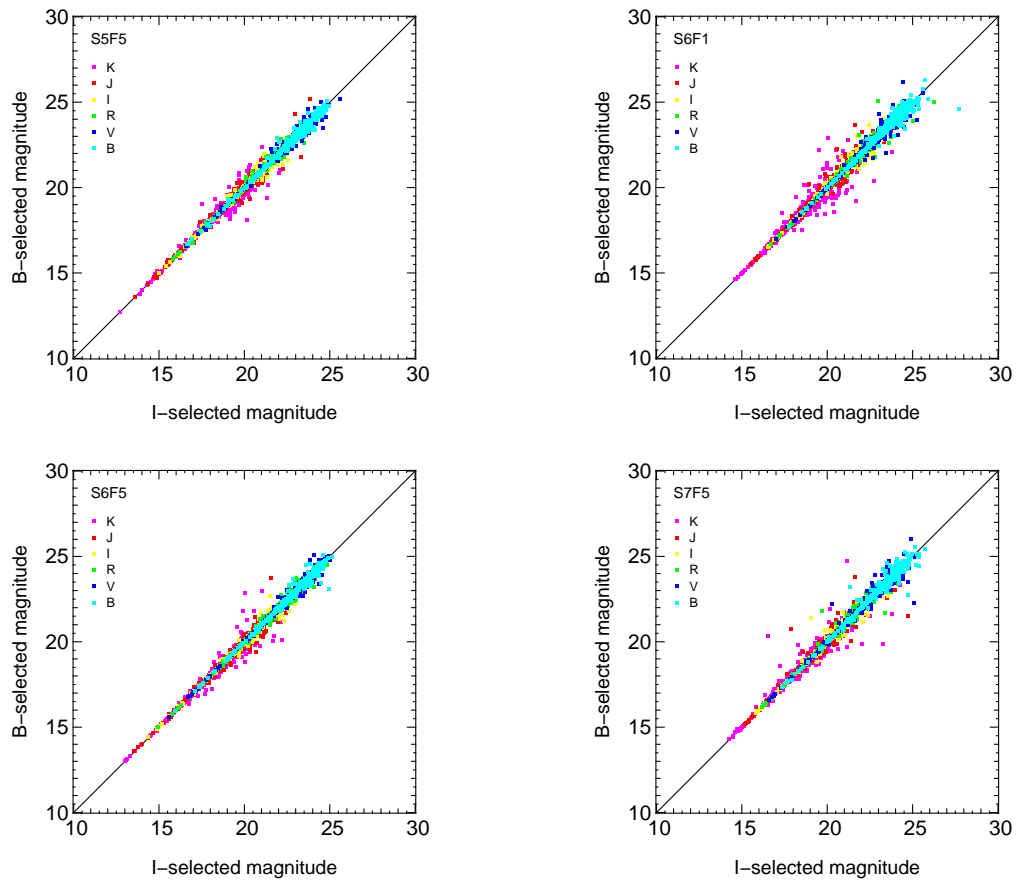


Figure B.2: Continued

Appendix C

Semi-Automatic Selection of PSF Stars for Morphological Image Classification

In this appendix we show diagrams illustrating the semi-automatic selection of stellar objects used for deriving the point-spread function (PSF) in each image. The detailed procedure is described in detail in Section 7.1. In brief, we select relatively bright symmetric objects for which we derive the Gaussian FWHM. Then we select all objects the FWHM of which is within 3σ around the stellar FWHM measured.

Note that in some cases the number of stars is so small, that this algorithm needed some manual interaction. Also note that the near-infrared (K and J band) images are mosaics of four individual images, so there is the possibility of slightly differing PSFs in the individual parts.

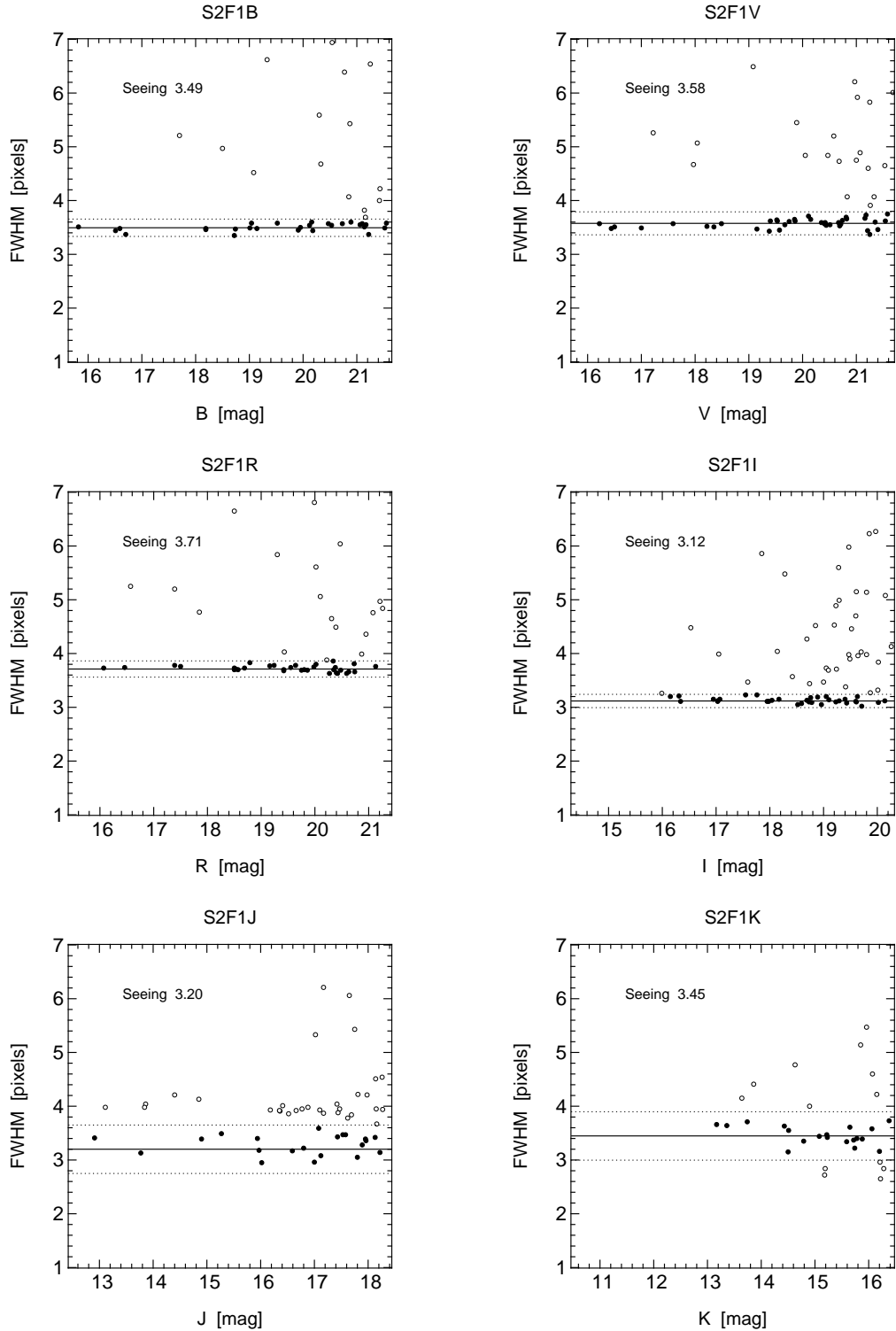


Figure C.1: Semi-automatic selection of PSF stars in the MUNICS fields. The measured seeing FWHM in pixels is given in each figure and denoted by the solid line. The circles represent bright, symmetric objects in each field. All objects between the dotted lines (filled circles) were selected for deriving the PSF necessary for morphological classification (see text for details).

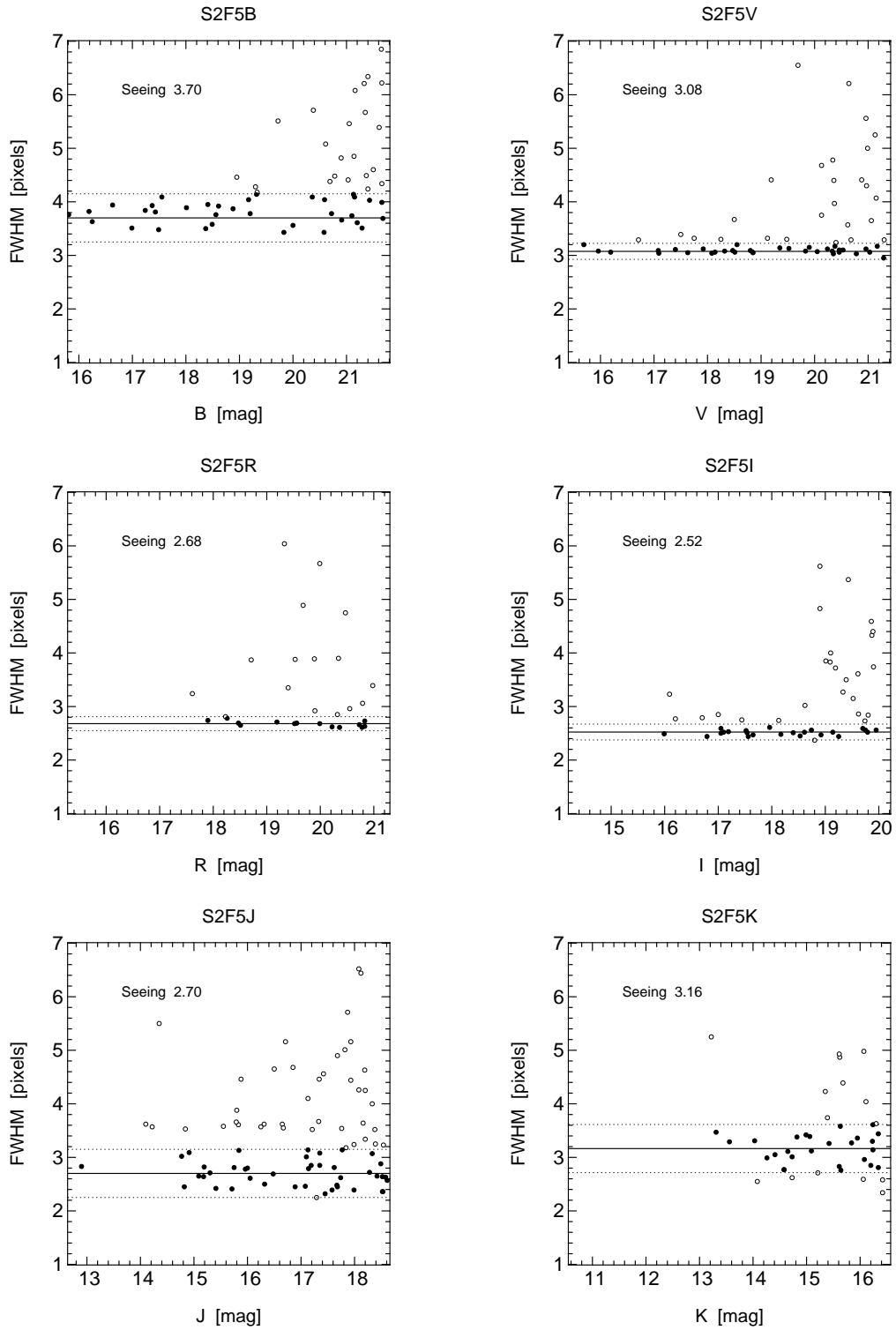


Figure C.1: Continued

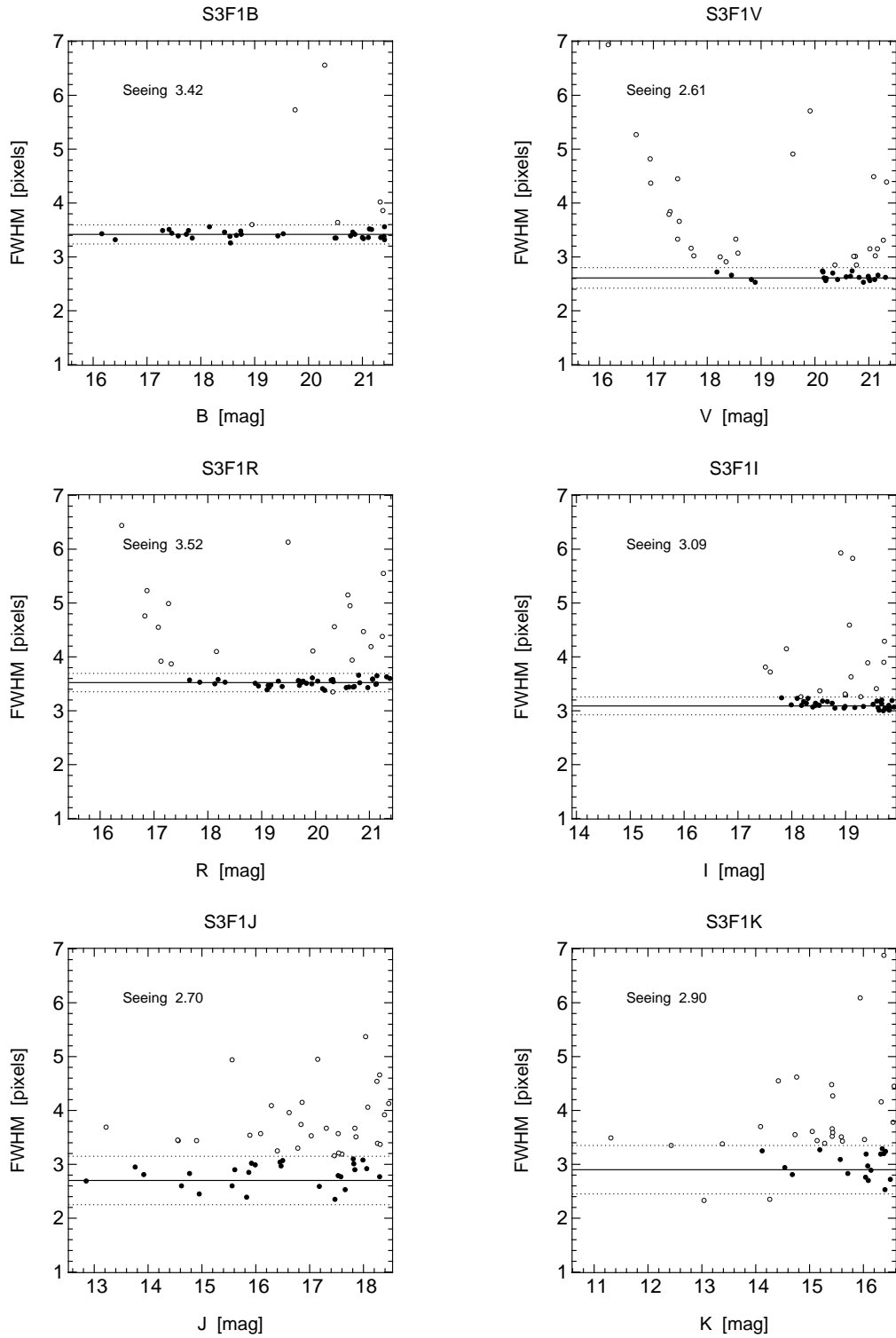


Figure C.1: Continued

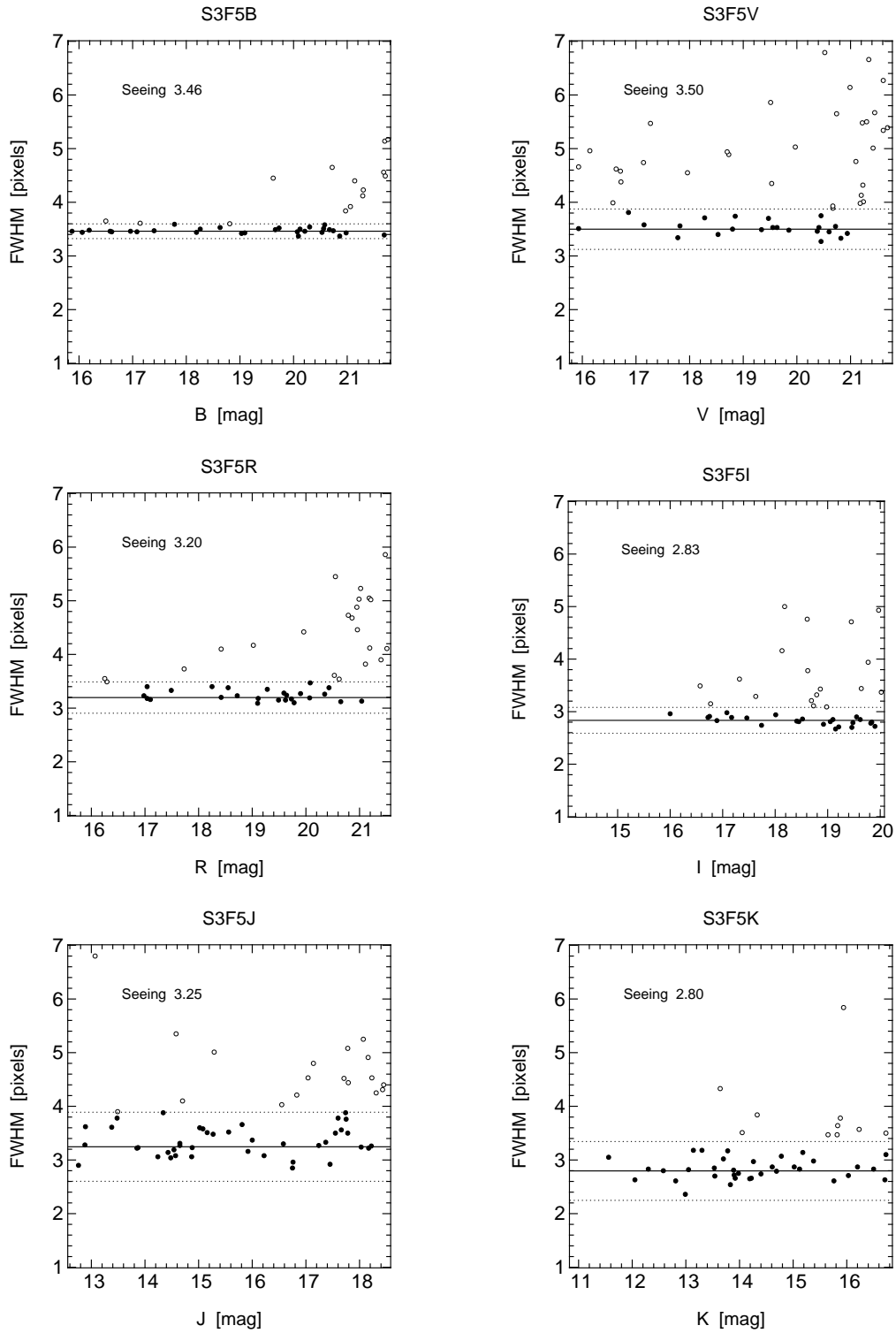


Figure C.1: Continued

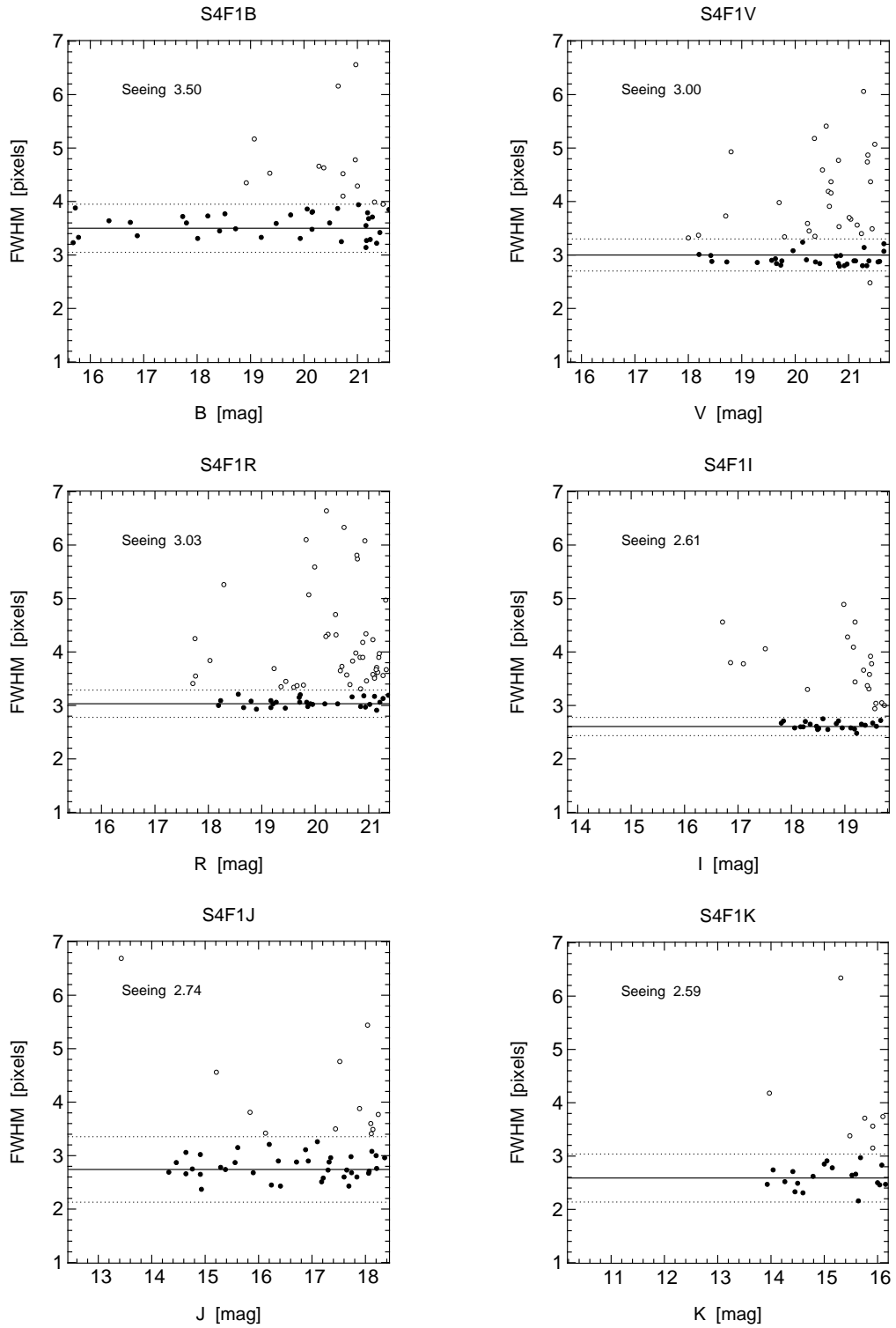


Figure C.1: Continued

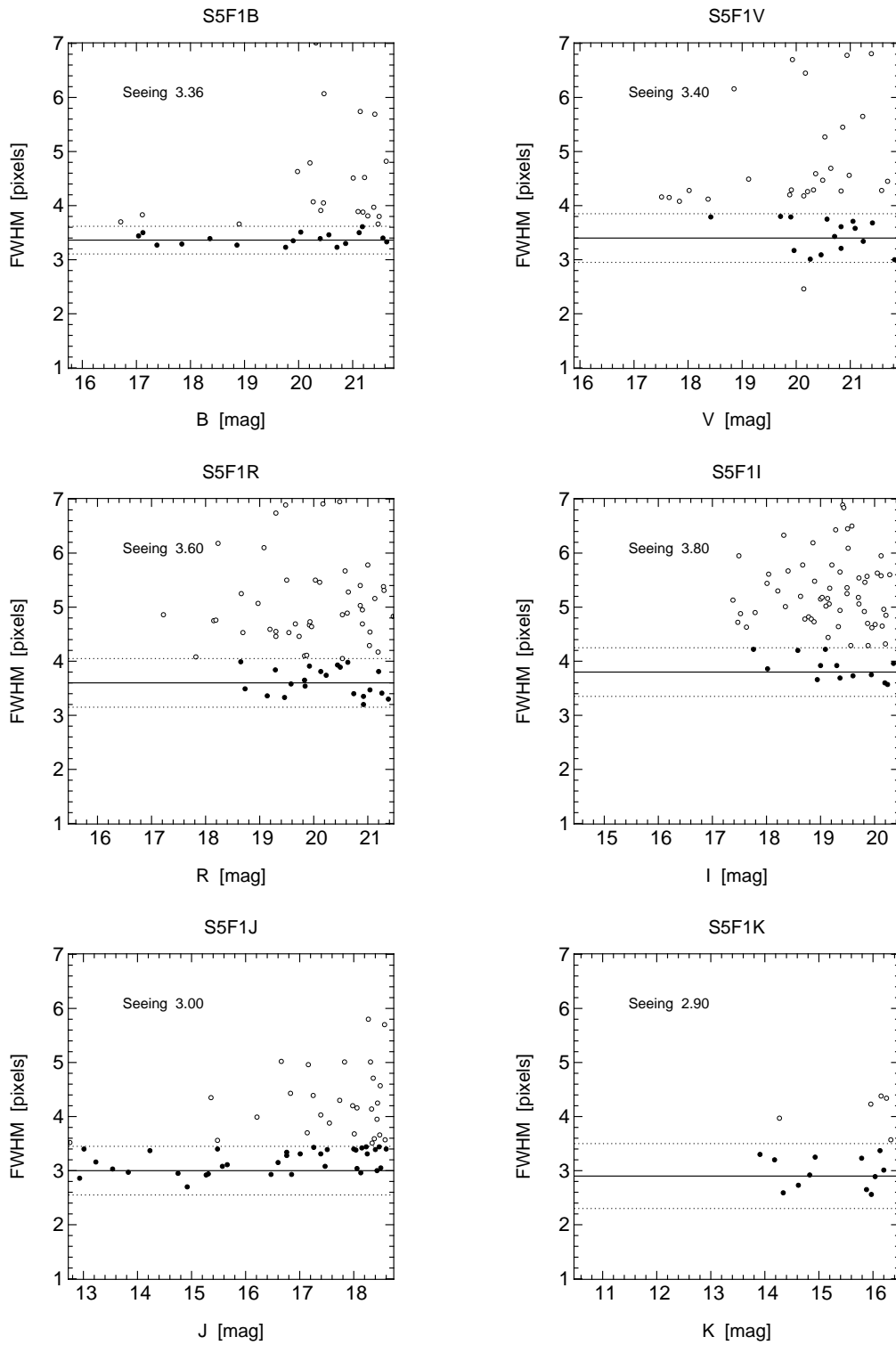


Figure C.1: Continued

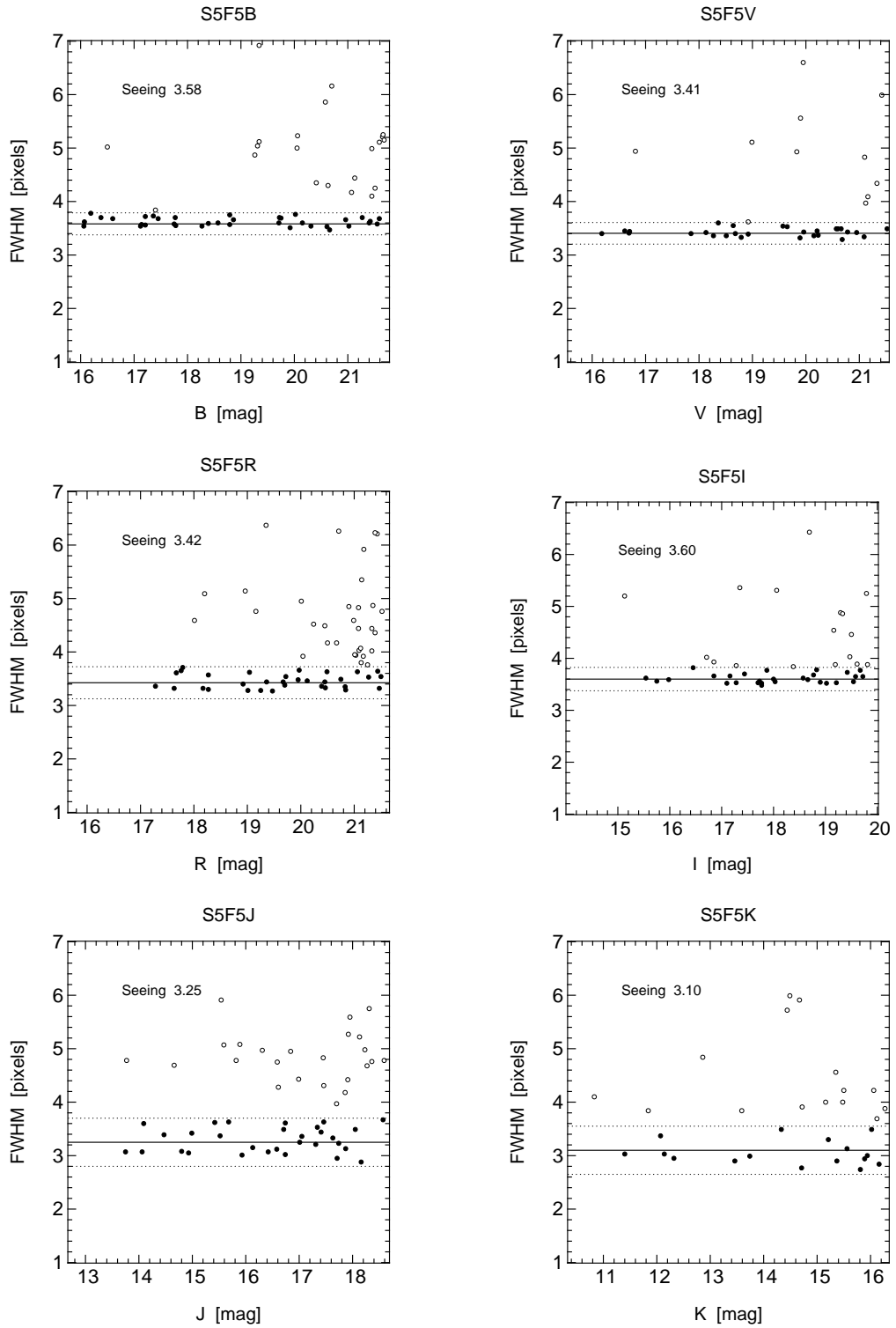


Figure C.1: Continued

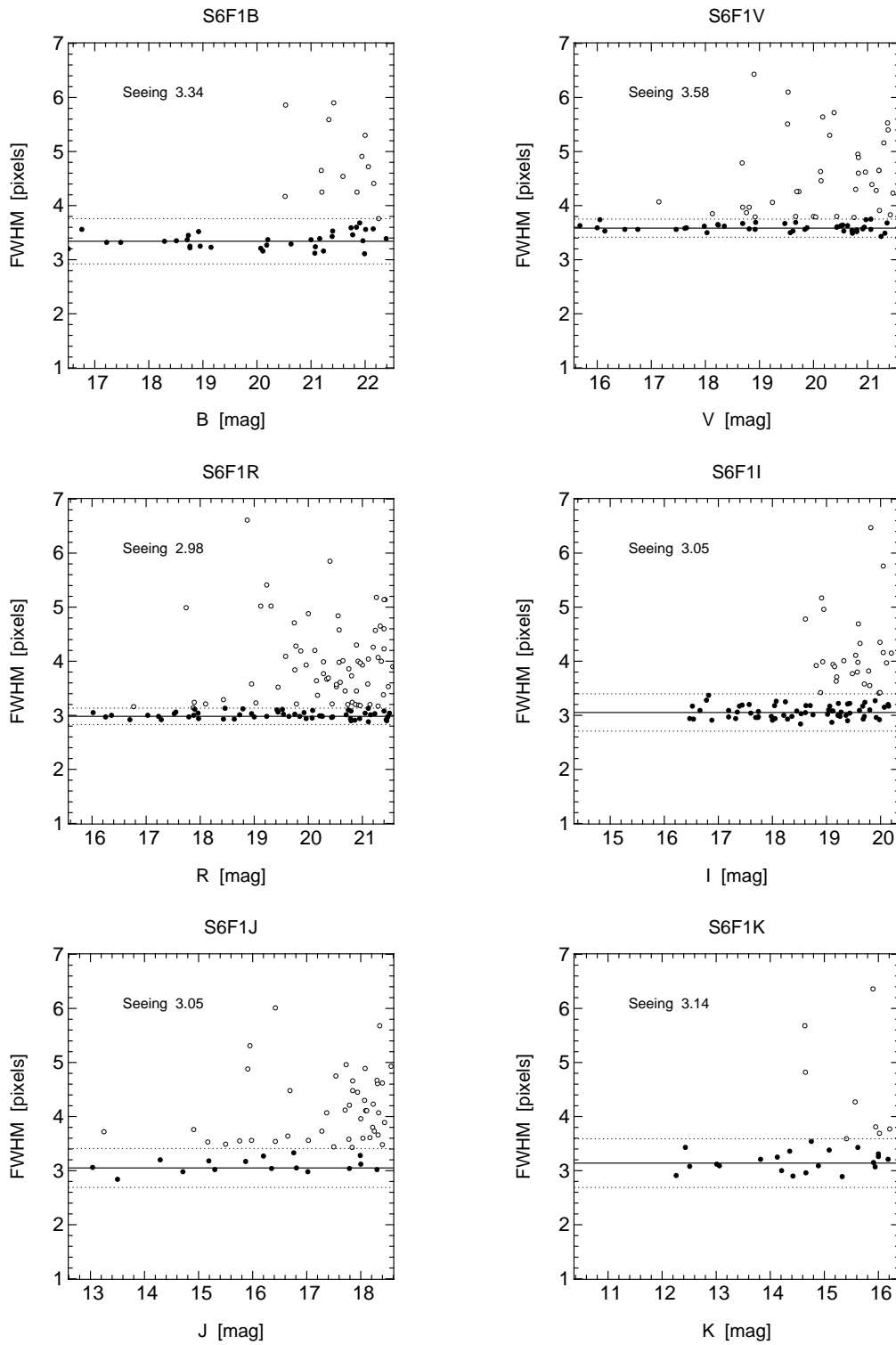


Figure C.1: Continued

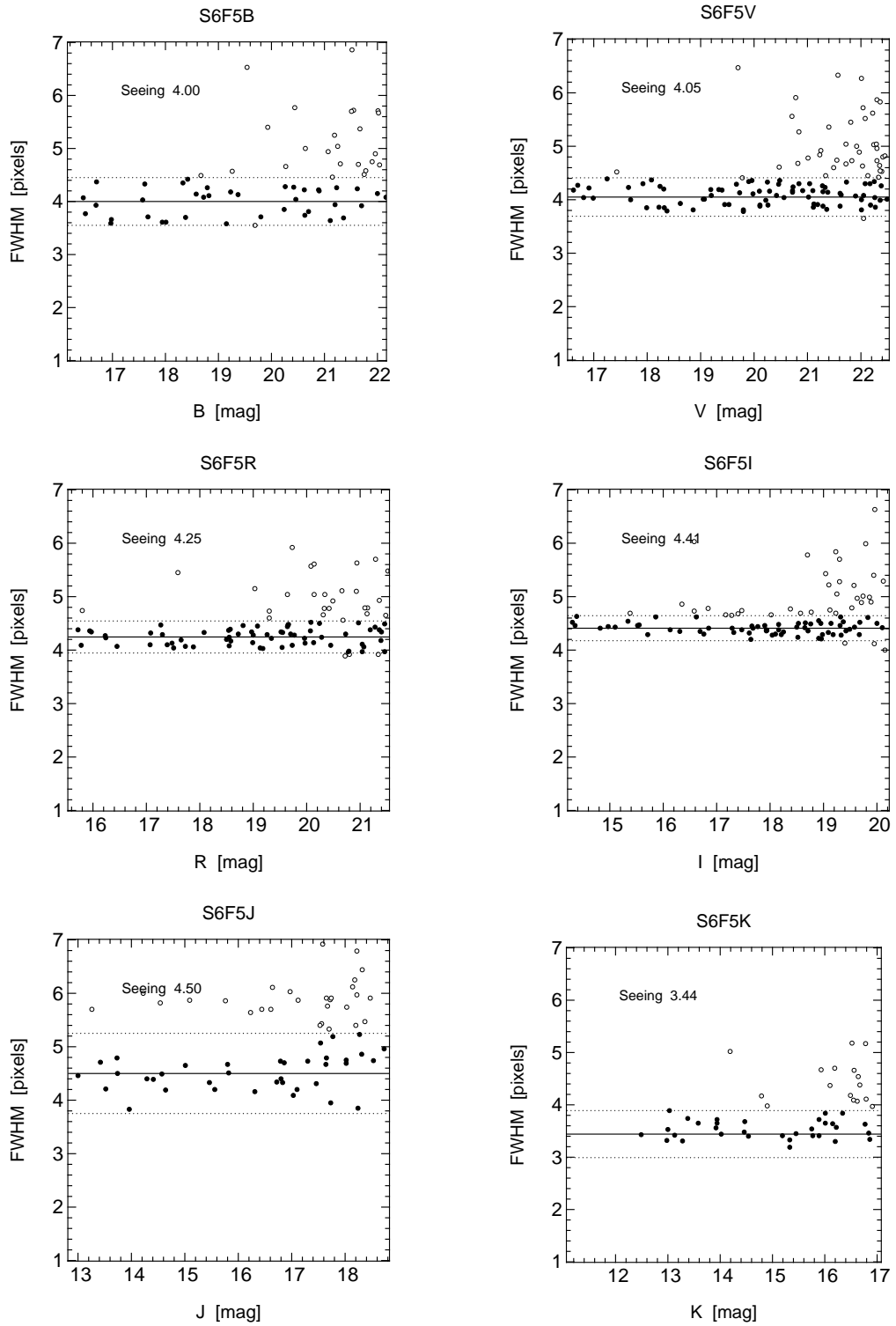


Figure C.1: Continued

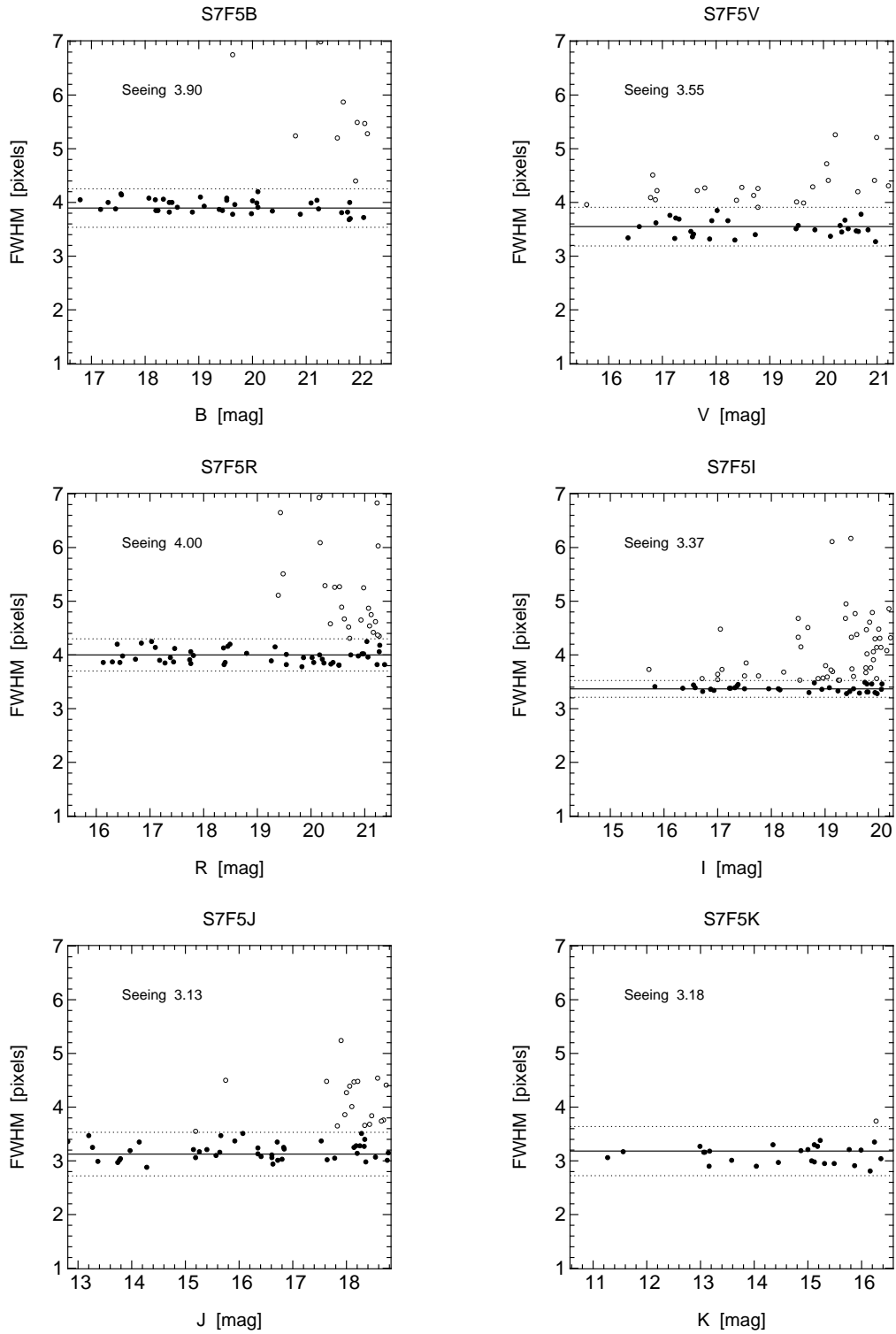


Figure C.1: Continued

Acknowledgements

First of all I would like to thank Ralf Bender, my thesis supervisor, for his help and support. Since my time as a student he has always had time for answering my questions and giving me advice. He has offered me a PhD position without which, quite naturally, this work would not have been possible. Also, I appreciate his administrative efforts, since I know that he would prefer to spend more time doing science.

My advisor, Ulrich Hopp, deserves my gratitude for everything he did for me during the last years. He taught me much of what I know about astronomy, asked important (and often quite nasty!) questions, in turn provided answers to my numerous questions, gave me honest advice, cared about me, my work and my future, and was so much more a friend than a colleague. I could not, and indeed would not, have done without him.

Harald Lesch has become a great friend. He was always interested in my work and its progress, agreed to be referee for this thesis, cheered me up when I was frustrated, taught me many things about relativistic astrophysics and plasmas, even more about politics (at the university and beyond), and was a constant source of interesting thoughts and initiator of enlightening discussions about life, the universe and everything.

It is a pleasure to thank Jan Snigula who helped me with numerous computer problems. Also, it was fun working with him on MUNICS problems in the good old days when he was still working on the project, and, of course, I enjoyed (and still do enjoy!) sharing an office with him, or, as he would put it, being allowed to stay in *his* office... Finally I will not forget all the meals he cooked and all the muffins he supplied for various parties at the institute.

I am deeply grateful to Armin Gabasch. We are both working on similar aspects of galaxy evolution, and working with him was always a pleasure, especially since our ideas of science and how it should be done agree so well. Sharing the exciting and frustrating aspects of science made our life a lot easier. Moreover, I remember many discussions about topics beyond astronomy and, of course, the exciting hours we spent in lectures on Greek history.

Thanks are due to Claus Gössl for help with data reduction and computer problems, and for making me laugh, and to Arno Riffeser for helpful discussions about data reduction and mathematics. The latecomer in the MUNICS team, Yulia Goranova, helped with producing the optically selected catalogues, and, together with Jan Snigula and Chris Botzler with the catalogue cleaning.

Jürgen Fliri is acknowledged for giving me a ride to numerous lectures or talks, for lots of cookies (too many in fact), and for cheering me up with stories about lost keys, yellowish postscript documents, Italian sports and politics, and many other things. I would also like to thank Claudia Maraston and Daniel Thomas for helpful comments on talks, interesting discussions and their friendly interest in my work.

Thanks also to Niv Drory for introducing me to MUNICS, the worlds of data reduction and extragalactic astronomy, and for supplying his galaxy model fitting algorithm.

Furthermore I would like to thank all current and former members of our group and all guest scientists, in particular Chris Botzler, Laura Greggio, Aleksii Halkola, Gary Hill, Claudia Mendes de Oliveira, Mark Neeser, Roberto Saglia, Regina Schulte-Ladbeck, Stella Seitz and Jens Thomas, for their help and their friendliness. The Universitäts-Sternwarte is a wonderful place with a very friendly atmosphere. I am grateful to all people working at the institute for making it such a special place. Special thanks to Veronika Junk for providing cookies every day.

I would like to thank Lutz Wisotzki for teaching me a lot on AGN and for his hospitality: Visits to Potsdam/Berlin were always an exciting combination of hard scientific work, memorable concerts, and wonderful food.

The Sonderforschungsbereich 375 *Astroteilchenphysik* der Deutschen Forschungsgemeinschaft is acknowledged for supporting the MUNICS project in general, but especially for paying my salary and for funding my travels to Calar Alto. The MUNICS project could not have been carried out without this generous support.

It is a pleasure to thank the Time Allocation Committee for Calar Alto for giving such a lot of nights to this project, and the staff at Calar Alto, ESO and McDonald Observatory for their support. I want to thank in particular Ulli Thiele for his help and the organisation of service observations, and all the night assistants at Calar Alto for carrying out service observations, helping me when I was observing, fixing technical problems, and for all the conversation in long nights at the observatory. Furthermore, I would like to thank Josef Fried and the people at the MPIA workshop for producing a very large number of MOSCA slit masks.

Special thanks also to the people at the astrophysics group at the Universität Potsdam and at the Astrophysikalisches Institut Potsdam for their hospitality during visits at their institutes. I would like to thank Nigel Metcalfe for making his compilation of galaxy number counts available to the public, and Amanda Bauer for helpful discussion on the specific star formation rate.

All my friends, in particular Andi Ammersbach, Chris Botzler, Kate English, Christine Gerstenecker, Claus Gössl, Jörg Hoffmann, Alexandra & Tobias Jung, Jasper Lewitton, Jan Snigula, Sofia Meier-Stiegen, Caryn Myers, Markus Schwald and James Watson, deserve my gratitude for their friendship and support throughout the years.

The same is true, of course, for my family, especially for my mother and my sisters. Their love and help was an invaluable contribution to the success of this work.

Finally I want to thank my wife Christine for her love, friendship and patience. She supported me at all times and shared all disappointing and joyous moments throughout my PhD time. Without her this work would have been hard to accomplish.

Curriculum Vitae (Lebenslauf)

Persönliche Daten:

Name: Georg Feulner
Geburtsdatum: 19. August 1974
Geburtsort: Wasserburg am Inn
Familienstand: verheiratet, keine Kinder
Anschrift: Kirchenstraße 38, 81675 München

Ausbildung:

1981 – 1985 Grundschule Babensham bei Wasserburg am Inn
1985 – 1994 Luitpold-Gymnasium Wasserburg am Inn
1994 Abitur
1994 – 2000 Studium der Physik an der Ludwig-Maximilians-Universität (LMU) München
1994 – 2000 Stipendium nach dem Bayerischen Begabtenförderungsgesetz (BayBFG)
1997 – 1998 Studium der Angewandten Mathematik und Theoretischen Physik an der University of Cambridge (UK)
1998 *Certificate of Advanced Study in Mathematics* (M.Sc.), University of Cambridge (UK)
1999 – 2000 Diplomarbeit an der Universitäts-Sternwarte München über „Optische Komplementärbeobachtungen zur Suche nach Galaxienhaufen im Infraroten“
1999 Stipendiat der Friedrich-Geissendörfer-Stiftung für Astronomie an der LMU München
2000 Diplom in Physik, LMU München
2000 – 2004 Promotion in Astronomie an der LMU München

Berufliche Tätigkeit:

2000 – Wissenschaftlicher Angestellter im Sonderforschungsbereich 375 Astro-Teilchenphysik der Deutschen Forschungsgemeinschaft
2000 – 2003 regelmäßige Tätigkeit als wissenschaftliche Hilfskraft an der LMU (Probestudium, Praktika, Übungsgruppen, Astropraktikum)